Geochemistry of vanadium in hyperalkaline environments

Andrew James Hobson

Submitted in accordance with the requirements for the degree of

Doctor of Philosophy

The University of Leeds

School of Earth and Environment

July 2017

The candidate confirms that the work submitted is his/her own, except where work which has formed part of jointly authored publications has been included. The contribution of the candidate and the other authors to the work has been explicitly indicated below. The candidate confirms that appropriate credit has been given within the thesis where reference has been made to the work of others.

The work in Chapter 4 of the thesis has appeared in publication as follows:

Hobson, A. J., Stewart, D. I., Bray, A. W., Mortimer, R. J. G., Mayes, W. M., Rogerson, M. and Burke, I. T. (2017) Mechanism of Vanadium Leaching during Surface Weathering of Basic Oxygen Furnace Steel Slag Blocks: A Microfocus X-ray Absorption Spectroscopy and Electron Microscopy Study. *Environmental Science & Technology (in press).*

Candidate's contribution – all experimental work, preparing samples for and performing XRD and SEM/EDX analysis, collection and interpretation of XANES data, writing the manuscript and producing all figures and tables therein. Douglas Stewart – assisted with data collection during beamtime and provided extensive manuscript review. Andrew Bray – provided XRF data, assisted with data collection during beamtime and commented on the manuscript. Robert Mortimer, William Mayes and Mike Rogerson – all provided comments on the manuscript. Ian Burke – initial concept, assisted with data collection during beamtime, interpretation of XANES data and provided extensive manuscript review.

The work in Chapter 5 of the thesis has been submitted for publication as follows:

Hobson, A. J., Stewart, D. I., Mortimer, R. J. G., Mayes, W. M., Rogerson, M. and Burke, I. T. Leaching behaviour of co-disposed steel making wastes: Effects of aeration on leachate chemistry and vanadium mobilisation. (*In preparation for Applied Geochemistry, July 2017).*

Candidate's contribution – all experimental work, preparing samples for and performing XRD and SEM/EDX analysis, data interpretation, manuscript preparation and all figures and tables therein. Douglas Stewart – provided extensive manuscript review. Robert Mortimer, William Mayes and Mike Rogerson – all provided comments on the manuscript. Ian Burke – initial concept, provided extensive manuscript review and assisted with data interpretation.

The work in Chapter 6 of the thesis is in preparation for submission for publication as follows:

Hobson, A. J., Stewart, D. I., Bray, A. W., Mortimer, R. J. G., Mayes, W. M., Riley, A. L. and Burke, I. T. Behaviour and fate of vanadium during the aerobic neutralisation of hyperalkaline steel slag leachate. *(In preparation for Science of the Total Environment, July 2017).*

Candidate's contribution – collection of field samples used in leachate neutralisation experiments, developing the method and carrying out leachate neutralisation experiments, collection and interpretation of XANES data, preparation of the manuscript and all tables and figures therein except where stated below. Douglas Stewart – assisted with data collection during beamtime and provided comments on the manuscript. Andrew Bray – assisted with data collection during beamtime. William Mayes – provided historical field data. Ian Burke – initial concept, assisted with data collection during beamtime, provided interpretation, figures and tables relating to EXAFS data and extensive manuscript review. Mike Ward – collected TEM-EDS data with the guidance of the candidate and Ian Burke.

Acknowledgements

I would like to express my sincere thanks to Ian Burke, Doug Stewart, Rob Mortimer and Will Mayes for all the help, support and encouragement I've received throughout the last few years. Ian in particular has endured (and answered) endless inane questions and stoically tolerated a distinctly relaxed approach to writing, and never once let the despair show. I couldn't have asked for more.

I would also like to thank the Cohen lab techs for making the labs such a great, fun place to work. Andy Connelly for all the support and some great competition in the occasional local fell race; you'll get those three minutes back next time! Also Stephen Reid for the ICP and endless chats about anything non-work related (but usually the Lakes) and Lesley Neve for the X-ray help and being generally bonkers. Elsewhere, Richard Walshaw, Duncan Hedges and Mike Ward at LEMAS, and Fred Mosselmans and Tina Geraki at Diamond Light Source all made the hours sitting underground in small boxes worthwhile with their technical knowledge and expertise.

A huge thanks to all the members of the Cohen Geochemistry group, past and present, especially Cindy Lockwood, Daniela van den Heuvel, Adam Fuller and Steffi Lutz. Particular thanks to Andy Bray for the bikes, being my occasional partner in crime and making field trips loads more fun, and Meg – I still think all of this is your fault.

Burko's Science Club and the other SCR exiles have really made the last few years something special. Huge, huge thanks are due to Jenny, Mark, Andrea and especially Ais (have a nice life), for being there from the beginning. I can't imagine a better group to have hung out with for the last few years. Thanks also to Emma and Kathy for putting up with some weapons-grade moaning/procrastination over the final few months without killing me. It's been a lot of fun.

Outside of Uni, a big thanks to the ex-geols – Ben, Kerry, Britney, Franki and Nic, and of course the ex-geols once-removed, Inga and Jules. All the midweek Malham and Kilnsey

crowd, the Depot regulars, P & B Tuesday nighters and anyone else I've climbed, cycled or run with; thank you all for providing plenty of much needed distractions and/or abuse, and helping me keep my sense of humour and perspective more or less intact.

To my family, and in particular my Mum and Dad – thank you so much for all your quiet, unwavering support and acceptance of my inability to just stop messing around and get a proper job. Finally to Julie – none of this would ever have happened without your love, support and encouragement. After all the ups, downs and sleepless nights of the last few years, I hope I've managed to do it justice.

Abstract

Hyperalkaline environments associated with leaching of industrial wastes such as steel slags can have a number of deleterious effects on their local environment including rapid carbonate precipitation and mobilisation of potentially toxic trace metals. Steel slag is the primary byproduct of steelmaking and is enriched in trace elements such as Al, Cr and V. V is of particular concern due to its high concentration in steel slag, its potential toxicity and its mobility in high pH leachate as the vanadate oxyanion (VO_4^{3-}). This study used aerated and air-excluded batch leaching tests, aerated leachate neutralisation tests, field observations, X-ray microanalysis and electron microscopy techniques to investigate the effects of environmental conditions on V mobility, leachate chemistry and secondary phase formation during weathering of steel slags. Scanning electron microscopy/energy-dispersive X-ray spectroscopy (SEM/EDX) identified four principal mineral phases in unweathered slag comprising dicalcium silicate (Ca_2SiO_4), dicalcium aluminoferrite ($Ca_2(Al,Fe)_2O_5$), a CaO-rich phase, and a Wüstite-like solid solution ($(Fe, Mn, Mg, Ca)O$). V was primarily incorporated in the dicalcium aluminoferrite (~1.1 wt%) and dicalcium silicate phases (~0.4 wt%). During leaching, alkalinity was rapidly produced by dissolution of dicalcium silicate and free lime resulting in a high pH (11.5 – 12.5) leachate. Dicalcium silicate dissolution leads to oversaturation with respect to calcium silicate hydrate (Ca-Si-H) phases and their subsequent precipitation. Under aerated conditions, in-gassing of atmospheric CO_2 resulted in $CaCO_3$ precipitation which consumed OH^- ions and subsequently lowered solution pH to ~8.0. Micro-focus X-ray absorption spectroscopy (μXAS) analysis showed that V was released as V^{5+} during dicalcium silicate dissolution. V release was significantly higher under aerated conditions than under air-excluded conditions (~850 ppb and 490 ppb respectively in block leaching tests). Aqueous V concentrations were influenced by $Ca_3(VO_4)_2$ solubility limits which imposed an inverse relationship on Ca and V concentrations. In air-excluded systems, leachate reaches

saturation with respect to $Ca_3(VO_4)_2$ which precipitates thus limiting aqueous V concentrations. Under aerated conditions, precipitation of $CaCO_3$ provided a sink for aqueous Ca. Leachate therefore remained undersaturated with respect to $Ca_3(VO_4)_2$, allowing higher concentrations of V to accumulate in solution. Leachate neutralisation experiments showed that some V was incorporated into neo-formed $CaCO_3$ at high pH. V removal was enhanced in the presence of goethite (α-FeOOH). Extended X-ray absorption fine structure (EXAFS) analysis showed that vanadate adsorbed to goethite by formation of inner-sphere complexes indicating that Fe (oxy)hydroxides provide an important environmental sink for V in steel slag leachates. This study highlights the importance of leaching environment for V mobility during weathering of steel slags and suggests that prospects for slag reuse and storage may be improved by the formation of a weathered region containing secondary phases including Ca-Si-H and $CaCO_3$. Leachate neutralisation results demonstrate removal mechanisms for aqueous V which will assist with environmental risk assessment and remediation at legacy sites where leachate has been released to the local aquatic environment.

Table of Contents

List of Figures

List of Tables

Table of Acronyms

BF	Blast furnace
BOF	Basic oxygen furnace
Ca-Si-H	Calcium silicate hydrate
DIW	Deionised water
EAF	Electric arc furnace
EDS/X	Energy-dispersive X-ray spectroscopy
EXAFS	Extended X-ray absorption fine structure
GGBF	Ground granulated blast furnace (slag)
ICP-MS/OES	Inductively coupled plasma mass spectrometry/optical emission spectrometry
PZC	Point of zero charge
SEM	Scanning electron microscopy
TEM	Transmission electron microscopy
XAS	X-ray absorption spectroscopy
XANES	X-ray absorption near edge structure
XRD	X-ray diffraction
XRF	X-ray fluorescence

Chapter 1   Introduction

1.1   Project background and rationale

Naturally occurring hyperalkaline groundwater environments have received relatively little attention due to their comparative scarcity. Such environments only occur rarely in nature. Highly alkaline environments created due to weathering and leaching of industrial byproducts and wastes (including steel slags (Roadcap et al., 2005), chromite or bauxite processing residue (Mayes et al., 2011; Stewart et al., 2007) and fly or soda ash (Effler et al., 2001; Mattigod et al., 1990)) are more common. However, in contrast to their acidic counterparts they remain relatively poorly understood. These wastes and their leachates are of particular concern for several reasons including extremes of alkalinity (which may be toxic in themselves, with pH values above 10.5 being considered hazardous to aquatic organisms (Wilkie and Wood, 1996)), high salinity and ionic strength, and high rates of calcite ($CaCO_3$) precipitation leading to smothering of benthos where highly alkaline leachate emerges and reacts with atmospheric CO_2 (Effler, 1987). Wastes are also often enriched in toxic oxyanion forming elements (e.g. As, V, Cr, Ni, Mo, Li; (Burke et al., 2012; Roadcap et al., 2005)) which may be mobile at the high pH conditions found in leachates. The increasing prevalence of these byproducts and wastes across the globe and the potential risks they pose has led to an increase in interest in their behaviour in recent years.

Steel slag is a primary byproduct of steelmaking which is formed when a fluxing agent (usually limestone or dolomite) is added to molten iron or steel to remove impurities and to control the composition of the final product. Steel slag is produced in large volumes worldwide (160 – 240 million tonnes, Ober (2017)) and increasingly stringent environmental regulations regarding its disposal have led to the development of a number

of alternative uses in order to reduce the quantity being stored in landfill. Some steel slag can be recycled directly in furnaces, however, they are mostly reused in the construction industry in cement clinker, road surfacing or as aggregate due to their high compressive strength and stability. Other potential afteruses include neutralisation of acidity in soils and CO_2 sequestration (Piatak et al., 2014). Steel slag may be enriched in phases such as free lime (CaO), periclase (MgO) and unstable forms of dicalcium silicate that expand on hydration resulting in significant volume changes thus making these materials unsuitable for engineering use. For this reason, or simply due to supply frequently outstripping demand, large quantities of steel slags are still stored in landfill (Motz and Geiseler, 2001; Proctor et al., 2000). Whilst steel slag is generally considered to be a non-hazardous material, concerns over its use and storage have been raised in recent years.

Steel slags primarily comprise Ca, Mg, Fe and Al oxides and silicates including free lime (CaO) and periclase (MgO), dicalcium silicate (larnite; β- and γ-Ca_2SiO_4), dicalcium ferrite (srebrodolskite; $Ca_2Fe_2O_5$), dicalcium aluminoferrite (brownmillerite; $Ca_2(Al, Fe)_2O_5$) and a refractory oxide solid solution similar to wüstite and containing Ca, Mn, and Mg ((Ca, Mn, Mg, Fe)O) (Chaurand et al., 2006; Yildirim and Prezzi, 2011). Weathering of these phases in contact with water leads to rapid generation of high pH (10 – 12.5) leachate due to dissolution of CaO and calcium silicates and subsequent release of hydroxyl ions (OH$^-$) (Mayes et al., 2008; Roadcap et al., 2005). When this high pH groundwater comes into contact with atmospheric CO_2 rapid precipitation of calcite takes place (Mayes and Younger, 2006). At legacy slag heaps which pre-date environmental legislation, these processes have had deleterious effects on local watercourses with a severe reduction in ecological diversity and abundance observed in affected waters (Hull et al., 2014).

Steel slag can be enriched in trace metal(loid)s including potentially toxic elements (e.g. Al, Fe, Li, Mo, Ni, Cr and V) which are concentrated during processing from primary

ores (Hull et al., 2014; Proctor et al., 2000). The potential mobilisation of these toxic elements during weathering has been raised as the primary environmental concern relating to weathering of steel slags and accumulation of metals in leachates is problematic with regard to long term management of landfilled slags.

V is of particular concern due to its relatively high concentrations in steel slags and past research has revealed the potential for it be mobilised in leachate in environmentally significant quantities (De Windt et al., 2011; Riley and Mayes, 2015). V is a redox sensitive transition element with oxidation states between 0 and +5 with the +3, +4 and +5 species being stable under aqueous conditions (Chaurand et al., 2007; Peacock and Sherman, 2004). Solubility and toxicity generally increase with valence, with V^{5+} (the most toxic form) being readily solubilised as the vanadate oxyanion (VO_4^{3-}) at the high pH ranges associated with steel slag leachate (Wehrli and Stumm, 1989). Previous research has suggested that V may accumulate at high concentrations (up to 15 ppm) in hyperalkaline leachates such as those associated with bauxite processing (Burke et al., 2013).

The complex leaching behaviour of V which is dependent on pH and redox, in addition to its potential toxicity, has prompted regulatory bodies to adopt 'worst case scenario' approaches when dealing with steelmaking wastes (Environment Agency, 2014) which may hamper reuse of slag and lead to overly stringent monitoring requirements at landfill sites. Increasing our understanding of the factors controlling the mobility and timing of metal leaching during weathering of steel slags is therefore crucial to cost-effective long term management of the waste as well as protection of groundwater and surface water resources during re-use and storage.

1.2   Research objectives

This thesis aimed to establish the principal location(s) of V within steel slag, the mechanisms behind its release in hyperalkaline leachate and to assess its mobility and fate in the environment.

Slag is frequently stored in open heaps where it is exposed to weathering processes that generate leachate that may subsequently be released to the environment (Fig 1.1). Therefore two general areas of research were identified within the context of the slag leaching environment:

1. Behaviour of V during leaching of steel slags and

2. Environmental behaviour of V and surface hydrochemistry of steel slag leachate

Within slag heaps, leachate generation may occur under aerated conditions, following infiltration of the unsaturated zone by rainwater, or anaerobic (air-excluded) conditions where slag is stored beneath the water table. Leaching is dominated by mass transport processes i.e. dissolution of primary phases (e.g. CaO and Ca-silicates) and precipitation of secondary phases (e.g. Ca-Si-H and carbonates). $CaCO_3$ precipitation in particular is constrained by CO_2 availability, therefore leaching behaviour in the unsaturated zone is likely to be influenced by the rate of CO_2 ingress into the slag heap. Over long timescales (10s – 100s years) precipitation of secondary phases (including $CaCO_3$) onto slag blocks may have a passivating effect, reducing the rate of reaction at their surfaces and effectively reducing the liquid : solid ratio within the slag heap. Deposition of $CaCO_3$ may also fill pore spaces and may therefore lead to changes in flow pathways over time, potentially exposing other regions of the heap to leaching.

Where leachate emerges at groundwater springs, the dominant process is precipitation of $CaCO_3$ which is kinetically controlled by the rate of in-gassing of
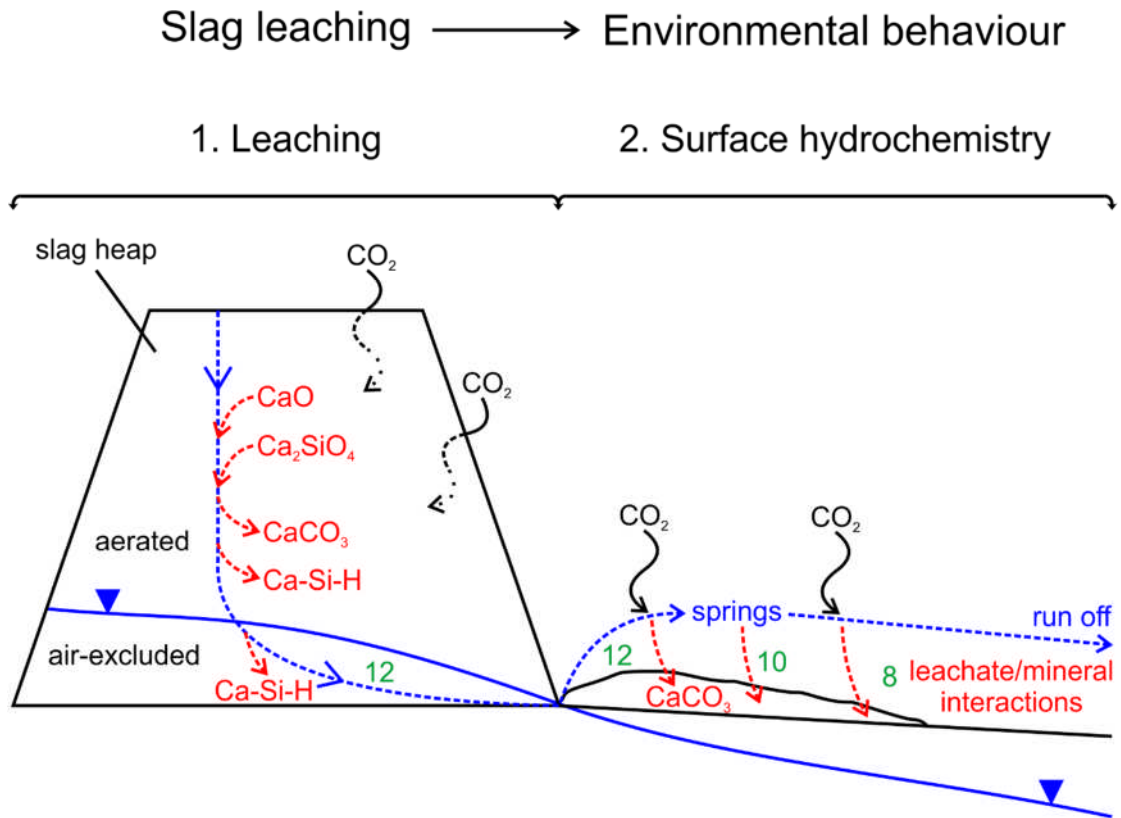
Figure 1.1 – Conceptual model showing steel slag leaching processes in relation to thesis objectives. Blue dashed lines represent approximate flow pathways. Red dashed lines represent dissolution/precipitation reactions. Black arrows represent CO_2 in-gassing. Green numbers represent hypothetical pH values.

atmospheric CO_2. Further reactions between leachate and colloidal particles, neo-formed precipitates and stream bed sediments may continue for some distance downstream following neutralisation of leachate pH.

Specific research objectives were therefore defined as follows:

1. Determine the distribution and speciation of V within basic oxygen furnace (BOF) steelmaking slag.

2. Determine whether leachate equilibrium atmosphere affects V release during slag leaching.

3. Investigate the effect of aeration and pH on leachate chemistry, phase dissolution behaviour, secondary phase formation and trace metal release during weathering of steel slags.

4. Investigate potential removal mechanisms behind attenuation of V during aerobic neutralisation of steel slag leachates.

5. Investigate the persistence of V in the aquatic environment downstream of a legacy steel slag heap.

6. Determine the behaviour of V during aerobic neutralisation of steel slag leachate in the presence of different mineral surfaces.

The research presented in this thesis is primarily concerned with the mobility of V during leaching of steel slags. Whilst redox conditions are an important control on V mobility, V^{5+} is the only V species soluble at the high pH values induced by weathering of steel slags (see Chapter 2, section 2.5). Therefore redox conditions were not systematically varied during experiments.

1.3 Thesis structure and experimental approach

This thesis comprises 7 chapters. The first chapter provides an introduction to steel slags, their chemical and mineralogical characteristics and outlines the particular environmental concerns associated with their use and storage. This is followed in Chapter 2 by a summary of the existing scientific literature concerning the formation of steel slags, problems arising during their use and storage, hydration and secondary phase formation during weathering of calcium silicates, processes influencing mobility of metals in the environment and the environmental chemistry of V. Descriptions of the study sites at Yarborough, Scunthorpe, Lincolnshire, UK and Hownsgill, Consett, Co. Durham, UK are also provided. The third chapter provides detailed methodology in addition to relevant background and theoretical information for all analytical techniques used during experimental work. Field data collection rationale and methodologies are also included.

Experimental data is presented in chapters 4 – 6, all of which have been or are being prepared for publication. Chapter 4 presents an investigation into the effects of aeration on surface leaching of Cr and V from basic oxygen furnace (BOF) steelmaking slag. A combination of X-ray spectroscopy (XAS) and scanning electron microscopy (SEM) techniques were employed to determine speciation of Cr and V in unweathered slag, leached zones and secondary phases formed under aerated or air-excluded conditions.

Chapter 5 presents data from batch leaching experiments performed on combined BOF slag and co-disposed refractories under aerated and air-excluded conditions. Aqueous and solid phase samples were taken at various time points which were tested for aqueous metal concentration, pH and mineralogical composition. This allowed time series data to be produced detailing the development of the leachate chemistry and the behaviour of different mineral phases during leaching, supported by data obtained from acid-neutralisation tests. Data was interpreted with particular emphasis on V behaviour under aerated and air-excluded conditions and its implications for disposal of steelmaking wastes.

Chapter 6 focuses on V behaviour in steel slag leachates and combines field observations and laboratory scale leachate neutralisation experiments. Aqueous samples were analysed over the course of neutralisation to build profiles of V removal in the presence of mineral surfaces including neo-formed $CaCO_3$, goethite and kaolinite. Solid samples were characterised using XAS to determine potential removal mechanisms and sorption environments for V during attenuation from leachates.

Chapter 7 summarises results from all experiments and highlights potential areas for future research. Finally, appendices containing additional data and a list of associated publications are also provided.

1.4 References

BURKE, I.T., MAYES, W.M., PEACOCK, C.L., BROWN, A.P., JARVIS, A.P., GRUIZ, K., 2012. Speciation of Arsenic, Chromium, and Vanadium in Red Mud Samples from the Ajka Spill Site, Hungary. Environ. Sci. Technol. 46, 3085-3092.

BURKE, I.T., PEACOCK, C.L., LOCKWOOD, C.L., STEWART, D.I., MORTIMER, R.J.G., WARD, M.B., RENFORTH, P., GRUIZ, K., MAYES, W.M., 2013. Behavior of Aluminum, Arsenic, and Vanadium during the Neutralization of Red Mud Leachate by HCl, Gypsum, or Seawater. Environ. Sci. Technol. 47, 6527-6535.

CHAURAND, P., ROSE, J., BRIOIS, V., SALOME, M., PROUX, O., NASSIF, V., OLIVI, L., SUSINI, J., HAZEMANN, J.L., BOTTERO, J.Y., 2007. New methodological approach for the vanadium K-edge X-ray absorption near-edge structure interpretation: Application to the speciation of vanadium in oxide phases from steel slag. J. Phys. Chem. B 111, 5101-5110.

CHAURAND, P., ROSE, J., DOMAS, J., BOTTERO, J.Y., 2006. Speciation of Cr and V within BOF steel slag reused in road constructions. Journal of Geochemical Exploration 88, 10-14.

DE WINDT, L., CHAURAND, P., ROSE, J., 2011. Kinetics of steel slag leaching: Batch tests and modeling. Waste Manage. 31, 225-235.

EFFLER, S.W., 1987. The impact of a chlor-alkali plant on Onondaga Lake and adjoining systems. Water, Air, and Soil Pollution 33, 85-115.

EFFLER, S.W., BROOKS, C.M.M., DRISCOLL, C.T., 2001. Changes in Deposition of Phytoplankton Constituents in a Ca2+ Polluted Lake. Environ. Sci. Technol. 35, 3082-3088.

ENVIRONMENT AGENCY, 2014. EA Bespoke permit 2014 Permit for Scunthorpe Aggregate processing. Permit number EPR/LP3537VV/A001.

HULL, S.L., OTY, U.V., MAYES, W.M., 2014. Rapid recovery of benthic invertebrates downstream of hyperalkaline steel slag discharges. Hydrobiologia 736, 83-97.

MATTIGOD, S.V., RAI, D., EARY, L.E., AINSWORTH, C.C., 1990. Geochemical Factors Controlling the Mobilization of Inorganic Constituents from Fossil Fuel Combustion Residues: I. Review of the Major Elements. Journal of Environmental Quality 19, 188-201.

MAYES, W.M., JARVIS, A.P., BURKE, I.T., WALTON, M., FEIGL, V., KLEBERCZ, O., GRUIZ, K., 2011. Dispersal and Attenuation of Trace Contaminants Downstream of the Ajka Bauxite Residue (Red Mud) Depository Failure, Hungary. Environ. Sci. Technol. 45, 5147-5155.

MAYES, W.M., YOUNGER, P.L., 2006. Buffering of Alkaline Steel Slag Leachate across a Natural Wetland. Environ. Sci. Technol. 40, 1237-1243.

MAYES, W.M., YOUNGER, P.L., AUMONIER, J., 2008. Hydrogeochemistry of alkaline steel slag leachates in the UK. Water Air Soil Pollut. 195, 35-50.

MOTZ, H., GEISELER, J., 2001. Products of steel slags an opportunity to save natural resources. Waste Manage. 21, 285-293.

OBER, J.A., 2017. Mineral commodity summaries 2017, Mineral Commodity Summaries, Reston, VA, p. 202.

PEACOCK, C.L., SHERMAN, D.M., 2004. Vanadium(V) adsorption onto goethite (alpha-FeOOH) at pH 1.5 to 12: A surface complexation model based on ab initio molecular geometries and EXAFS spectroscopy. Geochimica Et Cosmochimica Acta 68, 1723-1733.

PIATAK, N.M., PARSONS, M.B., SEAL, R.R., 2014. Characteristics and environmental aspects of slag: A review. Applied Geochemistry.

PROCTOR, D.M., FEHLING, K.A., SHAY, E.C., WITTENBORN, J.L., GREEN, J.J., AVENT, C., BIGHAM, R.D., CONNOLLY, M., LEE, B., SHEPKER, T.O., ZAK, M.A., 2000. Physical and chemical characteristics of blast furnace, basic oxygen furnace, and electric arc furnace steel industry slags. Environ. Sci. Technol. 34, 1576-1582.

RILEY, A.L., MAYES, W.M., 2015. Long-term evolution of highly alkaline steel slag drainage waters. Environ Monit Assess 187, 463.

ROADCAP, G.S., KELLY, W.R., BETHKE, C.M., 2005. Geochemistry of extremely alkaline (pH > 12) ground water in slag-fill aquifers. Ground Water 43, 806-816.

STEWART, D.I., BURKE, I.T., MORTIMER, R.J.G., 2007. Stimulation of Microbially Mediated Chromate Reduction in Alkaline Soil-Water Systems. Geomicrobiology Journal 24, 655-669.

WEHRLI, B., STUMM, W., 1989. Vanadyl in natural-waters - adsorption and hydrolysis promote oxygenation. Geochimica Et Cosmochimica Acta 53, 69-77.

WILKIE, M.P., WOOD, C.M., 1996. The adaptations of fish to extremely alkaline environments. Comparative Biochemistry and Physiology Part B: Biochemistry and Molecular Biology 113, 665-673.

YILDIRIM, I.Z., PREZZI, M., 2011. Chemical, Mineralogical, and Morphological Properties of Steel Slag. Advances in Civil Engineering 2011, 1-13.

Chapter 2   Literature review

This chapter provides an overview of the scientific literature relating to the production of ferrous slag, its chemical and mineralogical properties, general leaching behaviour and its various reuse possibilities. Detailed discussion of leaching processes including precipitation of secondary silicate phases and the deleterious environmental effects of leachates is also provided. Finally, a general overview of some processes affecting metal mobility in leachates and a more in-depth review of the environmental geochemistry of V is provided.

2.1   Characteristics of slag

2.1.1   Production

Slag is the silicate and oxide-based primary byproduct produced during the refinement of metallic ores to extract metals. In general. slags can be separated into two main groups; ferrous slags, which are formed during iron and steel making, and non-ferrous slags, which are derived from the smelting of non-ferrous metal ores (Eloneva et al., 2010; Piatak et al., 2014). For the purposes of this work, only the characteristics and processes concerning ferrous slags will be considered.

Ferrous slags are named according to the type of furnace in which they are produced (Fig. 2.1). Thus, slag from ironmaking is generally referred to as blast furnace (BF) slag and steelmaking slags are usually described as basic oxygen furnace (BOF, also known as Linz-Donawitz or LD, Juckes (2003); Oster (1982)), electric arc furnace (EAF) or ladle slag (Gomes et al., 2016b; Yildirim and Prezzi, 2011).

In a blast furnace, iron ore is reduced at high temperature using coke. Fluxing agents (usually limestone or dolomite) are added to the furnace to remove impurities from

the ore (Eloneva et al., 2010; Piatak et al., 2014; van Oss, 2003). These combine to form slag; a melt which principally comprises silicates and alumina-silicates of Ca which floats above the molten iron and is periodically tapped from the furnace separately from the iron (Lewis, 1982; van Oss, 2003). The iron produced in the blast furnace typically has a C content of ~4% and is known as 'pig iron' (van Oss, 2003).
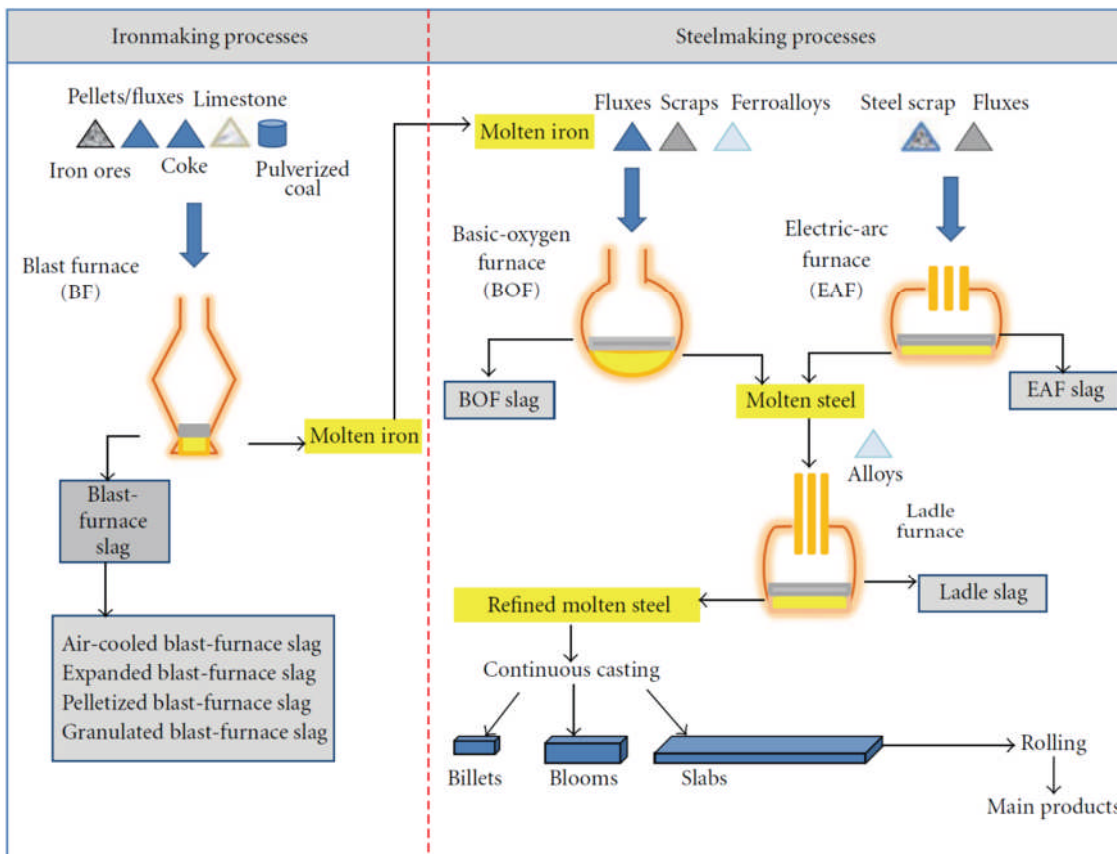
Figure 2.1 - Overview of iron and steelmaking processes (from Yildirim and Prezzi (2011)).

Primary steelmaking (in which iron is converted to steel) is carried out using either BOF or EAF processes. A BOF converter uses oxygen to reduce the C content of pig iron to < 0.5% (van Oss, 2003). A BOF will typically be charged with a combination of molten pig iron and scrap steel which is required to moderate the furnace temperature. Once charged, oxygen is blown through the melt which reacts with C in the steel to form CO,

thus removing it from the metal (Shi, 2004). An EAF is charged with steel scrap, as well as a small amount of molten pig iron, which is subsequently melted by the action of an electric current passing through the scrap between graphite electrodes (Piatak et al., 2014; Yildirim and Prezzi, 2011). As with ironmaking, in both BOF and EAF processes, lime or dolomite fluxes are added which combine with impurities in the melt to produce slag (Eloneva et al., 2010).

Following primary steelmaking, the composition of the molten steel may be refined within the ladle. Additional alloys and fluxes may be added to further adjust C concentration and to reduce the concentrations of S and unwanted metal impurities. Slags produced during secondary steelmaking are known as ladle slags and are compositionally distinct from those produced via BOF or EAF processes (Loncnar et al., 2016; Piatak et al., 2014; Shi, 2002).

2.1.2   Chemical composition

Detailed studies on ferrous slag chemistry are available from Proctor et al. (2000), (BF, BOF, EAF), Yildirim and Prezzi (2011) (BOF, EAF and ladle) and Piatak et al. (2014) (BF, BOF, EAF). Typical chemical compositions of these slag types are shown in Table 2.1.

Table 2.1 - Typical chemical compositions (in wt %) of ferrous slags (from Schwab et al. (2006)*, Motz and Geiseler (2001)** and Shi (2004)***. n.d. = not determined).

	CaO	SiO_2	Al_2O_3	MgO	MnO	P_2O_5	Fe_{tot}	CaO_{free}
BF*	32-45	32-42	7-16	5-15	0.2-1.0	n.d.	0.1-1.5	n.d.
BOF**	45-55	12-18	< 3	< 3	< 5	< 2	14-20	< 10
EAF**	30-40	12-17	4-7	4-8	< 6	< 1.5	18-28	< 3
Ladle***	30-60	2-35	5-35	1-10	0-5	< 0.2	0.1-15	n.d.

n.d. = not determined

Slag is formed during the reaction between limestone ($CaCO_3$) or dolomite ($CaMg(CO_3)_2$) with silica and other metal impurities in the ore. Consequently, ferrous slag chemistry is dominated by CaO and SiO_2 with other major constituents comprising FeO, Al_2O_3, MnO and MgO in varying quantities (Proctor et al., 2000). BF slag chemistry primarily comprises CaO and SiO_2 with smaller quantities of Al_2O_3 and MgO. CaO and SiO_2 content varies according to the age of the slag with BF slag produced before 1900 being relatively SiO_2 rich whilst more modern BF slags are dominated by CaO (Piatak et al., 2014).

Primary steelmaking slags (BOF and EAF) have a similar chemical composition to BF slag (Proctor et al., 2000). Fe concentrations are somewhat higher since not all the molten iron in the furnace can be recovered into steel, therefore BOF and EAF slags can be broadly represented by a CaO – MgO – SiO_2 – FeO quaternary system, the exact proportions of which will vary according to the raw materials used and the grade of steel being produced (Shi, 2004; Yildirim and Prezzi, 2011). CaO concentrations are relatively high in BOF slag due to the large volumes of flux which are added to the furnace. Concentrations of MnO are also elevated whilst SiO_2 concentrations are generally lower than those seen in BF slag. BOF and EAF slag compositions are generally comparable although EAF slags exhibit more variation and may contain free CaO and MgO (Yildirim and Prezzi, 2011).

The chemical compositions of ladle slags are highly variable and are dependent on the grade of steel being produced as well as any additives used (e.g. Al is often used for refinement leading to high Al_2O_3 concentrations in ladle slag (Shi, 2004)). The principal differences between ladle slags and primary steelmaking slags are a much lower FeO content and higher CaO and Al_2O_3 concentrations (Shi, 2002; Shi, 2004; Yildirim and Prezzi, 2011).

Slags also become enriched in trace elements which were originally present as impurities in the ore and are oxidised and partitioned into the slag in the furnace (Schwab et al., 2006). Proctor et al. (2000) found that BF slag contained elevated levels of Be, total Cr, Mn and Mo and Se compared to background soil concentrations. BOF slag was enriched in Sb, Cd, total Cr, Mn, Mo, Se, Ag, Tl, Sn and V whilst EAF slag contained relatively high concentrations of Sb, Cd, total Cr, Cr^{6+}, Cu, Mn, Mo, Ni, Se, Ag, Sn, V and Zn. Measured concentrations of Cr^{6+} (the most toxic form; Fendorf (1995)) in EAF slag are likely to be due to Cr^{3+} oxidation during cooling under ambient oxidising conditions (Proctor et al., 2000). EAF slags produced during alloy or stainless steelmaking have a different chemical profile to those produced making carbon steel and may contain Cr concentrations of up to 20% (w/w). This has led to EAF slag being classed as a hazardous waste in the US and Canada (Shi, 2004).

2.1.3   Mineralogy

The mineralogical compositions of BF slag is dominated by melilite group phases which can comprise up to 65% of the slag (Juckes, 2002; Lewis, 1982; Schwab et al., 2006). These can include the end-members åkermanite ($Ca_2Mg(Si_2O_7)$) and gehelenite ($Ca_2Al(AlSi)O_7$). Other mineral phases include dicalcium silicate (larnite; Ca_2SiO_4; which may constitute more than 10% (v/v) in historical slags, Juckes (2002)), wollastonite ($CaSiO_3$), dicalcium ferrite ($Ca_2Fe_2O_4$), merwinite ($Ca_3Mg(SiO_4)_2$), anorthite ($CaAl_2Si_2O_8$) and monticellite ($CaMgSiO_4$) (Lewis, 1982; Schwab et al., 2006).

By contrast, bulk mineralogy of BOF and EAF slag is dominated by olivine-group minerals, principally larnite (dicalcium silicate, fig. 2.2; Piatak et al. (2014)). This forms during cooling of the high temperature phase rankinite (Ca_3SiO_5), which transforms to produce Ca_2SiO_4 and CaO (Tossavainen et al., 2007). Other major phases reflect the

higher Fe concentrations in steel slags and comprise dicalcium aluminoferrite (brownmillerite; $Ca_2(Al, Fe)_2O_5$), free lime (CaO) and a refractory oxide solid solution of the form $(Ca, Fe, Mg, Mn)O$ which is often identified as wüstite-like (FeO) by X-ray diffraction analysis (Chaurand et al., 2006; Geiseler, 1996; Shi, 2004; Tossavainen et al., 2007; Yildirim and Prezzi, 2011). Due to its lower Fe content, ladle slag mineralogy is generally dominated by polymorphs of dicalcium silicate (Shi, 2002; Yildirim and Prezzi, 2011).
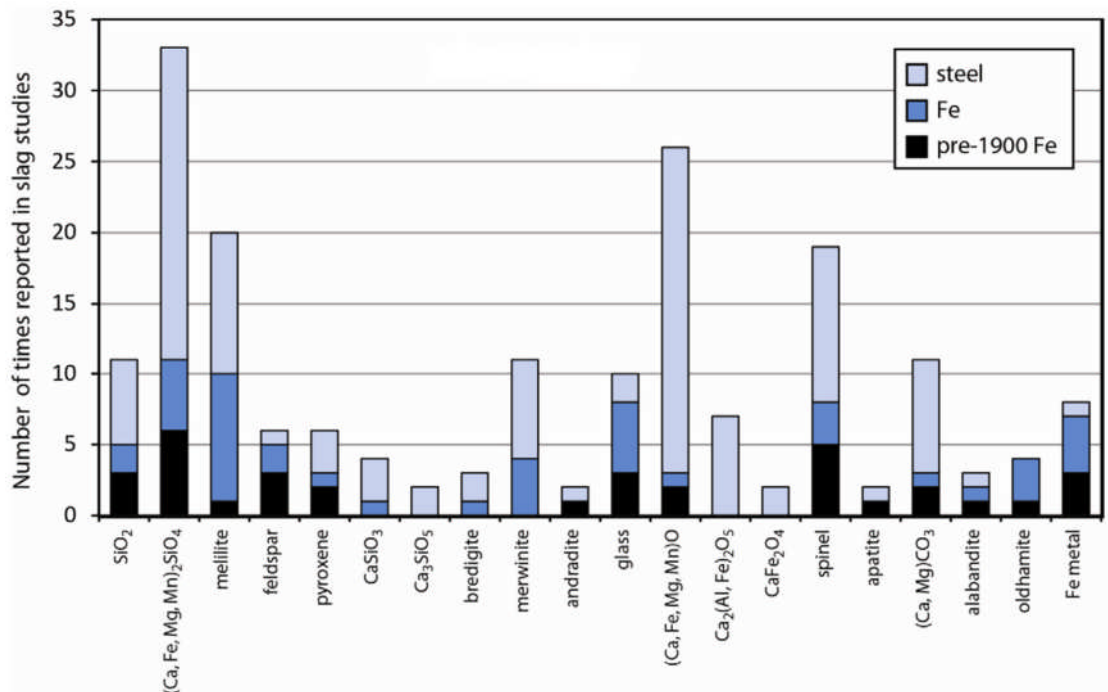
Figure 2.2 - Reported mineral phases in ferrous slag (from Piatak et al. (2014)).

Rapid cooling of BF slag (e.g. by quenching with water or air) results in the formation of a glassy, amorphous product rather than a crystalline slag (Lewis, 1982). Glass is generally present in steel slags although often only in trace quantities (Piatak et al., 2014). Experiments by Tossavainen et al. (2007) found that glass formation on rapid

cooling of BOF, EAF and ladle slag was highly variable with only ladle and one species of EAF slag showing significant production of glass.

2.1.3.1   *Refractories*

Refractory bricks are used to line the inside of furnaces to protect them from chemical damage and abrasion during smelting processes (Quaranta et al., 2014). A variety of materials may be used although MgO-C composites are most common in BOF and EAF, whilst ladles use refractories with a higher proportion of Al_2O_3 to protect against the more chemically aggressive nature of ladle slags (Resende et al., 2000; Rovnushkin et al., 2005).

The high MgO content of spent refractories means that in some cases they can be recycled in furnaces to control the composition of the molten slag. However, since spent refractories have little monetary value they are generally disposed of to landfill if this is not possible (de Sa et al., 2007; Hanagiri et al., 2008; Kwong and Bennett, 2002; Quaranta et al., 2014).

2.1.4   *Leaching behaviour*

Mineral phases in steel slags such as CaO and Ca-silicates are the products of high temperature reactions and are unstable under low temperature, aqueous conditions (De Windt et al., 2011; Ghosh et al., 1979; Shi et al., 2002). In contact with water, CaO rapidly hydrates to form $Ca(OH)_2$ (portlandite) which then readily dissociates into its component ions via the following reactions (Mayes et al., 2008; Shi et al., 2002):

$$CaO + H_2O \rightarrow Ca(OH)_2 \tag{2-1}$$

$$Ca(OH)_2 \rightarrow Ca^{2+} + 2OH^- \hspace{5cm} (2\text{-}2)$$

Ca-silicate phases present in ferrous slag are also soluble in contact with water (De Windt et al., 2011; Huijgen and Comans, 2005; Roadcap et al., 2005) e.g:

Dicalcium silicate:

$$Ca_2SiO_4 + 4H_2O \rightarrow 2Ca^{2+} + H_4SiO_4 + 4OH^- \hspace{3cm} (2\text{-}3)$$

Tricalcium silicate:

$$Ca_3Si_2O_7 + 7H_2O \rightarrow 3Ca^{2+} + 2H_4SiO_4 + 6OH^- \hspace{2.5cm} (2\text{-}4)$$

Åkermanite:

$$Ca_2MgSi_2O_7 + 7H_2O \rightarrow 2Ca^{2+} + Mg^{2+} + 2H_4SiO_4 + 6OH^- \hspace{1.5cm} (2\text{-}5)$$
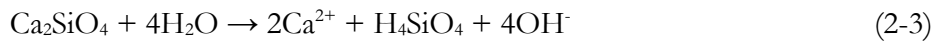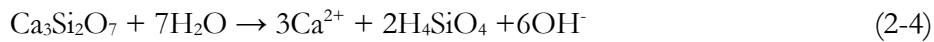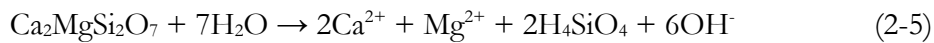
All of the above reactions produce Ca^{2+} and OH^- ions creating a characteristic Ca-OH^- dominated leachate during the initial stages of ferrous slag leaching (Piatak et al., 2014; Roadcap et al., 2005). Release of OH^- ions elevates solution pH, therefore leachates associated with ferrous slags typically have a pH in the 10 – 12.5 range (Bayless and Schulz, 2003; Mayes and Younger, 2006; Roadcap et al., 2005) which is readily attained via dissolution of dicalcium silicate and/or equilibrium with $Ca(OH)_2$ (Langmuir, 1997; Roadcap et al., 2005). Leachate chemistry generally reflects the bulk chemistry of the slag, therefore leachates produced during weathering of steel slags are dominated by Ca and Si with lower concentrations of Al, Fe and Mg and potentially Cr and Mn (Piatak et al., 2014).

Rapid dissolution can lead to oversaturation with respect to a range of minerals which may subsequently precipitate as secondary phases. Dissolution of Ca-silicates can

result in a solution which is oversaturated with respect to calcium silicate hydrate (Ca-Si-H) or ettringite phases (the latter phase only occurs if sulphate concentrations are sufficiently high; De Windt et al. (2011)), the exact structure of which is dependent on that ratio of Ca and Si released to solution (Huijgen and Comans, 2006; Walker et al., 2016). In general, Fe-rich phases are less soluble than Ca-rich phases at high pH. However, di- and trivalent cations may be released as impurities during dissolution of Ca-rich phases or as pH falls, leading to precipitation of spinel-like secondary phases (e.g. magnetite, Fe_3O_4) and ferric (oxy)hydroxides (De Windt et al., 2011; Engström et al., 2013; Huijgen and Comans, 2006).

The high Ca concentrations in ferrous slag leachates lead to immediate oversaturation with respect to $CaCO_3$ if affected by in-gassing of atmospheric CO_2 (e.g. on emergence at a groundwater spring) or following mixing with surface waters containing carbonate alkalinity (Mayes et al., 2008):

$$Ca^{2+} + OH^- + CO_2 \rightarrow CaCO_3 + H_2O \hspace{3cm} (2\text{-}6)$$

Carbonates can form on the surfaces of slag particles during heap leaching (Huijgen and Comans, 2005; Huijgen and Comans, 2006; Navarro et al., 2010) but may also precipitate in leachates downstream depending on the saturation index (SI) values and extent of CO_2 mixing (Gomes et al., 2017; Mayes et al., 2008; Riley and Mayes, 2015). Carbonate precipitation consumes OH^- ions leading to a decrease in leachate pH (Mayes et al., 2008) and the formation of carbonate rinds on slag particles appears to influence the leaching behaviour of trace metals (Costa et al., 2016; Huijgen and Comans, 2006; Navarro et al., 2010).

2.1.5   Reuse

Ferrous slag is a particularly voluminous byproduct with worldwide production of BF and steel slag estimated to be between 300 – 360 million tonnes and 160 – 240 million tonnes respectively in 2016 (Ober, 2017). BF slag production is dependent on the grade of the iron ore used but is generally of the order of 0.25 – 0.30 tonnes slag per tonne of crude Fe (van Oss, 2003). Steel slag production is generally lower since slag processing recovers metals (usually Fe) which are subsequently returned to the furnace. Thus, the output of primary steelmaking slag is usually around 10 – 15% (w/w) of steel production which equates to 220 – 370 kg per tonne Fe (Proctor et al., 2000; Shen et al., 2009; Shen and Forssberg, 2003; van Oss, 2003). Given these volumes and also to comply with increasingly stringent environmental guidelines restricting landfilling of wastes and industrial byproducts, ferrous slags are recycled where possible (Yüksel, 2017).

Depending on the method of cooling employed, BF slag can form a dense structure with a vesicular texture which is used as a general engineering aggregate, a similar but lighter structure (expanded slag) which binds well with cement pastes and is used as a lightweight concrete aggregate or a glassy, granular material with moderate cementitious properties that are improved by the addition of an alkaline precursor (e.g. CaO) (Lewis, 1982; Shi, 2004; van Oss, 2003). Concrete produced using ground granulated BF (GGBF) slag has been shown to have a greater long term strength and resistance to sulphate attack than ordinary Portland cement (Hadjsadok et al., 2012).

The reuse of steel slags (Fig. 2.3) is more problematic. Steel slags with high CaO content can be recycled directly as fluxing agents in blast furnaces (Das et al., 2007; Navarro et al., 2010), however, this is not possible if S and/or P concentrations are too high (Shen and Forssberg, 2003).
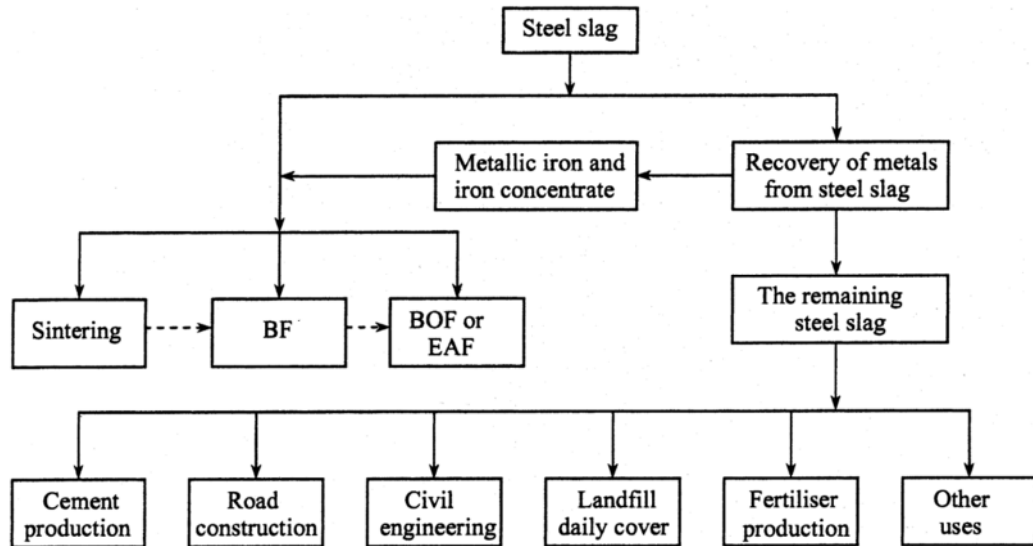
Figure 2.3 - Recycling and use of steelmaking slag (from Shen and Forssberg (2003))

In general, their cementitious properties do not compare favourably with those of blast furnace slag due to its crystalline nature and the presence of iron rich phases (including the refractory oxide phase) which do not readily hydrate (Muhmood et al., 2009; Wang and Yan, 2010), however, this may be mitigated by mixing with Portland cement, fly ash or GGBF slag to create a useful product (Shi, 2004). A more serious problem arises from the presence of phases such as CaO and MgO which undergo volumetric expansion on hydration and may comprise a large fraction of the total slag composition (Motz and Geiseler, 2001). This expansion can destabilise structures where steel slags have been used as concrete aggregate, limiting the reuse potential in these applications (Juckes, 2003; Yüksel, 2017). If slag cooling has been slow, further volumetric expansion can derive from the transformation of β-dicalcium silicate to γ-dicalcium silicate. This process involves and expansion of ~10% and breaks up the dicalcium silicate crystals into dust. Indeed, the abundance of dicalcium silicate in ladle slags has led to them being termed 'self-dusting' or 'falling' slags due to this phenomenon (Juckes, 2003; Shi, 2004; Yildirim and Prezzi, 2011). Despite these drawbacks, steel slags are widely used in civil engineering applications. The skid resistance of steel slags makes them useful as coarse aggretates in asphalt (Ahmedzade

and Sengoz, 2009; Asi, 2007; Shen et al., 2009; Wu et al., 2007) and they are widely used as a general fill material, particularly in road construction (Australasian Slag Association, 2002; Chaurand et al., 2007a; Geiseler, 1996; Motz and Geiseler, 2001; Yi et al., 2012).

Ca-silicates and oxides that are present in high concentrations in steel slags give it a high acid-neutralising capability (Navarro et al., 2010; Yan et al., 2000). This has led to some interest in their application for treating acid mine drainage (Goetz and Riefler, 2014). Similarly, the CaO content of ferrous slags has generated considerable interest in their use as a carbon sink via sequestration of atmospheric CO_2 (Bobicki et al., 2012; Bonenfant et al., 2008; Doucet, 2010; Huijgen and Comans, 2005; Huijgen and Comans, 2006; Renforth et al., 2011).

Steel slags have shown promise as adsorbents used to remove P from wastewater or agricultural runoff, as well as As and U from wastewaters and mine effluent (Bowden et al., 2009; Piatak et al., 2014). High concentrations of Si have enabled their use as a fertiliser (Haynes et al., 2013). However, problems have arisen due to its use in agriculture; for example the death of 23 heifers in northern Sweden following consumption of slag containing ~3% V which had been used as fertiliser (Frank et al., 1996).

2.2   Weathering of silicate minerals

Calcium silicate phases are ubiquitous in ferrous slags and are formed during the high temperature reactions between silicates in the iron ore and $CaCO_3$ added to the furnace as a fluxing agent (Lewis, 1982; Schwab et al., 2006). It is the overall Ca-silicate content and in particular, the relative proportions of different Ca-silicate species which determine the cementitious properties of BF and steelmaking slags (Shi, 2002; Shi, 2004).

The principal high temperature calcium silicate phase formed during iron and steel making is tricalcium silicate (Ca_3SiO_5). During the initial stages of cooling, this exsolves to form dicalcium silicate (Ca_2SiO_4) and CaO (Tossavainen et al., 2007). Dicalcium silicate has a number of polymorphs; α, α', β, and γ. The high temperature α polymorph transforms to β-dicalcium silicate at temperatures of ~630 ºC (Shi, 2002). If cooling continues, a further transformation from the β to γ form takes place at temperatures of around 400 – 550 ºC (Juckes, 2002; Shi, 2004). During this transformation rotation of the SiO_4 tetrahedra and movement of the Ca atoms lead to volumetric expansion of up to 10% and shattering of the crystals (Ghosh et al., 1979; Juckes, 2002; Shi, 2002; Yildirim and Prezzi, 2011). The extent of these transformations may be limited by ionic substitution of SiO_4^{4-} by similar oxyanions (e.g. VO_4^{3-}, PO_4^{3-} or SO_4^{2-}) in quantities as low as 0.1%, with any remnant charge differential balanced by trapping of additional Ca^{2+} ions (Ghosh et al., 1979; Juckes, 2002; Tossavainen et al., 2007). More simply, the rate of cooling can influence the extent of transformation with rapid cooling (e.g. by quenching with water) promoting the stability of tricalcium silicate and β-dicalcium silicate at lower temperatures (Juckes, 2002; Luxán et al., 2000; Tossavainen et al., 2007).

In the presence of water, tricalcium silicate and some dicalcium silicate phases can hydrate. In general these reactions are relatively slow (Taylor, 1997), particularly in the case of γ-dicalcium silicate (Ghosh et al., 1979; Shi, 2002) although this is improved in the latter case by the presence of excess Ca or hydration at high temperatures (Ghosh et al., 1979). Hydration of Ca-silicates generally involves dissolution of the crystalline phase followed by precipitation of calcium silicate hydrate (Ca-Si-H) phases (Eqn. 2-7; Garrault et al. (2006); Schwab et al. (2006); Scrivener and Nonat (2011); Taylor (1997)).

$$2Ca_2SiO_4 + Ca(OH)_2 + 5H_2O \rightarrow Ca_3Si_2O_7 \cdot 4H_2O \qquad (2\text{-}7)$$
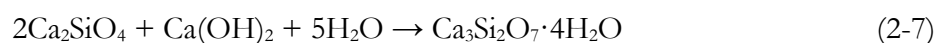
These phases have extremely variable composition and frequently precipitate as an amorphous gel. Two semi-crystalline phases with high Si or high Ca content have been identified that have similar structures to 1.4 nm tobermorite (known as Ca-Si-H (I); Eqn. 2-8) or jennite (known as Ca-Si-H (II); Eqn. 2-9) respectively (Gard and Taylor, 1976; Jennings, 1986; Taylor, 1986; Taylor, 1997).

$$6Ca_2SiO_4 + 12H_2O \rightarrow Ca_5Si_6O_{16}(OH)_2 \cdot 4H_2O + 7Ca^{2+} + 14OH^- \qquad (2\text{-}8)$$

$$6Ca_2SiO_4 + 14H_2O \rightarrow Ca_9Si_6O_{18}(OH)_6 \cdot 8H_2O + 3Ca(OH)_2 \qquad (2\text{-}9)$$
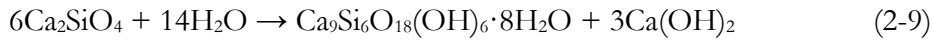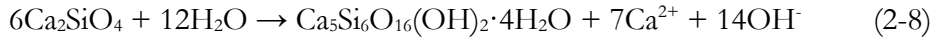
The Ca/Si ratio in Ca-Si-H phases is a function of the solution chemistry at the time of precipitation (specifically pH, Ca and Si concentrations) and can vary from 0.0 to 3.0 (Walker et al., 2016), although most cement/slag systems fall between 0.7 – 2.4 (Richardson, 1999). In general, higher pH values favour higher Ca/Si ratios (De Windt et al., 2011; Sugiyama and Fujita, 2006) and tend to lead to the formation of jennite-like Ca-Si-H (II) with a Ca/Si ratio of 1.5 – 2.2 (Gard and Taylor, 1976; Jennings, 1986). Lowering of solution pH and Ca concentrations can lead to transformation of Ca-Si-H (II) to form Ca-Si-H (I), which has a similar structure to 1.4 nm tobermorite and a Ca/Si ratio between 0.7 – 1.5 (Chen et al., 2004).

Ca-Si-H phases form rapidly by heterogeneous nucleation at the solid-solution interface and are characterised by a highly disordered layer structure at the nanometre scale (Allen et al., 2007; Garrault and Nonat, 2001; Taylor, 1993). Their exact structure remains unclear, however, comparison with 1.4 nm tobermorite and jennite suggests a central Ca – O sheet bonded to 'dreierketten', i.e. repeating groups of three silicate tetrahedra, with water molecules and additional Ca^{2+} ions occupying the interlayer spaces. In the jennite structure, alternating dreierkette are replaced by rows of OH groups which can bond to

interlayer Ca^{2+} (Chen et al., 2004). The structure of Ca-Si-H phases allows diffusion of ions; therefore, if Ca-Si-H is able to build up on a submerged surface, reactions at the interface between the anhydrous mineral and solution become limited by the rate of diffusion through the Ca-Si-H phase (Garrault et al., 2006).

Over time, Ca-Si-H reacts with CO_2 or CO_3^{2-} to form $CaCO_3$. Initially this decreases the Ca/Si ratio of the Ca-Si-H, however, subsequent reaction can destroy the Ca-Si-H and form hydrous silica (Taylor, 1997). The rate and extent to which this occurs is controlled by the rate of diffusion of CO_2 into the Ca-Si-H gel although this may be limited due to neo-formed $CaCO_3$ blocking pores (Groves et al., 1991). Furthermore, Ca-Si-H phases are generally only stable at high pH values (> 10). Lowering of solution pH below 10 will result in dissolution of any Ca-Si-H phases present (Ochs et al., 2016).

2.3   Environmental impacts of steel slag leachate

During storage of steel slags either in landfill or in legacy heaps, infiltration by rainwater is inevitable. Reactions between water and steel slag generate a leachate that can have deleterious effects on the local environment. These relate to the extreme pH of the waters, rapid carbonation following in-gassing of atmospheric CO_2 and mobilisation of toxic heavy metals in leachates (Hull et al., 2014).

High pH leachate can present an environmental risk in itself with high concentrations of the OH^- ion being toxic to many species of fish (Haslam, 1990; Koryak et al., 2002; Wilkie and Wood, 1996). Hull et al. (2014) found that invertebrate populations in streams impacted by steel slag leachate declined as pH increased, with diversity and abundance both severely reduced above ~pH 11. Koryak et al. (2002) noted that where slag heaps formed the bank of a river, they remained sparsely vegetated at best even after several decades and the river itself was found to contain no fish when its pH was > 10.

Where groundwater emerges from a spring, atmospheric CO_2 begins to diffuse into the water. In general, this raises the concentration of H^+ ions thus driving dissolution of carbonates. However, at high pH and in the presence of high concentrations of Ca, carbonate precipitation occurs which, at low temperature and pressure, is most likely to take the form of calcite ($CaCO_3$; Boylan et al. (2016); Roadcap et al. (2005)). $CaCO_3$ precipitation occurs when CO_3^{2-} is introduced to Ca-rich waters either by in-gassing of CO_2 from the atmosphere or by mixing with rain or surface waters containing HCO_3^- and H_2CO_3 leading to immediate supersaturation with respect to $CaCO_3$ (i.e. $SI_{calcite} > 0$) (Mayes et al., 2008; Roadcap et al., 2005). In the presence of nucleation sites, $CaCO_3$ will precipitate heterogeneously when $SI_{calcite} > \sim0.3$, although $SI_{calcite}$ values $> \sim1.5$ lead to homogeneous precipitation directly from solution in the absence of nucleation sites (Ford and Williams, 1989). $SI_{calcite}$ values of between +1.35 and +2.78 have been determined in watercourses containing steel slag leachate (Mayes et al., 2008).

$CaCO_3$ deposition rates vary proportionally with aeration and availability of carbonate alkalinity (the latter being a limiting factor at high pH) and at the SI values above correspond to $CaCO_3$ precipitation rates of up to 100.8 g day^{-1} m^{-2} in turbulent streams where carbonate alkalinity is sufficiently high. (Mayes et al., 2008). Under low flow conditions, deposition rates are lower but still regularly exceed 10 g day^{-1} m^{-2}, which far exceed rates observed in unaffected waters (Effler and Brooks, 1998; Mayes and Younger, 2006; Mayes et al., 2008).

Rapid precipitation of $CaCO_3$ can reduce the available O_2 in the water column by burial of phytoplankton. Furthermore, $CaCO_3$ precipitation increases turbidity of waters, preventing light from reaching benthic communities. Encrusting of macrophytes inhibits photosynthesis and the inorganic nature of the precipitates reduces nutrient availability in substrates. In addition, precipitates can clog substrates, effectively reducing the available habitat for benthic fauna (Effler, 1987; Fjellheim and Raddum, 1995; Koryak et al., 1998).

The presence of elevated concentrations of toxic trace metals in steel slags has become a major concern in recent years due to their potential solubility in leachate and consequent harmful effects on local ecology and human health (Chaurand et al., 2007a; Chaurand et al., 2006; Proctor et al., 2000). Some of these display complex leaching behaviour dependent on pH and/or redox conditions (e.g. Al, Fe, Li, Mo, Ni, Cr and V; Hull et al. (2014); Roadcap et al. (2005)) and thus may persist in leachates. A number of these are not routine analytes in water quality tests (including Sn, Ba, Li, Mo Sr, and V; Hull et al. (2014)) but nonetheless have been found in elevated concentrations in steel slag leachates when compared to background waters (Hem, 1985).

Release of metals into leachate is controlled by a complex mix of dissolution of Ca-rich phases and simultaneous precipitation of secondary phases and adsorption/surface complexation by leached elements (Apul et al., 2005). In some cases, metal release may be controlled by the solubility of the host phase or by secondary phases formed during leaching e.g. chromate-substituted $BaSO_4$ for Cr (Fällman, 2000) or Ca-vanadates for V (Cornelis et al., 2008a; De Windt et al., 2011; Huijgen and Comans, 2006; Schindler et al., 2000a). A number of mechanisms may subsequently attenuate metal concentrations downstream including sorption to organic matter (e.g. Mo to soils; Matern et al. (2013)) or neo-formed phases (e.g. divalent metals to $CaCO_3$; Zachara et al. (1991)) or incorporation into neo-formed $CaCO_3$ (Bayless and Schulz, 2003).

Cr and V have been identified as the principal contaminants of concern associated with steel slag leachates (Chaurand et al., 2007a; Chaurand et al., 2006). These pose potentially severe health risks with Cr^{6+} and V^{5+} listed as confirmed and potential human carcinogens respectively (IARC, 2006, 2012; Zwolak, 2014).

Studies such as those conducted by Proctor et al. (2000) and (Geiseler, 1996) found low release rates of V and Cr during leaching of steel slags. However, these tests were conducted using standardised leaching tests (e.g. toxicity characteristic leaching

procedure (TCLP); USEPA (1992)) at neutral or acidic pH which are likely not representative of leaching conditions and therefore may not be appropriate for testing alkaline wastes (Rubinos and Barral, 2013). Leaching environments associated with ferrous slags are characterised by high pH values (generally > pH 9; Cornelis et al. (2008a); Mayes and Younger (2006); Schwab et al. (2006)). Previous studies on similar hyperalkaline environments (e.g. red mud) have shown that high concentrations (up to ~15 ppm) of V can accumulate in leachates at this pH range (Burke et al., 2013; Czop et al., 2011; Gomes et al., 2016a; Mayes et al., 2011).

Whilst no drinking water standard (DWS) currently exists for V, a limit of 15 μg L^{-1} has been proposed in California and freshwater thresholds of 280 μg L^{-1} and 19 μg L^{-1} for acute and chronic exposures respectively (Buchman, 2008; Gerke et al., 2010). Analysis of leachates at slag disposal sites have shown elevated concentrations of V which frequently exceed these threshold values (Riley and Mayes, 2015; Roadcap et al., 2005) and have been shown to be toxic to benthic invertebrates in other settings (Chiffoleau et al., 2004; Fichet and Miramand, 1998). Concentrations of V which would be considered significant in the aqueous environment were also seen during laboratory scale pH$_{stat}$ leaching experiments under aerated conditions by Chaurand et al. (2006) at pH 5. These were thought to be due to oxidation of V^{3+} and V^{4+} to the more soluble V^{5+}, however, measurements were taken from crystals using bulk XANES techniques and no detailed observation of the weathered zone was performed.

2.4 Controls on metal mobility in the environment

2.4.1 *Adsorption*

Sorption processes are amongst the most important controls on the mobility of trace metals in the environment (Sparks, 2005). Adsorption can be described as the partitioning of an element from aqueous solution (sorbate) to a solid (sorbent) by the formation of surface complexes (Brown and Parks, 2001). Adsorption is distinct from other sorption processes (including surface precipitation or absorption) in that in involves accumulation of the aqueous species on the mineral surface in two dimensions only, i.e. without the formation of three dimensional mineral structures (Sposito, 1987). Surface complexes are most commonly formed in one of two structures. Inner-sphere complexes are formed when the sorbate forms ionic or covalent bonds directly to specific sites on the sorbent. Outer-sphere complexes are formed by electrostatic attraction between the sorbate and sorbent via water molecules which can loosely attach anywhere on the mineral surface and hence may be considered non-specific (Krauskopf and Bird, 1995; Sposito, 1989). In general, transition metals form inner-sphere complexes. The covalent bonds formed in this process depend on the electron configurations of both the surface group and the ion being complexed (Sposito, 1989).

Metal (oxyhydr)oxides (particularly those of Al, Fe and Mn) and clay minerals are particularly important sorbents for the retention of trace metals due to their high surface area and charge (Brown and Parks, 2001; Sparks, 2005). The surfaces of metal oxides become charged via protonation/deprotonation of atoms or by leaching of ionic species and their subsequent re-adsorption (Kosmulski, 2016). The distribution of this charge varies with pH and at a specific pH value known as the point of zero charge (PZC), the net distribution of charge on a submerged mineral surface will be zero (Sposito, 1989). At
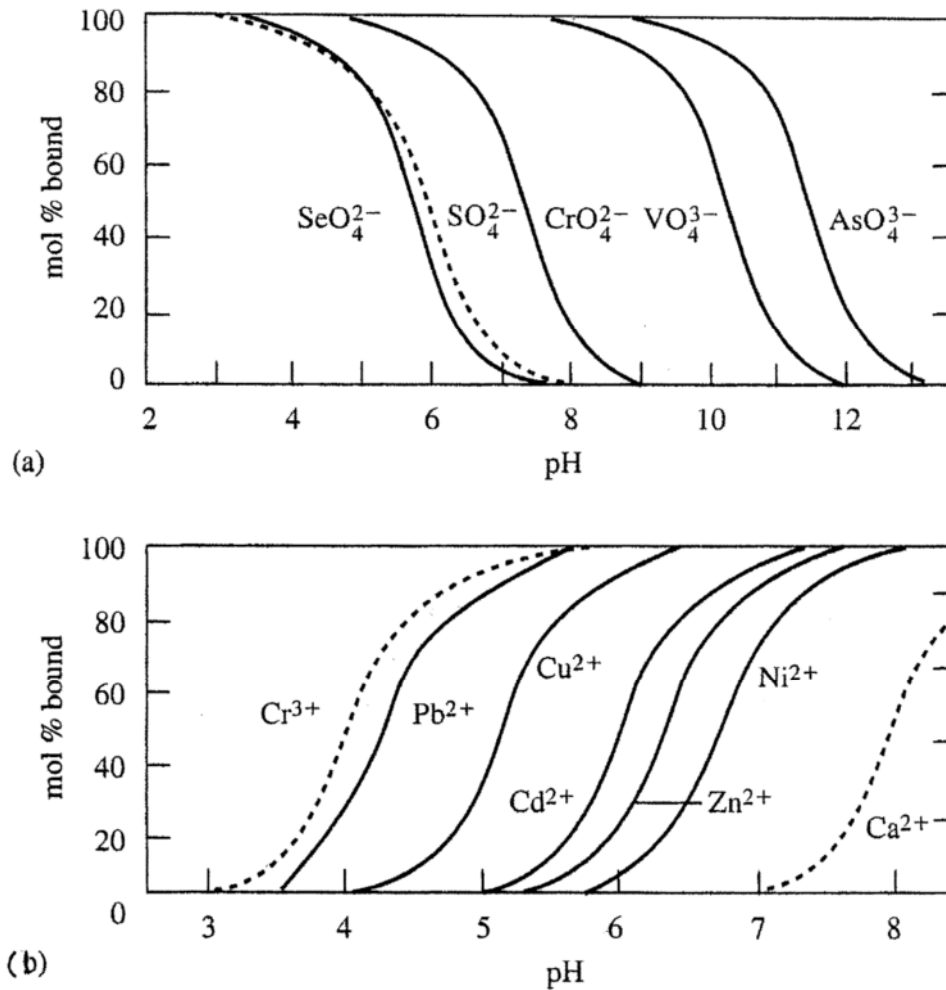
Figure 2.4 - Adsorption of a) metal(loid) oxyanions and b) metal cations (at 5 x 10^{-7} M) by ferrihydrite (ΣFe(III) = 10^{-3} M as a function of pH. Ionic strength = 0.1 mol/kg. Dashed curves have been calculated. After W. Stumm, *Chemistry of the solid-water interface*, Copyright © 1992 by John Wiley & Sons. From Langmuir (1997).

pH values below the PZC, oxide surfaces are dominated by positive surface sites which readily allow anion absorption and vice versa (Langmuir, 1997).

The amount of adsorption that takes place generally depends on the concentrations of the sorbate in solution and the available surface area of the sorbent. However, if these are kept constant along with temperature and pressure, pH becomes the most important controlling variable (Krauskopf and Bird, 1995). This becomes particularly significant when considering trace concentrations of toxic heavy metals, most of which are

adsorped across a narrow pH range known as the sorption edge (Fig. 2.4). Sorption of oxyanions is complete once the pH of the solution falls below the PZC of the sorbent (Langmuir, 1997).

2.4.2   Incorporation

During precipitation of a crystalline phase from solution, ions that are not present in sufficiently high concentrations to form their own mineral phase may be incorporated into the neo-formed phase(s) by substituting for more abundant ions. The extent to which this occurs is a function of the ionic radius and the charge of the ion compared to the site it substitutes into (Krauskopf and Bird, 1995).

The ionic radius and charge associated with a specific ion depend on its coordination environment which in turn is influenced by the valence of the cation. Coordination numbers refer to the number of number of atoms attached to atom in question (or ligands attached to an ion) and generally range from 3 to 12 (Housecroft and Constable, 2006; Krauskopf and Bird, 1995). The most common coordination number is 6 (known as octahedral coordination due to the arrangement of the surrounding ions in the shape of an octahedron) although 3 (trigonal), 4 (tetrahedral) and 8 (square planar) are also regularly observed in naturally occurring elements (Krauskopf and Bird, 1995).

Substitution of ions is constrained by a number of conditions. In general, ions are partitioned on the basis of their contribution to the overall energy of the crystal structure, with ions that contribute more being preferentially incorporated (Goldschmidt, 1937; Misra, 2012). If the ionic radius of a trace element is within 15% of that of a major element then substitution can readily occur. Ions with a charge difference of one unit but a similar ionic radius can still substitute for one another if the difference in charge can be accommodated by an additional substitution of a different ion. Where two ions can occupy

a site, the ion with the highest ionic potential forms the strongest bonds and is incorporated. If the covalent character of the bonds between substituting ions is substantially different, however, substitution will be limited (Krauskopf and Bird, 1995; Misra, 2012).

2.4.2.1   Ca-Si-H

Ca-Si-H phases display a highly disordered structure in which nm-scale Ca-silicate materials form layers which adhere strongly to each other by hydrogen bonding (Spence, 1992; Sugiyama and Fujita, 2006). This disordered, amorphous structure means that Ca-Si-H phases have a very high surface area and charge, which provide a particularly high density of potential sorption sites for both cations and anions (Ochs et al., 2016; Spence, 1992).

Ca-Si-H phases which form during the weathering of steel slags have been noted as having a high potential to remove toxic elements from leachate by adsorption and/or ionic substitution (Cornelis et al., 2008a; De Windt et al., 2011; Gougar et al., 1996). The surface charge on Ca-Si-H with Ca/Si ratios of 1.2 or higher is generally positive (Jönsson et al., 2004), which allows adsorption of oxyanions such as arsenate and chromate (Omotoso et al., 1998; Phenrat et al., 2005), although competing anions in the leachate (e.g. OH^-, SO_4^{2-}, CO_3^{2-}) may limit the extent to which this occurs (Cornelis et al., 2008a). In some Ca-Si-H structures the silicate sheets may be bridged by silicate tetrahedra which provide additional sites for ion substitution (Chen et al., 2004; Ochs et al., 2016). This mechanism has been demonstrated for chromate and arsenate (Cornelis et al., 2008a). Adsorption or incorporation of the vanadate oxyanion to Ca-Si-H structures has not been systematically investigated to date.

2.4.3 Dissolution/precipitation

The behaviour of a mineral phase in an aqueous system is predicted using the saturation index (SI). This is defined as the ratio between the ion activity products (IAP) and the mineral solubility products at equilibrium (K_{eq}):

$$SI = \log_{10}(IAP/K_{eq})$$

When the SI for a given mineral is < 0, dissolution of that phase is thermodynamically favoured. When the SI is > 0, precipitation is favoured (Boylan et al., 2016; Langmuir, 1997).

Dissolution of a solid phase involves a number of steps: 1) Reactant transport in solution to the mineral surface followed by adsorption of solutes, 2) interlattice transfer of chemically reactive species and subsequent reactions leading to 3) detachment of reactants from the solid and their transport into solution (Stumm and Morgan, 1996). Ions linked by bonds of predominantly ionic character are readily solvated and diffuse into solution. Minerals with covalent bonds (e.g. aluminosilicates and metal oxides) dissolve when protons, hydroxides or ligands in the solvent form inner-sphere complexes with framework anions or cations respectively in the crystal lattice. This adsorption polarises the metal – anion bonds, weakening them to the point that the whole complex can be detached and move into the aqueous phase (Sposito, 1989). Therefore, the rate of dissolution is controlled by both pH of the solvent and overall surface charge on the solute with minimum rates occurring at the pH_{pzc} (Stumm and Morgan, 1996).

Precipitation of a mineral phase may occur via two different types of nucleation; heterogeneous or homogeneous nucleation. Heterogeneous nucleation is the dominant mechanism in natural waters and occurs when the presence of foreign solids (e.g. inorganic

crystals, clays, sand etc.) reduce the activation energy required for nucleation to take place. Homogeneous nucleation occurs in an oversaturated solution when sufficient quantities of ions or molecules interact and produce a 'critical cluster' (nucleus). More ions (or molecules) are deposited on these nuclei forming crystallites which subsequently 'ripen' into large crystals. Stable nuclei are only formed once a certain activation energy has been achieved. For homogenous nucleation this requires a high level of supersaturation. In the presence of substrates with a similar interfacial energy to the precipitating phase, this activation energy is much lower and heterogeneous nucleation occurs (Stumm and Morgan, 1996).

In a situation where a phase may precipitate in one of several polymorphs, the Ostwald Step Rule states that the precipitate with the highest solubility (i.e. least stable solid phase) forms first. This is due to the lower solid-solution interfacial tension of lower stability phases kinetically favouring nucleation of these phases (Stumm and Morgan, 1996).

2.4.4   Redox

Electrons occupying the outermost orbital of an atom are known as valence electrons. A reduction in the number of these electrons is known as oxidation and the opposite is reduction therefore the oxidation state of an element refers to the number of valence electrons it has lost. Many elements are stable in natural systems in more than one oxidation state (redox elements). Transition metals in particular have many potential oxidation states due to the similar energies of the outermost d and s electron shells which allows d-shell electrons to act as additional valence electrons. The redox state of an element can influence both its toxicity and mobility in the environment and is therefore a critical parameter to consider during environmental risk assessment (Krauskopf and Bird,

1995; Langmuir, 1997). Redox reactions usually involve transfer of protons in addition to electrons. In general oxidation releases protons and reduction consumes them, thus raising or lowering the solution pH respectively (Langmuir, 1997).

The redox potential (Eh) of an environment is a measure of its ability to supply electrons to oxidising agents or remove them from a reducing agent and is analogous to pH insofar as pH can be considered a measure of the ability of an environment to supply protons to a base or remove them from an acid (Krauskopf and Bird, 1995). Thus, a particular oxidation state of a metal will be stable in an Eh/pH field where electron or proton transfer is not thermodynamically favoured.

Trace metals are generally transported in water as complexes, i.e. groups of atoms which consist of a metallic core cation (co-ordination centre) bonded to ligands (anions or neutral molecules) which surround it . The oxidation state of the central cation determines the ionic potential of the cation:

$$Ip = {}^z/_r$$

Where z is the charge on the atom and r the radius. When Ip is low, bonds between central cations and ligands are largely ionic in nature and thus complexes are readily soluble as cations, aquocations (i.e. hydrated cations) and occasionally hydroxycations. As Ip increases, bonds between the central cation and ligands become correspondingly more covalent in character. At Ip values between 3 and 8.5, the positive charge densities of the core cations are high enough to repel protons from coordinating water molecules and so they can only remain soluble if bonded to OH^- and O^{2-} ligands. Core cations in this Ip range therefore form soluble oxycations (e.g. VO^{2+}), hydroxycations (e.g. $FeOH^{2+}$) and hydroxyanions (e.g. $Al(OH)_4^-$; Fig. 2.5). At higher Ip values, bonds
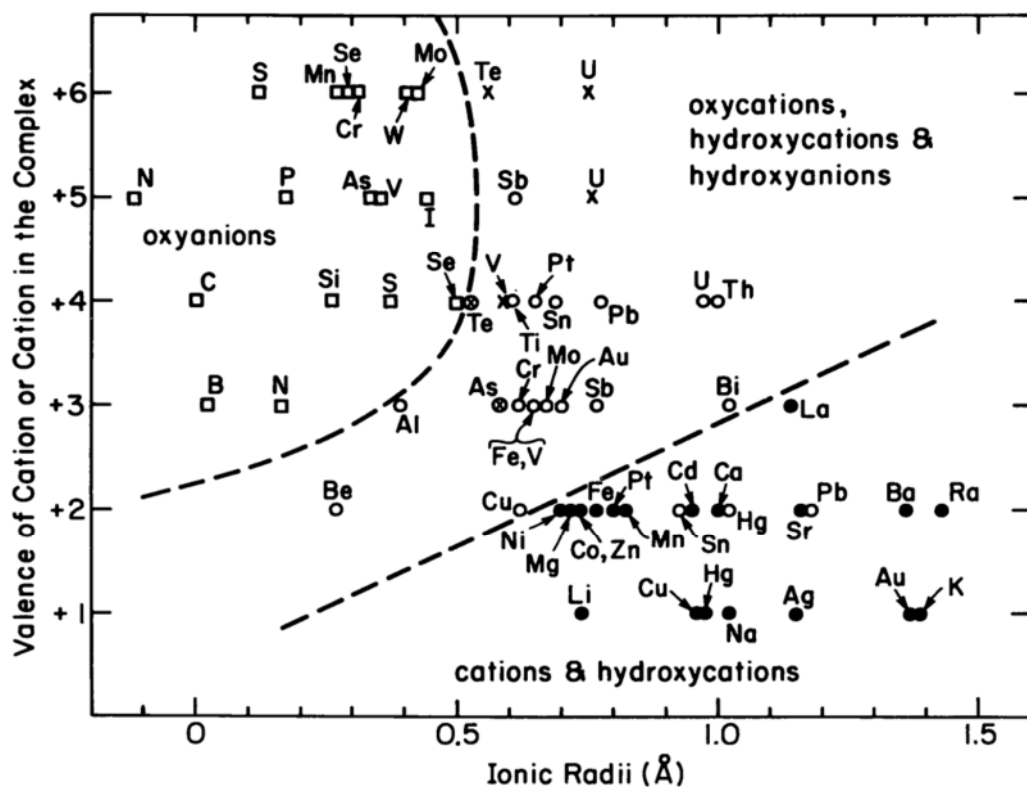
Figure 2.5 - Valence of core cations against apparent ionic radii. Dashed lines divide species according to their behaviour. (●) cations and aquocations; (○) hydroxycations and hydroxyanions; (x) oxycations; (□) oxyanions (from Langmuir (1979)).

between central cations and ligands are predominantly covalent leading to the formation of oxyanions which are soluble due to their overall low charge density (Langmuir, 1997). As discussed in section 2.4.1, soluble oxyanions and oxycations exhibit different adsorption characteristics above and below the PZC of a sorbent. Furthermore, ionic radii and ionic potential are both important factors in determining the likelihood of a complex to be incorporated into a precipitating mineral phase (section 2.4.2; Krauskopf and Bird (1995)). Thus, it is clear that the oxidation state of a metal is a significant factor in determining its mobility in the environment.

Redox conditions may also affect the behaviour of sorbents and therefore any sorbed material. Mn and Fe^{3+} (hydr)oxides are amongst the most abundant minerals and effective sorbents for many trace metals (Brown and Parks, 2001) and are insoluble at circum-neutral pH (Langmuir, 1997). Since Fe^{2+} is soluble at circum-neutral pH, reductive dissolution of Fe^{3+} (hydr)oxides can release any sorbed material into the surrounding waters, thus increasing contaminant concentrations (Fox and Doner, 2003; Huang et al., 2015; Langmuir, 1997; Zachara et al., 2001).

2.4.5   Chelation

The majority of inorganic ligands form complexes in which a single electron pair of electrons are shared between one atom in the ligand and the central cation. These are known as monodentate lignads When two or more functional groups in a ligand allow it to occupy multiple coordination positions in the complex, the ligand is said to be multidentate. Such ligands are typically organic and form multiple bonds with cations via intermediate N, S or O atoms to produce a cage-like structure around the central cation. The process of forming these multidentate compounds is called chelation and the structures themselves are known as chelates (Krauskopf and Bird, 1995; Langmuir, 1997; Sposito, 1989; Stumm and Morgan, 1996). Typical chelating agents include oxalate (bidentate), citrate (tridentate) and ethylenediamine tetraacetate (EDTA; hexadentate) (Stumm and Morgan, 1996) and humic and fulvic acids are also thought to form chelation complexes with metals (Langmuir, 1997). Chelation complexes are thought to be responsible for the enrichment of metals (e.g. V, Mo and Ni) in organic matter in some sediments (Krauskopf and Bird, 1995).

The exceptional strength of metal-chelate bonding has led to the development of chelation as a technique to remove heavy metals from wastewaters (Fu and Wang, 2011;

Langmuir, 1997) as well as contaminated soils (Peters, 1999). Chelation of metals can reduce their bioavailability and toxicity, thus reducing the risk posed to aquatic ecosystems (Stumm and Morgan, 1996). However, concern has been raised over the presence of persistent chelating agents in the environment which have the potential to remobilise heavy metals from sediments (Nowack and VanBriesen, 2005).

2.5 Environmental chemistry of vanadium

V is a redox active transition metal which can exist in oxidation states from -1 to +5 (Chaurand et al., 2007b). Of these, the +3, +4 and +5 oxidation states are the most common and stable under aqueous conditions (Langmuir, 1997; Peacock and Sherman, 2004; Wanty and Goldhaber, 1992). V is an essential nutrient at trace quantities (Nielsen, 1991; Rehder, 2003) and has medicinal uses in chemotherapy (Evangelou, 2002) and diabetes treatment (Thompson and Orvig, 2006). However, high doses of V are toxic and V^{5+} has been noted as a possible human carcinogen (IARC, 2006; Nriagu, 1998). In general the toxicity of V evolves with oxidation state with the V^{5+} forms being the most toxic (Barceloux, 1999).

V can occur in tetrahedral, square pyramidal or octahedral coordination environments (Huang et al., 2015). The coordination environment of V varies according to speciation. V^{3+} (electron configuration $[Ar]3s^23p^63d^2$) generally occurs in octahedral coordination. V^{4+} ($[Ar]3s^23p^63d^1$) can occur in octahedral or square pyramidal coordination and V^{5+} ($[Ar]3s^23p^63d^0$) occurs in tetrahedral, square pyramidal and octahedral coordination (Schindler et al., 2000b). Examples of V compounds, their respective coordination environments and bond lengths are provided in table 2.2.

Table 2.2 - Selected V compounds, their valence, coordination, bond type and bond lengths (after Chaurand et al. (2007b))

Compound	Valence	Coordination	Bond type	Bond distance (Å)
V metal	0	8	V-V	2.622
FeV_2O_4 (Coulsonite)	3	6	V-O	1.9782
V_2O_4	4	6	V-O	1.76, 1.86, 1.87, 2.01, 2.03, 2.05
$Ca(VO)(Si_4O_{10}) \cdot 4H_2O$	4	5	V-O	1.6, 1.98 x 4
$Ca_3(V_{10}O_{28}) \cdot 17H_2O$ (Pascoite)	5	6	V-O	1.598-2.312
V_2O_5	5	5	V-O	1.585, 1.780, 1.878, 1.878, 2.021
Na_3VO_4	5	4	V-O	1.677, 1.696 x 3
$Pb_5(VO_4)_3Cl$ (Vanadinite)	5	4	V-O	1.7

Due to its similar size and charge, V readily substitutes for Fe and Al in minerals. Octahedral V^{3+} and V^{4+} have been found to substitute for Fe^{3+} in Fe oxides and Al^{3+} in clay minerals respectively (Huang et al., 2015). V is found in high concentrations in steel slags (0.04 – 1.48 wt%; Proctor et al. (2000); Tossavainen et al. (2007)), where it occurs as octahedrally coordinated V^{3+} in dicalcium aluminoferrite as well as tetrahedrally coordinated V^{5+} in weathered regions (Chaurand et al., 2007b; Presslinger and Klepp, 2002). Incorporation of V into neo-formed precipitates is not well documented, however, Cornelis et al. (2008b) noted the potential for selenate and arsenate, which are of a similar size to vanadate, to be incorporated into calcite.

V speciation in natural systems depends strongly on pH and Eh, in addition to concentration and solution chemistry. In aqueous environments V^{4+} and V^{5+} are the dominant species in natural waters. V^{5+} species are stable across a wide pH range and are the dominant species in oxic environments at low pH and both oxic and anoxic systems above around pH 8 (Fig. 2.6; Huang et al. (2015); Takeno (2005)). V^{5+} is generally present
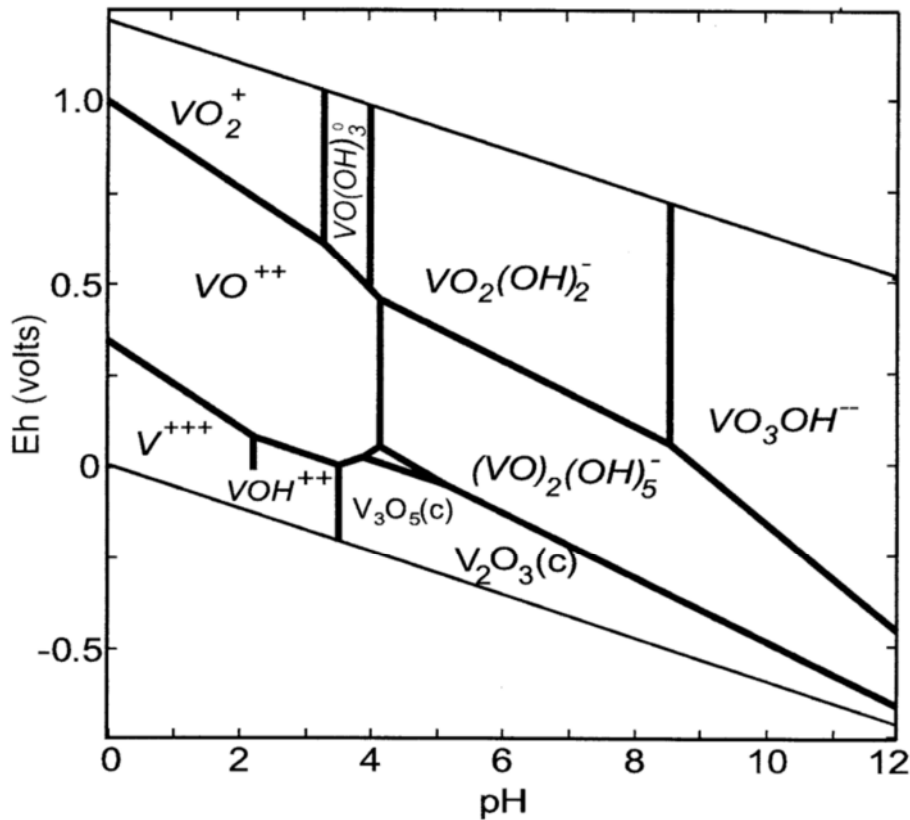
Figure 2.6 - Eh – pH diagram for aqueous V species V-O-H system. [V] ≈ 2.5 ppm. (c) denotes crystalline phases (from Peacock and Sherman (2004)).

as the vanadate oxyanion (VO_4^{3-}) at high pH and the VO_2^+ oxycation at low pH whilst at circum-neutral pH, the phosphate-like anion $H_2VO_4^-$ is the dominant species (Fig. 2.7; Huang et al. (2015); Wanty and Goldhaber (1992); Wehrli and Stumm (1989)).

V^{4+} and V^{3+} are the products of abiotic or biotic reduction of V^{5+} (Huang et al., 2015). V^{4+} generally occurs as the vanadyl cation (VO^{2+}) or its hydrolysed species, $VO(OH)^+$ under acidic or moderately reducing conditions. These species are not generally soluble above about pH 7 unless as part of inorganic or organic complexes, however, V^{4+} is readily complexed by a wide range of inorganic and organic ligands including humic and fulvic acids which can lead to its mobilisation to solution from solid phases (Huang et al., 2015; Wanty and Goldhaber, 1992). Whilst complexing of V^{5+} by organic matter is less common, V^{5+} organic complexes may be formed as intermediates during reduction to
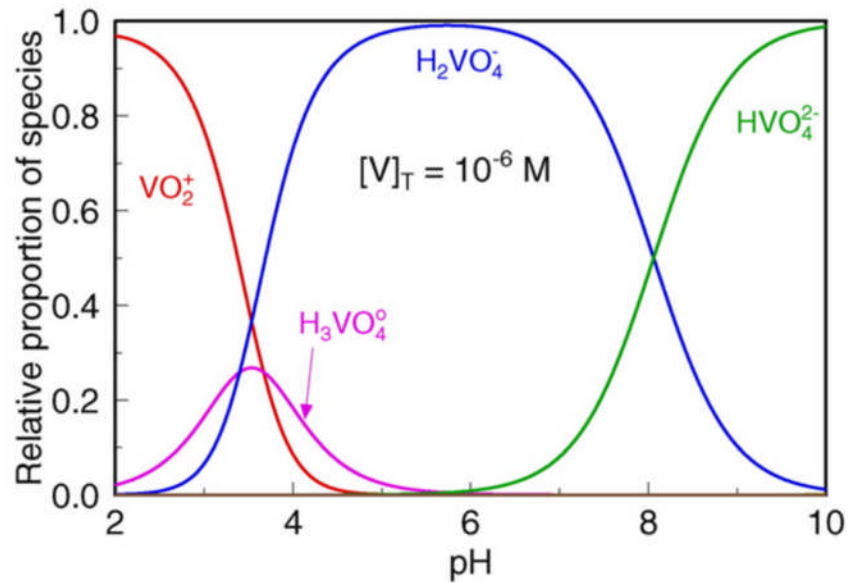
Figure 2.7 - V^{5+} speciation in dilute solutions (from (Huang et al., 2015)).

more stable V^{4+} complexes (Huang et al., 2015). V^{3+} is readily oxidised to V^{4+} or V^{5+} and is therefore rarely found in relatively well-oxidised near-surface environments. Under anoxic conditions V^{3+} species can persist in solution up to ~pH 10 whereupon they become unstable and V^{5+} becomes the dominant species (Huang et al., 2015).

Redox conditions, therefore, play a crucial role in controlling the mobility of V in natural systems. Reduction of V^{5+} to V^{4+} or V^{3+} (e.g. by organic acids or H_2S) results in the reduced species rapidly being removed from solution either by adsorption or complexation with particulates, or through the formation of insoluble hydroxides (Breit and Wanty, 1991; Huang et al., 2015; Szalay and Szilágyi, 1967). Conversely, oxidation of reduced and bound V^{3+} or V^{4+} can lead to mobilisation of toxic V^{5+} in the aqueous phase (Yang et al., 2014). Furthermore, the speciation of V strongly influences its adsorption behaviour. V^{4+} and V^{5+} adsorb readily to metal oxides by formation of monodentate and bidentate inner-sphere complexes (Peacock and Sherman, 2004; Wehrli and Stumm, 1989). Ligand exchange reactions can provide adsorption mechanisms where they would otherwise be inhibited by electrostatic repulsion; in particular, adsorption of vanadate oxycations to

positively charged FeOOH surfaces (Peacock and Sherman, 2004; Wehrli and Stumm, 1988; Wehrli and Stumm, 1989). Similarly, at higher pH, conjugate acids of the vanadate oxyanion (e.g. $VO_2(OH)_2^-$ and $VO_3(OH)^{2-}$) can behave like phosphate and bond to negatively charged surfaces by ligand exchange (Peacock and Sherman, 2004; Sigg and Stumm, 1981).

In natural systems, competition with other anions for sorption sites may reduce vanadate adsorption. Similar oxyanions can include phosphate, arsenate, selenate and molybdate (Huang et al., 2015). An order of $VO_4^{3-} > PO_4^{3-} > SeO_3^{2-} > MoO_4^{2-}$ has been proposed with SO_4^{2-}, NO_3^- and Cl^- having no effect during adsorption to Fe(III) and Cr(III) hydroxides (Prathap and Namasivayam, 2010). Adsorption effects may also be reduced in the presence of high concentrations of V^{5+}, either due to saturation of adsorption sites or due to the formation of polymeric V species (Peacock and Sherman, 2004). High concentrations of V in aqueous solutions tend to polymerise to form decavanadates and metavanadates at concentrations > 100 µM L^{-1} and at concenctrations > 0.1 M L^{-1} polynuclear species including decavandate, metavanadate and pyrovanadate are dominant in solution (Baes and Mesmer, 1976; Peacock and Sherman, 2004). Polymeric V species have a reduced affinity for adsorption and so may persist in solution at circum-neutral pH (Burke et al., 2012; Peacock and Sherman, 2004).

2.6   Study sites

2.6.1   *Scunthorpe steelworks & Yarborough landfill*

The steelworks at Scunthorpe, UK are an integrated iron and steel manufacturing site. Four blast furnaces are used to make molten Fe, which is put through an intermediate desulphurising process prior to being converted to steel in BOF converters. Subsequently,

secondary steelmaking is performed in ladles (British Steel, 2017a). BF slag from the site is recycled as clinker for the concrete industry. Approximately 10% of the waste produced on site (i.e. steelmaking slags from BOF and ladle processes, also including spent refractory liners) cannot be reprocessed or recycled and is stored in landfill at Yarborough (53°35′22.24″N 0°35′41.52″W; British Steel (2017b)).

2.6.2   Howden Burn, near Consett

The steelworks at Consett, County Durham, UK were a combined iron and steelmaking works which operated between 1864 and 1980. Both BF and steelmaking slags in addition to flue dust, ashes and demolition rubble, were dumped extensively in the area to a depth of up to 45 m. The resulting heaps cover an area of approximately 290 hectares and overlie superficial alluvium and glacial till above Lower Coal Measures strata (Mayes et al., 2008).

Since the closure of the site, the heaps have been extensively landscaped, however, rainwater can still infiltrate and percolate through the heaps. The high CaO content of the waste (~40 % w/w) leads to generation of a highly alkaline leachate which is drained by a number of streams (Fig 2.8). The northern part of the site which was previously occupied by the blast furnace, power station and steel plant is drained by Howden Burn (source 54°51'12.9"N 1°51'41.1"W). The watercourse has been heavily impacted by the large volumes of leachate (typically > 3 L s^{-1}) it receives. During site operations, the stream was dosed with sulphuric acid to control pH levels, however, it is currently characterised by elevated pH values of 9.0 – 12.5. The steep and narrow nature of the streamway (generally 0.6 – 2.2 m wide and with an average gradient of 0.09) leads to a turbulent flow, ensuring good aeration of the water. Consequently Ca precipitation rates have been estimated at between 14.0 and 48.2 g day^{-1} m^{-2}. This rate of precipitation has smothered the streambed

and the entire 0.9 km reach is devoid of benthic biota (Hull et al., 2014; Mayes and Younger, 2006; Mayes et al., 2008).
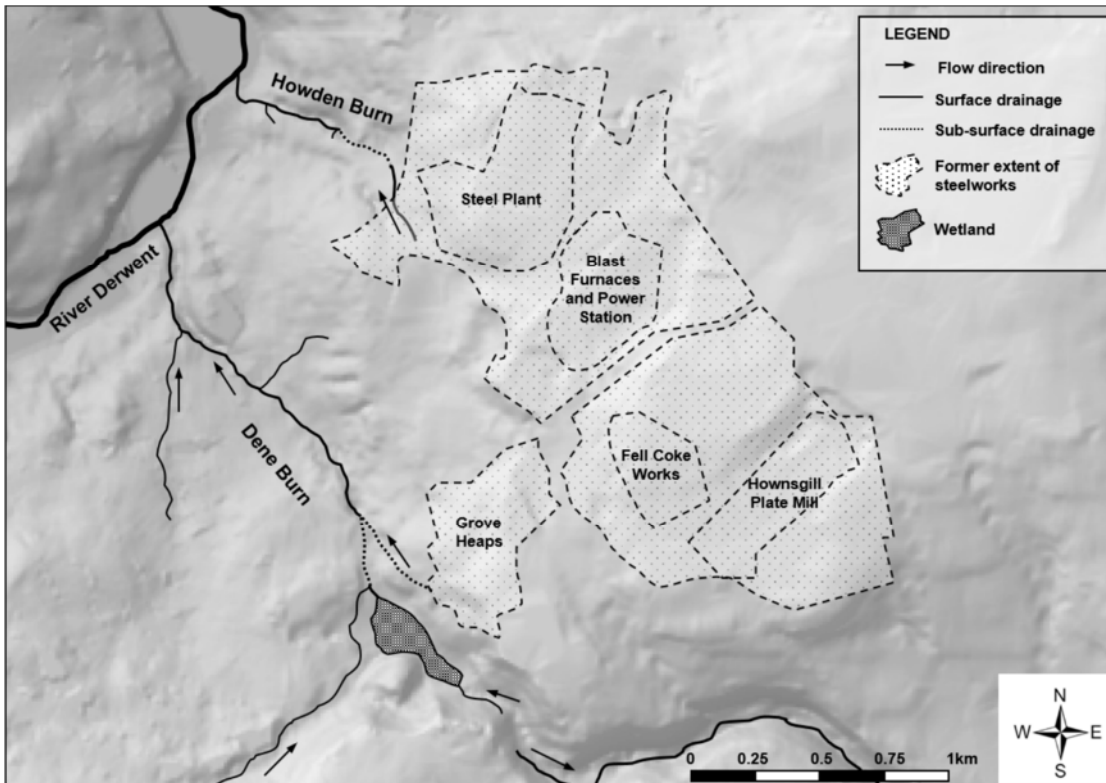
Figure 2.8 - Site plan of the former Consett Iron and Steel works showing location of drainage streams.

2.7   References

AHMEDZADE, P., SENGOZ, B., 2009. Evaluation of steel slag coarse aggregate in hot mix asphalt concrete. J. Hazard. Mater. 165, 300-305.

ALLEN, A.J., THOMAS, J.J., JENNINGS, H.M., 2007. Composition and density of nanoscale calcium-silicate-hydrate in cement. Nat Mater 6, 311-316.

APUL, D.S., GARDNER, K.H., EIGHMY, T.T., FÄLLMAN, A.M., COMANS, R.N.J., 2005. Simultaneous application of dissolution/precipitation and surface complexation/surface precipitation modeling to contaminant leaching. Environmental Science and Technology 39, 5736-5741.

ASI, I.M., 2007. Evaluating skid resistance of different asphalt concrete mixes. Building and Environment 42, 325-329.

AUSTRALASIAN SLAG ASSOCIATION, 2002. A guide to the use of iron and steel slag in roads. ISBN 0 9577051, 58.

BAES, C.F., MESMER, R.E., 1976. The hydrolysis of cations. Wiley.

BARCELOUX, D.G., 1999. Vanadium. Journal of toxicology. Clinical toxicology 37, 265-278.

BAYLESS, E.R., SCHULZ, M.S., 2003. Mineral precipitation and dissolution at two slag-disposal sites in northwestern Indiana, USA. Environmental Geology 45, 252-261.

BOBICKI, E.R., LIU, Q., XU, Z., ZENG, H., 2012. Carbon capture and storage using alkaline industrial wastes. Progress in Energy and Combustion Science 38, 302-320.

BONENFANT, D., KHAROUNE, L., SAUVE´, S., HAUSLER, R., NIQUETTE, P., MIMEAULT, M., KHAROUNE, M., 2008. CO2 Sequestration Potential of Steel Slags at Ambient Pressure and Temperature. Industrial & Engineering Chemistry Research 47, 7610-7616.

BOWDEN, L.I., JARVIS, A.P., YOUNGER, P.L., JOHNSON, K.L., 2009. Phosphorus Removal from Waste Waters Using Basic Oxygen Steel Slag. Environ. Sci. Technol. 43, 2476-2481.

BOYLAN, A.A., STEWART, D.I., GRAHAM, J.T., TRIVEDI, D., BURKE, I.T., 2016. Mechanisms of inorganic carbon-14 attenuation in contaminated groundwater: Effect of solution pH on isotopic exchange and carbonate precipitation reactions. Applied Geochemistry, in press.

BREIT, G.N., WANTY, R.B., 1991. Vanadium accumulation in carbonaceous rocks: A review of geochemical controls during deposition and diagenesis. Chemical Geology 91, 83-97.

BRITISH STEEL, 2017a. How we make steel, http://britishsteel.co.uk/what-we-do/how-we-make-steel/.

BRITISH STEEL, 2017B. Responsible Sourcing, http://britishsteel.co.uk/who-we-are/sustainability/responsible-sourcing/.

BROWN, G.E., PARKS, G.A., 2001. Sorption of Trace Elements on Mineral Surfaces: Modern Perspectives from Spectroscopic Studies, and Comments on Sorption in the Marine Environment. International Geology Review 43, 963-1073.

BUCHMAN, M.F., 2008. NOAA Screening Quick Reference Tables.

BURKE, I.T., MAYES, W.M., PEACOCK, C.L., BROWN, A.P., JARVIS, A.P., GRUIZ, K., 2012. Speciation of Arsenic, Chromium, and Vanadium in Red Mud Samples from the Ajka Spill Site, Hungary. Environ. Sci. Technol. 46, 3085-3092.

BURKE, I.T., PEACOCK, C.L., LOCKWOOD, C.L., STEWART, D.I., MORTIMER, R.J.G., WARD, M.B., RENFORTH, P., GRUIZ, K., MAYES, W.M., 2013. Behavior of Aluminum, Arsenic, and Vanadium during the Neutralization of Red Mud Leachate by HCl, Gypsum, or Seawater. Environ. Sci. Technol. 47, 6527-6535.

CHAURAND, P., ROSE, J., BRIOIS, V., OLIVI, L., HAZEMANN, J.L., PROUX, O., DOMAS, J., BOTTERO, J.Y., 2007a. Environmental impacts of steel slag reused in road construction: A crystallographic and molecular (XANES) approach. J. Hazard. Mater. 139, 537-542.

CHAURAND, P., ROSE, J., BRIOIS, V., SALOME, M., PROUX, O., NASSIF, V., OLIVI, L., SUSINI, J., HAZEMANN, J.L., BOTTERO, J.Y., 2007b. New methodological approach for the vanadium K-edge X-ray absorption near-edge structure interpretation: Application to the speciation of vanadium in oxide phases from steel slag. J. Phys. Chem. B 111, 5101-5110.

CHAURAND, P., ROSE, J., DOMAS, J., BOTTERO, J.Y., 2006. Speciation of Cr and V within BOF steel slag reused in road constructions. Journal of Geochemical Exploration 88, 10-14.

CHEN, J.J., THOMAS, J.J., TAYLOR, H.F.W., JENNINGS, H.M., 2004. Solubility and structure of calcium silicate hydrate. Cem. Concr. Res. 34, 1499-1519.

CHIFFOLEAU, J.-F., CHAUVAUD, L., AMOUROUX, D., BARATS, A., DUFOUR, A., PÉCHEYRAN, C., ROUX, N., 2004. Nickel and vanadium contamination of benthic invertebrates following the "Erika" wreck. Aquatic Living Resources 17, 273-280.

CORNELIS, G., JOHNSON, C.A., GERVEN, T.V., VANDECASTEELE, C., 2008a. Leaching mechanisms of oxyanionic metalloid and metal species in alkaline solid wastes: A review. Applied Geochemistry 23, 955-976.

CORNELIS, G., POPPE, S., VAN GERVEN, T., VAN DEN BROECK, E., CEULEMANS, M., VANDECASTEELE, C., 2008b. Geochemical modelling of arsenic and selenium leaching in alkaline water treatment sludge from the production of non-ferrous metals. J. Hazard. Mater. 159, 271-279.

COSTA, G., POLETTINI, A., POMI, R., STRAMAZZO, A., 2016. Leaching modelling of slurry-phase carbonated steel slag. J. Hazard. Mater. 302, 415-425.

CZOP, M., MOTYKA, J., SRACEK, O., SZUWARZYŃSKI, M., 2011. Geochemistry of the Hyperalkaline Gorka Pit Lake (pH > 13) in the Chrzanow Region, Southern Poland. Water, Air, & Soil Pollution 214, 423-434.

DAS, B., PRAKASH, S., REDDY, P.S.R., MISRA, V.N., 2007. An overview of utilization of slag and sludge from steel industries. Resources, Conservation and Recycling 50, 40-57.

DE SA, R.G., E SILVA, G.L., BITTTENCOURT, L., 2007. Recycling of spent refractories from metallurgical processing management and technological approach. 8th UNITECR, Dresden, Alemania.

DE WINDT, L., CHAURAND, P., ROSE, J., 2011. Kinetics of steel slag leaching: Batch tests and modeling. Waste Manage. 31, 225-235.

DOUCET, F.J., 2010. Effective CO2-specific sequestration capacity of steel slags and variability in their leaching behaviour in view of industrial mineral carbonation. Minerals Engineering 23, 262-269.

EFFLER, S.W., 1987. The impact of a chlor-alkali plant on Onondaga Lake and adjoining systems. Water, Air, and Soil Pollution 33, 85-115.

EFFLER, S.W., Brooks, C.M., 1998. Dry Weight Deposition in Polluted Onondaga Lake, New York, U.S.A. Water, Air, and Soil Pollution 103, 389-404.

ELONEVA, S., PUHELOINEN, E.-M., KANERVA, J., EKROOS, A., ZEVENHOVEN, R., FOGELHOLM, C.-J., 2010. Co-utilisation of CO2 and steelmaking slags for production of pure CaCO3 – legislative issues. Journal of Cleaner Production 18, 1833-1839.

ENGSTRÖM, F., ADOLFSSON, D., SAMUELSSON, C., SANDSTRÖM, Å., BJÖRKMAN, B., 2013. A study of the solubility of pure slag minerals. Minerals Engineering 41, 46-52.

EVANGELOU, A.M., 2002. Vanadium in cancer treatment. Critical Reviews in Oncology/Hematology 42, 249-265.

FÄLLMAN, A.M., 2000. Leaching of chromium and barium from steel slag in laboratory and field tests - A solubility controlled process? Waste Manage. 20, 149-154.

FENDORF, S.E., 1995. Surface reactions of chromium in soils and waters. Geoderma 67, 55-71.

FICHET, D., MIRAMAND, P., 1998. Vanadium toxicity to three marine invertebrates larvae: Crassostrea gigas, Paracentrotus lividus and Artemia salina. Chemosphere 37, 1363-1368.

FJELLHEIM, A., RADDUM, G.G., 1995. Benthic animal response after liming of three south Norwegian rivers. Water, Air, and Soil Pollution 85, 931-936.

FORD, D.C., WILLIAMS, P.W., 1989. Karst geomorphology and hydrology. Unwin Hyman London.

FOX, P.M., DONER, H.E., 2003. Accumulation, Release, and Solubility of Arsenic, Molybdenum, and Vanadium in Wetland Sediments. Journal of Environmental Quality 32, 2428-2435.

FRANK, A., MADEJ, A., GALGAN, V., PETERSSON, L.R., 1996. Vanadium poisoning of cattle with basic slag. Concentrations in tissues from poisoned animals and from a reference, slaughter-house material. Science of The Total Environment 181, 73-92.

FU, F.L., WANG, Q., 2011. Removal of heavy metal ions from wastewaters: A review. J. Environ. Manage. 92, 407-418.

GARD, J.A., TAYLOR, H.F.W., 1976. Calcium silicate hydrate (II) ("C-S-H(II)"). Cem. Concr. Res. 6, 667-677.

GARRAULT, S., BEHR, T., NONAT, A., 2006. Formation of the C−S−H Layer during Early Hydration of Tricalcium Silicate Grains with Different Sizes. The Journal of Physical Chemistry B 110, 270-275.

GARRAULT, S., NONAT, A., 2001. Hydrated Layer Formation on Tricalcium and Dicalcium Silicate Surfaces: Experimental Study and Numerical Simulations. Langmuir 17, 8131-8138.

GEISELER, J., 1996. Use of steelworks slag in Europe. Waste Manage. 16, 59-63.

GERKE, T.L., SCHECKEL, K.G., MAYNARD, J.B., 2010. Speciation and distribution of vanadium in drinking water iron pipe corrosion by-products. Science of The Total Environment 408, 5845-5853.

GHOSH, S.N., RAO, P.B., PAUL, A.K., RAINA, K., 1979. The chemistry of dicalcium silicate mineral. Journal of Materials Science 14, 1554-1566.

GOETZ, E.R., RIEFLER, R.G., 2014. Performance of steel slag leach beds in acid mine drainage treatment. Chemical Engineering Journal 240, 579-588.

GOLDSCHMIDT, V.M., 1937. The principles of distribution of chemical elements in minerals and rocks. The seventh Hugo Muller Lecture, delivered before the Chemical Society on March 17th, 1937. Journal of the Chemical Society (Resumed), 655-673.

GOMES, H.I., JONES, A., ROGERSON, M., BURKE, I.T., MAYES, W.M., 2016a. Vanadium removal and recovery from bauxite residue leachates by ion exchange. Environ. Sci. Pollut. Res. 23, 23034-23042.

GOMES, H.I., MAYES, W.M., ROGERSON, M., STEWART, D.I., BURKE, I.T., 2016b. Alkaline residues and the environment: a review of impacts, management practices and opportunities. Journal of Cleaner Production 112, 3571-3582.

GOMES, H.I., ROGERSON, M., BURKE, I.T., STEWART, D.I., MAYES, W.M., 2017. Hydraulic and biotic impacts on neutralisation of high-pH waters. Science of The Total Environment 601–602, 1271-1279.

GOUGAR, M.L.D., SCHEETZ, B.E., ROY, D.M., 1996. Ettringite and C • S • H Portland cement phases for waste ion immobilization: A review. Waste Manage. 16, 295-303.

GROVES, G.W., BROUGH, A., RICHARDSON, I.G., DOBSON, C.M., 1991. Progressive Changes in the Structure of Hardened C3S Cement Pastes due to Carbonation. Journal of the American Ceramic Society 74, 2891-2896.

HADJSADOK, A., KENAI, S., COURARD, L., MICHEL, F., KHATIB, J., 2012. Durability of mortar and concretes containing slag with low hydraulic activity. Cement and Concrete Composites 34, 671-677.

HANAGIRI, S., MATSUI, T., SHIMPO, A., ASO, S., INUZUKA, T., MATSUDA, T., SAKAKI, S., NAKAGAWA, H., 2008. Recent improvement of recycling technology for refractories. Shinnittetsu Giho 388, 93.

HASLAM, S.M., 1990. River pollution: an ecological perspective. Belhaven Press.

HAYNES, R.J., BELYAEVA, O.N., KINGSTON, G., 2013. Evaluation of industrial wastes as sources of fertilizer silicon using chemical extractions and plant uptake. Journal of Plant Nutrition and Soil Science 176, 238-248.

HEM, J.D., 1985. Study and interpretation of the chemical characteristics of natural water. Department of the Interior, US Geological Survey.

HOUSECROFT, C.E., CONSTABLE, E.C., 2006. Chemistry: An Introduction to Organic, Inorganic and Physical Chemistry. Pearson Prentice Hall.

HUANG, J.-H., HUANG, F., EVANS, L., GLASAUER, S., 2015. Vanadium: Global (bio)geochemistry. Chemical Geology 417, 68-89.

HUIJGEN, W.J.J., COMANS, R.N.J., 2005. Mineral CO2 Sequestration by Steel Slag Carbonation. Environ. Sci. Technol. 39, 9676-9682.

HUIJGEN, W.J.J., COMANS, R.N.J., 2006. Carbonation of steel slag for CO2 sequestration: Leaching of products and reaction mechanisms. Environmental Science and Technology 40, 2790-2796.

HULL, S.L., OTY, U.V., MAYES, W.M., 2014. Rapid recovery of benthic invertebrates downstream of hyperalkaline steel slag discharges. Hydrobiologia 736, 83-97.

IARC, 2006. Cobalt in hard metals and cobalt sulfate, gallium arsenide, indium phosphide and vanadium pentoxide. IARC monographs on the evaluation of carcinogenic risks to humans 86, 1.

IARC, 2012. Arsenic, metals, fibres, and dusts. IARC monographs on the evaluation of carcinogenic risks to humans 100, 11.

JENNINGS, H.M., 1986. Aqueous Solubility Relationships for Two Types of Calcium Silicate Hydrate. Journal of the American Ceramic Society 69, 614-618.

JÖNSSON, B., WENNERSTRÖM, H., NONAT, A., CABANE, B., 2004. Onset of Cohesion in Cement Paste. Langmuir 20, 6702-6709.

JUCKES, L.M., 2002. Dicalcium silicate in blast-furnace slag: a critical review of the implications for aggregate stability. Mineral Processing and Extractive Metallurgy 111, 120-128.

JUCKES, L.M., 2003. The volume stability of modern steelmaking slags. Mineral Processing and Extractive Metallurgy 112, 177-197.

KORYAK, M., STAFFORD, L.J., REILLY, R.J., HOSKIN, R.H., HABERMAN, M.H., 1998. The Impact of Airport Deicing Runoff on Water Quality and Aquatic Life in a Pennsylvania Stream. Journal of Freshwater Ecology 13, 287-298.

KORYAK, M., STAFFORD, L.J., REILLY, R.J., MAGNUSON, M.P., 2002. Impacts of Steel Mill Slag Leachate on the Water Quality of a Small Pennsylvania Stream. Journal of Freshwater Ecology 17, 461-465.

KOSMULSKI, M., 2016. Isoelectric points and points of zero charge of metal (hydr)oxides: 50years after Parks' review. Advances in Colloid and Interface Science 238, 1-61.

KRAUSKOPF, K.B., BIRD, D.K., 1995. Introduction to geochemistry. McGraw-Hill.

KWONG, K., BENNETT, J., 2002. Recycling Practices of Spent MgO-C Refractories. Journal of Minerals and Materials Characterization and Engineering 1, 69-78.

LANGMUIR, D., 1979. Techniques of Estimating Thermodynamic Properties for Some Aqueous Complexes of Geochemical Interest. Chemical Modeling in Aqueous Systems. American Chemical Society.

LANGMUIR, D., 1997. Aqueous Environmental Geochemistry. Prentice Hall.

LEWIS, D.W., 1982. Properties and uses of iron and steel slags National Slag Association, Presented at Symposium on Slag National Institute for Transport and Road Research South Africa, February, 1982
http://www.nationalslag.org/sites/nationalslag/files/documents/nsa_182-6_properties_and_uses_slag.pdf.

LONCNAR, M., VAN DER SLOOT, H.A., MLADENOVIČ, A., ZUPANČIČ, M., KOBAL, L., BUKOVEC, P., 2016. Study of the leaching behaviour of ladle slags by means of leaching tests combined with geochemical modelling and mineralogical investigations. J. Hazard. Mater. 317, 147-157.

LUXÁN, M.P., SOTOLONGO, R., DORREGO, F., HERRERO, E., 2000. Characteristics of the slags produced in the fusion of scrap steel by electric arc furnace. Cem. Concr. Res. 30, 517-519.

MATERN, K., RENNERT, T., MANSFELDT, T., 2013. Molybdate adsorption from steel slag eluates by subsoils. Chemosphere 93, 2108-2115.

MAYES, W.M., JARVIS, A.P., BURKE, I.T., WALTON, M., FEIGL, V., KLEBERCZ, O., GRUIZ, K., 2011. Dispersal and Attenuation of Trace Contaminants Downstream of the Ajka Bauxite Residue (Red Mud) Depository Failure, Hungary. Environ. Sci. Technol. 45, 5147-5155.

MAYES, W.M., YOUNGER, P.L., 2006. Buffering of Alkaline Steel Slag Leachate across a Natural Wetland. Environ. Sci. Technol. 40, 1237-1243.

MAYES, W.M., YOUNGER, P.L., AUMONIER, J., 2008. Hydrogeochemistry of alkaline steel slag leachates in the UK. Water Air Soil Pollut. 195, 35-50.

MISRA, K.C., 2012. Introduction to Geochemistry: Principles and Applications. Wiley.

MOTZ, H., GEISELER, J., 2001. Products of steel slags an opportunity to save natural resources. Waste Manage. 21, 285-293.

MUHMOOD, L., VITTA, S., VENKATESWARAN, D., 2009. Cementitious and pozzolanic behavior of electric arc furnace steel slags. Cem. Concr. Res. 39, 102-109.

NAVARRO, C., DIAZ, M., VILLA-GARCIA, M.A., 2010. Physico-Chemical Characterization of Steel Slag. Study of its Behavior under Simulated Environmental Conditions. Environ. Sci. Technol. 44, 5383-5388.

NIELSEN, F.H., 1991. Nutritional requirements for boron, silicon, vanadium, nickel, and arsenic: current knowledge and speculation. The FASEB Journal 5, 2661-2667.

NOWACK, B., VANBRIESEN, J.M., 2005. Chelating Agents in the Environment, Biogeochemistry of Chelating Agents. American Chemical Society, pp. 1-18.

NRIAGU, J.O., 1998. History, occurrence, and uses of vanadium. ADVANCES IN ENVIRONMENTAL SCIENCE AND TECHNOLOGY-NEW YORK- 30, 1-24.

OBER, J.A., 2017. Mineral commodity summaries 2017, Mineral Commodity Summaries, Reston, VA, p. 202.

OCHS, M., MALLANTS, D., WANG, L., 2016. Cementitious Materials and Their Sorption Properties, Radionuclide and Metal Sorption on Cement and Concrete. Springer International Publishing, Cham, pp. 5-16.

OMOTOSO, O.E., IVEY, D.G., MIKULA, R., 1998. Hexavalent chromium in tricalcium silicate: Part II Effects of CrVI on the hydration of tricalcium silicate. Journal of Materials Science 33, 515-522.

OSTER, S., 1982. The Diffusion of Innovation among Steel Firms: The Basic Oxygen Furnace. The Bell Journal of Economics 13, 45-56.

PEACOCK, C.L., SHERMAN, D.M., 2004. Vanadium(V) adsorption onto goethite (alpha-FeOOH) at pH 1.5 to 12: A surface complexation model based on ab initio molecular geometries and EXAFS spectroscopy. Geochimica Et Cosmochimica Acta 68, 1723-1733.

PETERS, R.W., 1999. Chelant extraction of heavy metals from contaminated soils. J. Hazard. Mater. 66, 151-210.

PHENRAT, T., MARHABA, T.F., RACHAKORNKIJ, M., 2005. A SEM and X-ray study for investigation of solidified/stabilized arsenic–iron hydroxide sludge. J. Hazard. Mater. 118, 185-195.

PIATAK, N.M., PARSONS, M.B., SEAL, R.R., 2014. Characteristics and environmental aspects of slag: A review. Applied Geochemistry.

PRATHAP, K., NAMASIVAYAM, C., 2010. Adsorption of vanadate(V) on Fe(III)/Cr(III) hydroxide waste. Environmental Chemistry Letters 8, 363-371.

PRESSLINGER, H., KLEPP, K.O., 2002. Vanadium in converter slags. Steel Research 73, 522-525.

PROCTOR, D.M., FEHLING, K.A., SHAY, E.C., WITTENBORN, J.L., GREEN, J.J., AVENT, C., BIGHAM, R.D., CONNOLLY, M., LEE, B., SHEPKER, T.O., ZAK, M.A., 2000. Physical and chemical characteristics of blast furnace, basic oxygen furnace, and electric arc furnace steel industry slags. Environ. Sci. Technol. 34, 1576-1582.

QUARANTA, N.E., CALIGARIS, M.G., DÍAZ, O., 2014. Characterization of Converter Refractories for Recycling, Materials Science Forum. Trans Tech Publ, pp. 605-610.

REHDER, D., 2003. Biological and medicinal aspects of vanadium. Inorganic Chemistry Communications 6, 604-617.

RENFORTH, P., WASHBOURNE, C.L., TAYLDER, J., MANNING, D.A.C., 2011. Silicate Production and Availability for Mineral Carbonation. Environ. Sci. Technol. 45, 2035-2041.

RESENDE, W.S., STOLL, R.M., JUSTUS, S.M., ANDRADE, R.M., LONGO, E., BALDO, J.B., LEITE, E.R., PASKOCIMAS, C.A., SOLEDADE, L.E.B., GOMES, J.E., VARELA, J.A., 2000. Key features of alumina/magnesia/graphite refractories for steel ladle lining. Journal of the European Ceramic Society 20, 1419-1427.

RICHARDSON, I.G., 1999. The nature of C-S-H in hardened cements. Cem. Concr. Res. 29, 1131-1147.

RILEY, A.L., MAYES, W.M., 2015. Long-term evolution of highly alkaline steel slag drainage waters. Environ Monit Assess 187, 463.

ROADCAP, G.S., KELLY, W.R., BETHKE, C.M., 2005. Geochemistry of extremely alkaline (pH > 12) ground water in slag-fill aquifers. Ground Water 43, 806-816.

ROVNUSHKIN, V.A., VISLOGUZOVA, E.A., SPIRIN, S.A., SHEKHOVTSOV, E.V., KROMM, V.V., METELKIN, A.A., 2005. Composition of Ladle Slag and Refractory Materials and Its Effect on the Wear Resistance of the Lining of an RH Vacuum Degasser. Refractories and Industrial Ceramics 46, 193-196.

RUBINOS, D.A., BARRAL, M.T., 2013. Fractionation and mobility of metals in bauxite red mud. Environ. Sci. Pollut. Res. 20, 7787-7802.

SCHINDLER, M., HAWTHORNE, F.C., BAUR, W.H., 2000a. A crystal-chemical approach to the composition and occurrence of vanadium minerals. The Canadian Mineralogist 38, 1443-1456.

SCHINDLER, M., HAWTHORNE, F.C., BAUR, W.H., 2000b. Crystal chemical aspects of vanadium: Polyhedral geometries, characteristic bond valences, and polymerization of (VOn) polyhedra. Chemistry of Materials 12, 1248-1259.

SCHWAB, A.P., HICKEY, J., HUNTER, J., BANKS, M.K., 2006. Characteristics of Blast Furnace Slag Leachate Produced Under Reduced and Oxidized Conditions. Journal of Environmental Science and Health, Part A 41, 381-395.

SCRIVENER, K.L., NONAT, A., 2011. Hydration of cementitious materials, present and future. Cem. Concr. Res. 41, 651-665.

SHEN, D.H., WU, C.M., DU, J.C., 2009. Laboratory investigation of basic oxygen furnace slag for substitution of aggregate in porous asphalt mixture. Constr. Build. Mater. 23, 453-461.

SHEN, H.T., FORSSBERG, E., 2003. An overview of recovery of metals from slags. Waste Manage. 23, 933-949.

SHI, C., 2002. Characteristics and cementitious properties of ladle slag fines from steel production. Cem. Concr. Res. 32, 459-462.

SHI, C., 2004. Steel slag - Its production, processing, characteristics, and cementitious properties. Journal of Materials in Civil Engineering 16, 230-236.

SHI, H., ZHAO, Y., LI, W., 2002. Effects of temperature on the hydration characteristics of free lime. Cem. Concr. Res. 32, 789-793.

SIGG, L., STUMM, W., 1981. The interaction of anions and weak acids with the hydrous goethite (α-FeOOH) surface. Colloids and Surfaces 2, 101-117.

SPARKS, D.L., 2005. Toxic metals in the environment: the role of surfaces. Elements 1, 193-197.

SPENCE, R.D., 1992. Chemistry and Microstructure of Solidified Waste Forms. Taylor & Francis.

SPOSITO, G., 1987. Distinguishing Adsorption from Surface Precipitation, Geochemical Processes at Mineral Surfaces. American Chemical Society, pp. 217-228.

SPOSITO, G., 1989. The Chemistry of Soils. Oxford University Press.

STUMM, W., MORGAN, J.J., 1996. Aquatic chemistry: chemical equilibria and rates in natural waters. Wiley.

SUGIYAMA, D., FUJITA, T., 2006. A thermodynamic model of dissolution and precipitation of calcium silicate hydrates. Cem. Concr. Res. 36, 227-237.

SZALAY, A., SZILÁGYI, M., 1967. The association of vanadium with humic acids. Geochimica et Cosmochimica Acta 31, 1-6.

TAKENO, N., 2005. Atlas of Eh-pH diagrams. Geological survey of Japan open file report 419, 102.

TAYLOR, H.F.W., 1986. Proposed Structure for Calcium Silicate Hydrate Gel. Journal of the American Ceramic Society 69, 464-467.

TAYLOR, H.F.W., 1993. Nanostructure of C • S • H: Current status. Advanced Cement Based Materials 1, 38-46.

TAYLOR, H.F.W., 1997. Cement Chemistry. Thomas Telford.

THOMPSON, K.H., ORVIG, C., 2006. Vanadium in diabetes: 100 years from Phase 0 to Phase I. Journal of Inorganic Biochemistry 100, 1925-1935.

TOSSAVAINEN, M., ENGSTROM, F., YANG, Q., MENAD, N., LIDSTROM LARSSON, M., BJORKMAN, B., 2007. Characteristics of steel slag under different cooling conditions. Waste Manage. 27, 1335-1344.

USEPA, 1992. Toxicity Characteristic Leaching Procedure. Method 1311.

VAN OSS, H.G., 2003. Slag-iron and steel. US geological survey minerals yearbook 1.

WALKER, C.S., SUTOU, S., ODA, C., MIHARA, M., HONDA, A., 2016. Calcium silicate hydrate (C-S-H) gel solubility data and a discrete solid phase model at 25°C based on two binary non-ideal solid solutions. Cem. Concr. Res. 79, 1-30.

WANG, Q., YAN, P., 2010. Hydration properties of basic oxygen furnace steel slag. Constr. Build. Mater. 24, 1134-1140.

WANTY, R.B., GOLDHABER, M.B., 1992. Thermodynamics and kinetics of reactions involving vanadium in natural systems - accumulation of vanadium in sedimentary-rocks. Geochimica Et Cosmochimica Acta 56, 1471-1483.

WEHRLI, B., STUMM, W., 1988. Oxygenation of vanadyl (IV). Effect of coordinated surface hydroxyl groups and hydroxide ion. Langmuir 4, 753-758.

WEHRLI, B., STUMM, W., 1989. Vanadyl in natural-waters - adsorption and hydrolysis promote oxygenation. Geochimica Et Cosmochimica Acta 53, 69-77.

WILKIE, M.P., WOOD, C.M., 1996. The adaptations of fish to extremely alkaline environments. Comparative Biochemistry and Physiology Part B: Biochemistry and Molecular Biology 113, 665-673.

WU, S., XUE, Y., YE, Q., CHEN, Y., 2007. Utilization of steel slag as aggregates for stone mastic asphalt (SMA) mixtures. Building and Environment 42, 2580-2585.

YAN, J., MORENO, L., NERETNIEKS, I., 2000. The long-term acid neutralizing capacity of steel slag. Waste Manage. 20, 217-223.

YANG, J., TANG, Y., YANG, K., ROUFF, A.A., ELZINGA, E.J., HUANG, J.-H., 2014. Leaching characteristics of vanadium in mine tailings and soils near a vanadium titanomagnetite mining site. J. Hazard. Mater. 264, 498-504.

YI, H., XU, G., CHENG, H., WANG, J., WAN, Y., CHEN, H., 2012. An Overview of Utilization of Steel Slag. Procedia Environmental Sciences 16, 791-801.

YILDIRIM, I.Z., PREZZI, M., 2011. Chemical, Mineralogical, and Morphological Properties of Steel Slag. Advances in Civil Engineering 2011, 1-13.

YÜKSEL, İ., 2017. A review of steel slag usage in construction industry for sustainable development. Environment, Development and Sustainability 19, 369-384.

ZACHARA, J.M., COWAN, C.E., RESCH, C.T., 1991. Sorption of divalent metals on calcite. Geochimica et Cosmochimica Acta 55, 1549-1562.

ZACHARA, J.M., FREDRICKSON, J.K., SMITH, S.C., GASSMAN, P.L., 2001. Solubilization of Fe(III) oxide-bound trace metals by a dissimilatory Fe(III) reducing bacterium. Geochimica et Cosmochimica Acta 65, 75-93.

ZWOLAK, I., 2014. Vanadium carcinogenic, immunotoxic and neurotoxic effects: a review of in vitro studies. Toxicology Mechanisms and Methods 24, 1-12.

Chapter 3   Methodology

This chapter provides general details of sample collection, methods used during reagent preparation and theoretical background relating to instrumental analytical techniques used throughout the study. Detailed methodology relating to specific experiments is provided in the relevant data chapters.

3.1   Materials and field data collection

3.1.1   *Yarborough steelmaking waste*

Combined steelmaking waste comprising BOF steelmaking slag and spent refractory liners was collected within one week of deposition from the Yarborough landfill, Scunthorpe, UK (LAT 53°35'22.24"N LONG 0°35'41.52"W) in May 2013. The sample consisted of 50-500 g blocks (~100 kg total). A randomly selected sub-sample (~500 g total consisting of ~50 g pieces) of the combined waste for use in aerated and air-excluded leaching experiments (Chapter 5) was ground using a pestle and mortar and agate mill to produce a homogenised powder comprising 20-100 μm particles. The crushed waste was stored in a polythene bag within an airtight glass jar containing soda lime to prevent weathering due to contact with atmospheric CO_2 and moisture.

3.1.2   *Consett leachate*

Leachate emerging from deposited steelmaking waste was collected from the Howden Burn source at (LAT 54°51'12.9"N LONG 1°51'41.1"W) on 30th September 2015. Preliminary measurements of pH (11.8) and conductivity (1986 μS) were determined in-situ using a Myron L Ultrameter II calibrated using pH 4, 7 and 10 buffer solutions and

7000 μS conductivity standard solution. 5 L of water was collected in a PET container and refrigerated on return to the lab. Two 1 L HDPE bottles were also filled and frozen at -20 °C on return to the lab. Laboratory measurements of the sample water pH were determined immediately prior to use in experiments and are detailed in the relevant data chapters.

3.2   Lab methodology

3.2.1   Goethite

Goethite (α-FeOOH) was synthesised from $Fe(NO_3)_3$ and KOH using the method of Schwertmann and Cornell (2007). 180 mL 5 M KOH was added to 100 mL 1 M $Fe(NO_3)_3$ in a 2 L HDPE flask (HDPE is used to prevent leaching of Si from glassware at high pH) whilst stirring rapidly. The solution was immediately diluted to 2 L using 18 MΩ deionised water (DIW) water. The flask was closed and stored in an oven at 70 °C for 60 hours. The sample was removed from the oven and centrifuged. The supernatant was removed and the solid was washed to remove OH^- and NO_3^- by placing in dialysis tubing, sealing both ends and leaving overnight in DIW water. The water was replaced every 24 hours until the conductivity of the surrounding water remained equal to that of DIW water for 24 hours. Subsequently, the solid goethite was removed from the dialysis tubing and dried in an oven at 40 °C prior to being stored in an airtight PET jar.

3.2.2   Ca(OH)$_2$ solution

Saturated $Ca(OH)_2$ solution was prepared in an anaerobic, CO_2 – free chamber using 2 L DIW water which was degassed by bubbling N_2 gas for 60 minutes prior to

moving to the chamber. 30 g powdered $Ca(OH)_2$ was added to a small quantity of DIW water to form a slurry which was then transferred to a length of dialysis tubing and sealed at both ends. The tubing was placed in a 2 L Schott bottle with the rest of the DIW water and left in the anaerobic cabinet to equilibrate for > 2 days until the pH and conductivity of the solution had stabilised. The solution was stored and handled in an anaerobic, CO_2-free cabinet. Periodically additional degassed DIW water was added to the solution and left for > 2 days until equilibrium with $Ca(OH)_2$ was re-established.

3.2.3   NaVO₃ stock solution

0.1 M NaOH solution was prepared by dissolving 3.99 g NaOH tablets into 1 L DIW water under a nitrogen atmosphere to prevent CO_2 ingasing. Subsequently 0.239 g $NaVO_3$ was dissolved into this to give a 1000 ppm V stock solution. A 100 ppm stock for use in experiments was created from this by transferring 10 mL of 1000 ppm stock to a 100 mL volumetric flask and diluting to volume using 0.1 M NaOH. Both $NaVO_3$ stock solutions were subsequently stored and handled in an anaerobic, CO_2-free chamber.

3.2.4   Preparation of high V synthetic 'leachate'- method development

Initial attempts to create a high-V synthetic leachate used 0.05, 0.5, 5 and 10 mL of 100 ppm $NaVO_3$ in 100 mL saturated $Ca(OH)_2$ solution to make flasks containing V concentrations of 0.05, 0.5, 5 and 10 ppm. On mixing $NaVO_3$ and $Ca(OH)_2$ solutions, a white precipitate formed immediately in 10 and 5 ppm flasks and after several days in 0.5 and 0.05 ppm flasks (Table 3.1). ICP-MS analysis of the solution showed V concentrations which were considerably lower than expected. Therefore, the solution was assumed to have become oversaturated with respect to calcium vanadate during mixing resulting in its

precipitation removing V from solution. To prevent this, the saturated $Ca(OH)_2$ solution was diluted by a factor of 10 with degassed DIW water prior to use in V uptake experiments. An experimental control was set up in the form of a replicate flask in an anaerobic, CO_2-free chamber and sampled daily to demonstrate that 2.5 ppm V concentrations were stable in 10 % $Ca(OH)_2$ solution over time periods equal to the leachate neutralisation experiments preformed in Chapter 5 (Table 3.2).

Table 3.1 - V concentrations at 21 hours and 92 hours during initial attempts to create synthetic leachate using saturated $Ca(OH)_2$ solution.

$[V]_{initial}$ ppb	21 hours, ppb	92 hours, ppb
5	4.25	2.29
50	17.2	17.5
5000	128	39.8
10,000	112	69.0

Table 3.2 - V concentrations in control flask during neutralisation experiments (Chapter 5) using 10% $Ca(OH)_2$.

	0 hours	28 hours	48 hours	70 hours
[V] ppb	2560	2580	2500	2500

3.2.5 *pH measurement*

Where required, solution pH was determined electrochemically using a an Orion DualStar pH/ISE benchtop meter (Thermo Scientific, USA) with electrodes that were calibrated daily using pH 4, 7 and 10 buffer solutions.

3.3   Analytical techniques

3.3.1   X-ray fluorescence (XRF)

XRF is a non-destructive, analytical technique which uses x-rays to determine the elemental composition of a sample. An x-ray source (usually an x-ray tube) is used to irradiate the sample under analysis thus providing energy to electrons. If the energy provided is greater than the binding energy of the electron at a given level, an electron from that level may be ejected, leaving the atom in an unstable, excited state. To achieve stability, an electron from a higher energy shell is transferred to fill the initial electron site. In the process, the electron loses its excess energy as a secondary x-ray photon which may be detected as fluorescence. The energy of this photon is dependent on the energy difference between the initial hole and the energy of the electron which falls to fill it. Most atoms have several electron shells (e.g. K, L, M) and hence a variety of potential electron transitions may take place, each providing its own secondary x-rays. Therefore each element will produce a unique fluorescence spectrum which can be used to identify chemical species present in the sample (Brouwer, 2006).

Spectral peaks are named according to the energy level of the expelled electron and a Greek letter to denote the intensity of the line (known as Siegbahn notation) e.g. V K_α indicates the most intense peak caused by an electron ejected from the V K-shell. Key electron transitions and their Siegbahn notations are shown in Figure 3.1. In general K lines are the most intense, followed by L and then M lines (Jenkins, 1988).

XRF analysis of BOF slag (Chapter 4) was undertaken on multiple solid samples using an Olympus X-5000 XRF Analyser using user-defined calibrations to determine both major and minor elemental composition. Elements were auto-detected by the acquisition software (i.e. measurement was only quantified where peak height was at 3 standard deviation above background), and the elemental limit of detection was normally several
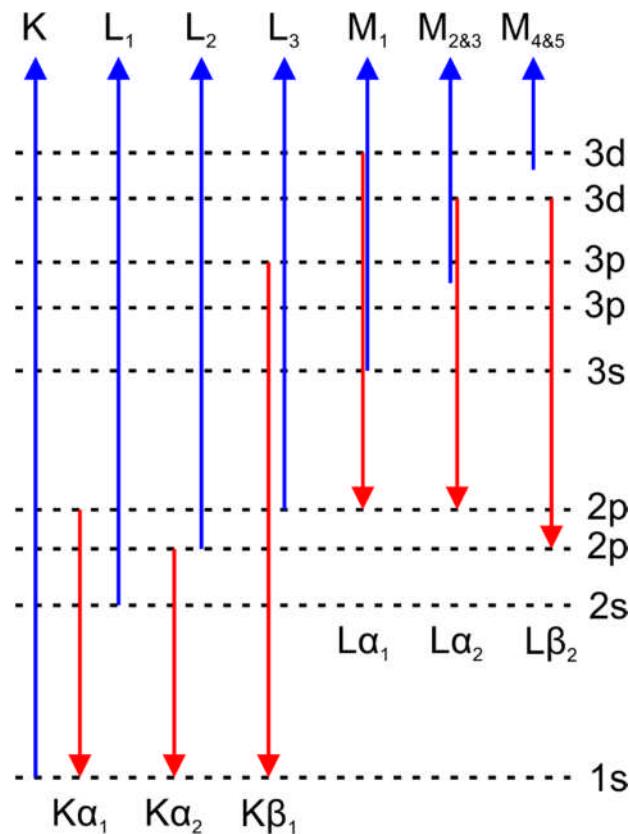
Figure 3.1 - Schematic showing key electron transitions during XRF/XAS. Blue arrows show transitions at absorption edges. Red arrows show transitions producing fluorescence lines.

orders of magnitude below measured values (Chapter 4, Table 4.2). Absolute uncertainty (versus certified standards) was $< \pm 30\%$ for Mg, $< \pm 20\%$ for S and, $< \pm 10\%$ for all other elements.

XRF analysis of the combined steelmaking waste from the Yarborough landfill (comprising BOF steelmaking slag and spent refractory lining; Chapter 5) was performed at the Department of Geology, University of Leicester on a PANalytical Axios Advanced XRF spectrometer using WROXI analytical package. Samples were dried overnight at 105 ºC prior to ignition at 950 ºC for 90 minutes in an air-ventilated electric muffle furnace and determination of loss on ignition (LOI). Major element analysis was performed on fused glass beads prepared from ignited powders using 100% lithium tetraborate flux (Fluxana FX-X100) in a 1:10 sample to flux ratio. Minor/trace element analysis was

undertaken using approximately 10 g of dried sample prepared as a pressed pellet using ~10 – 20 drops of 6.6% w/v polyvinyl alcohol in a 1:6 mix of methanol and distilled deionized water as a binder (Moviol 88 solution). Lower limits of detection (LLD) for this method are provided in Appendix A.

3.3.2   X-ray powder diffraction (XRD)

XRD is a non-destructive, x-ray technique used to determine the mineralogical composition of a sample.

Atomic spacing in a crystal lattice is comparable to the wavelength of x-rays, therefore these structures can act as a diffraction grating for incident x-rays (Dinnebier and Billinge, 2008). When x-rays are applied to an atom, electrons within the atom begin to oscillate at the same frequency as the incident ray. This produces secondary waves which propagate outwards from the atoms in a spherical pattern (Stanjek and Häusler, 2004). The arrangement of atoms within the crystal lattice may intensify the diffracted beam by constructive interference of the secondary waves resulting in a diffracted x-ray beam leaving the sample at a specific angle or angles whilst at all other angles, destructive interference attenuates the waves (Dinnebier and Billinge, 2008). The angle at which constructive interference occurs is determined according to Bragg's Law:

$$n\lambda = 2\text{d}\sin\theta$$

where n is a positive integer, λ is the wavelength of the incident wave, d is the interplanar distance of the crystal lattice and θ is the scattering angle of the diffracted ray (Bragg and Bragg, 1913). By using monochromatic radiation of a known frequency and scanning the sample through a range of 2θ values, all possible diffraction peaks associated with the sample can be determined. Using Bragg's Law, the angles at which these peaks occur can

be converted to d-spacings. Since each mineral has its own unique set of d-spacings, these can be compared to standard reference databases to determine the mineral phases present (Dutrow and Clark, 2017; Thermo ARL, 1999, Powder Diffraction File, 1974).

Samples were ground in a pestle and mortar until they passed a 100 μm sieve. Powder samples were then loaded into PMMA sample holders of Ø 25 mm x 1 mm depth and levelled using a glass slide. For low volume samples, powder was suspended in ethanol before being transferred to a Si crystal slide using a glass pipette. Samples were analysed on a Bruker D8 x-ray diffractometer configured in vertical $\theta/2\theta$ Bragg-Brentano using Cu K$_\alpha$ radiation and scanning between 2-150° 2θ. Diffraction peaks from unknown samples were matched to known standard reference patterns using Diffrac.Suite Eva v3.0 software using the International Centre for Diffraction Data (ICDD) PDF2 database.

3.3.3   Electron microscopy

Electron microscopy operates on the principle that electron beams can be focused using magnetic or electric fields in a similar manner to lenses being used to focus light in an optical microscope (Clarke and Eberhardt, 2002; McLaren, 1991). The main advantage over optical microscopy is that the potential resolution of an electron microscope is determined by the wavelength of the electron beam which may be up to 100,000 times smaller than optical wavelengths. Other advantages include a larger depth of field enabling more of the sample to be in focus at any given time despite surface roughness and the possibility of gathering additional data such as elemental composition (Vernon-Parry, 2000).

3.3.3.1   *Scanning electron microscopy*

Scanning electron microscopes (SEM) use a field emission gun (FEG) under a high vacuum (generally 10^{-10} Torr or higher) to produce an incident electron beam with an energy typically ranging between 2-40 keV and are capable of a resolution of 1 nm using secondary electrons (Vernon-Parry, 2000). Interactions between the incident beam and the sample produce different signals from which two imaging methods were used in this study:

Secondary electrons are low energy electrons (generally < 50 eV) that are produced at shallow depth (0.5 – 1.5 nm) when an electron is knocked from its orbit by an incident electron. These provide the highest resolution images and are primarily used for topographic imaging, however, some backscattered electrons may also be detected which can provide some compositional data (Seiler, 1983).

Backscatter electrons are incident electrons that are scattered by the nuclei of atoms within the sample and re-emerge from the surface. Since they originate from deeper within the sample, the resolution of backscatter images is generally not as good as those formed by secondary electrons and they mostly provide compositional data in which phases containing heavier elements produce a brighter image (Lloyd, 1987).

The ability of the SEM to image relatively large sample areas of the order of mm^2 makes it ideal for making visual comparisons between weathered and unweathered regions in steel slag. Samples were cut to size under water using a diamond saw before being set in epoxy resin and polished using diamond paste and water-free lubricant to remove the top 1 – 2 mm of material potentially exposed to water during cutting. To accelerate electrons to the sample and then to prevent build-up of charge during the analysis, samples need to be conductive (Reed, 1996). Accordingly, polished blocks were carbon coated (10 nm thickness) and earthed during analysis.

3.3.3.2   *Energy-dispersive x-ray spectroscopy (EDX)*

EDX uses the incident electron beam of an SEM or TEM as an excitation source to elevate core electrons from their orbitals. When a valence electron falls to fill the core hole, energy is released as x-rays which are detected by the EDX detector. The energies of these x-rays vary from element to element with generally minimal overlap of peaks allowing rapid 'fingerprinting' of the chemical composition of a sample by either point or bulk analysis. Depending on the detector used, all elements from the atomic mass of C upwards can be detected (McLaren, 1991).

EDX can also be used to produce false colour element maps of a sample in which specific elements within a spectrum are assigned a colour to clearly display the elemental distribution at the sample surface (Reed, 1996). EDX analysis (both point and false colour mapping) was used extensively in this study to identify and characterise different mineral phases within slag and their persistence during weathering. EDX can also be used to produce semi-quantitative analysis of phase composition providing certain conditions are established (normally including a flat sample surface, constant working distance, a constant accelerating voltage and regular detector calibration against a known standard with homogeneous elemental composition) (Oxford Instruments, 2011). Semi-quantitative EDX spot analysis was used in Chapter 4 to determine the elemental composition of selected V-containing phases, with multiple analyses averaged to determine variability in phase composition. For EDX analysis, the working distance was 10 mm, the accelerating voltage was 15 keV and a Co metal target was used regularly for flux calibration during data collection.

3.3.3.3   *Transmission electron microscopy*

A TEM uses an FEG to direct a focused electron beam at a sample held under vacuum in a similar manner to an SEM. TEM uses a thin sample (< 200 nm) to allow

penetration by the electron beam . The image is formed due to spatial variations in intensity of the transmitted electron beam. These variations are caused by both elastic and inelastic scattering of electrons as they pass through the sample (i.e. diffraction without energy loss and loss of energy with absorption respectively) (McLaren, 1991).

Sample preparation is crucial to the overall quality of the TEM images obtained and need to be thin enough to allow transmission of the beam. TEM imaging was undertaken to determine the occurrence and composition of nano-particulate phases within the precipitates forming during slag leachate neutralisation (Chapter 5).

Approximately 10 mg was suspended in ethanol, placed on a Cu support grid with holey carbon support film and air dried prior to analysis. The specimen was examined using an FEI Tecnai TF20: FEGTEM Field emission gun TEM/STEM fitted with HAADF detector, Oxford Instruments INCA 350 EDX system/80 mm X-Max SDD detector and Gatan Orius SC600A CCD camera running Aztec software.

3.3.4   X-ray absorption spectroscopy (XAS)

XAS provides a relatively straightforward and non-destructive method of collecting data concerning the atomic structure of individual atomic species in a sample. X-rays are used to excite core electrons, whereupon a series of photoelectron transitions takes place. The binding energies of core electrons in different elements are well defined and do not overlap and so absorption spectra can be obtained for individual elements by applying x-rays with a photon energy equal to or greater than the core binding energy of the element of interest . At this point there is a rapid rise in absorption known as the absorption edge (Bianconi, 1980; Newville, 2004; Penner-Hahn, 2003). The absorption edge is named according to the core electron transition taking place and relates to the principal quantum numbers n=1, 2 and 3. Excitation of a 1s electron is known as the K-

edge, 2s or 2p is known as the L-edge and 3s, 3p, or 3d transitions constitutes the M-edge (Fig. 3.1)(Penner-Hahn, 2003). The two mechanisms by which the atom decays to its ground state are by x-ray fluorescence (see section 3.3.1) or by emission of an auger electron, in which the energy lost by the falling electron is transferred to a second orbital electron which may be emitted to the continuum (or out of the sample) if the energy transferred is greater than its orbital binding energy. Absorption can be determined by observing either process; however, the fluorescence method is most common (Newville, 2004).

If a sample is sufficiently concentrated in an element (>10 wt%), x-ray absorption can be measured more directly by measuring the attenuation of the transmitted beam as it passes through the sample. The absorption coefficient (μ) is determined by Beer's Law:

$$I = I_0 e^{-\mu t}$$

where I_0 and I are the incident and transmitted beams respectively and t is the thickness of the sample. μ varies logarithmically with energy, thus the energy dependence of the absorption coefficient, $\mu(E)$, can be determined by:

$$\mu(E) = \log(I_0/I)$$

In more dilute samples (typically < 2 wt%) the X-ray fluorescence yield induced during absorption is used as a proxy for beam attenuation. If fluorescence measurements are being taken, the above formula becomes:

$$\mu(E) \propto I_f/I_0$$

where I_f is the intensity of the fluorescence or electron emission (Newville, 2004).

The x-ray absorption spectrum comprises two discrete regions (Fig. 3.2). X-ray absorption near edge spectroscopy (XANES) consists of the area within ~50 eV of the main absorption edge and is used to determine the elemental speciation and coordination chemistry of the absorbing atom. Extended x-ray absorption fine structure (EXAFS)
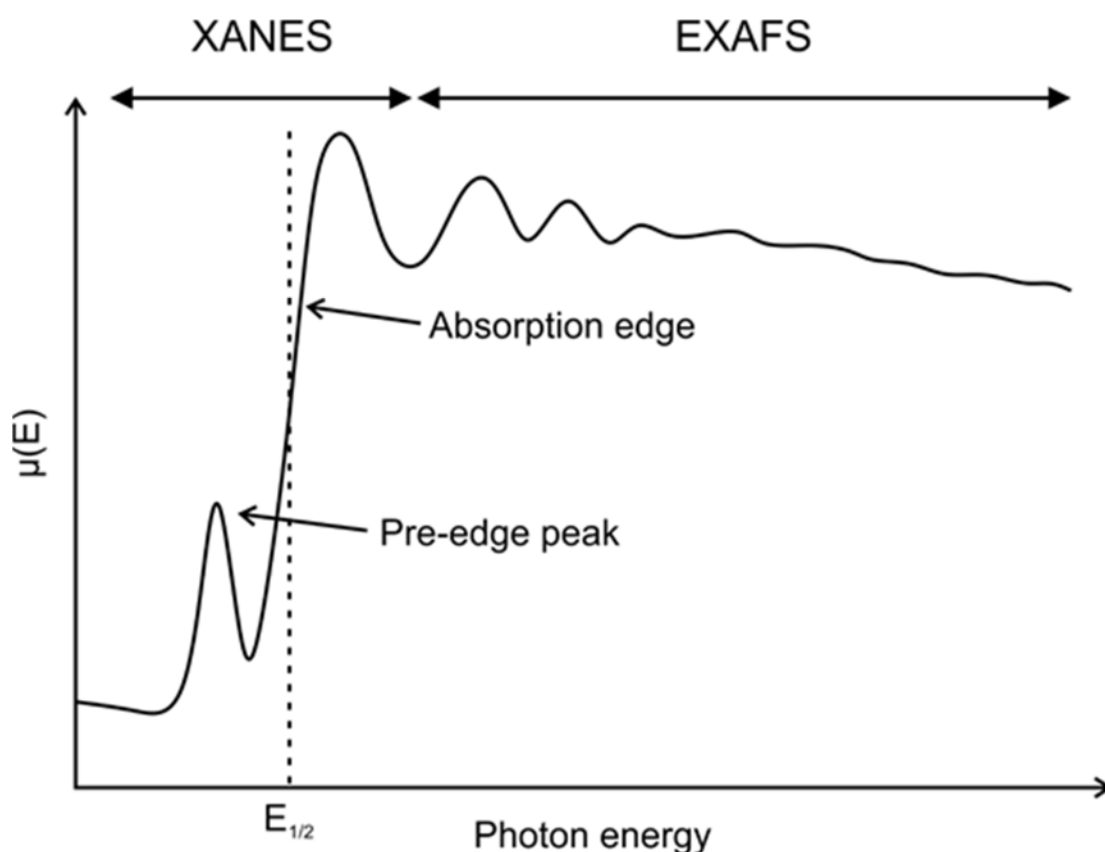
Figure 3.2 - Typical features associated with V K-edge XAS spectra.

accounts for the remainder of the spectrum at higher energy levels. Fourier transformation of the EXAFS region can provide the coordination number of the element under analysis as well as interatomic distances and species of neighbouring atoms (Newville, 2004). It has been suggested that the boundary between the two regions lies at the point at which the wavelength of the excited electron is equal to the interatomic distance between the absorbing atom and its nearest neighbour (Bianconi, 1980).

Since XAS is an element-specific technique, it can be used to gather information about elements which are present even at very low concentrations or in the presence of a large background signal and so is an ideal method for establishing the atomic structure of trace elements in steel slag (Chaurand et al., 2006; Newville, 2004). In this study, XAS was used to determine V and Cr speciation and the coordination environment of V within

both weathered and unweathered steel slags as well as speciation of V incorporated into $CaCO_3$ and sorbed to mineral surfaces during neutralisation of steel slag leachate.

3.3.4.1   *Synchrotrons*

The element specific nature of XAS analysis requires a source of intense, tunable, soft x-rays (i.e. those with a low photon energy, typically $<5 – 10$ keV) and so it is generally performed at synchrotron radiation sources (Alp, 1990). These are purpose built structures designed to produce synchrotron light. They use of a series of particle accelerators to accelerate electrons to relativistic speeds giving them an energy in the GeV range. The electron beam is held under high vacuum (to reduce destruction of electrons through collisions with gas molecules) in a storage ring which consists of straight sections interspersed with bends. When the electron beam is bent by a magnetic field, synchrotron light is produced. This light spans the electromagnetic spectrum and is particularly notable for its brilliance (defined as the photon flux per unit area of the radiation source per unit solid angle of the radiation cone per unit spectral bandwidth) when compared to alternative sources (Diamond Light Source, 2017; Thompson et al., 2001).

The brilliance of synchrotron light is an important factor in XAS analysis. Spectral resolution is inversely proportional to monochromator slit size therefore the higher the brilliance of the source, the higher the photon flux through the monochromator, ultimately improving the spectral resolution achievable at the sample (Thompson et al., 2001). Third generation synchrotrons (such as Diamond Light Source) are primarily concerned with optimisation of the brilliance of synchrotron light. Straight sections of the storage ring between the bending magnets contain insertion devices known as wigglers and undulators which are designed to intensify the beam and are used as light sources in their own right. Undulators produce a particularly brilliant light in a very narrow beam, the energy of which can be varied across a continuous range by adjusting the separation of the

magnets inside the device, thus making them ideal light sources for μXAS, in which a beam focused to a 2 μm x 2 μm spot is used to collect μXANES, μXRF and EXAFS data at high resolution (Diamond Light Source, 2017).

Synchrotron light is produced at a tangent to the curved path of the electrons from where it is channelled into beamlines. The 'white light' is subsequently modified using a monochromator to select the required wavelength for analysis. For XAS, the shifts in absorption edge position due to valence changes in transition metals are frequently of the order of a few eV and therefore steps in photon energy must be resolvable to at least this size. Si 111 crystal monochromators provide sufficient x-ray energy resolution (~0.3 eV) between 2.5 and 20 keV enabling analysis of all elements from the S K-edge to the U L_3-edge (Alp, 1990).

V K-edge spectra (5465 eV) and Cr K-edge spectra (5989 eV) were collected on beamline I18 at the Diamond Light Source operating at 3 GeV with a typical current of 250 mA, using a nitrogen cooled Si(111) double crystal monochromator and focusing optics. A pair of plane mirrors was used to reduce the harmonic content of the beam and Kirkpatrick-Baez mirrors were used to produce a focused beam (approximately 2 μm diameter at the sample). For standards prepared as pressed pellets, K-edge spectra were collected in transmission mode at room temperature (~295 °K). For samples and solutions, data were collected in fluorescence mode using a 9 element solid state Ge detector at room temperature.

Multiple scans (n = 5 – 9) were averaged to improve the signal to noise ratio using Athena version v0.9.24 (Ravel and Newville, 2005). For μXANES spectra absorption was also normalised in Athena over the full data range and plotted from approximately -20 eV to +40 eV relative to the edge position with no correction required for drift in E_0. V and Cr data was calibrated using E_0 measured from thin metal foils. The V pre-edge peak energy was determined by calculation of the area normalised centroid energy position

following the method of Chaurand et al. (2007) and $E_{1/2}$ energy (energy of the main absorption edge where the normalised amplitude = 0.5) was measured from plotted spectra in Athena.

3.3.4.2 *μXRF elemental mapping*

μXRF elemental maps were collected for selected regions within the slag blocks (~150 x 100 pixels; 2 μm^2 per pixel) for Ca, Ti, V, Cr, Mn and Fe. Each individual pixel in the maps could be interrogated by the acquisition software to produce a XRF spectra that could be compared to SEM-EDX spectra collected previously from slag phases. A combination of the μXRF maps, XRF spectra and position within the sample was used to identify specific points of interest within the sample for μXANES analysis as shown in Chapter 4, Figure 4.2.

3.3.4.3 *XANES*

The XANES region of the XAS spectrum consists of any pre-edge features, the main absorption edge and the initial oscillations beyond the absorption edge.

The absorption edge position is defined as either the maximum of the derivative spectrum, which corresponds to the first inflection point of the main absorption edge, or as the energy halfway up the normalised absorption edge step ($E_{1/2}$; used in this study)(Penner-Hahn, 2003). Any peaks in the spectra which appear before this value are known as 'pre-edge' peaks. Pre-edge peaks provide information on local geometry and speciation and are caused by electron transitions to empty bound states (Newville, 2004; Penner-Hahn, 2003). Since electron transitions must be dipole allowed, 1s electrons which are excited at the K-edge must end up in p-orbitals (Newville, 2004). The p-orbitals of transition metal oxides are often filled, preventing these transitions from taking place. However, under certain conditions, full p-orbitals may be hybridised with unfilled d-

orbitals, allowing electron transitions to this level which would otherwise not be possible (Newville, 2004; Penner-Hahn, 2003). The extent to which this hybridisation occurs is a function of coordination environment with tetrahedral coordination producing a much more pronounced effect and consequently a more intense pre-edge peak whereas in octahedral coordination the effect is much reduced (Newville, 2004). This is clearly seen in Cr XANES where tetrahedral Cr^{6+} spectra display a prominent pre-edge peak whereas octahedral Cr^{3+} do not, making analysis of Cr speciation relatively straightforward (Peterson et al., 1996). Pre-edge peaks in V XANES spectra are dependent on 1s transitions to hybridised 3d/4p orbitals which readily occur in tetrahedral coordination resulting in a prominent pre-edge peak (Chaurand et al., 2007). These transitions are reduced in square pyramidal coordination and again in octahedral coordination leading to correspondingly smaller pre-edge peaks (Wong et al., 1984). However, XANES analysis has shown that in sorption environments or where polyvanadate species are present, V tetrahedra become distorted, reducing the effect of hybridisation and thus the intensity of the pre-edge peak (Bronkema and Bell, 2007; Tanaka et al., 1988).

The absorption edge itself is formed due to electron transitions to continuum states. Its position may be used to infer the oxidation state of the absorbing atom as it increases with oxidation state due to the increased core binding energies of higher valence atoms (Penner-Hahn, 2003).

A robust method for determining V speciation and coordination symmetry from XANES spectra has been developed by Chaurand et al. (2007). They found that the position of the absorption edge alone is not sufficient to determine the oxidation state of V as it can overlap more than one valence state (e.g. V^{3+} and V^{4+} are not well resolved using this method). Similarly, pre-edge peak intensity cannot be relied upon due to a considerable overlap between V^{4+} in square pyramidal coordination and V^{5+} in octahedral

or square pyramidal coordination. Detailed examination of both can resolve both coordination symmetry and oxidation state of V^{3+}, V^{4+} and V^{5+}.

3.3.4.4   EXAFS

The EXAFS region of the XAS spectrum consists of a series of sinusoidal oscillations which gradually decrease in amplitude. These are caused by constructive and destructive interference due to backscattering of the outgoing photoelectron by neighbouring atoms. These provide information on the local environment of the absorbing atom, up to a range of ~5Å (Bianconi, 1980; Penner-Hahn, 2003).

Since the features associated with the EXAFS region are smaller, a more concentrated sample is needed in order to obtain a suitable signal to noise ratio for analysis (Specific LODs are highly element and substrate dependant but generally will be in the 100 – 2000 ppm range; Proux et al. (2017)). Collection of V K-edge EXAFS from environmental samples may be further complicated by a poor signal to noise ratio compounded by interference from La and Nd L-edges (Thompson et al., 2001).

EXAFS oscillations are extracted from the XAS spectrum by performing a background subtraction. Due to the dependence of EXAFS on the wave nature of the photoelectrons, x-ray energy (E) is converted to photoelectron wavenumber (k) using the following formula:

$$k = \sqrt{\frac{8\pi^2 m_e}{h}(E - E_0)}$$

where m_e is the mass of an electron, h is the Planck constant, E is the energy of the incoming photon and E_0 is the energy of the absorption edge. The EXAFS part of the $\mu(k)$ spectrum is then isolated by removing the 'bare atom' background (i.e. the spectra that would result from an isolated atom of the absorber; $\mu_0(k)$) and normalising:

$$X(k) = \frac{\mu(k) - \mu_0(k)}{\mu_0(k)}$$

Since the EXAFS decay quickly with increasing k, the spectrum is k-weighted, typically by k^2 or k^3 to improve the signal at high k. Finally, a Fourier transform is applied to the spectrum. The resulting peaks in the Fourier transformed EXAFS data are representative of the scattering paths of the photoelectron (i.e. peaks relate to the number and distance of backscattering atoms surrounding the central atom; Newville, (2004); Penner-Hahn, (2003)).

For the work presented in Chapter 5, multiple (6 – 10) V K-edge EXAFS spectra (k = 0 - 12Å^{-1}) were collected on beamline I18 of the Diamond Light Source. UK, from selected V-containing samples, Spectra were then averaged, background subtracted and normalised using Athena application (part of the Demeter software package v0.9.24;). The processed spectra was then fit *ab initio* to model spectra in Artemis (also included in Demeter v0.9.24) to determine the atomic coordination surrounding the central V atom (Ravel and Newville, 2005).

3.3.5   *Inductively coupled plasma optical emission spectrometry (ICP-OES)*

ICP-OES is used to determine elemental concentrations in an aqueous matrix which uses intense heat (ca. 7500 K for an Ar plasma) from an electrical plasma (a partially ionised gas, usually Ar) to decompose a sample into free atoms and ions (Boss and Fredeen, 1999; Hall, 1992).

An ICP discharge is created when Ar gas, supported on a quartz torch, is stripped of some of its electrons by the application of a spark. The torch is surrounded by a copper coil (called a load coil) which is connected to a radio frequency generator. This creates oscillating electric and magnetic fields within which the free electrons are accelerated (this

process is known as inductive coupling). A chain reaction is established whereby highly energised free electrons collide with more Ar atoms, ionising them and thus creating a plasma comprising Ar atoms, Ar ions and electrons (Boss and Fredeen, 1999; Vogel and Jeffery, 1989).

Sample is introduced to the plasma as an aerosol via a nebuliser whereupon it is volatilised and dissociated into its component atoms (Vogel and Jeffery, 1989). The energy produced by the plasma is sufficient to cause excitation of the atoms by promotion of electrons from low-energy to high-energy orbitals, or ionisation by emission of the electron from the atom. The subsequent fall of a high-energy shell electron to the lower energy shell to fill the vacancy results in the emission of a photon. The pattern of photon emission is unique to each individual element and so by examining the peaks present, the sample can be 'fingerprinted' to determine its composition, and quantified by comparison of sample emission to matrix-matched standards of known composition (Boss and Fredeen, 1999).

Samples were prepared for ICP analysis by filtration (0.2 μm, PES) to remove particulates. Subsequently samples were acidified in high purity 0.1 M HNO_3 (Aristar) in a 1:10 sample:acid ratio to ensure all species of interest were solubilised.

3.3.6   *Inductively coupled plasma mass spectrometry (ICP-MS)*

ICP-MS uses an Ar plasma source to dissociate and ionise samples in the same manner as the ICP-OES technique. Once ionised, electrostatic lenses focus the central portion of the ion beam into the mass spectrometer where they are separated according to their mass to charge ratio using a quadrupole mass filter. This uses alternating DC and AC voltages to effectively establish an electrostatic filter which will only allow ions with a specific mass to charge ratio to pass through at a given time. Once separated, ions are

detected when they strike a detector which runs a high negative voltage to attract the positively charged ions. This releases electrons which strike a second surface behind the first which amplifies the signal (Wolf, 2005).

Certain elements are known to be susceptible to interference from polyatomic ions with an identical mass to charge ratio to the ions of interest which leads to poor detection limits for those elements. $^{35}Cl^{16}O$ is one such example which interferes with the analysis of ^{51}V. To negate these effects, when analysing V, the ion stream is passed through a helium-filled collision cell before it reaches the quadrupole mass filter. In the collision cell, collisions between polyatomic ions and molecules of the gas convert the interfering molecules to harmless, non-interfering species. The analyte ions are able to leave the cell and enter the mass spectrometer for normal analysis (Thomas, 2002).

Sample preparation and calibration is very similar to that used for the ICP-OES; the principle advantages conferred by ICP-MS when compared with ICP-OES systems are its superior detection limits for the same samples and simpler spectra to interpret (Hall, 1992). ICP-MS was used to determine concentrations of trace elements in site waters and experimentally derived leachates.

3.4 References

ALP, E.E., MINI, S.M., & RAMANATHAN, M., 1990. X-ray absorption spectroscopy: EXAFS and XANES - A versatile tool to study the atomic and electronic structure of materials https://inis.iaea.org/search/search.aspx?orig_q=RN:22075463.

BIANCONI, A., 1980. Surface X-ray absorption spectroscopy: Surface EXAFS and surface XANES. Applications of Surface Science 6, 392-418.

BOSS, C.B., FREDEEN, K.J., 1999. Concepts, instrumentation and techniques in inductively coupled plasma optical emission spectrometry. Perkin Elmer Norwalk.

BRAGG, W.H., BRAGG, W.L., 1913. The Reflection of X-rays by Crystals. Proceedings of the Royal Society of London. Series A 88, 428-438.

BRONKEMA, J.L., BELL, A.T., 2007. Mechanistic Studies of Methanol Oxidation to Formaldehyde on Isolated Vanadate Sites Supported on MCM-48. The Journal of Physical Chemistry C 111, 420-430.

BROUWER, P., 2006. Theory of XRF. Almelo, Netherlands: PANalytical BV.

CHAURAND, P., ROSE, J., BRIOIS, V., SALOME, M., PROUX, O., NASSIF, V., OLIVI, L., SUSINI, J., HAZEMANN, J.L., BOTTERO, J.Y., 2007. New methodological approach for the vanadium K-edge X-ray absorption near-edge structure interpretation: Application to the speciation of vanadium in oxide phases from steel slag. J. Phys. Chem. B 111, 5101-5110.

CHAURAND, P., ROSE, J., DOMAS, J., BOTTERO, J.Y., 2006. Speciation of Cr and V within BOF steel slag reused in road constructions. Journal of Geochemical Exploration 88, 10-14.

CLARKE, A.R., EBERHARDT, C.N., 2002. Microscopy Techniques for Materials Science. CRC Press.

DIAMOND LIGHT SOURCE, 2017. How Diamond Works, http://www.diamond.ac.uk/Home/About/How-Diamond-Works.html.

DINNEBIER, R.E., BILLINGE, S.J.L., 2008. Powder Diffraction: Theory and Practice. Royal Society of Chemistry.

DUTROW, B.L., CLARK, C.M., 2017. X-ray powder diffraction (XRD), http://serc.carleton.edu/research_education/geochemsheets/techniques/XRD.html.

HALL, G.E.M., 1992. Inductively coupled plasma mass spectrometry in geoanalysis. Journal of Geochemical Exploration 44, 201-249.

JENKINS, R., 1988. X-Ray Fluorescence Spectrometry. Wiley.

LLOYD, G.E., 1987. Atomic number and crystallographic contrast images with the SEM: a review of backscattered electron techniques. Mineralogical Magazine 51, 3-19.

MCLAREN, A.C., 1991. Transmission Electron Microscopy of Minerals and Rocks, 2 ed. Cambridge University Press, Cambridge.

NEWVILLE, M., 2004. Fundamentals of X-ray absorption fine structure. Consortium for Advanced Radiation Sources, University of Chicago (USA).

OXFORD INSTRUMENTS, 2011. Quantitative EDS analysis using AZtec software platform, good practices, https://depts.washington.edu/moleng/wordpress/wp-content/uploads/2015/02/Oxford-Quantitative-EDS-Guide.pdf.

PENNER-HAHN, J.E., 2003. 2.13 - X-ray Absorption Spectroscopy A2 - McCleverty, Jon A, in: Meyer, T.J. (Ed.), Comprehensive Coordination Chemistry II. Pergamon, Oxford, pp. 159-186.

PETERSON, M.L., BROWN, G.E., PARKS, G.A., 1996. Direct XAFS evidence for heterogeneous redox reaction at the aqueous chromium/magnetite interface. Colloids and Surfaces A: Physicochemical and Engineering Aspects 107, 77-88.

JOINT COMMITTEE ON POWDER DIFFRACTION STANDARDS, 1974. Powder Diffraction File.

PROUX, O., LAHERA, E., DEL NET, W., KIEFFER, I., ROVEZZI, M., TESTEMALE, D., IRAR, M., THOMAS, S., AGUILAR-TAPIA, A., BAZARKINA, E.F., 2017. High-Energy Resolution Fluorescence Detected X-Ray Absorption Spectroscopy: A Powerful New Structural Tool in Environmental Biogeochemistry Sciences. Journal of Environmental Quality.

RAVEL, B., NEWVILLE, M., 2005. ATHENA, ARTEMIS, HEPHAESTUS: data analysis for X-ray absorption spectroscopy using IFEFFIT. Journal of synchrotron radiation 12, 537-541.

REED, S.J.B., 1996. Electron Microprobe Analysis and Scanning Electron Microscopy in Geology. Cambridge University Press.

SCHWERTMANN, U., CORNELL, R.M., 2007. Goethite, Iron Oxides in the Laboratory. Wiley-VCH Verlag GmbH, pp. 67-92.

SEILER, H., 1983. Secondary electron emission in the scanning electron microscope. Journal of Applied Physics 54, R1-R18.

STANJEK, H., HÄUSLER, W., 2004. Basics of X-ray Diffraction. Hyperfine Interactions 154, 107-119.

TANAKA, T., YAMASHITA, H., TSUCHITANI, R., FUNABIKI, T., YOSHIDA, S., 1988. X-ray absorption (EXAFS/XANES) study of supported vanadium oxide catalysts. Structure of surface vanadium oxide species on silica and [gamma]-alumina at a low level of vanadium loading. Journal of the Chemical Society, Faraday Transactions 1: Physical Chemistry in Condensed Phases 84, 2987-2999.

THERMO ARL, 1999. Basics of x-ray diffraction, introduction to powder/polycrystalline diffraction, https://old.vscht.cz/clab/RTG/dokumenty/thermo/xrd/Introduction%20to%20powder%20diffraction.pdf.

THOMAS, R., 2002. A beginner's guide to ICP-MS-Part IX-Mass analyzers: Collision/reaction cell technology. Spectroscopy 17, 42-+.

THOMPSON, A.C., VAUGHAN, D., Optics, C.f.X.-r., optics, C.f.X.-r., source, a.l., Source, L.B.N.L.A.L., 2001. X-ray Data Booklet. Lawrence Berkeley Laboratory.

VERNON-PARRY, K.D., 2000. Scanning electron microscopy: an introduction. III-Vs Review 13, 40-44.

VOGEL, A.I., JEFFERY, G.H., 1989. Vogel's Textbook of Quantitative Chemical Analysis. Longman Scientific & Technical.

WOLF, R.E., 2005. What is ICP-MS...and more importantly, what can it do? USGS, https://crustal.usgs.gov/laboratories/icpms/What_is_ICPMS.pdf.

WONG, J., LYTLE, F.W., MESSMER, R.P., MAYLOTTE, D.H., 1984. K-EDGE ABSORPTION-SPECTRA OF SELECTED VANADIUM COMPOUNDS. Physical Review B 30, 5596-5610.

Chapter 4   Mechanism of Vanadium Leaching During Surface Weathering of Basic Oxygen Furnace Steel Slag Blocks: A μXANES and SEM Study

Summary

Basic oxygen furnace (BOF) steelmaking slag is enriched in potentially toxic metals including Cr and V which may become mobilised in high pH leachate during weathering. BOF slag was weathered under aerated and air-excluded conditions for 6 months prior to SEM/EDS and μXANES analysis to determine V host phases and speciation in both primary and secondary phases. Leached blocks show development of an altered region in which free lime and dicalcium silicate phases were absent and Ca-Si-H was precipitated ($CaCO_3$ was also present under aerated conditions). μXANES analyses show that V was released to solution as V^{5+} during dicalcium silicate dissolution and some V was incorporated into neo-formed Ca-Si-H. Higher V concentrations were observed in leachate under aerated conditions than in the air-excluded leaching experiment. Aqueous V concentrations were controlled by $Ca_3(VO_4)_2$ solubility as demonstrated by an inverse relationship between Ca and V concentrations. Under air-excluded conditions Ca concentrations were controlled by dicalcium silicate dissolution and Ca-Si-H precipitation, leading to relatively high Ca and correspondingly low V concentrations. Formation of $CaCO_3$ under aerated conditions provided a sink for aqueous Ca, allowing higher V concentrations limited by kinetic dissolution rates of dicalcium silicate. Thus V release may be slowed by the precipitation of secondary phases in the altered region, improving the prospects for slag reuse.

4.1   Introduction

Basic oxygen furnace (BOF) steelmaking is a primary method of steelmaking which accounts for ~2/3 of worldwide steel production (Smil, 2006; UK Steel, 2016). In a basic oxygen converter low carbon steel is produced by blowing oxygen through molten pig iron and recycled scrap steel to remove carbon. BOF slag is the primary by-product of BOF steelmaking and is produced when limestone (or dolomite) is added to the molten iron as a fluxing agent to draw out impurities (Yildirim and Prezzi, 2011). Due to the large quantities of steel slag produced worldwide (170 – 250 million metric ton/year; Ober (2016)) reuse has become increasingly important in order to comply with environmental regulations limiting disposal of wastes. Currently steel slag that cannot be recycled in blast furnaces is primarily reused as aggregate in road surfacing and construction due to its high stability and skid resistance (Ahmedzade and Sengoz, 2009; Australasian Slag Association, 2002), whilst other uses include neutralisation of acidity in soils or mine wastes and possibly for CO_2 sequestration (Bobicki et al., 2012; Doucet, 2010; Huijgen and Comans, 2005; Huijgen and Comans, 2006). Depending on its precise mineralogy, some steel slag may be unsuitable for reuse, particularly in engineering applications. Steel slag may be enriched in phases such as free lime (CaO) and periclase (MgO) which expand on hydration, resulting in significant volume change (Motz and Geiseler, 2001). In situations where slag cannot be reused, or where supply exceeds after-use demand, slag is generally disposed to landfill (Euroslag, 2012).

Steel slag formed during primary steelmaking (i.e. from BOF or electric arc furnace (EAF) processes) typically comprises a mixture of Ca oxides, Fe oxides and silicates. The precise chemical composition varies by iron source and processing, however, the bulk chemical composition is relatively consistent between locations worldwide (Table 4.1).

Table 4.1 - Chemical composition of BOF Steel slags including XRF analysis of the slag used in this study ±1 standard deviation. Data is presented in nominal oxide format.

Major Elements Nominal oxide wt%	Indiana, USA; (Yildirim and Prezzi, 2011)	Sweden; (Tossavainen et al., 2007)	Taiwan, China; (Shen et al., 2009)	Yarborough UK; this study n=21
CaO	39	45	39	40 ±5.4
FeO	30	22	38	32 ±9.4
SiO_2	12	11	7.8	14 ±3.4
MgO	10	9.6	8.6	5.2 ±1.1
MnO	2.7	3.1	4.2	4.5 ±0.8
Al_2O_3	2.2	1.9	1.0	1.2 ±0.4
P_2O_5	1.0	0.52	n.d.	1.3 ±0.4
V_2O_5	n.d	2.6	n.d.	0.81 ±0.24
TiO_2	0.40	1.4	0.94	0.30 ±0.13
Cr_2O_3	0.20	0.07	n.d	0.24 ±0.13
SO_3	0.12	n.d	0.05	0.23 ±0.09
TOTAL	*97.6*	*97.2*	*99.6*	*98.7*

Typically BOF slag is dominated by Ca, Fe and Si, with minor amounts of Mg, Mn and Al (Shen et al., 2009; Tossavainen et al., 2007; Yildirim and Prezzi, 2011). The mineralogical composition can be complex but typically contains a range of calcium-containing silicate phases (e.g. larnite, β-Ca_2SiO_4; merwinite $Ca_3Mg(SiO_4)_2$), calcium and aluminium ferrite phases (e.g. brownmillerite, Ca_2FeAlO_5, srebrodolskite, $Ca_2Fe_2O_5$), free Mg and Ca oxides (e.g. lime, CaO; periclase, MgO) and a refractory oxide solid solution of Fe-Mg-Mn-Ca- oxides (e.g. wüstite, FeO) (Chaurand et al., 2006; Motz and Geiseler, 2001; Navarro et al., 2010; Piatak et al., 2014; Yildirim and Prezzi, 2011).

When stored in contact with water, CaO and Ca-silicates in BOF slag readily react with water to generate a high pH leachate (typically pH 10 – 12.5), e.g. via reactions such as 4-1 and 4-2 (Mayes et al., 2008; Roadcap et al., 2005):

$$CaO + H_2O \rightarrow Ca^{2+} + 2OH^-$$ (Eqn. 4-1)

$$Ca_2SiO_4 + 2H_2O \rightarrow 2Ca^{2+} + H_2SiO_4^{2-} + 2OH^-$$ (Eqn. 4-2)
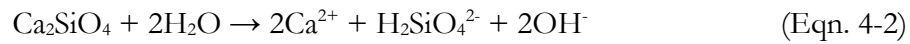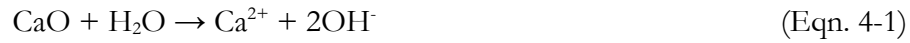
The release of Ca^{2+} and $H_2SiO_4^{2-}$ to solution can lead to oversaturation with respect to calcium silicate hydrates (Ca-Si-H; Eqn. 4-3), and secondary carbonates in the presence of atmospheric CO_2 (Eqn. 4-4; Mayes et al. (2008)). Spinels (e.g. Magnetite; Eqn. 4-5) and hydroxide phases can also form, where di- and trivalent metal ions are released (De Windt et al., 2011).

$$3Ca^{2+} + 2H_2SiO_4^{2-} + 2OH^- \rightarrow 3CaO \cdot 2SiO_2 \cdot 3H_2O$$ (Eqn. 4-3)

$$Ca^{2+} + CO_2 + 2OH^- \rightarrow CaCO_3 + H_2O$$ (Eqn. 4-4)

$$Fe^{2+} + 2Fe^{3+} + 4H_2O \rightarrow Fe_3O_4 + 8H^+$$ (Eqn. 4-5)
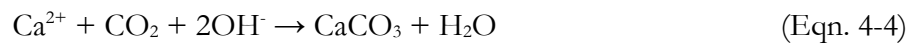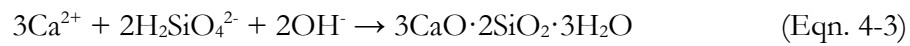
Steel slags usually contain a variety of trace elements from the primary ore that become concentrated by processing. At high pH, several potential toxic metals are solubilised and become mobile in leachate including Al, Fe, and V (De Windt et al., 2011; Mayes et al., 2008; Proctor et al., 2000; Roadcap et al., 2005).

In recent years Cr and V leaching has received significant attention due to their relative enrichment in BOF slag (V, 0.04 – 1.48 wt% and Cr, 0.04 – 0.24 wt%; Proctor et al. (2000); Tossavainen et al. (2007)) and the potential mobility and toxicity of V^{5+} and Cr^{6+} species in alkaline leachates. Cr and V can be present in steel slag in multiple oxidation states (Cr^{3+} and Cr^{6+}; V^{3+}, V^{4+} and V^{5+}; Chaurand et al. (2007a); Proctor et al. (2000)), although the highest oxidation states cause most concern because they are mobile in aqueous systems and are the most toxic (Barceloux, 1999; Fendorf, 1995). However, there

is uncertainty about V and Cr host phases and their oxidation state within those phases, making evaluation of their potential leaching behaviour and toxicity difficult. This uncertainty is compounded by the use of leaching data acquired from powdered specimens, which may be unrepresentative of slag aggregate weathering in civil engineering applications (De Windt et al., 2011; Huijgen and Comans, 2006). As a result, regulatory bodies, such as the UK Environment Agency, are adopting worst case scenario assumptions when considering V leaching from steel slags (Environment Agency, 2014). This will have an adverse effect on beneficial reuse of slag, and could lead to overly stringent long-term monitoring requirements for landfills.

Previous research has shown that under air-excluded leaching conditions Cr is not released from slag in significant quantities because it is incorporated as Cr^{3+} into a secondary chromite-like phase which is very stable (<0.05% of total Cr is released; De Windt et al. (2011); Geiseler (1996)). In contrast, V release is higher (up to 1.7% of total V, De Windt et al. (2011)). This is due to the relatively high reactivity of the V hosting phase, and the prediction that V^{3+} and V^{4+} can be oxidised to V^{5+} during slag weathering (Chaurand et al., 2007a; Chaurand et al., 2006; De Windt et al., 2011). No data are available concerning leaching of steel slags under aerated conditions that will be more favourable to Cr and V oxidation. Equally, the role of secondary phase formation in controlling V release is currently unknown, although the potential for aqueous V to be incorporated into Ca-Si-H has been noted (De Windt et al., 2011).

A thorough understanding of weathering processes in BOF slag is essential to enable long-term, cost effective management and use of steel slag whilst protecting both the environment and human health from its potentially hazardous components. This study used scanning electron microscopy (SEM) and X-ray absorption near-edge spectroscopy (XANES) to determine the distribution and speciation of V within BOF steel slag, and to determine whether leachate equilibrium atmosphere affects V release

during slag leaching. This research provides new insights into the distribution of V within both unweathered and weathered BOF slag, and investigates the mechanisms underpinning enhanced V leaching and its fate in neo-formed phases.

4.2 Methods

4.2.1 Sample collection and characterisation

Combined steelmaking waste was collected from the Yarborough landfill following the methodology detailed in Chapter 3, section 3.1.1. An Olympus X-5000 X-ray fluorescence (XRF) analyser was used to determine the composition of individual waste blocks. 21 no. blocks with a chemical composition consistent with reported elemental profiles of BOF slag found in previous studies (e.g. Table 4.1) were selected. Of these, one sample was selected and was either cut into smaller 8 g blocks (20 x 10 x 10 mm) using a diamond saw for use in leaching experiments, or ground to < 150 μm powder for compositional analysis. Major and minor element composition was determined using an Olympus X-5000 XRF analyser. Mineralogical analysis was performed using 50 – 100 mg samples mounted on silicon slides on a Bruker D8 X-ray diffractometer (XRD) using Cu K-alpha radiation and scanning between 2° and 70° 2θ.

4.2.2 Leaching experiments

Leaching tests were designed to replicate conditions during heap leaching of steel slags in both the unsaturated and saturated zones (see Chapter 1, Fig. 1.1).

Two 8 g slag blocks were placed in a 2 L graduated glass screw-top bottle containing 2 L deionised water (DIW). Air-excluded (O_2 and CO_2-free; saturate)

conditions were established by purging for 45 minutes with N_2 gas before the bottle was capped and stored in a Coy anaerobic cabinet (95% N_2: 5% H_2, Coy Ltd. USA). Two further blocks were leached in DIW in a bottle stoppered with a foam bung and continually aerated with laboratory air using an aquarium pump (flow rate 6 L min^{-1}). In the aerated system, DIW was added periodically to replace water that had evaporated. Leaching continued for 6 months before the blocks were removed from the bottles and dried under N_2: H_2 atmosphere in the Coy Cabinet. Leachate pH was determined following removal of the blocks using an Orion DualStar pH/ISE benchtop meter (Thermo Scientific, USA) with electrodes calibrated at pH 4, 7 and 10. Metal concentrations in aqueous leachate samples (0.2 μm; PTFE filtered) were determined (with an analytical uncertainty of < ±3%) either on a Thermo iCAP 7400 radial ion-coupled plasma optical emission spectrometer (ThermoFisher Scientific, USA, ICP-OES; major elements), or on a Thermo iCAP Qc ion-coupled plasma mass spectrometer (ThermoFisher Scientific, USA, ICP-MS; minor elements).

4.2.3   *Scanning electron microscopy*

The leached blocks and an unleached control block were cut in half widthways under water using a diamond saw and the resultant ~1 cm^3 blocks were set into epoxy resin. The surface to be examined was then polished using a water-free diamond paste removing the top 1 – 2 mm of material potentially exposed to water during cutting. The samples were carbon coated (~10 nm) and backscatter electron images were collected on a FEI Quanta 650 FEGESEM environmental Scanning Electron Microscope (SEM) equipped with an Oxford Instruments INCA 350 Energy-dispersive X-ray spectroscopy system that had an 80 mm X-Max Silicon drift detector. Energy-dispersive X-ray spectroscopy (EDS) mapping and quantitative point analysis were processed using the Oxford Instruments

AZtec acquisition and analysis software. False colour SEM-EDS composite elemental maps were used to identify phases, and phase composition was subsequently determined both near and remote from the leached surface of each slag block by point counting using randomly oriented 20 x 20 µm grids (Plas and Tobi, 1965); (e.g. Fig. 4.1a). EDS was also used to quantify phase composition in selected V-containing BOF slag phases. Multiple EDS spot analyses (analysis volume of 2 µm^3; working distance, 10 mm) were collected and elemental composition was determined using the AZtec software (a Co metal target was used as the calibration standard and regular recalibration was undertaken to prevent drift in total detector counts between analyses).

4.2.4   µX-ray absorption spectroscopy

Polished BOF slag blocks were produced from samples recovered from both the aerated, air-excluded leaching experiments and from identical unweathered samples. Standard materials (V_2O_5; $VOSO_4$) were also prepared as pressed pellets using cellulose as a diluent to reduce chemical thickness (to achieve an edge step between 0.5 and 1.5 in transmission mode, see below). Pellets were held in Kapton™ tape. A sodium vanadate solution was prepared in 0.1 mol.L^{-1} NaOH, also at 1000 mg.L^{-1}, and held in a polythene bag.

µXAS spectra and µ XRF maps were collected at the V and Cr K-edges (5465 and 5989 eV respectively) on beamline I18 at the Diamond Light Source operating at 3 GeV with a typical current of 250 mA, using a nitrogen cooled Si(111) double crystal monochromator and focussing optics. A pair of plane mirrors was used to reduce the harmonic content of the beam and Kirkpatrick-Baez mirrors were used to produce a focused beam (approximately 2 µm diameter at the sample). For standards prepared as pressed pellets, K-edge spectra were collected in transmission mode at room temperature
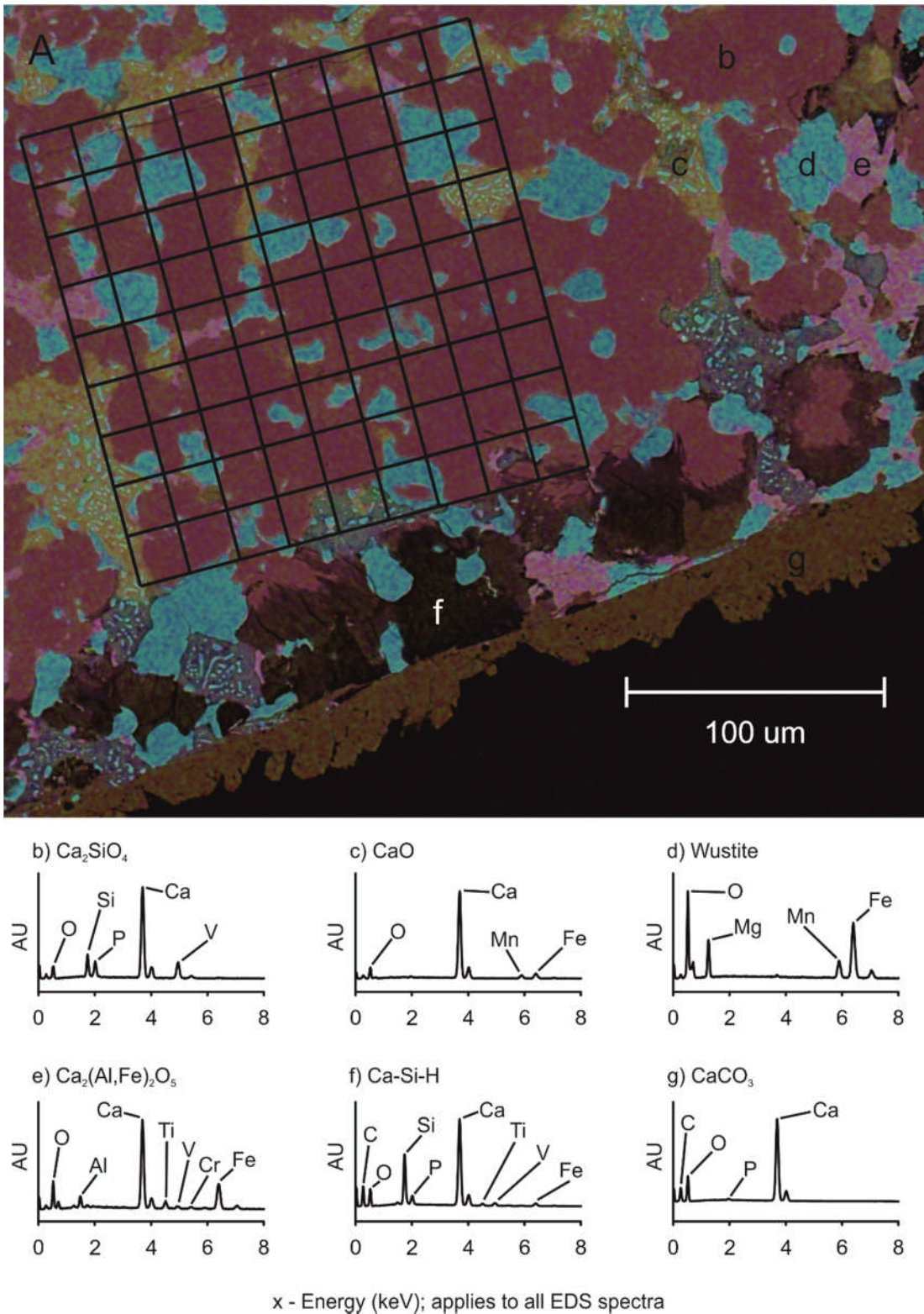
Figure 4.1 - A) Example composite false colour SEM-EDS elemental maps showing phase discrimination within the BOF slag samples and location of typical randomly orientated 20 x 20 μm grid used to determine phase concentrations (v/v) within the bulk slag and weathered regions. Data from several locations and maps were used to allow for averaging of micron-scale heterogeneity in phase composition. b-g) Example EDS spectra collected from each of the 6 major phases detected.
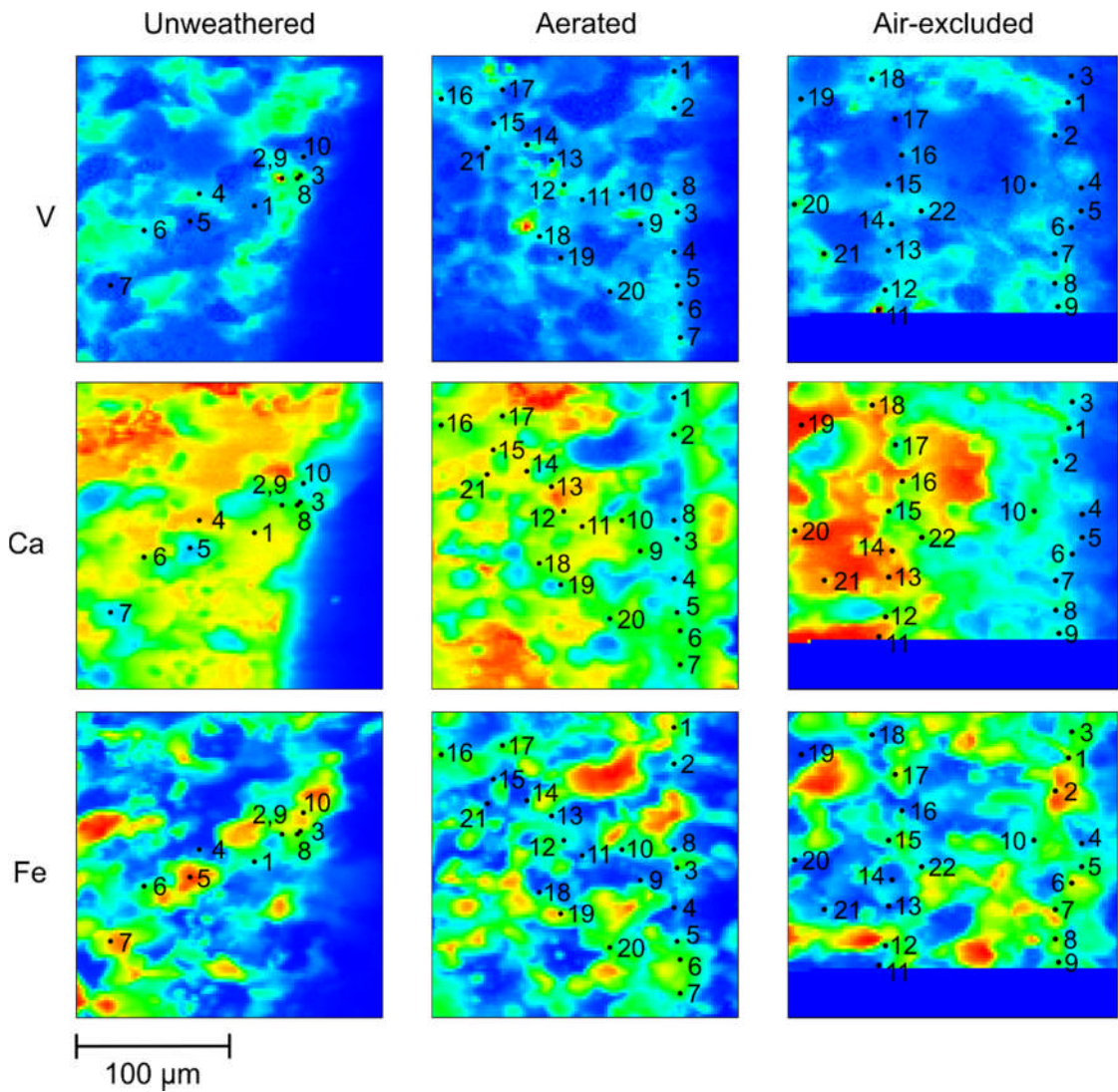
Figure 4.2 - V, Ca and Fe µXRF maps collected from the slag blocks recovered from the aerated, air-excluded leaching experiments and from an unweathered sample; numbered points indicate locations where µXANES spectra were collected.

(~295 °K). For samples and solutions, data were collected in fluorescence mode using a 9 element solid state Ge detector at room temperature.

µXRF elemental maps were collected from continuous regions (i.e. free from cracks or bubbles) on the edges of the slag blocks (~150 x 100 pixels; 2 µm^2 per pixel) for Ca, Ti, V, Cr, Mn and Fe (Fig. 4.2). Each individual pixel in the maps could be interrogated by the acquisition software to produce an XRF spectrum that could be compared to SEM-EDS spectra collected previously from slag phases. A combination of

the μXRF maps, XRF spectra and position within the sample was used to identify specific points of interest within the sample for μXANES analysis as shown in Fig. 4.2. Multiple scans (n = 5-9; k = 0-8 Å^{-1}) were averaged to improve the signal to noise ratio using Athena version v0.9.24 (Ravel and Newville, 2005). The step size was 0.3 eV over the XANES region (-50 – 100 eV) and 3 – 5 eV in the pre- and post-edge regions. For μXANES spectra absorption was normalised in Athena over the full data range and plotted from approximately -20 eV to +40 eV relative to the edge position with no correction required for drift in E_0. V data was calibrated using E_0 measured from thin metal foils.

4.3   Results

4.3.1   *Slag composition*

The elemental composition of the slag was dominated by Ca, Fe and Si, with Mn and Mg as minor constituents; the V and Cr concentrations were 0.45 ±0.13 and 0.16 ±0.08 wt% repectively (Table 4.1; Table 4.2). XRD analysis showed slag contained larnite (dicalcium silicate; β-Ca$_2$SiO$_4$), brownmillerite (dicalcium Aluminoferrite; Ca$_2$(Al, Fe)$_2$O$_5$), free lime (CaO) and wüstite (refractory oxide; FeO) (Fig. 4.3).

4.3.2   *SEM microanalysis*

SEM analysis showed that the centre of slag blocks consists of an interlocking crystalline matrix (Fig. 4.4). EDS mapping showed that each sub-region within the matrix had relatively uniform composition and four different chemically discrete phases were identified. Quantitative EDS spot analyses (e.g. Fig. 4.1b – e; Table 4.3) were used to

further characterise these phases. The first phase had an average molar Ca:Si ratio of 2.2 ±0.1, corresponding to the dicalcium silicate phase identified by XRD; this phase also contained P, V and trace Fe. The composition of the second phase was dominated by Ca, Al and Fe suggesting that it is the dicalcium aluminoferrite phase identified by XRD; this phase also contained Mn, Ti, Mg, Cr and V. EDS spot analysis indicated that the third phase was principally CaO, but this free lime phase was also substituted with Mn and Fe. The fourth phase contained FeO, MnO, MgO and CaO, suggesting it is a refractory oxide solid solution (e.g. a phase indistinguishable from wüstite by XRD). The proportion of each phase in the slag (by volume) as determined by quantitative SEM-EDS spot analysis is shown in Table 4.4.

Table 4.2 - Mean (± 1 standard deviation) chemical composition determined by XRF for set of 21 no. BOF Steel slag samples collected from Yarborough, UK. Data is presented in both nominal oxide and elemental composition formats. Absolute uncertainty (versus certified standards) was < ±30% for Mg, < ±20% for S and, < ±10% for all other elements.

Nominal Oxide Composition*	Oxide Weight %	Elemental Composition	Weight %	Elemental Limit of Detection
CaO	40 ±5.4	Ca	29 ±3.9	<0.05
FeO	32 ±9.4	Fe	25 ±7.3	<0.001
SiO_2	14 ±3.4	Si	6.5 ±1.6	<0.1
MgO	5.2 ±1.1	Mg	3.1 ±0.7	<0.5
MnO	4.5 ±0.8	Mn	3.5 ±0.6	<0.001
Al_2O_3	1.2 ±0.4	Al	0.71 ±0.24	<0.2
P_2O_5	1.3 ±0.4	P	0.57 ±0.17	<0.05
V_2O_5	0.81 ±0.24	V	0.45 ±0.13	<0.001
TiO_2	0.30 ±0.13	Ti	0.18 ±0.08	<0.001
Cr_2O_3	0.24 ±0.13	Cr	0.16 ±0.08	<0.001
SO_3	0.23 ±0.09	S	0.09 ±0.04	<0.02
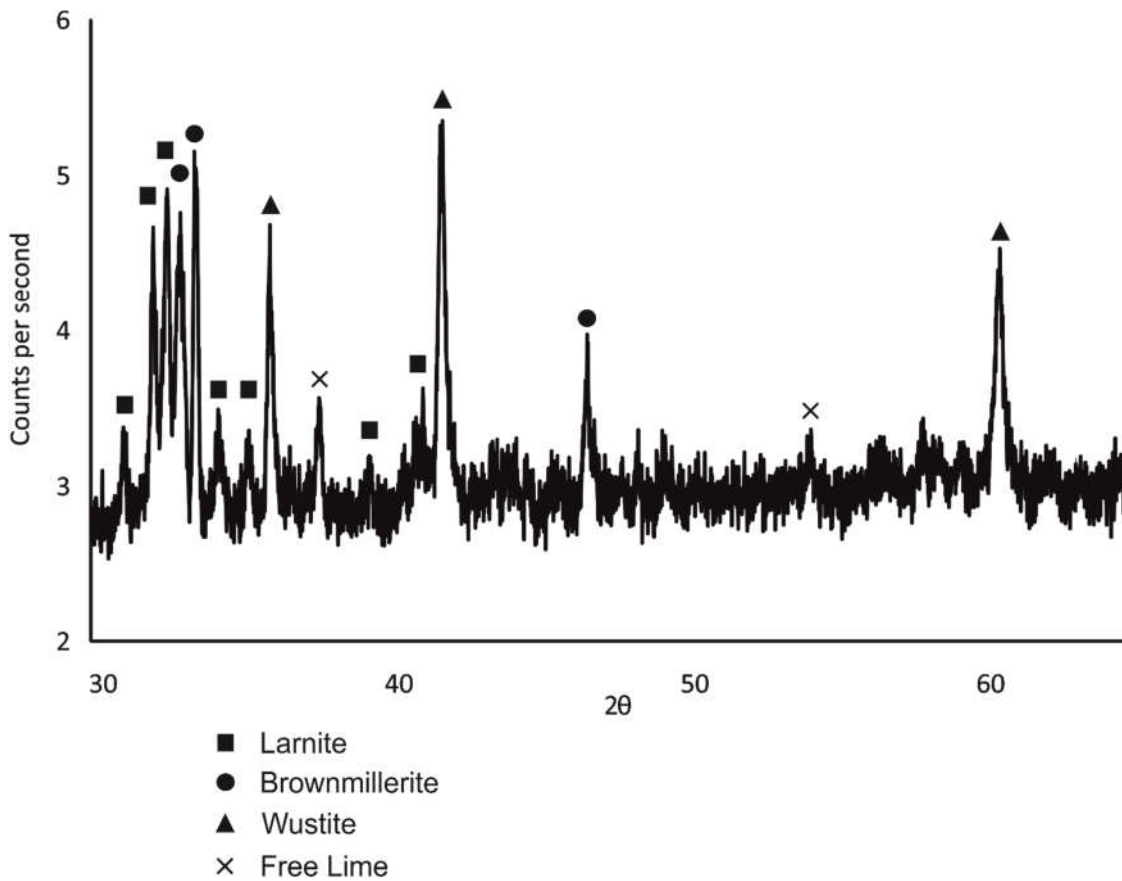
Figure 4.3 - XRD pattern collected from the crushed steel slag sample annotated with major phase peaks detected.

V was present in only the dicalcium silicate (0.44 ±0.23 wt%) and the dicalcium aluminoferrite phase (1.14 ±0.14 wt%) and not detectable in the free lime and wüstite phases. Cr was only associated with dicalcium aluminoferrite (0.42 ±0.14 wt%).

SEM imaging of experimental blocks showed the presence of a compositionally distinct altered region at the block surface that was absent in unweathered samples (Fig. 4.4; Fig. 4.5). EDS analysis showed that this region was depleted in both Ca and Si. High resolution imaging showed that dicalcium silicate is depleted and free lime is absent, but the refractory oxide and dicalcium aluminoferrite phases appear largely unaltered (Table 4.4). A low density Ca and Si containing phase (Ca:Si ratio of 2.1 ±0.4) is observed in this region whose compositions are consistent with calcium silicate hydrate phases (Ca-Si-H; Fig. 4.6) (Allen et al., 2007; Richardson, 1999).
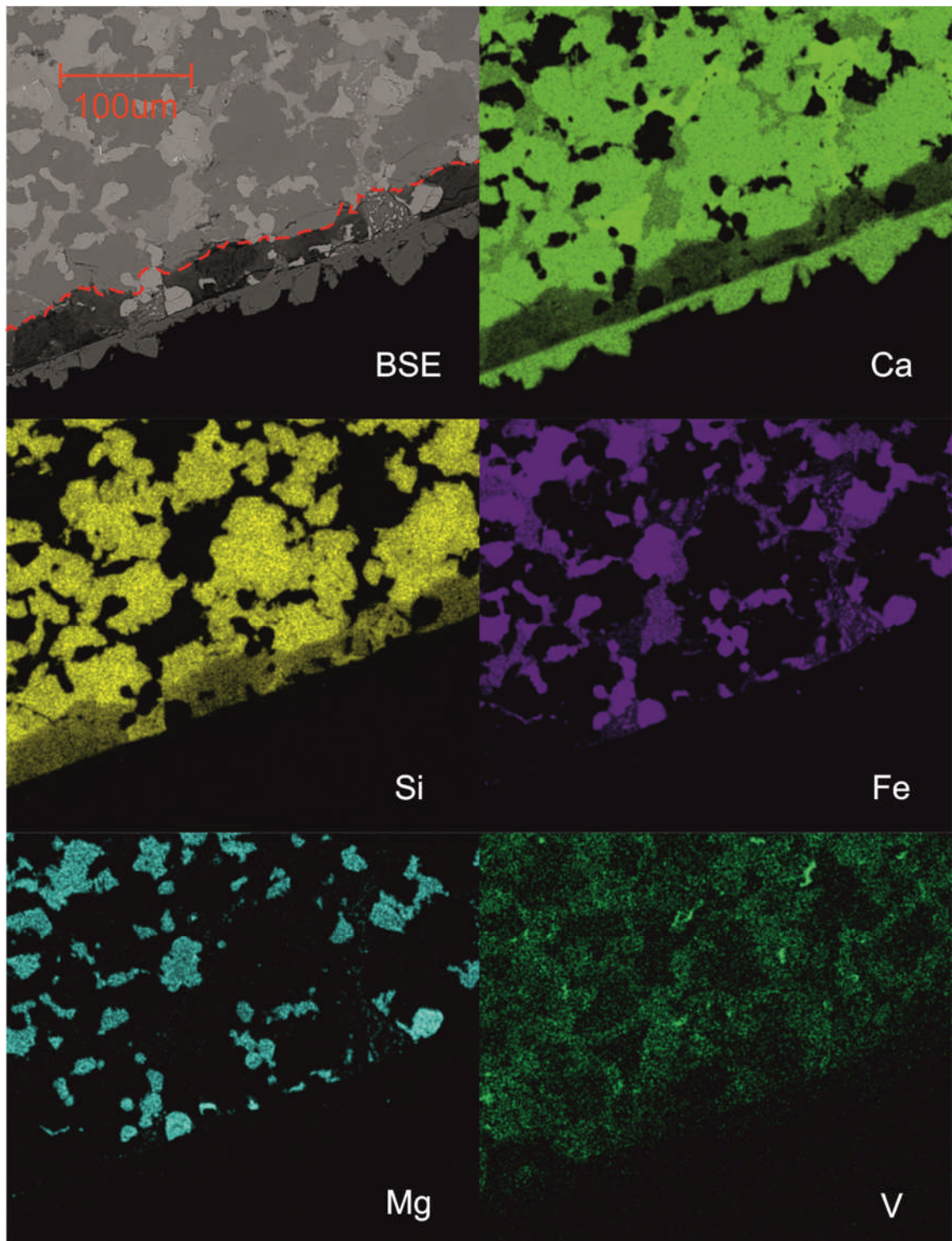
Figure 4.4 – Slag surface structure after 6 months weathering under aerated conditions; backscatter electron image and false colour EDS element maps. The red dashed line indicates the approximate boundary between the altered and unaltered regions.

Table 4.3 - Average of quantitative SEM-EDS spot analysis collected from selected primary and secondary phases within weathered and unweathered BOF slag samples. LoD typically = 0.1 wt% for most elements. C is not determined in the analysis and element totals less than 100% are, therefore, due to the inclusion of C-based resin (which also contains S and Cl) in the sample volume ($\sim$2 μm^3); or in the case of the $CaCO_3$ phase, C within the carbonate moiety itself. Expected elemental proportions of each phase are noted in brackets where appropriate. Elemental proportions of Ca and Si in Ca-Si-H are variable and have not been added.

Element	Ca_2SiO_4 (wt%; n=11)	$Ca_2(AlFe)_2O_5$ (wt%; n=17)	Ca-Si-H (wt%; n=23)	$CaCO_3$ (wt%; n=1)
O	37.9 ±1.6 (37.2)	31.3 ±2.6 (32.9)	21.2 ±9.7	48.7 (48)
Mg	n.d.	0.49 ±0.09	0.08 ±0.05	n.d.
Al	0.16 ±0.06	3.1 ±0.4 (11.1)	0.33 ±0.19	n.d.
Si	13.2 ±0.7 (16.3)	0.50 ±0.14	4.7 ±2.2	n.d.
P	1.5 ±0.1	n.d.	2.5 ±1.0	0.17
S	n.d.	n.d.	0.10 ± 0.10	n.d.
Cl	n.d.	n.d.	0.15 ±0.11	n.d.
Ca	41.5 ±1.5 (46.5)	28.2 ±2.5 (32.9)	13.9 ±5.8	40.4 (40)
Ti	0.21 ±0.09	3.2 ±0.8	0.60 ±0.29	n.d.
V	0.44 ±0.23	1.14 ±0.14	0.70 ±0.57	n.d.
Cr	n.d.	0.42 ±0.14	0.06 ±0.01	n.d.
Mn	n.d.	0.81±0.0.8	0.18 ±0.16	n.d.
Fe	0.81 ±0.09	24.9 ±2.3 (23.0)	1.9 ±0.8	n.d.
TOTAL	*95.7 ±3.4*	*94.1 ±8.0*	*44.2 ±18.7*	*89.3*

n.d. = not detected; n =number of data points

Table 4.4 - Point counting analysis of phase distribution (% by volume) in the unweathered slag and the altered surface regions.

Phases	Unweathered slag	Altered region Aerated conditions[#]	Altered region Air-excluded conditions
Ca_2SiO_4	57 ±3	n. d.	n. d.
Ca-Si-H	n.d.	64 ±3	63 ±3
Wüsite	21 ±3	20 ±3	20 ±3
$Ca_2(Fe,Al)_2O_5$	13 ±3	10 ±3	14 ±3
Lime	8 ±2	n.d.	n. d.
Ca-Si-H / Fe-O	n.d.	6 ±2	4 ±2
Total counts	*1012*	*920*	*848*

n.d., not detected.
[#] Where present, the $CaCO_3$ layer was excluded from this analysis.
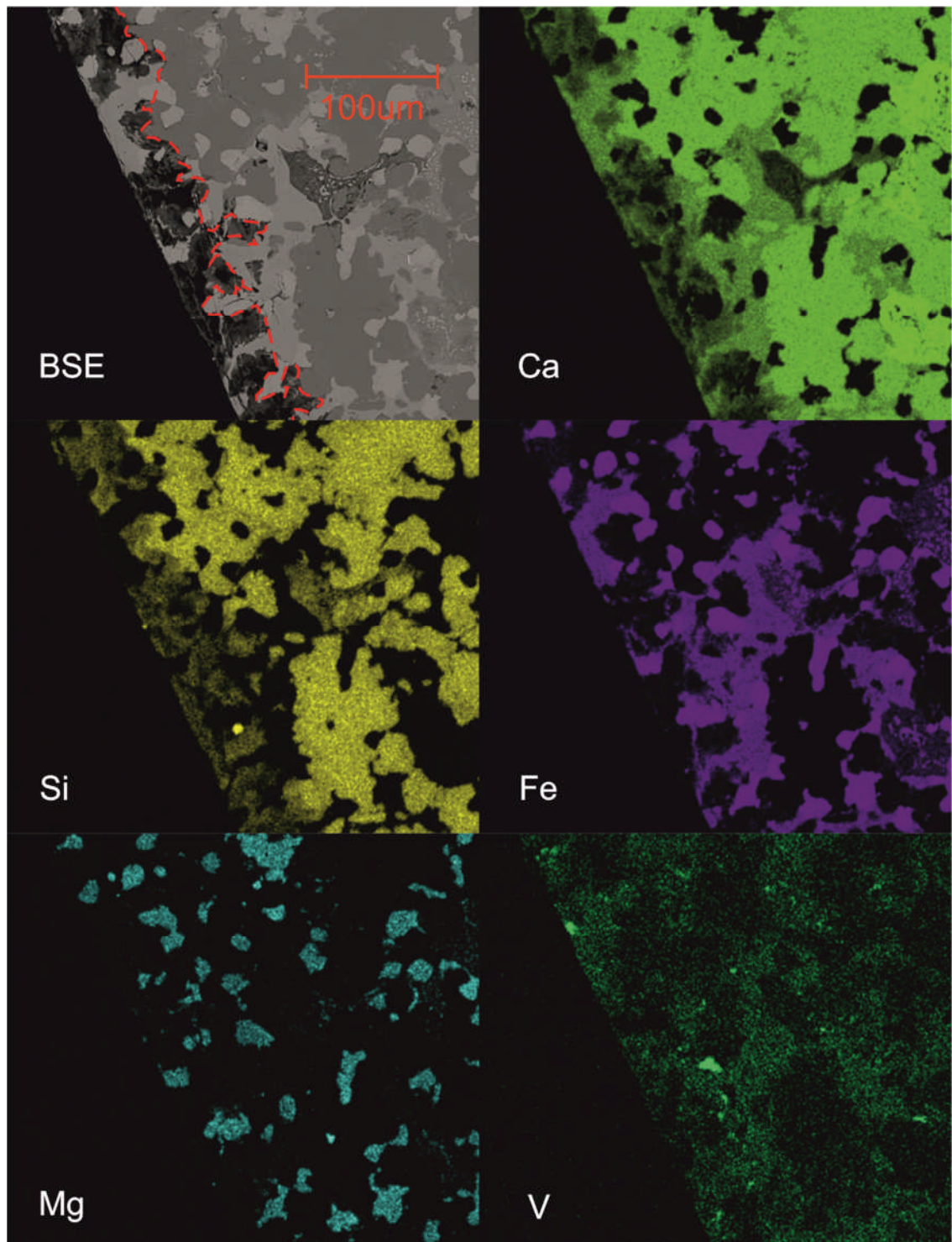
Figure 4.5 – Slag surface structure after 6 months weathering under air-excluded conditions; backscatter electron image and false colour EDS element maps. The red dashed line indicates the approximate boundary between the altered and unaltered regions.

Occasional blade-like morphology is is consistent with Ca-Si-H(II), which has an imperfect Jennite-like structure and a Ca:Si ratio in the range 1.5 – 2.2 (Chen et al., 2004; Gard and Taylor, 1976). This Ca-Si-H phase also contained V (0.70 ±0.57 wt%, Table 4.3), Fe and P (Fig. 4.1f). The thickness of this altered region was 38 ±11 (n = 92) and 45 ±14 μm (n = 76) in the aerated and air-excluded tests respectively, and this difference is statistically significant (Mann Whitney U, p = <0.001). Blocks from the aerated experiment had an additional continuous 10 – 30 μm layer outside the altered region, which consisted of blocky crystals that contained principally Ca, C and O with trace P consistent with precipitation of $CaCO_3$ (Fig. 4.1g, Fig. 4.4).
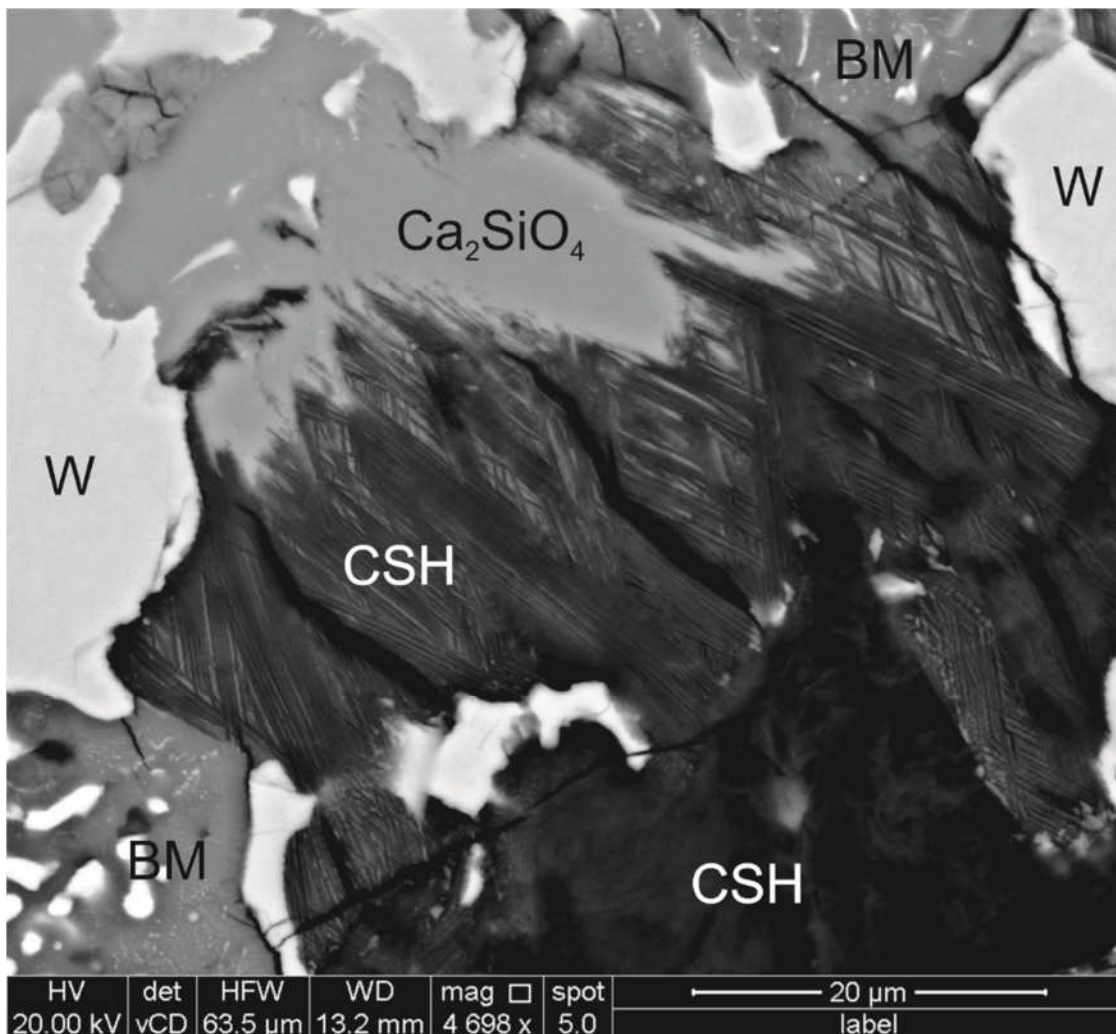
Figure 4.6 - Backscattered electron image showing an example altered region where Ca-Si-H is replacing dicalcium silicate. Visible phases include dicalcium aluminoferrite (brownmillerite; BM), dicalcium silicate (Ca_2SiO_4), refractory oxide (wüstite; W) and Ca-Si-H (CSH).

4.3.3   Leachate composition.

The pH values and the concentration of key elements in the leachate after 6 months are shown in Table 4.5. Both leachates were dominated by Ca and Si. The pH values of the leachate from the aerated and air-excluded systems were 8.0 and 11.9 and V concentrations were 859 µg L^{-1} and 493 µg L^{-1} respectively.

Table 4.5 - Leachate composition determined after 6 months in the aerated and air-excluded slag leaching experiments.

	Aerated	Air-excluded
pH	8.0	11.9
Major ions (mg L^{-1})		
Ca	23.5	85.2
Si	23.4	29.5
Mg	0.1	0.1
K	0.2	0.4
Na	1.7	2.4
Minor ions (µg L^{-1})		
Al	<2	390
Cr	6.5	9.6
Fe	122.7	251.3
Li	<0.1	<0.1
Mn	8.5	13.1
V	859.1	492.8

4.3.4   µXANES analysis

Representative XANES spectra for each V-bearing phase in experimental samples and standards are shown in Fig. 4.7a. Vanadium K-edge µXANES spectra (n = 49) collected from all phases present have a prominent pre-edge peak at 5470 eV (±0.25 eV). Normalised intensity (±0.10) of the pre-edge peak for spectra collected from V-bearing

phases range from; 0.36 to 1.00 in dicalcium silicate, 0.17 to 1.00 in dicalcium aluminoferrite and 0.61 to 0.94 in the Ca-Si-H (Fig. 4.7b). The main absorption edge ($E_{1/2}$; the point at which absorption reaches 50% of normalised absorption) varied from 5479.0 to 5482.3 eV in dicalcium silicate, 5478.9 to 5482.3 eV in dicalcium aluminoferrite and from 5480.1 to 5482.2 eV in Ca-Si-H (Fig. 4.7b).

Chromium µXANES spectra collected from dicalcium aluminoferrite grains in both the unweathered and altered regions were lacking the large pre-edge peak diagnostic of Cr^{6+} (Peterson et al., 1996), and had adsorption edge positions similar to the Cr^{3+}-containing standards (e.g. Fig. 4.8).
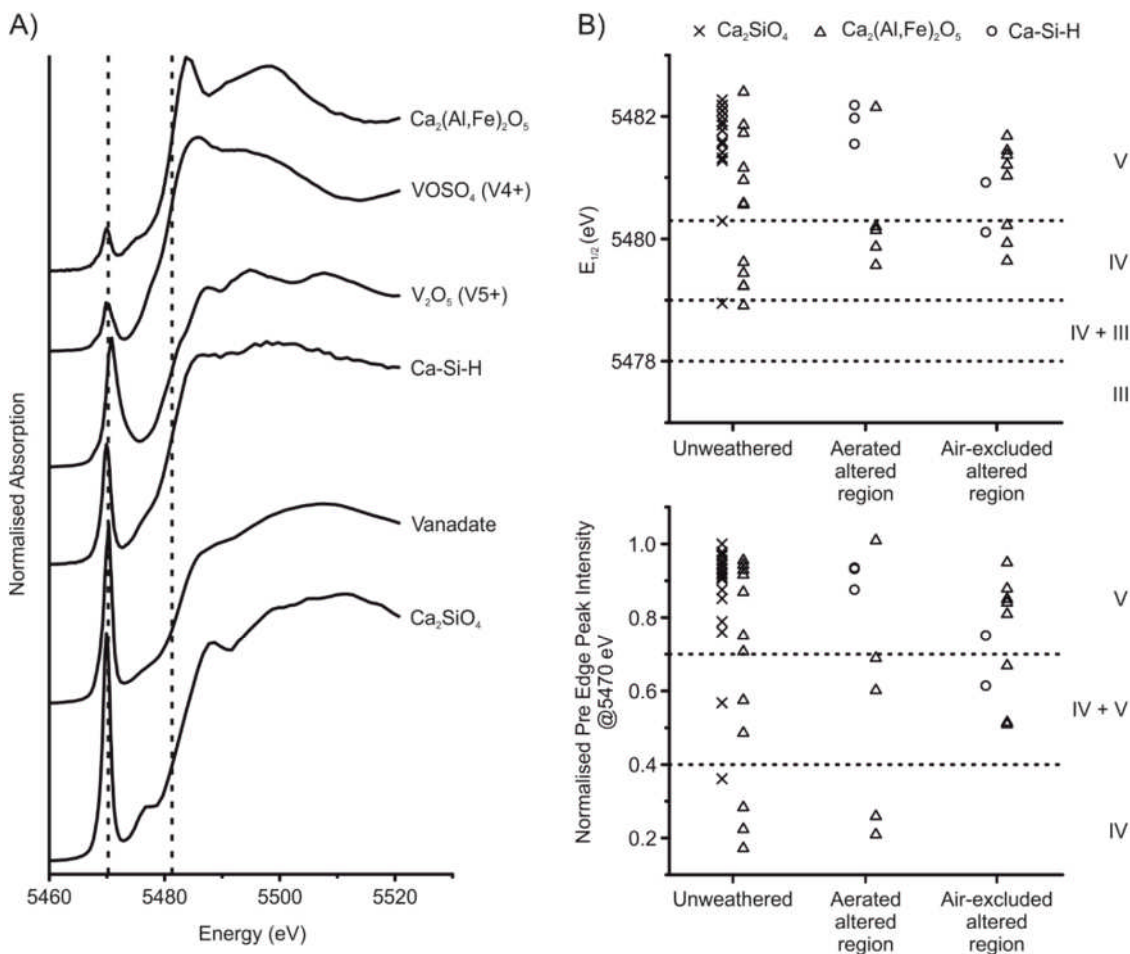
Figure 4.7 - A) Representative V K-edge µXANES spectra collected from V-containing slag phases and standards; and B) $E_{1/2}$ position and normalised pre-edge peak height intensity determined from all data collected from slag blocks.
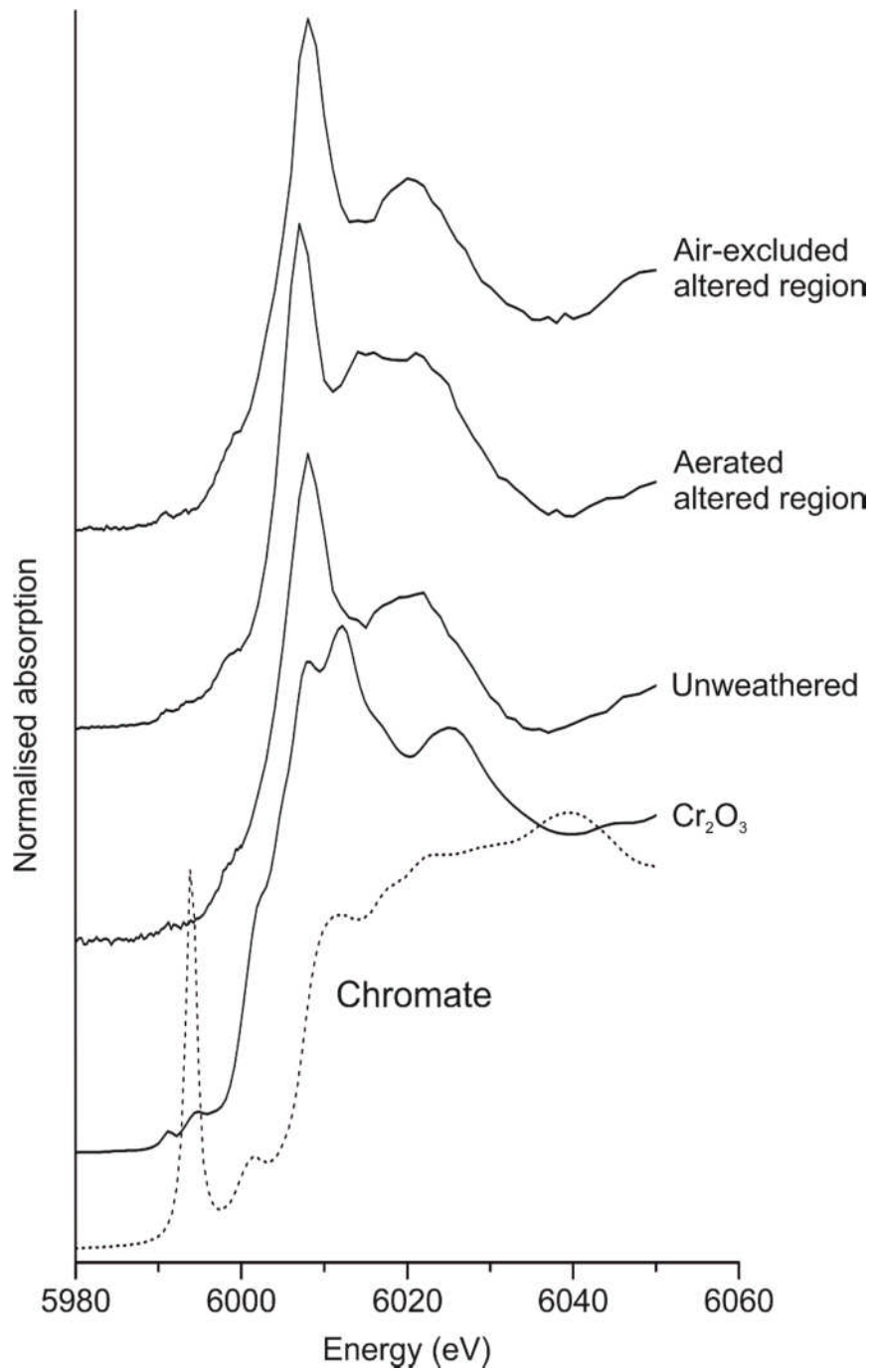
Figure 4.8 - Example Cr K-edge XANES spectra collected from altered and unaltered regions of BOF slag blocks and Cr^{3+} and Cr^{6+} standards.

4.4   Discussion

4.4.1   *Reactivity of phases during weathering*

The development of a compositionally distinct region at the surface of the blocks shows alteration of slag phases has taken place during the 6 month leaching experiments. SEM imaging and EDS analyses show depletion of dicalcium silicate and complete dissolution of free lime phases in this altered region, hence these must be considered the reactive phases during slag weathering (Equations 4-1 and 4-2). The Fe-rich phases (dicalcium aluminoferrite and refractory oxide) showed no evidence of alteration over the time period of the experiments. The thickness of the altered region was significantly greater in air-excluded samples than aerated equivalents, indicating that the presence or absence of air is a significant factor contributing to the rate and overall extent of altered region formation on short time-scales.

4.4.2   *Secondary phase formation Ca-Si-H and CaCO₃*

Dissolution of dicalcium silicate in the slag blocks released Ca and Si to solutions, which results in precipitation of a Ca-Si-H phase (Eqn. 4-3) in place of dicalcium silicate in the altered region under both aerated and air-excluded conditions. Low elemental totals from EDS spot analyses (Table 4.3) of Ca-Si-H phases represent areas with high volumes of carbon-rich resin (as carbon is not determined in EDS analysis). This indicates that Ca-Si-H has a porous structure which will allow diffusion of water and ions through the altered region. Thus it is likely that dicalcium silicate dissolution switched from initially solubility limited to a diffusion limited process as the altered region developed (i.e. the rate of removal of Ca and Si from the slag surface controls rate of weathering). Therefore, formation of Ca-Si-H may have an armouring effect on slag, slowing the rate of dicalcium

silicate weathering. Pseudomorphs of lime were also found in the altered region, containing Ca, Si, Fe, Mn and O (Fig. 4.1). This may represent a distinct Fe(Mn)-substituted Ca-Si-H phase or co-precipitated Ca-Si-H and Fe(Mn) spinel phases. Formation of $CaCO_3$ is only observed in aerated experiments, as it requires the in-gassing of atmospheric CO_2 to allow aqueous Ca to precipitate (Roadcap et al., 2005). Such in-gassing consumes OH^-, which reduces the pH (Eqn. 4-4) and significantly lowers the Ca concentration in the aerated leachate.

The presence of Ca-Si-H phases in the aerated system provides information as to the timing of $CaCO_3$ precipitation. Ca-Si-H becomes reacts with CO_2 to form $CaCO_3$ and is soluble at pH values < 10. The boundary between $CaCO_3$ and Ca-Si-H in the aerated system is distinct and in line with the cut surface of the block (defined by unreacted dicalcium aluminoferrite and refractory oxide phases), indicating that no alteration of the Ca-Si-H has taken place. Therefore $CaCO_3$ precipitation must occur prior to leachate pH falling below 10 and also provides a significant armouring effect to slag blocks under aerated conditions.

4.4.3   *V speciation, behaviour and controls on solubility*

The position of the main absorption edge ($E_{1/2}$) and the normalised pre-edge peak intensity determined from V K-edge XANES spectra can be used to define V oxidation state (Chaurand et al. (2007b); see Chapter 3 for further information). Spectra collected from the BOF slag samples indicate that V is present as either V^{4+} or V^{5+} (Fig 4.7b). Vanadium is present throughout the dicalcium silicate phase as V^{5+} in tetrahedral co-ordination with just one spectrum displaying characteristics of V^{4+}, however, this was taken from a region of high V concentration and may not be representative of the bulk phase. In the dicalcium aluminoferrite phase V is present as both V^{4+} in octahedral co-

ordination and V^{5+} in tetrahedral co-ordination. Both oxidation states can be accommodated in dicalcium aluminoferrite because it contains octahedral Fe^{3+} sites into which V^{4+} can readily substitute (due to similar size and charge) and tetrahedral Al sites into which V^{5+} substitutes (Colville and Geller, 1971). No V^{3+} was detected within the slag.

Spectra from neo-formed Ca-Si-H phase generally show tetrahedral V^{5+} with only one exception of V^{4+}. Ca-Si-H phases, like dicalcium silicate, contain tetrahedral Si sites which can easily accommodate the tetrahedral vanadate ions, but the phases do not contain any octahedral anion sites (Taylor, 1997). The presence of V^{5+} in Ca-Si-H suggests that some of the vanadate released to solution by dicalcium silicate dissolution has been reincorporated into Ca-Si-H.

XANES spectra collected from BOF slag show little, if any depletion of V^{4+} in the altered region. Also, the small quantities of V^{4+} that have been observed in the dicalcium silicate phase are unlikely to be sufficient to significantly contribute to V release. Hence, the results do not support oxidation of V^{4+} to V^{5+} as a mechanism contributing to enhanced vanadium leaching under aerated conditions, a scenario which would require significant dissolution of dicalcium aluminoferrite (the principal host phase for V^{4+}), which is not observed. Thus, over timescales measured in months, it is proposed that essentially all V released to solution must originate from the dicalcium silicate phase as V^{5+}, which is predicted to be soluble as aqueous vanadate species at the measured solution pH (Peacock and Sherman, 2004; Wehrli and Stumm, 1989).

In both aerated and air-excluded systems, dicalcium silicate is initially dissolved during leaching, releasing V to solution. Aqueous V concentrations were much higher in the aerated test, despite evidence that total dicalcium silicate dissolution was probably ~ 20% lower in this test (Table 4.5). The ratio of V:Si in unweathered dicalcium silicate is 0.033 and the ratio of V:Si in leachate from the aerated system is 0.036 which is consistent

with congruent dissolution of the host phase. The V:Si ratio in leachate from the air-excluded test is 0.015 which suggests a lower V release than would be expected from congruent dissolution of dicalcium silicate and that oversaturation with respect to another solid phase has led to retention of V in secondary precipitates. The Ca-Si-H phase has taken up some of the V released but due to the relatively poorly ordered nature of Ca-Si-H phases (Taylor, 1993) this uptake is expected to be unselective, with V incorporation approximately stoichiometric with the V/Si ratio in solution at the time of formation. However, the proportion of Si released by dicalcium silicate dissolution that remains in solution was proportionally much greater than V ($\sim$ 65% vs < 10%). Therefore, aqueous V concentrations are not well explained by uptake to the Ca-Si-H phase alone. Previous modelling of V solubility in BOF leachates has highlighted the role of calcium vanadate phases in controlling V concentration (Cornelis et al., 2008; De Windt et al., 2011; Huijgen and Comans, 2006; Schindler et al., 2000), with $Ca_3(VO_4)_2$ (Log K_{sp} = -17.97) identified as the relevant phase at high pH.

$$3Ca^{2+} + 2VO_4^{3-} \rightleftharpoons Ca_3(VO_4)_2 \qquad\qquad \text{(Eqn. 4-6)}$$

Therefore, the maximum possible aqueous V concentration will be inversely proportional to the aqueous Ca^{2+} concentration. The variation in V seen under different experimental conditions (Fig. 4.9) can be explained by the different phases that control the aqueous Ca^{2+} concentration.

Under air-excluded conditions, equilibrium with Ca-Si-H phases will permit relatively high aqueous Ca^{2+} concentrations to develop, which result in vanadate concentrations either at or very close to the solubility limit of $Ca_3(VO_4)_2$. Subsequently precipitation of $Ca_3(VO_4)_2$ controls the concentration of vanadate in solution. $Ca_3(VO_4)_2$
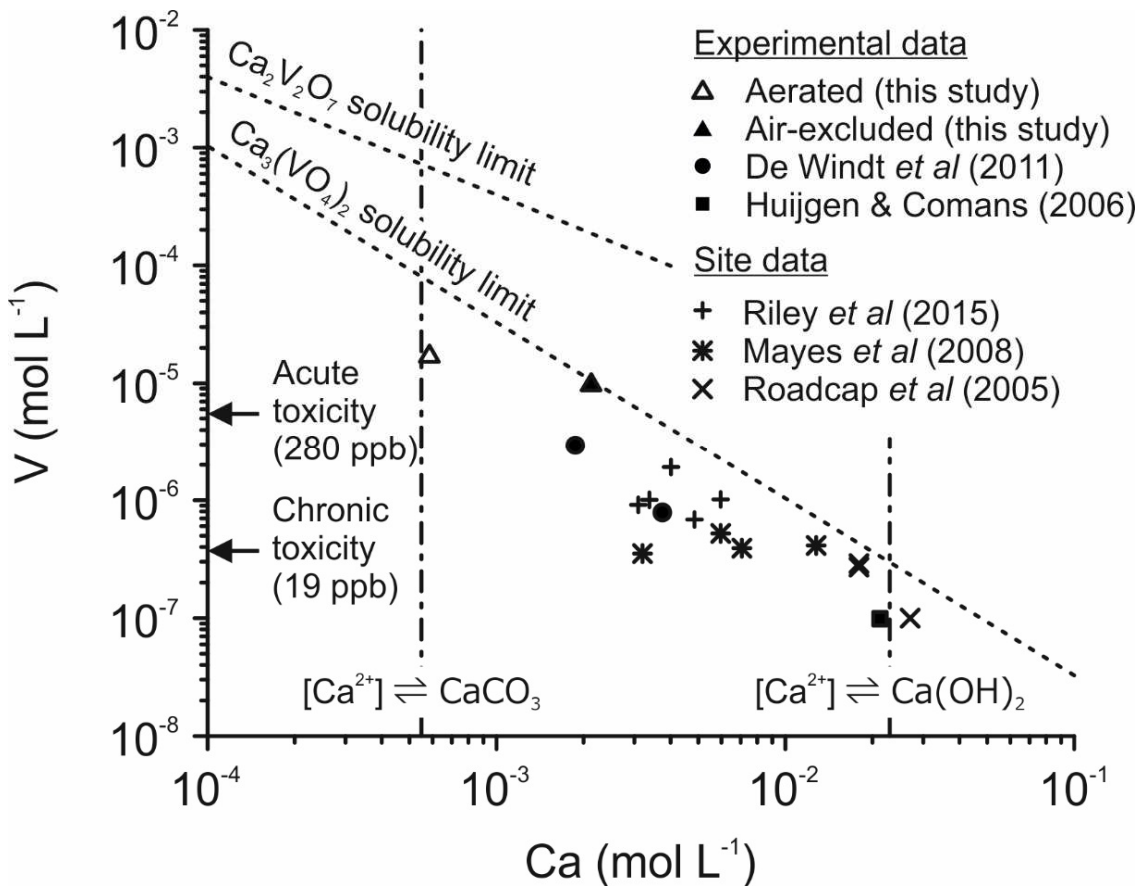
Figure 4.9 - Plot of [V] versus [Ca] for selected experimental and site data (site data from (Mayes et al., 2008; Riley and Mayes, 2015; Roadcap et al., 2005)). Dashed lines marks the solubility limits for $Ca_3(VO_4)_2$ and $Ca_2V_2O_7$ at 20 °C (Allison et al., 1991). Data plotting below the solubility limit is undersaturated with respect to that phase. Vertical dashed lines indicate [Ca] in solutions in equilibrium with calcite in contact with atmospheric CO_2 or with $Ca(OH)_2$ respectively (both at 20 °C). Horizontal arrows indicate acute and chronic freshwater toxicity guideline limits (Buchman, 2008)

was not detected experimentally, however, the lack of discrete V hotspots and higher concentration of V in Ca-Si-H within the altered region from the air-excluded system (0.75 wt% c.f. 0.57 wt% in the aerated system) suggests that $Ca_3(VO_4)_2$ may have been precipitated as finely divided crystallites within the Ca-Si-H structure at a concentration which would be undetectable by EDX. $Ca_3(VO_4)_2$ may also have precipitated on the block surface or as colloidal particles in suspension within the leachate.

Under aerated conditions the presence of atmospheric CO_2 leads to the formation of $CaCO_3$, providing an additional sink for aqueous Ca. Under these conditions, leachate

remains under-saturated with respect to $Ca_3(VO_4)_2$, allowing much higher V concentrations to accumulate in solution. As there is still dicalcium silicate available in the blocks, this indicates that the leachate composition is limited by kinetic effects related to slower dissolution of dicalcium silicate, partially protected by Ca-Si-H in the altered region. In addition, calcium pyrovanadate ($Ca_2V_2O_7$) solubility (Log K_{sp} = -12.0) and surface complexation reactions involving sorption to solids have been suggested as important in controlling V concentrations at pH < 9.5 (Huijgen and Comans, 2006; Schindler et al., 2000). In the aerated tests however, where pH was 8.0, V concentrations were broadly consistent with $Ca_3(VO_4)_2$ solubility limits and the data presented do not indicate that other phases or surface sorption process were important in these tests.

4.4.4   Chromium speciation and behaviour

All Cr XANES spectra from unweathered regions, and the aerated and air-excluded altered regions showed Cr to be present as Cr^{3+}. Chromium is primarily associated with dicalcium aluminoferrite in octahedral co-ordination, suggesting that Cr^{3+} is substituted for Fe^{3+} (Geelhoed et al., 2000; Theopold, 2006). Since this phase is stable during weathering in these experiments, little Cr is released to solution.

4.4.5   Implications for slag weathering, use and storage.

Heap leaching of BOF slag by rainfall inevitably occurs during storage in large land based repositories, and is often actively promoted to reduce the free lime content of BOF slag to permit its beneficial reuse. During the early stages of heap leaching free lime will be relatively abundant due to the high solid : solution ratios present (8 – 10 kg L^{-1}). Aqueous CO_2 species in the rainwater (from contact with atmosphere) will precipitate

rapidly as it enters the waste, so Ca concentrations will be controlled largely by $Ca(OH)_2$ equilibrium, producing highly alkaline, Ca-rich, leachates with corresponding low V concentrations (Fig 4.9). However the concentration of other trace metals solubilised at high pH (e.g. Al, Fe; Table 4.1) will potentially be maximised by these conditions.

In contrast, most lab based leaching tests are performed at much lower solid : solution ratios (e.g. $0.01 - 0.1$ kg L^{-1}; this study, De Windt et al. (2011)). In such leaching tests the free lime phase can be exhausted. Thus, under air-excluded conditions, the Ca concentrations are controlled primarily by the balance of kinetic processes involving dicalcium silicate dissolution and equilibrium processes involving Ca-Si-H precipitation. Typically this produces order of magnitude lower Ca concentrations than found in $Ca(OH)_2$ equilibrated water and correspondingly higher V concentrations due to the inverse relationship between V and Ca concentrations implied by $Ca_3(VO_4)_2$ solubility limit. Further, aerated leaching tests are often conducted to investigate the leaching end-point when the slag reaches equilibrium with CO_2 species in the influent rainwater, although this will only occur on extremely long time scales in real waste heaps. Under aerated conditions, Ca concentrations are controlled by equilibrium with secondary $CaCO_3$ precipitates that typically have low solubility (e.g. calcite Log Ksp = -8.44; Lide (2001)) producing solutions with relatively low Ca concentrations. In this situation, much higher V concentrations are predicted (Fig 4.9).

One important implication is that these results may represent the sequence of slag leaching expected over time: firstly CaO / $Ca(OH)_2$ dominated systems with low V concentrations; then calcium silicate / Ca-Si-H dominated systems with higher V concentrations; and finally $CaCO_3$ dominated systems with the potential for very high V concentrations. However, pH decrease is associated with depletion of reactive V-containing calcium silicate phases (or, more accurately, the availability of these phases for dissolution as particle surfaces become protected by reaction products). Therefore, in a

heap leaching situation where the pore water is continually replaced, V release is kinetically limited and V concentrations are very unlikely to reach the solubility limit of calcium vanadate.

Release of V may also be influenced by the stability of secondary phases incorporating V (i.e. Ca-Si-H, which is soluble at pH values < 10) as well as long term (> 6 month) stability of V incorporated into the less reactive dicalcium aluminoferrite phase. It has been suggested that in general these phases become increasingly soluble if the pH of their environment falls over time (Engström et al., 2013). In these experiments the use of an aquarium pump to aerate the leachate maintained a pCO_2 approximately equivalent to that of the ambient laboratory air (~400 ppm) resulting in sufficient $CaCO_3$ precipitation to prevent dissolution of Ca-Si-H (or its reaction with CO_2 to form calcite) once solution pH had fallen to < 10. Diffusion of CO_2 into the unsaturated zone of slag heaps and uptake during $CaCO_3$ precipitation is likely to result in progressively lower CO_2 concentrations deeper in the heap (pCO2 of ~70 ppm was measured in a borehole in the Consett Iron and Steel Works, Consett, Co. Durham, UK (P. Renforth, personal communication, September 2017); see also Chapter 1, Fig. 1). These experiments may therefore overestimate both the rate of deposition and final thickness of the $CaCO_3$ portion of the altered region, particularly in unsaturated regions of slag heaps which are remote from the surface. Thus, in the long term, as alkalinity-generating phases are depleted within the slag heap and leachate pH falls, dissolution of unprotected Ca-Si-H may represent a future source of V to leachate.

Comparison of real site leachates also indicates that heap weathering process can be very slow. Steel slags deposited in the UK and USA all produce high pH leachates that are largely dominated by $Ca(OH)_2$ derived alkalinity and hence have low V concentrations (Fig 4.9; Mayes et al., (2008); Riley and Mayes, (2015); Roadcap et al., (2005)). Monitoring of leachates from BOF slag deposited at Consett UK has shown only modestly reduced

alkalinity and Ca concentrations over 36 years since closure, leading to only slightly elevated V concentrations (compared to younger systems) (Mayes et al., 2008; Riley and Mayes, 2015). Nevertheless, it should be noted that V concentrations in site leachates often exceed chronic toxicity thresholds (19 μg L^{-1}; Buchman, (2008)) and that this work indicates that a reducing trend in alkalinity and Ca concentrations over time may not necessarily correspond to a reducing trend in V concentrations.

In general, the presence of a Ca-Si-H-rich altered region, combined with any additional $CaCO_3$ precipitate has positive implications for slag after-uses (e.g. as an aggregate) as the presence of an alteration rind may limit (or significantly slow) further dissolution, preventing significant alkalinity generation or metal leaching. On the other hand, calculations of the CO_2 capture potential of BOF slag (often based on the reactivity of crushed powder samples or theoretical maximums based on whole mass conversion (Renforth et al., 2011)) may overestimate both the total extent and the rates of carbonation observed in real-life situations.

4.5   References

AHMEDZADE, P., SENGOZ, B., 2009. Evaluation of steel slag coarse aggregate in hot mix asphalt concrete. J. Hazard. Mater. 165, 300-305.

ALLEN, A.J., THOMAS, J.J., JENNINGS, H.M., 2007. Composition and density of nanoscale calcium-silicate-hydrate in cement. Nat Mater 6, 311-316.

ALLISON, J.D., BROWN, D.S., NOVO-GRADAC, K.J., 1991. MINTEQA2/PRODEFA2, a geochemical assessment model for environmental systems: version 3.0 user's manual. Environmental Research Laboratory, Office of Research and Development, US Environmental Protection Agency.

AUSTRALASIAN SLAG ASSOCIATION, 2002. A guide to the use of iron and steel slag in roads. ISBN 0 9577051, 58.

BARCELOUX, D.G., 1999. Vanadium. Journal of toxicology. Clinical toxicology 37, 265-278.

BOBICKI, E.R., LIU, Q., XU, Z., ZENG, H., 2012. Carbon capture and storage using alkaline industrial wastes. Progress in Energy and Combustion Science 38, 302-320.

BUCHMAN, M.F., 2008. NOAA Screening Quick Reference Tables.

CHAURAND, P., ROSE, J., DOMAS, J., BOTTERO, J.Y., 2006. Speciation of Cr and V within BOF steel slag reused in road constructions. Journal of Geochemical Exploration 88, 10-14.

CHAURAND, P., ROSE, J., BRIOIS, V., OLIVI, L., HAZEMANN, J.L., PROUX, O., DOMAS, J., BOTTERO, J.Y., 2007a. Environmental impacts of steel slag reused in road construction: A crystallographic and molecular (XANES) approach. J. Hazard. Mater. 139, 537-542.

CHAURAND, P., ROSE, J., BRIOIS, V., SALOME, M., PROUX, O., NASSIF, V., OLIVI, L., SUSINI, J., HAZEMANN, J.L., BOTTERO, J.Y., 2007b. New methodological approach for the vanadium K-edge X-ray absorption near-edge structure interpretation: Application to the speciation of vanadium in oxide phases from steel slag. J. Phys. Chem. B 111, 5101-5110.

CHEN, J.J., THOMAS, J.J., TAYLOR, H.F.W., JENNINGS, H.M., 2004. Solubility and structure of calcium silicate hydrate. Cem. Concr. Res. 34, 1499-1519.

COLVILLE, A.A., GELLER, S., 1971. The crystal structure of brownmillerite, Ca2FeAlO5. Acta Crystallographica Section B 27, 2311-2315.

CORNELIS, G., JOHNSON, C.A., GERVEN, T.V., VANDECASTEELE, C., 2008. Leaching mechanisms of oxyanionic metalloid and metal species in alkaline solid wastes: A review. Applied Geochemistry 23, 955-976.

DE WINDT, L., CHAURAND, P., ROSE, J., 2011. Kinetics of steel slag leaching: Batch tests and modeling. Waste Manage. 31, 225-235.

DOUCET, F.J., 2010. Effective CO2-specific sequestration capacity of steel slags and variability in their leaching behaviour in view of industrial mineral carbonation. Minerals Engineering 23, 262-269.

ENGSTRÖM, F., ADOLFSSON, D., SAMUELSSON, C., SANDSTRÖM, Å., BJÖRKMAN, B., 2013. A study of the solubility of pure slag minerals. Minerals Engineering 41, 46-52.

ENVIRONMENT AGENCY, 2014. EA Bespoke permit 2014 Permit for Scunthorpe Aggregate processing. Permit number EPR/LP3537VV/A001.

EUROSLAG, 2012. Statistics 2012, http://www.euroslag.com/products/statistics/2012/.

FENDORF, S.E., 1995. Surface reactions of chromium in soils and waters. Geoderma 67, 55-71.

GARD, J.A., TAYLOR, H.F.W., 1976. Calcium silicate hydrate (II) ("C-S-H(II)"). Cem. Concr. Res. 6, 667-677.

GEELHOED, J.S., MEEUSSEN, J.C.L., FARMER, J.G., PATERSON, E., 2000. CHARACTERISATION AND GEOCHEMICAL MODELLING OF THE BEHAVIOUR OF pH AND CHROMIUM(VI) IN CHROMITE ORE PROCESSING RESIDUE, Contaminated Soil, pp. 2: 705-712.

GEISELER, J., 1996. Use of steelworks slag in Europe. Waste Manage. 16, 59-63.

HUIJGEN, W.J.J., COMANS, R.N.J., 2005. Mineral CO2 Sequestration by Steel Slag Carbonation. Environ. Sci. Technol. 39, 9676-9682.

HUIJGEN, W.J.J., COMANS, R.N.J., 2006. Carbonation of steel slag for CO2 sequestration: Leaching of products and reaction mechanisms. Environmental Science and Technology 40, 2790-2796.

LIDE, D.R., 2001. CRC Handbook of Physics and Chemistry. CRC Press.

MAYES, W.M., YOUNGER, P.L., AUMONIER, J., 2008. Hydrogeochemistry of alkaline steel slag leachates in the UK. Water Air Soil Pollut. 195, 35-50.

MOTZ, H., GEISELER, J., 2001. Products of steel slags an opportunity to save natural resources. Waste Manage. 21, 285-293.

NAVARRO, C., DIAZ, M., VILLA-GARCIA, M.A., 2010. Physico-Chemical Characterization of Steel Slag. Study of its Behavior under Simulated Environmental Conditions. Environ. Sci. Technol. 44, 5383-5388.

OBER, J.A., 2016. Mineral commodity summaries 2016. US Geological Survey.

PEACOCK, C.L., SHERMAN, D.M., 2004. Vanadium(V) adsorption onto goethite (alpha-FeOOH) at pH 1.5 to 12: A surface complexation model based on ab initio molecular geometries and EXAFS spectroscopy. Geochimica Et Cosmochimica Acta 68, 1723-1733.

PETERSON, M.L., BROWN, G.E., PARKS, G.A., 1996. Direct XAFS evidence for heterogeneous redox reaction at the aqueous chromium/magnetite interface. Colloids and Surfaces A: Physicochemical and Engineering Aspects 107, 77-88.

PIATAK, N.M., PARSONS, M.B., SEAL, R.R., 2014. Characteristics and environmental aspects of slag: A review. Applied Geochemistry.

PLAS, L.V.D., TOBI, A.C., 1965. A chart for judging the reliability of point counting results. American Journal of Science 263, 87-90.

PROCTOR, D.M., FEHLING, K.A., SHAY, E.C., WITTENBORN, J.L., GREEN, J.J., AVENT, C., BIGHAM, R.D., CONNOLLY, M., LEE, B., SHEPKER, T.O., ZAK, M.A., 2000. Physical and chemical characteristics of blast furnace, basic oxygen furnace, and electric arc furnace steel industry slags. Environ. Sci. Technol. 34, 1576-1582.

RAVEL, B., NEWVILLE, M., 2005. ATHENA, ARTEMIS, HEPHAESTUS: data analysis for X-ray absorption spectroscopy using IFEFFIT. Journal of synchrotron radiation 12, 537-541.

RENFORTH, P., WASHBOURNE, C.L., TAYLDER, J., MANNING, D.A.C., 2011. Silicate Production and Availability for Mineral Carbonation. Environ. Sci. Technol. 45, 2035-2041.

RICHARDSON, I.G., 1999. The nature of C-S-H in hardened cements. Cem. Concr. Res. 29, 1131-1147.

RILEY, A.L., MAYES, W.M., 2015. Long-term evolution of highly alkaline steel slag drainage waters. Environ Monit Assess 187, 463.

ROADCAP, G.S., KELLY, W.R., BETHKE, C.M., 2005. Geochemistry of extremely alkaline (pH > 12) ground water in slag-fill aquifers. Ground Water 43, 806-816.

SCHINDLER, M., HAWTHORNE, F.C., BAUR, W.H., 2000. A crystal-chemical approach to the composition and occurrence of vanadium minerals. The Canadian Mineralogist 38, 1443-1456.

SHEN, D.H., WU, C.M., DU, J.C., 2009. Laboratory investigation of basic oxygen furnace slag for substitution of aggregate in porous asphalt mixture. Constr. Build. Mater. 23, 453-461.

SMIL, V., 2006. Transforming the twentieth century: technical innovations and their consequences. Oxford University Press on Demand.

TAYLOR, H.F.W., 1993. Nanostructure of C • S • H: Current status. Advanced Cement Based Materials 1, 38-46.

TAYLOR, H.F.W., 1997. Cement Chemistry. Thomas Telford.

THEOPOLD, K.H., 2006. Chromium: Inorganic & Coordination Chemistry, Encyclopedia of Inorganic Chemistry. John Wiley & Sons, Ltd.

TOSSAVAINEN, M., ENGSTROM, F., YANG, Q., MENAD, N., LIDSTROM LARSSON, M., BJORKMAN, B., 2007. Characteristics of steel slag under different cooling conditions. Waste Manage. 27, 1335-1344.

UK STEEL, 2016. Key Statistics, https://www.eef.org.uk/uk-steel/about-uk-steel.

WEHRLI, B., STUMM, W., 1989. Vanadyl in natural-waters - adsorption and hydrolysis promote oxygenation. Geochimica Et Cosmochimica Acta 53, 69-77.

YILDIRIM, I.Z., PREZZI, M., 2011. Chemical, Mineralogical, and Morphological Properties of Steel Slag. Advances in Civil Engineering 2011, 1-13.

Chapter 5   Leaching behaviour of co-disposed steel making wastes: Effects of aeration on leachate chemistry and vanadium mobilisation

Summary

Steelmaking wastes stored in landfill, such as slag and spent refractory liners, are often enriched in toxic trace metals (including V). These may become mobile in highly alkaline leachate generated during weathering. Fresh steelmaking waste was characterised using XRD, XRF, and SEM-EDX. Batch leaching tests were performed under aerated, air-excluded and acidified conditions to determine the impact of atmospheric CO_2 and acid addition on leachate chemistry. Phases commonly associated with slag including dicalcium silicate, dicalcium aluminoferrite, a wüstite-like solid solution and free lime were identified, as well as a second group of phases including periclase, corundum and graphite which are representative of refractory liners. During air-excluded leaching, dissolution of free lime and dicalcium silicate results in a high pH, high Ca leachate in which the V concentration is low due to the constraint imposed by $Ca_3(VO_4)_2$ solubility limits. Under aerated conditions, carbonation lowers the leachate pH and provides a sink for aqueous Ca, allowing higher concentrations of V to accumulate. Below pH 10, leachate is dominated by periclase dissolution and secondary phases including monohydrocalcite and dolomite are precipitated. Storage of waste under saturated conditions that exclude atmospheric CO_2 would therefore provide the optimal environment to minimise V leaching during weathering.

5.1   Introduction

Steel slag is a ubiquitous byproduct of the steelmaking industry that is produced in large quantities worldwide. It is estimated that 160-240 million tonnes of steel slag were produced in 2016 (Ober, 2017) which corresponds to approximately 10-15 % of crude steel output (Piatak et al., 2014). Primary steelmaking (i.e. conversion of iron to steel) produces steel slag via two principal production methods; 1) basic oxygen furnace (BOF) steelmaking in which molten iron from a blast furnace is used and 2) electric arc furnace (EAF) steelmaking which uses a combination of scrap steel, directly reduced iron and pig iron. In both processes lime (or limestone) is added to the furnace as a fluxing agent to remove impurities from the molten metal (Eloneva et al., 2010, Piatak et al., 2014). The composition of BOF and EAF slag is broadly similar and consistent across location and process (Tossavainen et al., 2007, Yildirim and Prezzi, 2011, Proctor et al., 2000). These predominantly consist of Ca, Mg, Fe and Al oxides and silicates (Proctor et al., 2000); the relative proportions of which will vary according to the raw materials used during manufacture. Secondary steelmaking slags are formed during secondary steelmaking where both BOF and EAF derived steels are further processed in ladle furnaces, producing BOF(L) or EAF(L) slags respectively. These are much more variable in composition and are also relatively enriched in Mg and Al due to additives used in the process (Shi, 2002). In addition to slag production, a wide variety of refractories (MgO-C; Al-silicate; MgO-Al_2O_3-C) are used as furnace liners during steelmaking to protect the furnace (Quaranta et al., 2014). Refractories that are in contact with molten slag wear over time and the build-up of solidified slag above the melt (due to sputtering) and in conduits also requires regular removal. Therefore, periodic renewal of the entire liner is required. The result is a mixed waste containing both slag and refractories which is difficult to separate and are often co-disposed (Hanagiri et al., 2008).

Primary steelmaking slags are recycled where possible, usually as aggregate in civil engineering applications, such as road construction and as a general fill material due to its stability (Geiseler, 1996, Yi et al., 2012). However, in some cases elevated concentrations of free lime (CaO) and periclase (MgO), which expand on hydration, preclude reuse in engineering applications. Ladle slags and refractories can also be recycled during primary steelmaking (as an alternative source of CaO or MgO flux) but virgin materials are often preferred due to their more uniform composition and the increased effort that would be required in slag sorting and processing (Kwong and Bennett, 2002, de Sa et al., 2007). For this reason, and also because supply frequently exceeds the demand for secondary aggregates, steelmaking byproducts are often stored either in landfill or in open 'heaps'. However, as recycling rates increase, materials with problematic properties (e.g. high metal content, high % of CaO or MgO, or simply uncertain or variable composition) will make up an ever greater proportion of materials stored in landfill. It is therefore increasingly import to understand the leaching behaviour of such non-standard by-products as they become a significant part of the disposed inventory.

Steel slags contain free lime (CaO) and periclase (MgO; also in present in refractories) that hydrate to form portlandite ($Ca(OH)_2$) or brucite ($Mg(OH)_2$). These phases dissolve in water to generate high pH (10.5-12.5) leachate (Mayes et al., 2008):

$$CaO_{(s)} + H_2O \rightarrow Ca(OH)_{2(aq)} \rightleftharpoons Ca^{2+} + 2OH^- \qquad pH_{(eq.)} = 12.46 \quad \text{(Eqn. 5-1)}$$

$$MgO + H_2O \rightarrow Mg(OH)_{2(aq)} \rightleftharpoons Mg^{2+} + 2OH^- \qquad pH_{(eq.)} = 10.40 \quad \text{(Eqn. 5-2)}$$
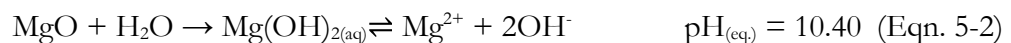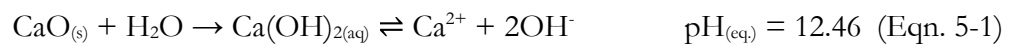
Alkalinity may also be produced by the dissolution of Ca-silicates, (e.g. β-dicalcium silicate, larnite; Roadcap et al. (2005)):

$$Ca_2SiO_4 + 2H_2O \rightarrow 2Ca^{2+} + H_2SiO_4^{2-} + 2OH^- \qquad \text{(Eqn. 5-3)}$$
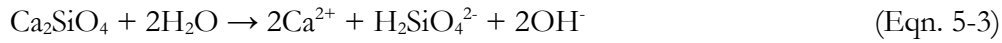
In addition, under aerated conditions, reactions involving the in-gassing of CO_2 results in conversion of Ca/Mg hydroxide based alkalinity to carbonate alkalinity.

$$Ca^{2+}_{(aq)} + CO_{2(aq)} + 2OH^-_{(aq)} \rightarrow CaCO_{3(s)} + H_2O_{(l)} \qquad \text{(Eqn. 5-4)}$$

$$CaCO_3 + H_2O \rightleftharpoons Ca^{2+} + HCO_3^- + OH^- \qquad pH_{(eq.)} = 9.36 \quad \text{(Eqn. 5-5)}$$
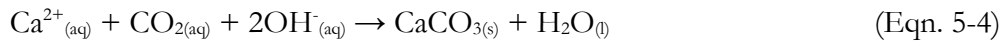
Whilst steel slag has historically been considered to be a non-hazardous waste, concerns have been raised in recent years regarding the high concentrations of potential toxic trace metal(loid)s (including Al, Cr, Pb, Mo and V) present in the slag (Tossavainen et al., 2007, Proctor et al., 2000, Matern et al., 2013) which may be mobilised in the alkaline leachate (Cornelis et al., 2008). V leaching in particular has received a lot of recent attention (Chaurand et al., 2006, De Windt et al., 2011, Huijgen and Comans, 2006, Navarro et al., 2010) due to its relative enrichment in steel slags and regulatory concern over high V concentrations in leachates (Environment Agency, 2014). Steelmaking wastes at disposal sites are often deposited in both saturated and unsaturated settings, however, few data currently exist concerning slag leachate generation and chemistry under aerated conditions (Bayless and Schulz, 2003, Roadcap et al., 2005, Mayes and Younger, 2006). Under aerated conditions, $CaCO_3$ precipitation results in a drop in solution pH as OH^- ions are consumed (Eqn. 5-4). Changes in both pH and redox have significant implications for the mobility of many potentially toxic metals; for example Al, Cr , and V mobility and toxicity are all highly dependent on their speciation (with higher oxidation states generally regarded as more toxic and mobile) (Pourbaix, 1966, Barceloux, 1999).

This study investigates leaching behaviour of co-disposed steelmaking waste under aerated and air-excluded conditions. These represent contrasting conditions present either near the surface (good contact with atmosphere) and below the water table deeper within waste heaps. The waste has been characterised using x-ray diffraction (XRD) and fluorescence (XRF) techniques, as well as scanning electron microscopy (SEM) with energy-dispersive x-ray spectroscopy (EDX) to determine the mineral phases present. Fully aerated and air-excluded water leaching tests have been performed to determine how phase dissolution behaviour, secondary mineral formation and trace metal release are affected by changes in pH and availability of air. Results will assist prediction of metal release from waste when stored in landfill above and below the water table, enabling effective environmental risk assessment and cost-effective long-term management of the waste.

5.2 Methods

5.2.1 Sample collection and characterisation

See Chapter 3, section 3.1.1 for details of sample collection.

Elemental analysis of the powdered waste was undertaken using a PANalytical Axios Advanced X-ray Fluorescence (XRF) spectrometer (data corrected for loss on ignition at 1050 °C). Samples were prepared for major element analysis as fused beads with lithium metaborate/tetraborate flux (Johnson Matthey Spectroflux JM100B) (0.6 g sample; 3 g flux). For minor/trace element analysis pressed pellets were prepared containing ~10 g of dried waste using ~10–20 drops of 6.6 % w/v polyvinyl alcohol in a 1:6 mix of methanol and distilled deionized water as a binder (Moviol 88 solution). Mineralogical analysis was undertaken by powder X-ray diffraction (XRD) using a Bruker D8

diffractometer, where powder samples were mounted on silicon slides and scanned between 2° and 70° 2θ using Cu K$_\alpha$ radiation.

Two polished blocks were prepared by first cutting waste pieces to size under water and setting the resultant ~2 cm^3 blocks into epoxy resin with the cut surface exposed. This surface was then polished using a water-free diamond paste to remove the top 1-2 mm of material potentially exposed to water during cutting. Electron micrographs were subsequently collected on a FEI QUANTA 650 FEG ESEM, which was equipped for Oxford Instruments INCA 350 energy-dispersive X-ray spectroscopy (EDS) system/80 mm X-Max silicon drift detector. EDS spectra and elemental maps were collected and analysed using Oxford Instruments AZtec software.

5.2.2   *Acid Neutralisation Capacity (ANC)*

Homogenised powdered waste (0.4 g) was mixed with 40 mL HCl with concentrations ranging from 1 M to 0.001 M in 50 mL polypropylene Oak Ridge tubes (Nalgene, USA). Experiments were performed in triplicate. Headspaces were flushed with N$_2$ gas prior to sealing. All tubes were stored in airtight 2 L glass jars (Le Parfait, France) filled with N$_2$ gas and containing ~100 g soda lime as a CO$_2$ absorbent. After 1 and 50 days equilibration the tubes were centrifuged for 5 minutes at 6000 *g* to separate aqueous and solid phases. 1 mL of the supernatant was removed and immediately added to 9 mL 0.1 M HNO$_3$ prior to ICP analysis, and the pH of the remaining solution was measured (pH measurement is described below).

5.2.3   Leaching tests

Triplicate aerated experiments containing 1 g homogenised powdered waste and 100 mL deionised water were established in open 500 mL PETG Erlenmeyer flasks. A low liquid : solid ratio was used to ensure that leachate composition was not limited by water availability. These were shaken on an orbital shaker at 175 rpm. At regular intervals over a 50 day period 3 mL aliquots of slurry were removed from the flasks and centrifuged for 5 minutes at 16,000 g to separate aqueous and solid phases. 1 mL of supernatant was removed and acidified in 0.1 M HNO_3 and the pH of the remaining supernatant was determined. The moist solid samples were stored at -20 °C prior to drying at 40 °C overnight for further analysis.

Replicate air-excluded experiments were established containing 0.4 g homogenised powdered waste and 40 mL deionised water in 50 mL Oak ridge tubes. All tubes were handled anaerobically as described above for the ANC tests. Periodically over a 50 day period 3 tubes were sacrificially sampled. Solid and solution samples were taken and stored following the procedures above.

5.2.4   Aqueous Analysis

Solution pH was measured using an Orion DualStar pH/ISE benchtop meter (Thermo Scientific, USA) with an electrode that was calibrated daily at pH 4, 7 and 10. Nitrogen gas was bubbled through the sample tube during pH measurements made in solutions from the air-excluded experiments to prevent contact with atmosphere. Metal concentrations in acidified aqueous samples from the air-excluded leaching experiments were determined using a Thermo iCAP 7400 ICP-OES ion-coupled plasma, optical emission spectrometer (ICP-OES; for Ca, Si, Mg) and Thermo iCAP Qc OES ion-coupled

plasma, mass spectrometer (ICP-MS; for V, Fe, Mn, Li and Cr). Aqueous elemental concentrations from the aerated leaching experiments were determined using a Perkin Elmer Optima 5300DV ICP-OES for all elements.

5.3 Results

5.3.1 Material Characterisation

The elemental composition (Table 5.1) of the powder sample was dominated by Ca, Fe, Mg, Si and Al with Cr and Mn as minor constituents. Trace elements included P, V, K, Ti and S.

Mineralogical analysis of the crushed waste using XRD (Fig. 5.1a) identified the presence of periclase (MgO), corundum (Al_2O_3), larnite (dicalcium silicate, β-Ca_2SiO_4), brownmillerite (dicalcium aluminoferrite, $Ca_2(Al,Fe)_2O_5$), wüsite (FeO), brucite ($Mg(OH)_2$) and elemental carbon (C). The principal XRD peak of free lime (CaO) overlaps with a secondary peak of corundum at ~37.5° 2θ, however, the secondary peaks at ~32 and 54° 2θ were present, suggesting its presence. There was no calcite peak in the XRD pattern for the unreacted waste (the principle $CaCO_3$ peak is at ~29° 2θ).

SEM analysis of a polished block (Fig. 5.2) showed a material that was composed of intergrown 10-30 μm crystallites, EDS element mapping indicated that there were three dominant compositions. The dominant composition by area (~65% of the sample viewed) was a Ca-Si-O rich phase containing trace amounts of Al, P, Ti, V and Fe by EDS analysis,

Table 5.1 Chemical composition of BOF steel slag samples (Chapter 4) from the Yarbrough Repository, Scunthorpe UK, and the powder sample of combined steelmaking waste used in leaching tests.

Major Elements Nominal Oxide wt%	BOF slag (Hobson et al., 2017)	Powder sample ($\pm$ < 10%)
CaO	40 ±5	19.0
FeO	32 ±9	16.0
SiO_2	14 ±3	11.3
MgO	5.2 ±1	27.9
MnO	4.5 ±1	2.1
Al_2O_3	1.2 ±0.4	18.3
P_2O_5	1.3 ±0.4	0.87
V_2O_5	0.81 ±0.24	0.33
TiO_2	0.30 ±0.13	0.86
Cr_2O_3	0.24 ±0.13	3.3
SO_3	0.23 ±0.09	0.33
K_2O	n.d.	0.12
Na_2O	n.d.	0.18
SrO	n.d.	0.14
ZrO_2	0.02 ±0.01	0.14
BaO	n.d.	0.01
NiO	0.02 ±0.01	n.d.
CuO	0.01±0.01	n.d.
ZnO	n.d.	0.02
PbO	n.d.	0.03
LOI	*n.d.*	*0.96*
TOTAL	**98.9**	**100.9**

consistent with the larnite phase identified by XRD. The second most abundant composition by area (~25%) was a Mg-Fe-O rich phase containing trace amounts of Na, Ca, Cr and Mn, corresponding to the wüstite phase identified by XRD. The third most abundant composition by area (~10%) was a Ca-Fe-Al-O rich phase containing trace amounts of Ti, V, Cr and Mn, corresponding to the brownmillerite phase identified by XRD. Regions of the dicalcium silicate phase contain lamellae identified as CaO rich
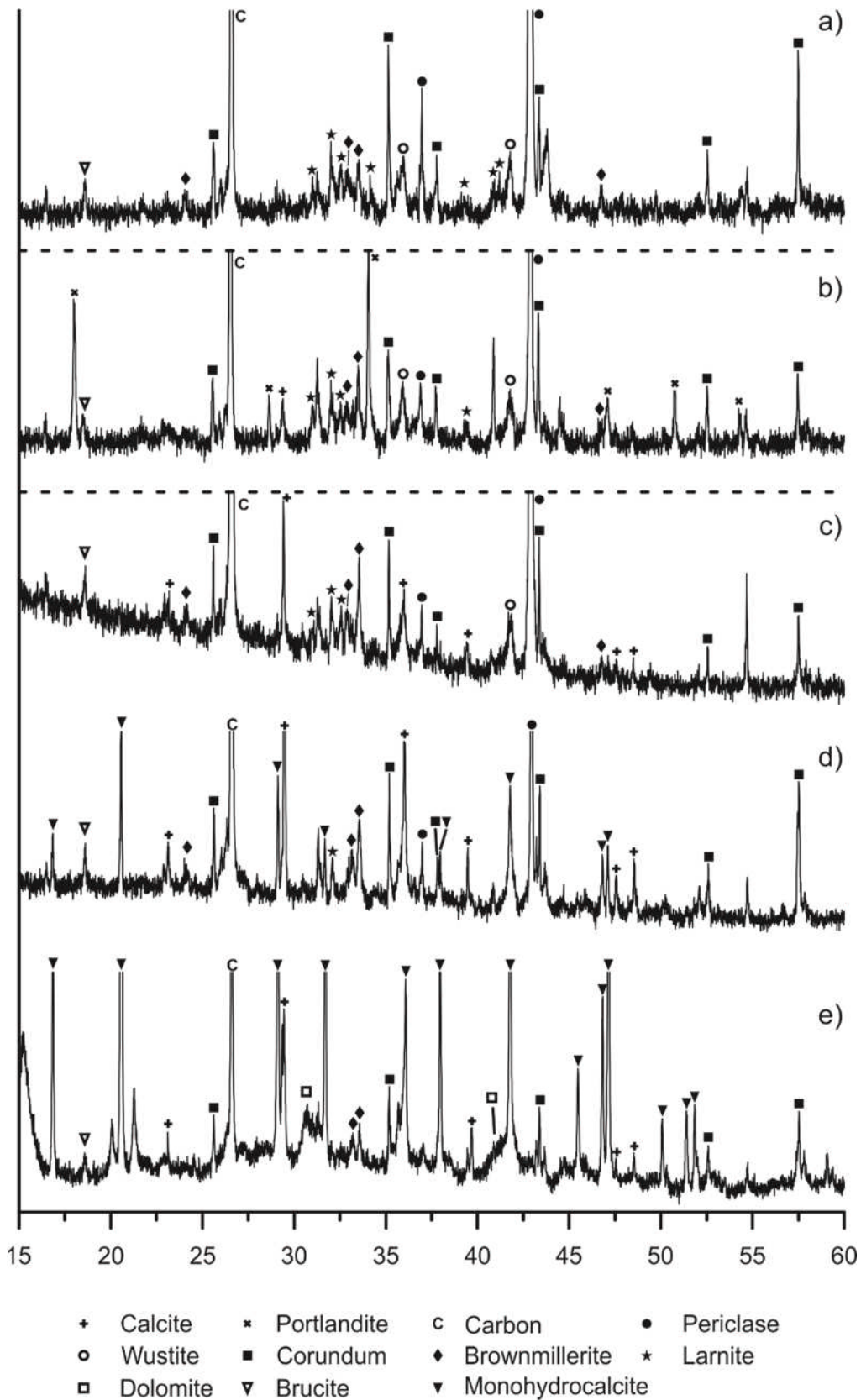
Figure 5.1 - XRD patterns from (a) unweathered steelmaking waste, (b) steelmaking waste leached for 50 days under air-excluded conditions, and steelmaking waste leached under aerated conditions for (c) 1 hour, (d) 6 days and (e) 50 days
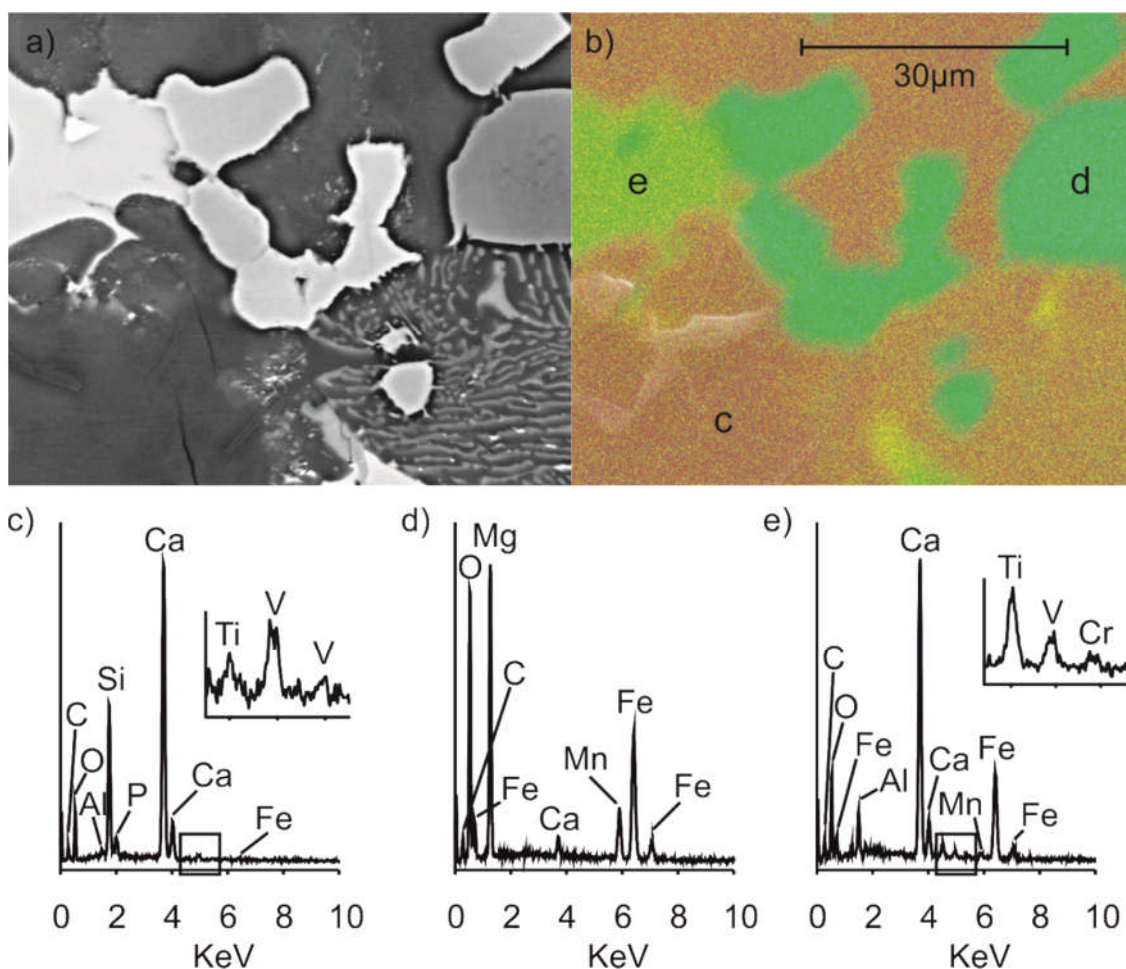
Figure 5.2 - Backscattered electron micrograph (top left) with corresponding false colour element map (top right) and EDS spectra from c) dicalcium silicate, d) wüstite and e) dicalcium aluminoferrite phases. The laminae containing phase (bottom right) also contains discrete CaO laminae.

regions associated with dicalcium silicate. The second polished block was composed of a single Al-Si-O rich composition containing no significant trace elements (data not shown).

5.3.2   Acid Neutralisation Tests.

For crushed waste, the relationship between the final solution pH value and the amount of acid added was similar after 1 day and 50 days of equilibration (Fig. 5.3a). The acid neutralisation capacity (to pH 7) was very similar at the two time-points (11.0 and 9.5 M H^+ kg^{-1} waste, respectively). In tests where the final pH value was greater than 7, the

pH value increased with time. The solution Ca and Mg concentrations at a particular pH value were broadly similar after 1 day and 50 days (Fig. 5.3c, d), however, Si (Fig. 5.3b) was present in solution at all final pH values <10 after 1 day, but was present at significantly reduced concentrations at 50 days at all pH values. Ca was released to solution at all pH values, with generally higher concentrations at lower pH values. Mg was only present in solution below ~pH 10, but also has generally higher concentrations at lower pH values.
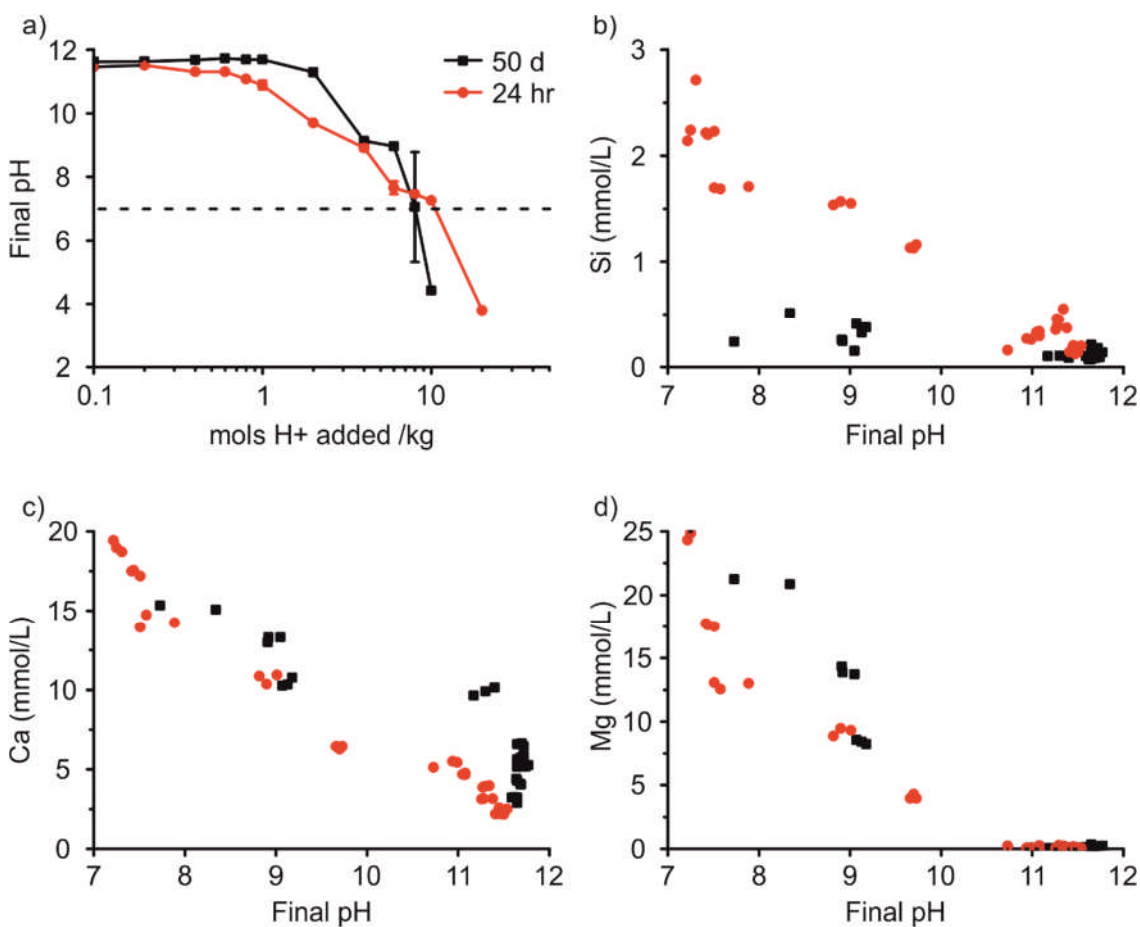
Figure 5.3 - Acid neutralisation results showing (a) final pH values after 24 hours (red circles) and 50 days (black squares) as a function of initial acid concentration (each point represents the mean value and error bars +/- 1σ from triplicate samples; dashed line is added at pH 7 to guide the eye) and (b)-(d) metal concentrations leached from waste over 24 hours and 50 days as a function of final pH. Initial test conditions in all cases were 10g waste L^{-1}.

5.3.3   Batch leaching tests

During air-excluded leaching (Fig. 5.4), the leachate pH rose rapidly within the first hour to a value of 11.4, and then increased more slowly to a maximum value of 11.9 after 52 days. The Ca concentration increased rapidly to ~2.5 mmol L^{-1} over the first 24 hrs, and then more steadily to ~3.0 mmol L^{-1} after 5 days. Between 5 days and 10 days the Ca concentration decreased to ~2.5 mmol L^{-1}, but thereafter increased steadily to ~3.4 mmol L^{-1} after 50 days. The Mg concentration showed no trend with time and was less than 0.4 mmol L^{-1} throughout the experiment. The Si concentration increased to ~0.15 mmol L^{-1} over the first 24 hrs, and then to ~0.25 mmol L^{-1} after 5 days. After about 10 days the Si concentration decreased to ~0.15 mmol L^{-1} but subsequently varied between ~0.15 and ~0.25 mmol L^{-1} until the end of the test. The V concentration gradually increased from ~0.002 mmol L^{-1} after 24hrs to ~0.007 mmol L^{-1} after 50 days. There is some scatter in the aqueous Fe concentrations but they range from 0.002 to 0.07 mmol L^{-1}. There was very little change in XRD patterns collected from the solid residue over time, except that portlandite was detected in samples collected from the experiment end points (Fig 5.1b).

During the aerated experiments (Fig. 5.4), pH increased rapidly within the first hour to a maximum value of 11.6. This was followed by a decrease to pH 8.9 after 1 day and then by a second rise to pH 10.0 after 6 days. Subsequently pH steadily declined to 9.3 after 50 days of leaching. The Ca concentration increased rapidly to ~2 mmol L^{-1} within the first two hours, but then decreased to ~0.25 mmol L^{-1} after 6-7 days. Initially the Mg concentration was low but it increased rapidly after day 2 to reach a concentration above 12.5 mmol L^{-1} by day 20, which persisted until the end of the test. The Si concentration was ~0.15 mmol L^{-1} after 1 hour, decreased to ~0.03 mmol L^{-1} after 2 days but then rose to ~0.25 mmol L^{-1} at 6 days. Subsequently Si concentrations remained above 0.2 mmol L^{-1} for the remainder of the test. The V concentration increased steadily over the duration of
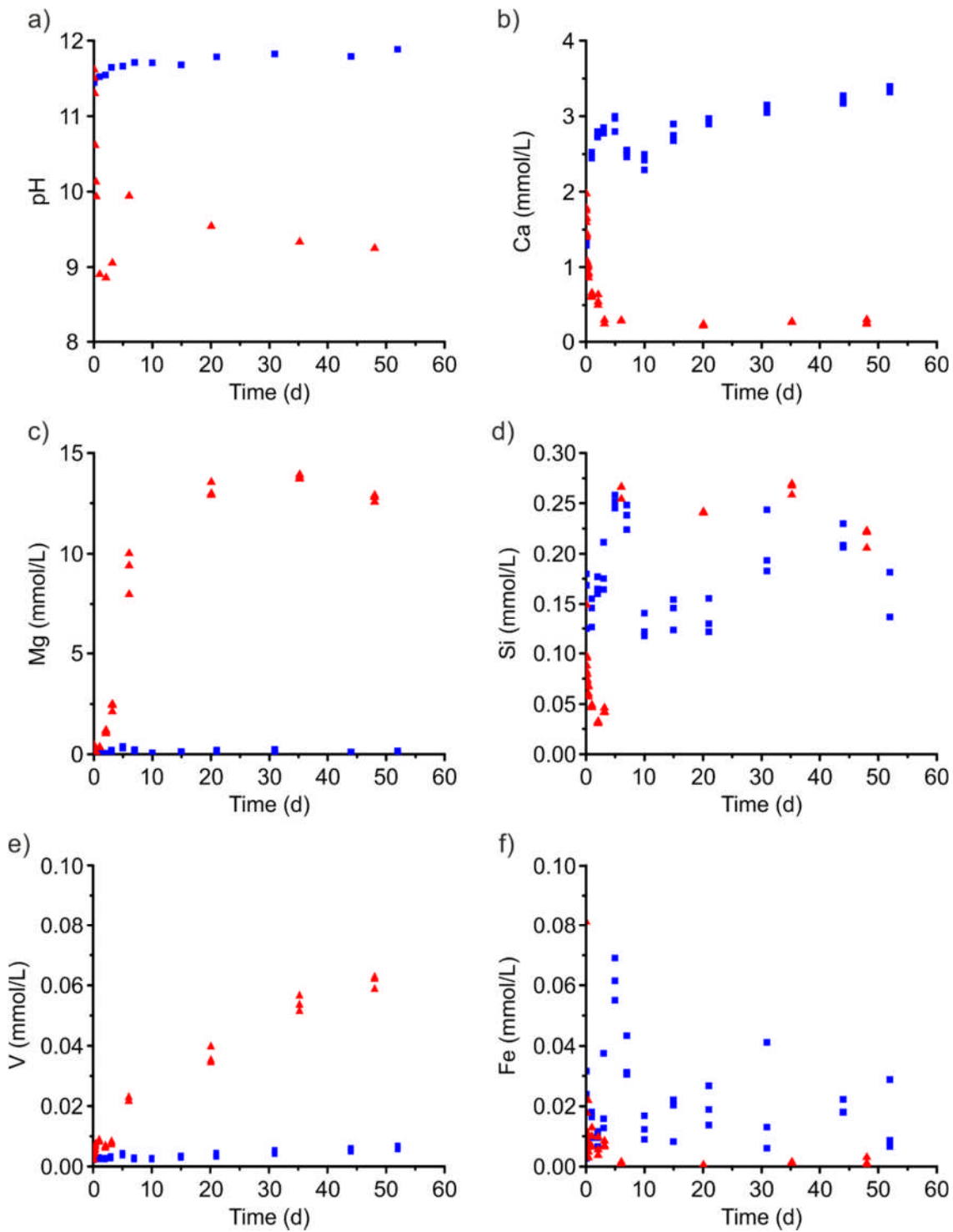
Figure 5.4 - Leachate composition during the aerated (red triangle) and air-excluded (blue square) batch leaching test on steelmaking waste (initial test conditions: 10g solid/L deionised water). Data from triplicate experiments shown separately.

the test to reach a maximum of ~0.065 mmol L^{-1} after 48 days. The aqueous Fe

concentrations were initially around 0.05 mmol L^{-1} and decreased over 5 days to < 0.002

mmol L^{-1} for the remainder of the tests. XRD patterns collected from solid residue after 1 day show that calcite was present (Fig. 5.1c), after 6 days the periclase and larnite peaks had reduced in relative intensity and monohydrocalcite was detected (Fig 5.1d). After 50 days monohydrocalcite was the dominant secondary phase detected (although some dolomite was also present) and periclase and larnite peaks were absent (Fig. 5.1e).

Concentrations of other trace elements considered to be potential environmental risk drivers for steel slags (e.g. Mn, Cr, Li) were low in both the aerated and the air-excluded tests (and were present at concentrations close to or below to the limit of detection).

5.4   Discussion

5.4.1   *Waste characterisation*

The bulk chemical and mineralogical composition of the waste was distinct from BOF slag samples collected at the Yarborough site (Table 5.1). Compared to BOF slag the material was relatively depleted in elements such as Ca, Fe, Mn and V; but enriched in Mg, Al, Ti and Cr. The waste mineralogy could be split into two distinct groups. The first group included a range of phases commonly occurring in BOF slag (i.e. larnite, brownmillerite, lime, and wüstite; Yildirim and Prezzi (2011), Proctor et al. (2000), Geiseler (1996)), which were observed in SEM as discrete particle assemblages within an intergrown matrix of 20-50 μm crystallites. The second group of minerals identified by XRD included corundum, periclase and graphite that are rare in BOF slag and are more commonly associated with refractory liner materials (e.g. in MgO-C and AL_2O_3-MgO-C refractories; Rovnushkin et al. (2005)). Aluminosillicate was also observed in SEM analysis. This was most likely the high temperature phase mullite ($Al_6Si_2O_{13}$; Schneider et al. (1994),

Chesters (1973), Mazdiyasni and Brown (1972), Tamari et al. (1993)) which is also used as a refractory material or can form in slags from reaction of corundum and Si (Dana and Das, 2004, Zhao et al., 2014). Therefore, the waste can be characterised as a mixed steelmaking waste containing both BOF slag and refractory materials. The potential for re-use of mixed wastes is low due to uncertainties about their chemical and physical behaviour, however, it is important to understand their potential leaching behaviour during disposal.

5.4.2   *Acid neutralisation behaviour*

The acid neutralisation capacity experiments were conducted under air-excluded conditions and provide information on phase dissolution in the waste as a function of the acid addition and final solution pH. At low acid additions (< 1 mol H^+ kg^{-1}) the waste buffered pH to values > 11.5 due to the dissolution of free lime and dicalcium silicate (Eqns. 5-1 and 5-3), with dissolution of brucite from periclase hydration also consuming acid when the pH < 10.4 (Eqn. 5-2). Ca was released to solution at all pH values with the amount of release increasing with decreasing pH (Fig. 5.3c), and Mg was released to solution when pH values < 10 with the amount of release also increasing with decreasing pH (Fig. 5.3d), which is consistent with the dissolution behaviour of these phases (Eqns 5-1 and 5-2). The alkalinity producing phases were progressively exhausted by larger acid additions and the final pH decreased steadily until neutral values were reached with an acid addition of ~ 8 mols H^+ kg^{-1}. CaO hydration is a very fast reaction (Shi et al., 2002), whereas dicalcium silicate hydration and dissolution is generally considered to be slower (Taylor, 1986). However, here we find that both are involved in buffering the pH in the first 24 hrs as Si is released to solution. Nevertheless, the 10:1 ratio in the aqueous Ca and Si concentrations indicated an excess of Ca release relative to pure dicalcium silicate

dissolution (i.e. Ca : Si ≈ 2:1) suggesting that free lime was the dominant Ca bearing phase that was dissolving over 24 hrs.

The difference in the final pH of the 1 and 50 day tests with the same acid addition indicates that part of the alkalinity generation occurs over longer time periods. At high pH this was most likely associated with continued dissolution of dicalcium silicate, although the Si concentrations decreased between day 1 and 50. This Si decrease was most likely associated with the formation of secondary Si-containing phases. These phases were most probably calcium-silicate-hydrate (Ca-Si-H) phases at pH values > 9 (Walker et al., 2016, Costa et al., 2016) and amorphous silica (SiO_2 $_{(am)}$) at lower pH values (Langmuir, 1997). The increase in Mg concentration between day 1 and 50 at pH values < 9 suggests periclase hydration also continued beyond 24 hours.

5.4.3   Leaching behaviour under aerated conditions

At the initial sampling point (1 hr) during the aerated leaching tests, the pH value was > 11.5 and both Ca and Si were released to solution. This rapid initial release of alkalinity, Ca and Si was due to the hydration and dissolution of both free lime and dicalcium silicate phases present in the waste. Previous slag leaching tests using granulated BOF slag pieces found dicalcium silicate dissolution to be significantly slower than free lime dissolution (Stewart et al, in review; Appendix B). The use of crushed powder samples in these tests, which will have contained high surface area fines, must have promoted rapid initial dissolution of dicalcium silicate. However, as dicalcium silicate dissolution releases Ca and Si to solution in an approximately 2:1 ratio (Hobson et al., 2017), the much higher initial Ca/Si ratios in solution (between 13 and 20) indicates that free lime dissolution was most likely to be the predominant source of rapidly leached alkalinity in these tests.

In the 2 days after the initial release of alkalinity, Ca and Si to solution, the pH reduced to 8.9 contemporaneously with rapid Ca and Si removal. The decrease in pH and Ca concentrations coincides with the appearance of calcite peaks in the XRD plots after 1 hour (Fig. 5.1) indicating that the initial spike in pH was buffered down to 8.9 due to in-gassing of atmospheric CO_2 and the subsequent precipitation of $CaCO_3$, which consumes both OH^- and Ca^{2+} ions (Eqn. 5-4). The contemporaneous decrease in Si concentrations may be evidence of the formation of a calcium silicate hydrate phase (Ca-Si-H). Indeed, low Ca/Si ratio (< 1) Ca-Si-H phases are predicted to form under the observed initial pH and Ca concentrations on a timescale of 24 – 48 hours (Walker et al., 2016). The peaks associated with dicalcium silicate (larnite) in XRD patterns became less prominent over time and were ultimately absent by the end of the experiments, indicating continued dicalcium silicate dissolution beyond day 6. Despite this no further increase in Ca concentration was observed after 2 days, probably because most of the Ca released by dicalcium silicate dissolution was precipitated as $CaCO_3$ under aerated conditions (monohydrocalcite peaks became increasingly prominent in the XRD pattern over time). Si concentration increased to a maximum value between 2-6 days contemporaneously with a second observed peak in pH. There are only modest changes in Si concentrations observed after 6 days, suggesting that equilibrium with secondary Si-containing phases such as Ca-Si-H or amorphous SiO_2 (Langmuir, 1997, Costa et al., 2016, De Windt et al., 2011) was limiting Si concentrations in these experiments.

XRD analysis indicates that there was progressive loss of periclase from the solids over time, such that it was absent from the final XRD pattern. There were also small brucite peaks in the XRD patterns from all time points. Periclase hydrates in water to form brucite ($Mg(OH)_2$), which readily dissolves at pH values < 10.4 (Eqn. 5-2). No significant Mg release to solution was observed during the first 24 hours of leaching because brucite is relatively insoluble at the then prevailing high pH value that was imposed by CaO and

calcium silicate weathering. After the initial spike in the pH value on the first day, the solution pH was lower than the brucite equilibrium value, and the aqueous Mg concentration increased as brucite dissolved. As a result, periclase hydration and brucite dissolution provided an additional source of alkalinity to the system. Dissolution of brucite leads to a switch in solution chemistry from a Ca to an Mg dominated system. Monohydrocalcite was observed in XRD patterns after day 6, after which it becomes the dominant carbonate phase, demonstrating a switch from calcite formation in the Mg-free early part of the experiments to predominately monohydrocalcite formation in the Mg-dominated system present after day 6. Recent studies have shown that an Mg-rich environment, such as that observed after 5 days, may support the precipitation of monohydrocalcite ($CaCO_3 \cdot H_2O$) into which Mg may be incorporated (Rodriguez-Blanco et al., 2014). At later time points dolomite ($CaMg(CO_3)_2$) was detected in XRD analysis, which may also form due to the high Mg concentrations suppressing calcite or aragonite formation during recrystallisation of monohydrocalcite (Rodriguez-Blanco et al., 2014).

5.4.4   *Leaching behaviour under air-excluded conditions*

After 1 hr the pH value and the Ca and Si concentrations were very similar to those observed in the aerated experiments, indicating similar processes were occurring (i.e. rapid dissolution of free lime and fine grained dicalcium silicate particles). As a saturated $Ca(OH)_2$ solution will reach a pH of ~12.5 (Eqn. 5-1) and experimental pH values were between 11 and 12 at all-time points, it suggests that the magnitude of the initial rise in pH was mass limited (i.e. controlled by the amounts of CaO and reactive dicalcium silicate that are readily available for dissolution) rather than $Ca(OH)_2$ solubility limited. Between the first sampling point and day 5 there was a slow increase in pH, Ca and Si which was probably the result of continued dicalcium silicate dissolution.

Between day 5 and 10 in the air-excluded experiments there was a decrease in Ca concentrations that coincided with a decrease in Si concentrations, which suggests that a Ca-Si-H phase formed. The pH, Ca and Si concentrations present at the time of formation in the leaching experiments were consistent with precipitation of a Ca-Si-H phase with Ca/Si ratio of close to 1 (Walker et al., 2016). The continuing slow rise in pH, Ca and Si concentrations during the remainder of the experiment indicate that under air-excluded conditions, the solution composition slowly evolves towards dicalcium silicate solubility limits over time (also observed by De Windt et al. (2011)). However, Ca-Si-H gel formation can cover particle surfaces, making alkalinity generation a diffusion-limited process (Hobson et al., 2017, Costa et al., 2016, Nikolić et al., 2016), slowing the dissolution of the remaining reactive solid phases, and leading to the incomplete dissolution of larnite (dicalcium silicate) observed at the end of these experiments (Fig. 5.1b). No Mg was released to solution under air-excluded conditions because the pH remained above 10.4 throughout the experiments, and therefore, dissolution of the Mg containing phases was inhibited.

5.4.5   Control of trace metal release

Fe can be released to solution during dissolution of both free lime and dicalcium silicate (in which it can be a minor constituent; Hobson et al. (2017)), and therefore Fe is present in the leachate throughout the air-excluded experiments (the slightly lower Fe concentrations after 5 days under air-excluded conditions may be due in part to incorporation of some Fe into Ca-Si-H phases). Conversely, under aerated conditions Fe is only present in significant concentrations during the first 3 days during which time the leachate pH falls from 11.5 to 9. Under aerated conditions, any Fe(II) released is likely to be readily oxidised to Fe(III) and precipitated either as an insoluble hydroxide or

incorporated into spinel-like secondary phases (e.g. magnetite, Fe_3O_4: De Windt et al. (2011)) at pH 9, limiting Fe accumulation in solution.

Vanadium release in the air-excluded experiments is low (maximum of ~0.007 mmol L^{-1}) compared to that observed in the aerated experiments (maximum of ~0.065 mmol L^{-1}). Previous work on BOF slag weathering suggests that it is V^{5+} associated with dicalcium silicate which is most readily leached to solution (Hobson et al., 2017), which is present in high pH solution as the vanadate oxyanion (VO_4^{3-}; Wehrli and Stumm (1989)). Thus, V concentrations observed during BOF slag leaching are likely to be controlled by $Ca_3(VO_4)_2$ solubility limits (K_{sp} = $10^{-17.97}$; Huijgen and Comans (2006), Cornelis et al. (2008), Allison et al. (1991)) which impose an inverse relationship between Ca and V concentrations in the leachate (Fig. 5.5).

$$3Ca^{2+} + 2VO_4^{3-} \rightleftharpoons Ca_3(VO_4)_2 \qquad \text{(Eqn. 5-6)}$$

Under air-excluded conditions (i.e. saturated, see Chapter 1, Fig. 1.1) Ca released from CaO and dicalcium silicate weathering accumulated in solution, producing a leachate with high Ca concentrations. The leachate solution, therefore, quickly reached $Ca_3(VO_4)_2$ solubility limits, which precipitated, preventing further release of V to solution thus limiting V concentrations in the leachate.

Aerated conditions (i.e. unsaturated), however, allow in-gassing of atmospheric CO_2 and associated formation of secondary carbonate minerals. This process provides a sink for Ca, lowering aqueous Ca concentrations. The V that is released therefore persists in solution (due to the lower $[Ca^{2+}].[VO_4^{3-}]$ ion activity product), leading to much higher concentrations than those seen under air-excluded conditions. Monohydrocalcite is relatively soluble (Ksp = 1 x $10^{-7.1}$; Kralj and Brečević (1995)), therefore, the relevant

equilibrium phase limiting Ca concentrations in these experiments is probably dolomite (CaMg(CO₃)₂; Ksp = 1 x 10⁻¹⁷·², Sherman and Barak (2000)). Indeed, the predicted Ca concentration in solutions equilibrated with dolomite and atmospheric pCO₂ are similar to those found at the end of these experiments (Fig 5.5; Langmuir, (1997)). In the aerated experiments, the overall leachate chemistry remains undersaturated with respect to Ca₃(VO₄)₂, which is consistent with the observed depletion of the V-hosting dicalcium silicate phase by the end of the aerated experiments.
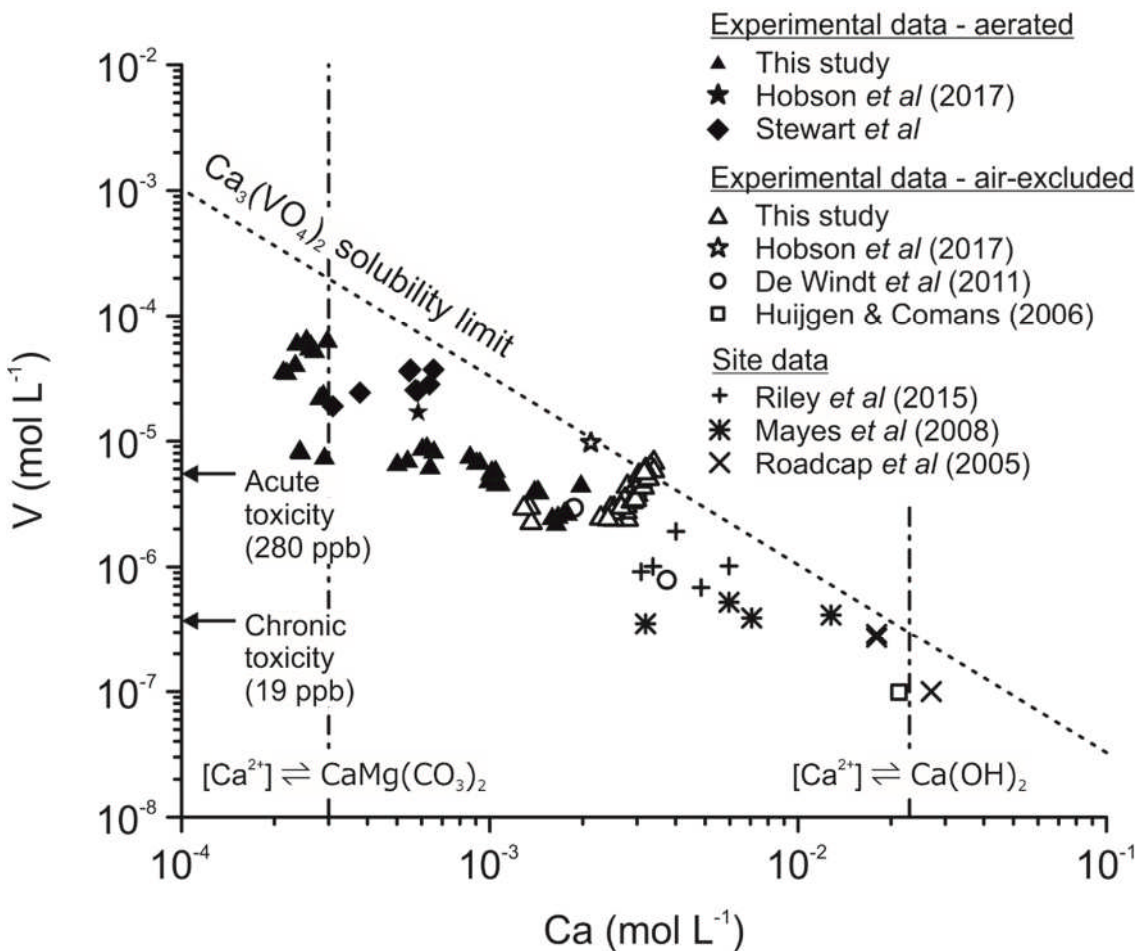
Figure 5.5 - Plot of [V] versus [Ca] for selected experimental and site data (site data from Riley and Mayes (2015), Roadcap et al. (2005), Mayes et al. (2008)). The dashed line marks the solubility limits for Ca₃(VO₄)₂ at 20 °C (Allison et al., 1991). Data plotting below the solubility limit is undersaturated with respect to that phase. Vertical dashed lines indicate [Ca] in solutions in equilibrium with dolomite in contact with atmospheric CO₂, or with Ca(OH)₂, respectively (both at 20 °C). Horizontal arrows indicate acute and chronic freshwater toxicity guideline limits (Buchman, 2008) (after Hobson et al. (2017)).

5.4.6   Implications for waste management

Co-disposed wastes such as those used in this study are unattractive for reuse in furnaces due to their highly variable composition making it difficult to control the steelmaking processes. Furthermore, the presence of MgO makes their reuse in civil engineering applications difficult, since periclase hydration to form brucite leads to significant volumetric expansion and cracking. Given these problematic characteristics, combined steelmaking wastes are generally stored in landfill.

Over time, rainwater inevitably infiltrates and reacts with landfilled waste to generate leachate. Therefore, the storage environment plays a key role in establishing leachate composition. Under air-excluded conditions, the leaching profile of the combined waste is similar to that of BOF slag (Hobson et al., 2017, De Windt et al., 2011, Huijgen and Comans, 2006, Costa et al., 2016). Rapid dissolution of Ca-bearing phases without in-gassing of CO_2 leads to a high pH, $Ca(OH)_2$ dominated leachate. High Ca concentrations limit V release due to $Ca_3(VO_4)_2$ solubility limits. Consequently, water saturated environments with limited opportunity for CO_2 ingress will provide the safest environment for waste storage. Leachate could either be recirculated (and reach equilibrium with $Ca(OH)_2$) or be removed and treated off site to lower pH and allow carbonation without triggering V release (Gomes et al., 2017). Under aerated conditions, lower alkalinity and Ca concentrations allow much higher V concentrations to accumulate in leachate, as well as allowing dissolution of MgO to form a $Mg(OH)_2$ dominated leachate which favours the formation of monohydrocalcite and dolomite as secondary carbonate phases. Leaching under aerated conditions rapidly produces leachate with V concentrations in excess of acute toxicity thresholds (280 ppb; Fig 5.5) and all experiments display V concentrations higher than chronic toxicity thresholds (Buchman, 2008). Whilst formation of $CaCO_3$/Ca-Si-H weathering rinds may eventually limit V release under aerated conditions, damage to either these or the blocks themselves would expose fresh

surfaces and lead to more weathering and V release. Therefore, leachate generated under these circumstances would require careful management to avoid the potential for environmental harm.

Extrapolating from experimental results to field scale predictions must always be done with caution. For example, these experiments were performed on crushed powder samples at much lower solid to liquid ratios than would typically be found in a heap leaching scenario. It is much more likely that during heap leaching (due to high solid : solution ratios present) free lime and dicalcium silicate dissolution will control leachate quality resulting in higher Ca concentrations (i.e. leachate saturated with respect to $Ca(OH)_2$) and therefore lower V concentrations compared to those seen in experimental systems (indeed most real site leachates commonly contain V at order of magnitude lower concentrations than found in laboratory experiments; Fig 5.5). However, the experimental results indicate that as waste carbonation progresses with time, leachate composition evolves to conditions which might promote the accumulation of higher V concentrations in leachates against the overall trend of decreasing conductivity and alkalinity.

5.5   Conclusions

The co-disposed waste investigated in this study was composed of BOF steelmaking slag containing dicalcium silicate, wüstite, dicalcium aluminoferrite and free lime; and refractory oxides comprising corundum, periclase, graphite and high temperature aluminosilicate. V was predominately associated with the dicalcium silicate and dicalcium aluminoferrite phases. During leaching, alkalinity was produced by dissolution of free lime and dicalcium silicate. Under air-excluded conditions high Ca concentrations and the inverse relationship between Ca and V concentrations imposed by $Ca_3(VO_4)_2$ solubility limits restricted V release to the leachate. Under aerated conditions in-gassing of CO_2

promoted carbonation reactions and secondary carbonate formation. Leachate pH and Ca concentrations were reduced and MgO hydration and dissolution was promoted leading to a switch from a Ca to an Mg dominated leachate and precipitation of monohydrocalcite and dolomite. V concentrations in leachate were higher under aerated conditions where formation of carbonate minerals provides a sink for aqueous Ca following in-gassing of CO_2. Under these conditions, the inverse relationship imposed by $Ca_3(VO_4)_2$ solubility limits allows higher concentrations of V to accumulate in leachate than those seen under air-excluded conditions. Therefore, when considering long-term leaching behaviour, it is important that risk assessments consider the expected *in situ* environmental chemistry of specific waste storage environments.

5.6 References

ALLISON, J. D., BROWN, D. S. & NOVO-GRADAC, K. J. 1991. MINTEQA2/PRODEFA2, a geochemical assessment model for environmental systems: version 3.0 user's manual, Environmental Research Laboratory, Office of Research and Development, US Environmental Protection Agency.

BARCELOUX, D.G., 1999. Vanadium. Journal of toxicology. Clinical toxicology 37, 265-278.

BAYLESS, E. R. & SCHULZ, M. S. 2003. Mineral precipitation and dissolution at two slag-disposal sites in northwestern Indiana, USA. Environmental Geology, 45, 252-261.

BUCHMAN, M. F. 2008. NOAA Screening Quick Reference Tables.

CHAURAND, P., ROSE, J., DOMAS, J. & BOTTERO, J. Y. 2006. Speciation of Cr and V within BOF steel slag reused in road constructions. Journal of Geochemical Exploration, 88, 10-14.

CHESTERS, J. H. 1973. Refractories: production and properties, Iron and Steel Institute.

CORNELIS, G., JOHNSON, C. A., GERVEN, T. V. & VANDECASTEELE, C. 2008. Leaching mechanisms of oxyanionic metalloid and metal species in alkaline solid wastes: A review. Applied Geochemistry, 23, 955-976.

COSTA, G., POLETTINI, A., POMI, R. & STRAMAZZO, A. 2016. Leaching modelling of slurry-phase carbonated steel slag. Journal of Hazardous Materials, 302, 415-425.

DANA, K. & DAS, S. K. 2004. Partial substitution of feldspar by B.F. slag in triaxial porcelain: Phase and microstructural evolution. Journal of the European Ceramic Society, 24, 3833-3839.

DE SA, R. G., E SILVA, G. L. & BITTTENCOURT, L. 2007. Recycling of spent refractories from metallurgical processing management and technological approach. 8th UNITECR, Dresden, Alemania.

DE WINDT, L., CHAURAND, P. & ROSE, J. 2011. Kinetics of steel slag leaching: Batch tests and modeling. Waste Management, 31, 225-235.

ELONEVA, S., PUHELOINEN, E.-M., KANERVA, J., EKROOS, A., ZEVENHOVEN, R. & FOGELHOLM, C.-J. 2010. Co-utilisation of CO2 and steelmaking slags for production of pure CaCO3 – legislative issues. Journal of Cleaner Production, 18, 1833-1839.

ENVIRONMENT AGENCY 2014. EA Bespoke permit 2014 Permit for Scunthorpe Aggregate processing. Permit number EPR/LP3537VV/A001.

GEISELER, J. 1996. Use of steelworks slag in Europe. Waste Management, 16**,** 59-63.

GOMES, H. I., ROGERSON, M., BURKE, I. T., STEWART, D. I. & MAYES, W. M. 2017. Hydraulic and biotic impacts on neutralisation of high-pH waters. Science of The Total Environment, 601–602**,** 1271-1279.

HANAGIRI, S., MATSUI, T., SHIMPO, A., ASO, S., INUZUKA, T., MATSUDA, T., SAKAKI, S. & NAKAGAWA, H. 2008. Recent improvement of recycling technology for refractories. Shinnittetsu Giho, 388**,** 93.

HOBSON, A. J., STEWART, D. I., BRAY, A. W., MORTIMER, R. J. G., MAYES, W. M., ROGERSON, M. & BURKE, I. T. 2017. Mechanism of Vanadium Leaching During Surface Weathering of Basic Oxygen Furnace Steel Slag Blocks: A μXANES and SEM Study. Environmental Science & Technology.

HUIJGEN, W. J. J. & COMANS, R. N. J. 2006. Carbonation of steel slag for CO2 sequestration: Leaching of products and reaction mechanisms. Environmental Science and Technology, 40**,** 2790-2796.

KRALJ, D. & BREČEVIĆ, L. 1995. Dissolution kinetics and solubility of calcium carbonate monohydrate. Colloids and Surfaces A: Physicochemical and Engineering Aspects, 96**,** 287-293.

KWONG, K. & BENNETT, J. 2002. Recycling Practices of Spent MgO-C Refractories. Journal of Minerals and Materials Characterization and Engineering, 1**,** 69-78.

LANGMUIR, D. 1997. Aqueous Environmental Geochemistry, Prentice Hall.

MATERN, K., RENNERT, T. & MANSFELDT, T. 2013. Molybdate adsorption from steel slag eluates by subsoils. Chemosphere, 93**,** 2108-2115.

MAYES, W. M. & YOUNGER, P. L. 2006. Buffering of Alkaline Steel Slag Leachate across a Natural Wetland. Environmental Science & Technology, 40**,** 1237-1243.

MAYES, W. M., YOUNGER, P. L. & AUMONIER, J. 2008. Hydrogeochemistry of alkaline steel slag leachates in the UK. Water Air and Soil Pollution, 195**,** 35-50.

MAZDIYASNI, K. S. & BROWN, L. M. 1972. Synthesis and Mechanical Properties of Stoichiometric Aluminum Silicate (Mullite). Journal of the American Ceramic Society, 55**,** 548-552.

NAVARRO, C., DIAZ, M. & VILLA-GARCIA, M. A. 2010. Physico-Chemical Characterization of Steel Slag. Study of its Behavior under Simulated Environmental Conditions. Environmental Science & Technology, 44, 5383-5388.

NIKOLIĆ, I., DRINČIĆ, A., DJUROVIĆ, D., KARANOVIĆ, L., RADMILOVIĆ, V. V. & RADMILOVIĆ, V. R. 2016. Kinetics of electric arc furnace slag leaching in alkaline solutions. Construction and Building Materials, 108, 1-9.

OBER, J. A. 2017. Mineral commodity summaries 2017. Mineral Commodity Summaries. Reston, VA.

PIATAK, N. M., PARSONS, M. B. & SEAL, R. R. 2014. Characteristics and environmental aspects of slag: A review. Applied Geochemistry.

POURBAIX, M. 1966. Atlas of electrochemical equilibria in aqueous solutions, Pergamon Press.

PROCTOR, D. M., FEHLING, K. A., SHAY, E. C., WITTENBORN, J. L., GREEN, J. J., AVENT, C., BIGHAM, R. D., CONNOLLY, M., LEE, B., SHEPKER, T. O. & ZAK, M. A. 2000. Physical and chemical characteristics of blast furnace, basic oxygen furnace, and electric arc furnace steel industry slags. Environmental Science & Technology, 34, 1576-1582.

QUARANTA, N. E., CALIGARIS, M. G. & DÍAZ, O. Characterization of Converter Refractories for Recycling. Materials Science Forum, 2014. Trans Tech Publ, 605-610.

RILEY, A. L. & MAYES, W. M. 2015. Long-term evolution of highly alkaline steel slag drainage waters. Environ Monit Assess, 187, 463.

ROADCAP, G. S., KELLY, W. R. & BETHKE, C. M. 2005. Geochemistry of extremely alkaline (pH > 12) ground water in slag-fill aquifers. Ground Water, 43, 806-816.

RODRIGUEZ-BLANCO, J. D., SHAW, S., BOTS, P., RONCAL-HERRERO, T. & BENNING, L. G. 2014. The role of Mg in the crystallization of monohydrocalcite. Geochimica et Cosmochimica Acta, 127, 204-220.

ROVNUSHKIN, V. A., VISLOGUZOVA, E. A., SPIRIN, S. A., SHEKHOVTSOV, E. V., KROMM, V. V. & METELKIN, A. A. 2005. Composition of Ladle Slag and Refractory Materials and Its Effect on the Wear Resistance of the Lining of an RH Vacuum Degasser. Refractories and Industrial Ceramics, 46, 193-196.

SCHNEIDER, H., OKADA, K. & PASK, J. A. 1994. Mullite and mullite ceramics, J. Wiley.

SHERMAN, L. A. & BARAK, P. 2000. Solubility and Dissolution Kinetics of Dolomite in Ca–Mg–HCO3/CO3 Solutions at 25°C and 0.1 MPa Carbon Dioxide. Soil Science Society of America Journal, 64, 1959-1968.

SHI, C. 2002. Characteristics and cementitious properties of ladle slag fines from steel production. Cement and Concrete Research, 32, 459-462.

SHI, H., ZHAO, Y. & LI, W. 2002. Effects of temperature on the hydration characteristics of free lime. Cement and Concrete Research, 32, 789-793.

TAMARI, N., KONDOH, I., TANAKA, T. & KATSUKI, H. 1993. Mechanical Properties of Alumina-Mullite Whisker Composites. Journal of the Ceramic Society of Japan, 101, 721-724.

TAYLOR, H. F. W. 1986. Proposed Structure for Calcium Silicate Hydrate Gel. Journal of the American Ceramic Society, 69, 464-467.

TOSSAVAINEN, M., ENGSTROM, F., YANG, Q., MENAD, N., LIDSTROM LARSSON, M. & BJORKMAN, B. 2007. Characteristics of steel slag under different cooling conditions. Waste Management, 27, 1335-1344.

WALKER, C. S., SUTOU, S., ODA, C., MIHARA, M. & HONDA, A. 2016. Calcium silicate hydrate (C-S-H) gel solubility data and a discrete solid phase model at 25°C based on two binary non-ideal solid solutions. Cement and Concrete Research, 79, 1-30.

WEHRLI, B. & STUMM, W. 1989. Vanadyl in natural-waters - adsorption and hydrolysis promote oxygenation. Geochimica Et Cosmochimica Acta, 53, 69-77.

YI, H., XU, G., CHENG, H., WANG, J., WAN, Y. & CHEN, H. 2012. An Overview of Utilization of Steel Slag. Procedia Environmental Sciences, 16, 791-801.

YILDIRIM, I. Z. & PREZZI, M. 2011. Chemical, Mineralogical, and Morphological Properties of Steel Slag. Advances in Civil Engineering, 2011, 1-13.

ZHAO, L., LI, Y., ZHOU, Y. & CANG, D. 2014. Preparation of novel ceramics with high CaO content from steel slag. Materials & Design, 64, 608-613.

Chapter 6   Behaviour and fate of vanadium during the aerobic neutralisation of hyperalkaline steel slag leachate

Summary

Steel slag is the primary byproduct of steelmaking which was historically dumped in open air slag heaps. Weathering of dumped steel slag can have deleterious effects on local watercourses through generation of high pH leachate (9 – 12.5), rapid carbonation (leading to smothering of benthic communities) and transport of potentially toxic trace metals such as V. Field observations of a heavily impacted stream draining a legacy slag heap revealed removal of V from leachates downstream which was contemporaneous with a fall in pH, Ca, Al and Fe concentrations. Aerated leachate neutralisation experiments, where the leachates were exposed to CO_2 present in air, led to a reduction in pH from 12 $\rightarrow$ 8. Limited quantities of V were incorporated into the neo-formed $CaCO_3$ precipitate and the presence of kaolinite clay (i.e. SiOH and AlOH surfaces) during neutralisation had no measureable effect on V uptake at alkaline – circumneutral pH. XANES analysis showed that V was present in the precipitates recovered after neutralisation as adsorbed or incorporated V^{5+} indicating its likely presence in leachates as the vanadate oxyanion (VO_4^{3-}). TEM analysis showed that nano-scale particles of 2-line ferrihydrite also formed in the neutralised leachates potentially providing an additional sorption surface for V uptake. Indeed, removal of V from leachates was significantly enhanced by the addition of goethite (i.e. FeOOH surfaces) to experiments. EXAFS analysis of goethite samples recovered from neutralisation experiments showed VO_4^{3-} adsorption to goethite by the formation of strong inner-sphere complexes, facilitating V removal from solution at pH <10. Results show that although carbonate formation leads to some V removal from leachates during leachate neutralisation, the presence of both naturally occurring and neo-

formed Fe (oxy)hydroxides provide a potent sink for V in steel slag leachates, preventing the spread of V in the environment.

6.1   Introduction

Steel slag is a byproduct formed during steelmaking when limestone or dolomite is added to the furnace as a fluxing agent to draw out impurities from the molten metal. Steel slag production is approximately $10 - 15\%$ of crude steel production (Proctor et al., 2000; Van Oss, 2016), which is increasing year on year worldwide (production in 2016 estimated at $160 - 240$ million tonnes; Ober (2017)). A range of potential after uses for steel slag exist, primarily as aggregate in civil engineering applications, however, supply frequently exceeds demand, so 25-50% of current steel slag production is stored in landfill (Euroslag, 2012; Van Oss, 2016; Yi et al., 2012). Furthermore, numerous legacy slag heaps exist which pre-date modern environmental legislation and consequently have the potential to impact local watercourses.

The major element chemistry of steel slag is dominated by Ca, Fe and Si, with lesser amounts of Mg, Mn and Al (Hobson et al., 2017; Shen et al., 2009; Tossavainen et al., 2007; Yildirim and Prezzi, 2011). It has complex mineralogy but usually comprises Ca-silicates (e.g. larnite, β-Ca_2SiO_4), Ca-Fe-Al-oxides (e.g. brownmillerite, Ca_2FeAlO_5), free lime (CaO) and refractory oxides (frequently as a solid solution containing Fe, Mg, Mn and Ca) (Geiseler, 1996; Hobson et al., 2017; Piatak et al., 2014; Roadcap et al., 2005). During weathering, hydration and dissolution of Ca oxides and silicates rapidly generates a high pH leachate (typically pH $11.5 - 12.5$; eqns. 6-1 & 6-2) dominated by compositions in equilibrium with $Ca(OH)_2$:

$$CaO + H_2O \rightarrow Ca^{2+} + 2OH^-$$
(Eqn. 6-1)

$$Ca_2SiO_4 + 2H_2O \rightarrow 2Ca^{2+} + H_2SiO_4^{2-} + 2OH^-$$
(Eqn. 6-2)
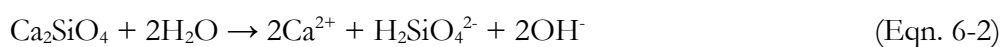
This produces a highly alkaline leachate with high Ca^{2+} concentrations. Therefore, ingress of atmospheric CO_2 to the system leads to the leachate immediately becoming supersaturated with respect to $CaCO_3$ (e.g. $SI_{calcite}$ values $= +1.4 - +2.8$ have been determined across a number of locations where leachates emerged to atmosphere at UK legacy sites; Mayes et al. (2008)). Since heterogeneous precipitation of $CaCO_3$ onto existing solid surfaces readily occurs when $SI > +0.3$ and homogenous precipitation occurs when $SI > +1.5$ (Boylan et al., 2016; Ford and Williams, 1989), in-gassing of atmospheric CO_2 into steel slag leachate leads to rapid precipitation of $CaCO_3$ (Eqn. 6-3):

$$Ca^{2+} + CO_2 + 2OH^- \rightarrow CaCO_3 + H_2O \qquad \text{(Eqn. 6-3)}$$

This reaction consumes OH^- ions leading to a progressive fall in pH contemporaneous with precipitation of Ca downstream of the leachate source. The rate of Ca precipitation generally varies proportionally with leachate aeration (Gomes et al., 2017; Mayes et al., 2008) but is also affected by mixing with carbonate alkalinity present in surface waters. Where both are high, $CaCO_3$ deposition rates up to 100 g day^{-1} m^{-2} have been estimated (Mayes et al., 2008).

A significant ecological impact form leachates has been observed at legacy sites, where a decrease in biological diversity has been observed as pH and metal loadings increase closer to the leachate source (Hull et al., 2014; Koryak et al., 2002). Ecological stressors associated with steel slag leachate include the high pH itself, with pH values over 10.5 being considered toxic to aquatic organisms (Wilkie and Wood, 1996). In addition, rapid precipitation of $CaCO_3$ forms hardpans that can smother benthic ecosystems and prevent light from reaching primary producers (Effler, 1987; Fjellheim and Raddum, 1995). Furthermore, steel slag is often enriched in potentially toxic metals (Chaurand et al.,

2007a; Proctor et al., 2000; Roadcap et al., 2005) and a large range of potentially problematic trace metals have been reported to be present in alkaline steel slag leachates including Al, Fe, As, Pb, Mn, Mo, and V (Hull et al., 2014; Roadcap et al., 2005). V is of particular concern due to its toxicity relative to other mobile metals and high concentrations in slags (0.04 – 1.48 wt%, Proctor et al. (2000); Tossavainen et al. (2007)). Although much of the V present in BOF slag is incorporated into relatively unreactive dicalcium aluminoferrite phases (Chaurand et al., 2007a; Hobson et al., 2017), significant concentrations of V are also found as V^{5+} in dicalcium silicate phases (e.g. larnite; Hobson et al., (2017)). Hydration and dissolution of dicalcium silicate (Eqn. 6-2) can therefore result in V release to solution. V^{5+} is very soluble as the vanadate ion (Wehrli and Stumm, 1989), which at high pH interacts poorly with mineral surfaces, thus enabling its release to the wider environment.

Long term monitoring of steel slag leachate shows a general decline in both pH and Ca concentrations over time as available CaO and Ca-silicate phases are depleted and weathering rinds comprising Ca-Si-H and carbonate minerals are formed (Costa et al., 2016; Riley and Mayes, 2015). It has been observed that the high pH, Ca-dominated leachate formed during the early stages of slag weathering inhibits V release due to the inverse relationship between Ca and V concentrations imposed by Ca-Vanadate solubility limits (Cornelis et al., 2008; De Windt et al., 2011; Hobson et al., 2017; Huijgen and Comans, 2006). However, when Ca concentrations are reduced, V concentrations can significantly increase in leachates (see Chapters 4 and 5). Therefore a decline in pH and Ca concentrations over time may not necessarily lead to a corresponding fall in V concentrations and may in fact allow higher concentrations of V to accumulate in leachate.

Currently there is little information available concerning the behaviour and fate of leached V in the environment affected by steel slag leachates. The difficulty inherent in predicting its leaching behaviour coupled with its potential toxicity and complex redox

chemistry have led to regulatory bodies (such as the UK Environment Agency) adopting highly precautionary approaches when dealing with disposal of steel slag (Environment Agency, 2014) which may lead to unnecessarily onerous monitoring requirements at landfill and legacy sites. Improving understanding of the behaviour of leached V will enable the environmental risks posed by legacy slag heaps to be fully assessed and assist in the implementation of effective remedial measures if required.

This study investigated the persistence of V in streams affected by steel slag leachate downstream of a legacy steel slag heap and determined the environmental behaviour of V during aerobic neutralisation of steel slag leachate in the presence of different mineral surfaces. Field observations of a stream affected by leachate from slag heaps at the former site of the Consett steelworks, Co. Durham were used to understand the range of processes occurring in natural watercourses. Laboratory experiments were then used to determine the mechanism of V removal occurring when both real and synthetic slag leachates were neutralised by ingress of atmospheric CO_2. To determine its fate in solids, V speciation and coordination environment was determined in precipitates recovered after neutralisation using a combination of X-ray absorption spectroscopy (XAS) and high resolution electron microscopy. Finally, these data were used to develop a conceptual model for V behaviour in rivers affected by hyperalkaline steel slag leachates.

6.2   Methods

6.2.1   Study site

Howden Burn drains the area beneath the northern part of the former Consett Iron and Steel Works located in the Hownsgill Valley, County Durham UK (source 54°51'12.9"N 1°51'41.1"W; Fig. 6.1. See Chapter 2, section 2.6.2 for site background).
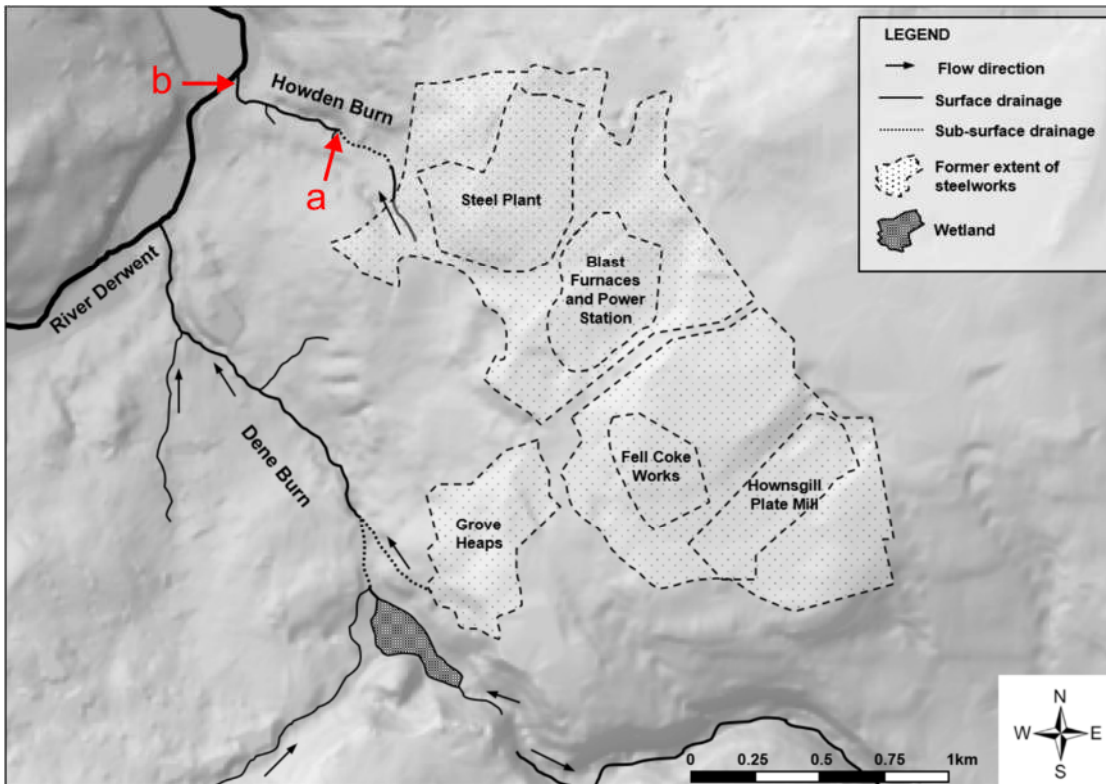
Figure 6.1 - Site plan for former Consett Iron and Steel Works showing drainage streams including Howden Burn. Red arrows represent a) maximum upstream field sampling locations and sampling point for leachate neutralisation experiments and b) maximum downstream field sampling locations (after Mayes et al. (2008) and Hull et al. (2014)).

Waters in Howden Burn are characterised by high pH values (9.0 – 12.5) and high Ca concentrations (median of 149 mg L^{-1} between 1978 and 2004, n = 86; Riley and Mayes (2015)) which decline downstream due to $CaCO_3$ precipitation. SI$_{calcite}$ values between 1.76 and 2.25 have been calculated corresponding to Ca deposition rates of between 14.0 and 48.2 g day^{-1} m^{-2}. In common with Ca, V concentrations are also reported to decline downstream (Mayes et al., 2008).

6.2.2   Howden Burn leachate and sediment sampling

Water samples were collected by the University of Hull on a total of 4 occasions from Howden Burn between November 2006 and May 2015. Leachate pH was measured

in-situ using a Myron L Ultrameter® calibrated using pH 12.4, 10, 7 and 4 buffer solutions. Samples were filtered (0.45 μm, cellulose – nitrate) and aqueous V concentrations were determined using a Perkin Elmer Elan DRCII inductively coupled plasma mass spectrometer (ICP-MS; detection limits 1 ppb) and all other elements were determined on a Perkin Elmer Optima 5300 inductively coupled plasma optical emission spectrometer (ICP-OES; detection limits 10 – 100 ppb).

Sediment samples ($n = 10$) were collected from the Howden Burn stream bed in September 2015. Sediments were dried overnight at 40 °C and sieved to remove the coarse (> 2 mm) size fraction. Representative samples were ground to < 150 μm and their V concentration determined using an Olympus X-5000 X-ray fluorescence (XRF) analyser.

6.2.3   *Leachate neutralisation experiments*

Leachate emerging from deposited steel making wastes was collected for use in neutralisation experiments from the source of Howden Burn in September 2015 (see Chapter 3, section 3.1.2; hereafter referred to as HB source water). BOF slag leachate was generated by leaching of two 2 x 2 x 1 cm blocks of BOF slag in 2L Milli-Q water over 6 months under air excluded conditions (block leachate) (Hobson et al., 2017). Synthetic leachate was made under air excluded conditions by diluting saturated $Ca(OH)_2$ by a factor of ten with nitrogen purged deionised water before adding an aliquot of 100 ppm $NaVO_3$ solution to achieve a final concentration of 2500 ppb V.

Leachate neutralisation experiments were established in triplicate 500 mL Erlenmeyer flasks that contained 200 mL of either HB source leachate, block leachate or synthetic leachate with:

1. No mineral surface (unamended),
2. 1.0 or 0.2 g L^{-1} α-FeOOH (goethite-amended) and

3.   1.0 or 0.2 g L^{-1} kaolinite (kaolinite-amended).

Excess kaolinite and goethite (relative to real stream concentrations) were added to ensure interactions with these minerals were not masked by effects of carbonation. Flasks were loosely capped to allow ingress of air and were shaken at 175 rpm on an orbital shaker. At 2 – 3 hour intervals (until leachate reached ~pH 8), 3 mL aliquots of slurry were removed and filtered (0.2 μm, PES). The pH of the filtrate was determined using an Orion DualStar pH/ISE benchtop meter (Thermo Scientific, USA) with electrodes that were calibrated daily using pH 4, 7 and 10 buffer solutions. Aqueous metal concentrations were determined from acidified filtrate (0.2 μm filtered; 0.1 M HNO$_3$) either on a Thermo iCAP 7400 radial ion-coupled plasma optical emission spectrometer (ICP-OES; major elements), or on a Thermo iCAP Qc ion-coupled plasma mass spectrometer (ICP-MS; minor elements).

Experiments were stopped following stabilisation of solution pH (24 – 65 hours after starting). Leachates were vacuum filtered (0.2 μm, polycarbonate). Residues were dried in an oven at 40 $^{\circ}$C prior to further analysis described below.

6.2.4   *Transmission electron microscopy (TEM) analysis*

Approximately 10 mg dried solid residue from the HB source leachate experiment was suspended in ethanol, placed on a Cu support grid with holey carbon support film and air dried prior to analysis. The specimen was examined using an FEI Tecnai TF20: FEGTEM Field emission gun TEM/STEM fitted with HAADF detector, Oxford Instruments INCA 350 EDX system/80 mm X-Max SDD detector and Gatan Orius SC600A CCD camera using AZtec data acquisition software.

6.2.5   XAS

XAS spectra were collected from solid residues recovered from leachate neutralisation experiments at the V K-edge (5465 eV) on beamline I18, Diamond Light Source, UK in February 2016. Spectra were also collected from a range of V-containing laboratory chemicals and an aqueous vanadate solution (1000 ppm). Kaolinite and goethite V sorption standards were prepared by adding 20 mL 100 ppm $NaVO_3$ dropwise over 20 minutes to 0.2 g goethite or kaolinite suspended in 2 L Milli-Q DIW to achieve a sorbed V concentration of ~1 wt %. Solution pH was maintained at pH 8 by adding 0.1 M HCl or 0.1 M NaOH as required. Once all $NaVO_3$ had been added the suspension was left overnight prior to vacuum filtering at 0.2 μm. The residue was dried in an oven at 40 ºC for 24 hours. All solid samples were analysed as pressed pellets (diluted with cellulose as required) and held in Kapton™ tape. Multiple spectra were averaged to improve signal to noise ratio, normalised and plotted in the XANES data region (-50 – 100 eV) using Athena v0.9.24 (Ravel and Newville (2005); see Chapter 4, section 4.2.4 for detailed methodology). For selected samples (with sufficiently high V concentrations) V K-edge EXAFS data was also collected and fit to molecular coordination models using Artemis v0.9.24 using reduced chi-squared and R values as measures of goodness of fit.

6.3   Results

6.3.1   Howden Burn leachate

Average composition of groundwater emerging at the Howden Burn source is shown in Table 6.1. When normalised to allow for variation in source concentrations over time, the Ca, V, Fe, and Al concentrations showed distinct declining trends downstream from the Howden Burn (Fig. 6.2). V concentrations declined from 37 ±14 ppb at the source to 24

±8 close to the junction with the River Derwent. Ca and Fe concentrations fell from 104 ±31 ppm and 58 ±8 ppb, to 79 ±22 and 33 ±14 over the same distance. Al had an initial concentration of 129 ±39 ppb and was completely removed from solution by a point 400 m downstream from the source. Si and K showed little variation decreasing only slightly from 1300 ±340 ppb and 127 ±57 ppm to 1280 ±480 and 123 ±60 respectively. pH was generally high but fell from 11.9 ±0.5 to 11.01 ±0.9 before the River Derwent was reached.

Table 6.1 - Aqueous composition of all site waters and leachates used in neutralisation experiments.

	HB source (average of all site data)	HB source (sample used in experiments)	Block (BL)	Synthetic (SL) (average)
pH	11.9 ±0.5	11.9	11.9	12.0 ±0.1
Major ions (ppm)				
Ca	104 ±31	194	85.2	79.0
Si	1.3 ±0.3	2.5	29.5	
Mg	0.6 ±0.3	< LOD	0.1	
K	127 ±57	149	0.4	
Na	33 ±8	99	2.4	
Minor ions (ppb)				
Al	129 ±39	< LOD	390	
Cr	5 ±2	7	10	
Fe	58 ±8	166	251	
Li	448 ±175	709	<0.1	
Mn	15 ±3	39	13	
V	37 ±14	35	493	2495

V concentrations in stream sediments ranged from 12.7 – 48.0 ppm. The mean concentration was 34.3 ppm and standard deviation was 10.6.
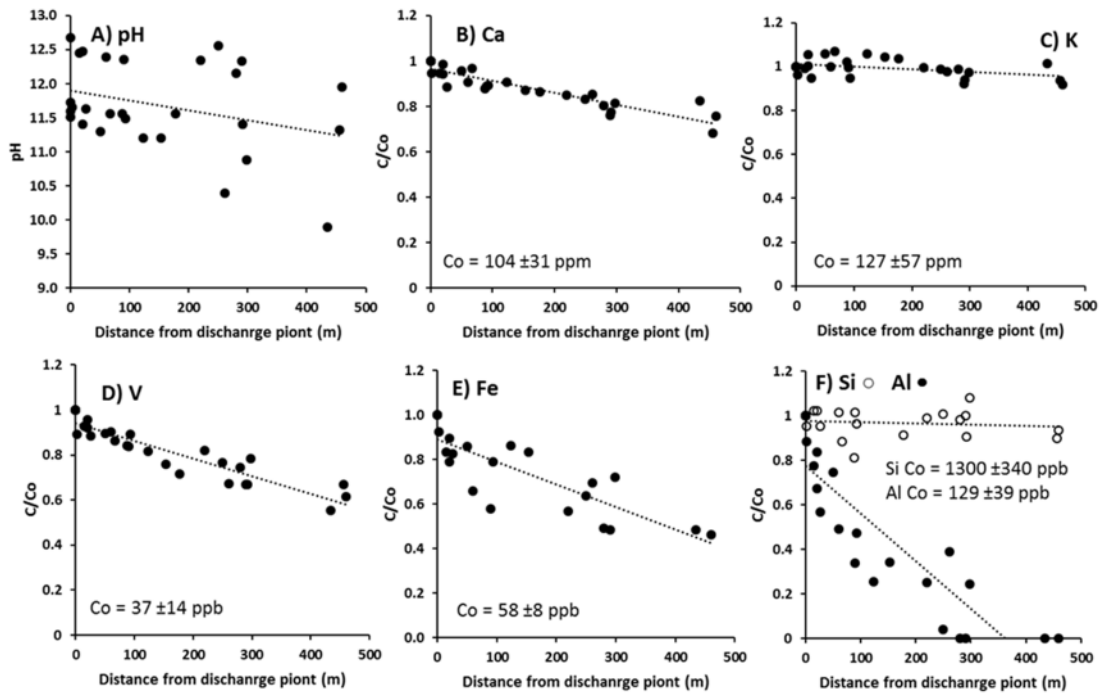
Figure 6.2 - Relative changes in pH and selected elements concentrations in Howden Burn, Consett, UK, for water samples (filtered at 0.45 μm) collected downstream from a culvert feed by groundwater in contact with mixed iron and steel slags. Data from Mayes et al., (2008); Riley and Mayes, (2015). Dashed best fit lines are added to guide the eye.

6.3.2   Leachate neutralisation

The composition of each leachate type used during neutralisation experiments is shown in Table 6.1. In all leachate systems, pH was buffered down to final values between pH 7.5 and 8.5 (Fig. 6.3). Mineral-amended HB source water took 10 hours to reach a final pH of 7.5, however, unamended HB source water took 20 hours to reach the same final pH. Block leachate took 30 hours to equilibrate under all three conditions. Unamended synthetic leachate took 45 hours to equilibrate and both mineral-amended synthetic leachate systems took ~55 hours to equilibrate.
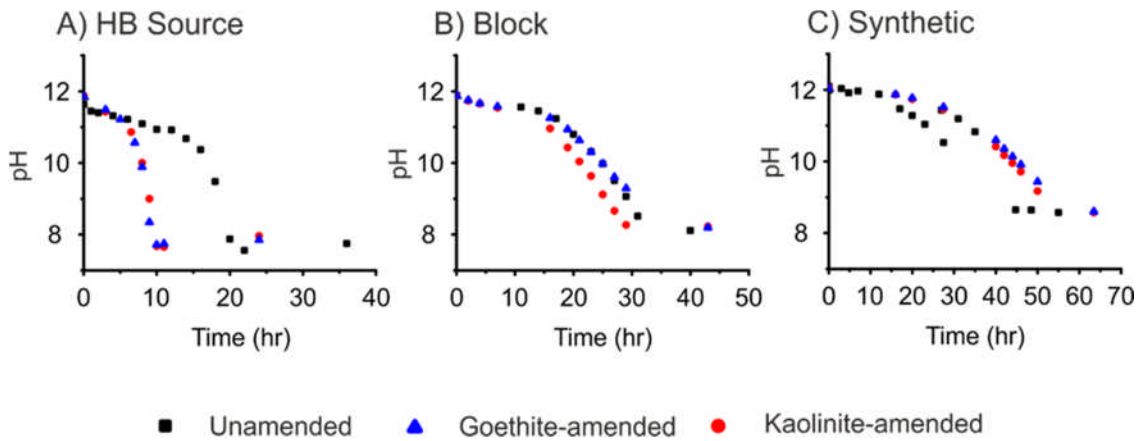
Figure 6.3 - pH measurements over time during neutralisation of steel slag leachate. Initial conditions in goethite and kaolinite-amended systems: A) 1.0 g L^{-1} goethite/kaolinite; B) and C) 0.2 g L^{-1} goethite/kaolinite. Data points represent mean values from triplicate measurements.

Ca and V concentrations all decreased during leachate neutralisation (Fig. 6.4). Ca removal was broadly comparable in the unamended, goethite-amended and kaolinite-amended systems for all three leachate types, with rapid removal as the pH fell from 12 to 11 followed by a slower removal thereafter. Total Ca removals in all HB source water and block leachate systems were 195 to 120 ppm and 90 to 15 ppm respectively. All synthetic leachate systems showed complete removal of Ca during the initial drop to pH 11.5 followed by a slight increase in concentration below pH 9. Similar increases at final pH (when the pH ≤ 8.5) were seen in both the HB source water and block leachate systems.

V was removed from solution in all neutralisation experiments. The most removal occurred as the pH fell from 12 to 11. Subsequently, V concentrations remained relatively stable in all unamended and all kaolinite-amended systems. In the unamended and kaolinite-amended block leachate system, initial V removal lowered V concentrations from ~550 to ~490 ppb. Unamended HB source water showed a similar trend with an initial fall from 35 to 25 ppb. The kaolinite-amended HB source water had a large amount of scatter but followed a similar profile. V removal in the unamended and kaolinite-amended synthetic leachate systems took place between pH 12 and 11.5. V concentrations fell from
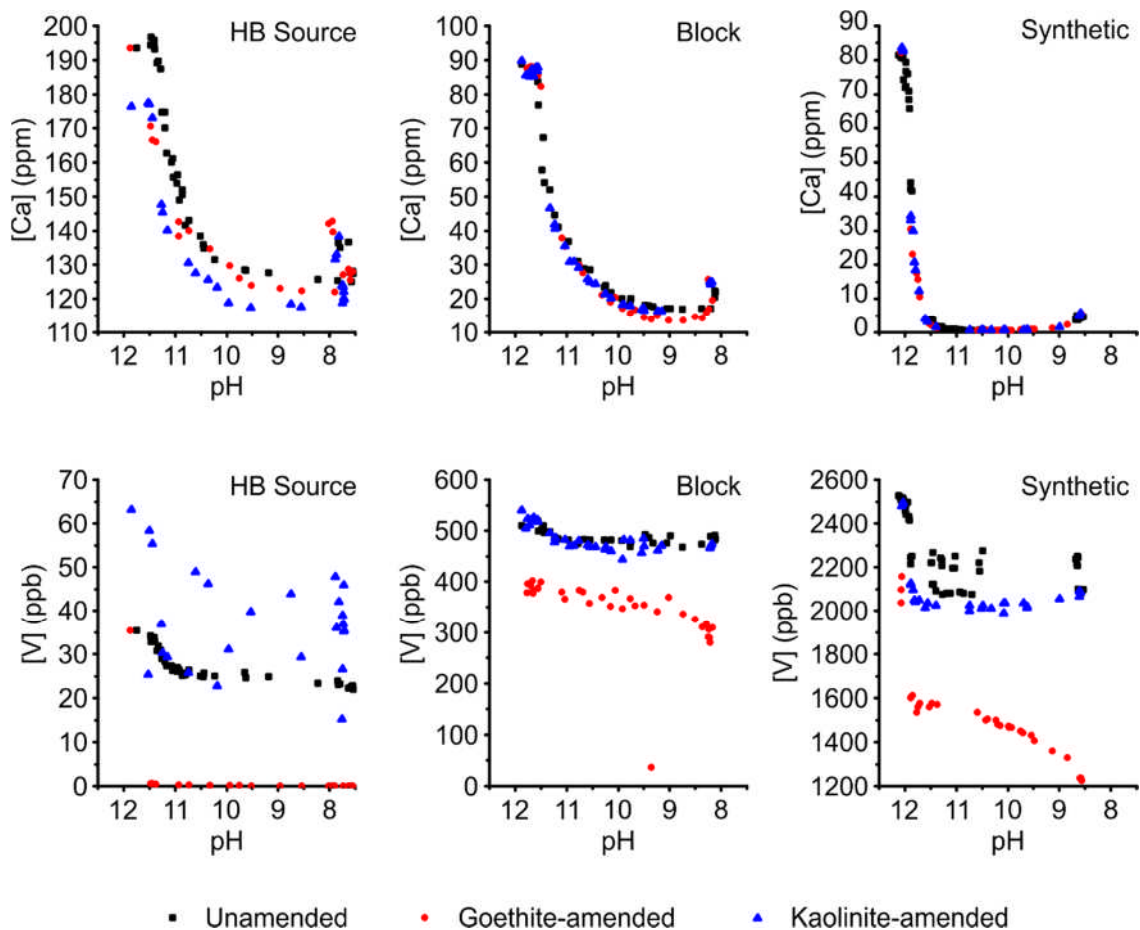
Figure 6.4 - Ca and V concentrations from all leachate systems. Data points represent samples from individual flasks. Initial conditions in goethite and kaolinite-amended systems: in HB source water: 1.0 g L^{-1} goethite/kaolinite; in block and synthetic leachates: 0.2 g L^{-1} goethite/kaolinite

2500 to ~2000 ppm in the kaolinite-amended synthetic leachate then increased slightly to ~2100 ppm between pH 9.5 and 8.5. V concentrations in the unamended synthetic leachate showed more scatter but remained stable at ~2200 ppm after the initial removal from solution.

V uptake is significantly enhanced under goethite-amended conditions. In the goethite-amended HB source water experiments, V was completely removed within the initial drop of pH from 12 to 11.5, however, these flasks had a higher solid : solution ratio of goethite (1.0 g L^{-1}) compared to the goethite-amended block leachate and goethite-amended synthetic leachate systems (0.2 g L^{-1}). In these latter two systems, initial V

removal at pH 12 was very rapid (~500 to ~400 ppb and ~2500 to ~1600 ppb in goethite-amended block and synthetic systems respectively). This was followed by a steady decrease in V concentration throughout the remainder of the experiments to a minimum of ~300 ppb in the goethite-amended block leachate and ~1200 ppb in the goethite-amended synthetic leachate.

6.3.3   TEM

Low resolution TEM imaging (Fig. 6.5a) of the solid residue recovered from the unamended HB source water neutralisation experiments showed the presence of 100 – 1000 nm rhomboid crystals with EDS spot analysis spectra that contained Ca, C and O (data not shown). This mineral shape and composition are consistent with the calcium carbonate mineral calcite ($CaCO_3$). Distinct 100 – 300 nm Fe and O rich particles were also present. High resolution imaging (Fig. 6.5b) showed these to be aggregates of 5 – 10 nm spherical crystallites, which were identified as two-line ferrihydrite by selected area electron diffraction.

6.3.4   XAS

V K-edge XANES spectra (n=9) collected from the leachate neutralisation solid residues all had a prominent pre-edge peak at 5470 eV (±0.25 eV), the normalised intensity of which varied between 0.64 and 0.90. The position of the main absorption edge ($E_{1/2}$; the point at which absorption reaches 50% of normalised absorption) varied between 5477 and 5482 eV (Fig. 6.6). Comparison with standard spectra suggested that V was present in all samples in either the V^{4+} or V^{5+} oxidation state. Following the spectra characterisation method of Chaurand et al. (2007b), it was determined that V in all samples was present as
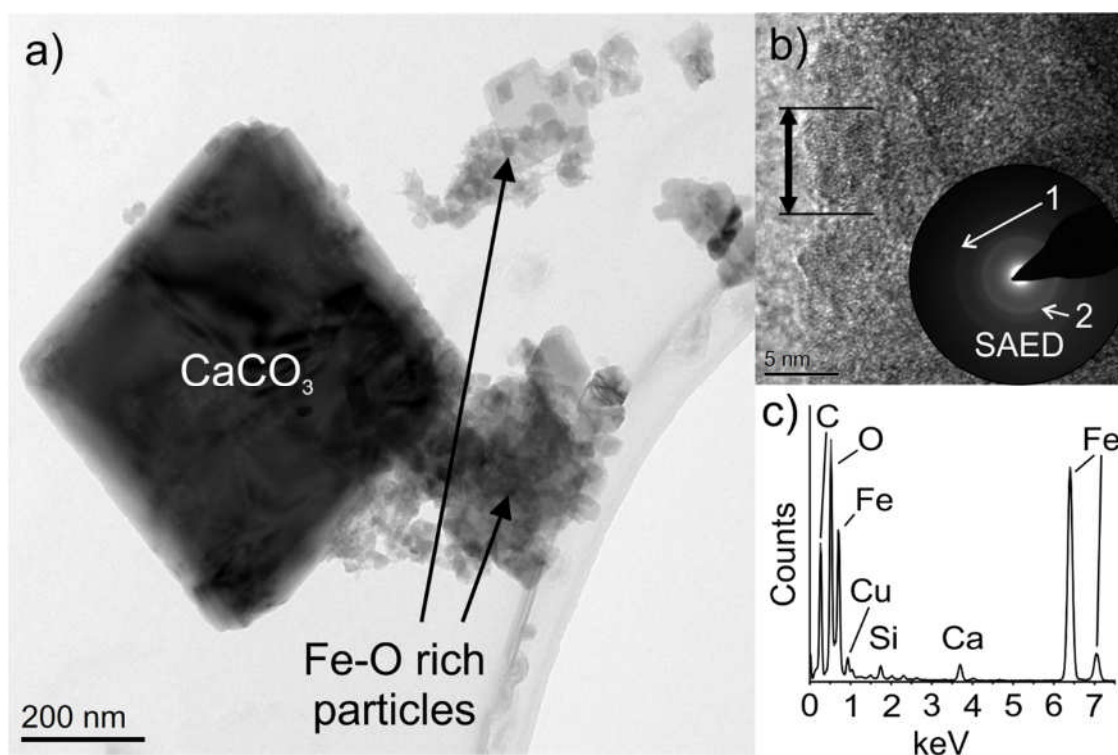
Figure 6.5 - Solid residue recovered from unamended HB source water neutralisation experiments. A) Low resolution TEM image showing calcite and Fe-O-rich crystals. B) High resolution TEM image and SAED pattern from Fe-O-rich crystals; arrows show extent of crystallite structure and C) EDS spectrum from Fe-O-rich crystallites.

V^{5+}. Due to generally very low V concentrations in samples, usable EXAFS data was only collected for the sample recovered from the goethite-amended, synthetic leachate neutralisation experiment. This spectrum was compared to data collected from the 1 wt% V-goethite standard (Fig. 6.7). Both samples were best-fit with a similar coordination model consisting of 4 V-O single scattering pathways at 1.7 Å and 2 V-Fe single scattering pathways at 3.3 Å (Table 6.2), consistent with V sorption to goethite surfaces via bidentate inner-sphere complexation (Peacock and Sherman, 2004).
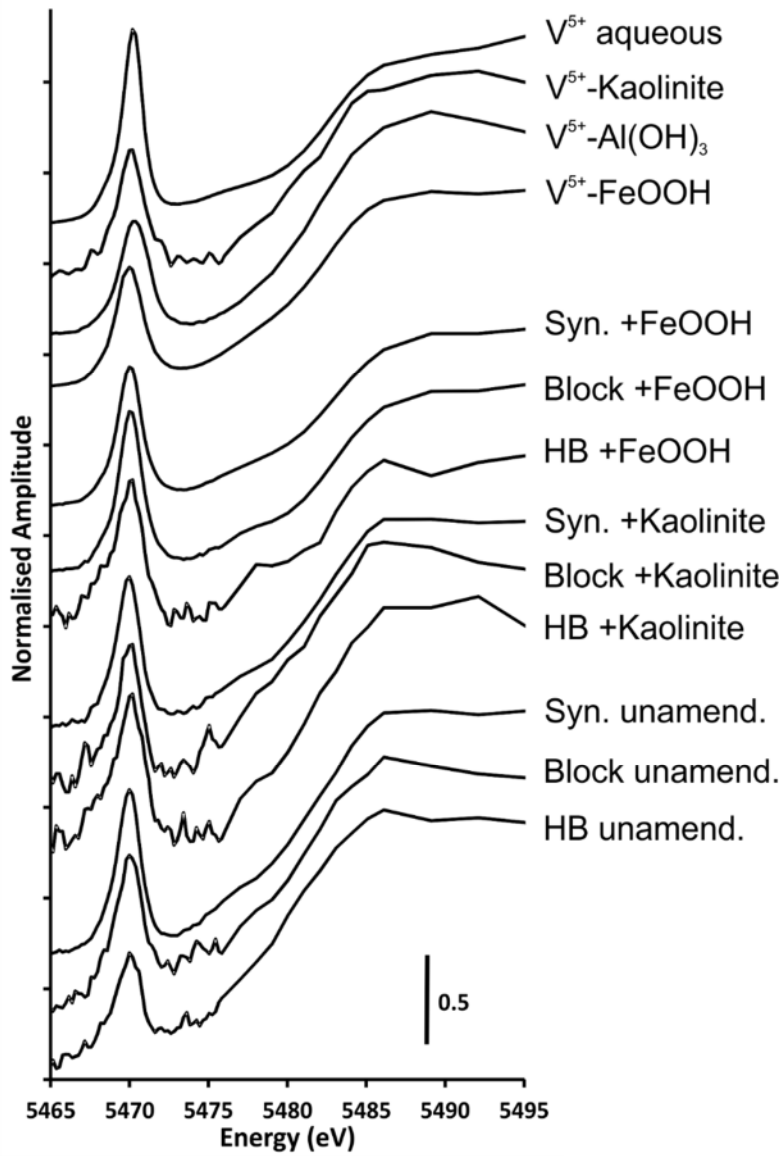
Figure 6.6 - V K-edge XANES spectra collected from precipitates recovered from the leachate experiments after aerobic neutralisation and from V^{5+} containing standards.
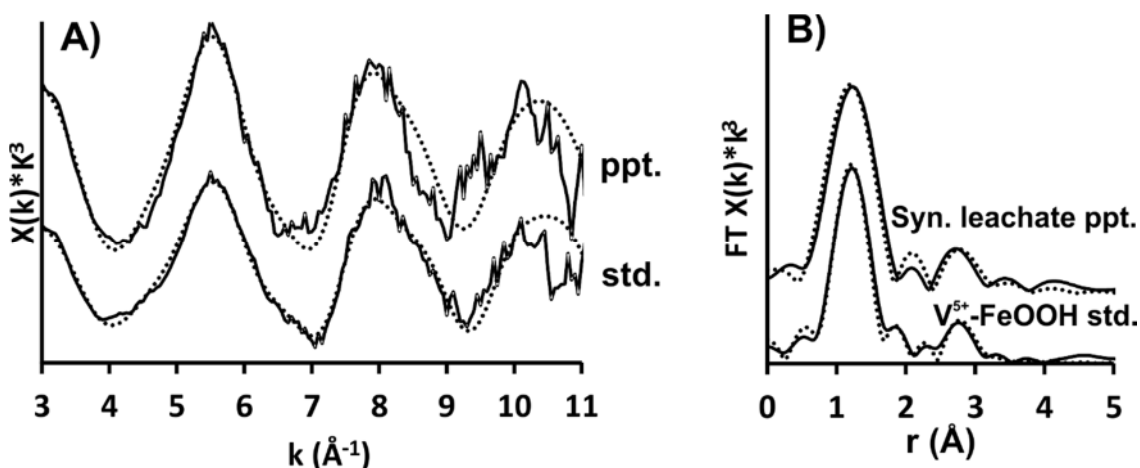
Figure 6.7 - A) V K-edge EXAFS spectra collected from precipitates formed in the goethite-amended synthetic leachate experiment after aerobic neutralisation; and the vanadate – FeOOH sorption standard at pH 8; and B) corresponding Fourier transformations. Dashed lines represented best fits to the data calculated in Artemis (Demeter v0.9.47) using the parameters given in Table 6.2.

Table 6.2 - V K-edge EXAFS fits, where N is the Occupancy ($\pm$ 25%; only whole number fits used), r is the interatomic distance, σ^2 is the Debye–Waller Factor and reduced χ^2 and R are the goodness of fit parameters. Uncertainties in the last digit(s) shown in parentheses. MS VO_4 = multiple scattering pathways within the VO_4 tetrahedral.

Experiment Description	Pathway	N	r (Å)	σ^2 (Å²)	χ^2; *R*
1. Syn. Leachate + FeOOH ppt @pH8.	V-O	4	1.69(2)	0.004(3)	215; 0.0170
	V-Fe	2	3.33(6)	0.004(7)	
$\delta e0 = -6(3)$ $S^2_0 = 0.68(17)$	MS VO_4	4	2.97(4)	0.007(6)	
2. FeOOH-Vanadate std. @pH 8.	V-O	4	1.67(1)	0.003(2)	161; 0.0178
$\delta e0 = -10(2)$ $S^2_0 = 0.45(7)$	V-Fe	2	3.31(3)	0.006(4)	
	MS VO_4	4	2.91(4)	0.005(4)	

6.4   Discussion

6.4.1   Leachate composition and downstream trends

Field monitoring of water emerging at the Howden Burn source showed pH values between 11.5 and 12.7 as well as elevated concentrations of Ca with trace concentrations of Al, V, K, Fe and Si. These concentrations are consistent with reported elemental compositions of leachate generated during weathering of steelmaking waste (Mayes et al., 2008; Roadcap et al., 2005). The source water was $Ca(OH)_2$ dominated in composition and the presence of elevated Si concentrations indicated that it was primarily formed via hydration and dissolution of Ca-silicate phases and free lime under relatively CO_2-free conditions (De Windt et al., 2011; Roadcap et al., 2005). The presence of other trace elements, including V, Fe and Al, is likely to be due to the release of impurities present in Ca-silicates (Chaurand et al., 2007a; De Windt et al., 2011; Hobson et al., 2017).

The pH of the emerging leachate decreases downstream to the lowest recorded value of 10 shortly before the junction with the River Derwent. Over the same length of Howden Burn there is a decrease in Ca concentrations. As tufa formations are observed in the stream bed it is likely that ingasing of atmospheric CO_2 has resulted in Ca being precipitated from solution as $CaCO_3$ (Eqn. 6-3). This reaction consumes OH^- ions, thus contributing to the fall in pH.

Normalised Fe, V and Al concentrations all show a trend of decreasing solution concentration downstream from the source on any given measurement day. However the Si concentrations were relatively constant along the Burn despite the changes in pH. This is probably because Si was highly undersaturated with respect to $SiO_{2(am)}$ (SI < -2) and therefore behaves conservatively. The conservative behaviour of Si and K throughout the sampled area suggests that dilution of the leachate is minimal in Howden Burn. Therefore removal mechanisms exist for V, Al and Fe which are independent of dilution and

contemporaneous with pH reduction and the precipitation of Ca as $CaCO_3$. Fe and Al removal are easily explained via formation of insoluble (oxy)hydroxide phases during pH reduction from pH 12 to 10 (Langmuir, 1997), however, V^{5+} is not predicted to precipitate as (oxy)hydroxides over this pH range (Wanty and Goldhaber, 1992) highlighting the likely role of mineral sorption processes in V removal.

6.4.2   Mechanism of V removal during leachate neutralisation.

All three leachate neutralisation systems show removal of Ca from solution as well as pH reduction over time, indicating that ingress of atmospheric CO_2 has led to the precipitation of $CaCO_3$. The slight increase in Ca concentrations seen below pH 8.5 is due to continued CO_2 ingress, which in this pH range results in the generation of H^+ ions, leading to minor amounts of $CaCO_3$ dissolution.

Most Ca removal occurs during the initial reduction in leachate pH from 12 to 11. Modest V removal is also observed in all three leachate systems across the same pH range. Aqueous Al and Fe form insoluble hydroxides and precipitate from the leachate which lowers solution pH and could lead to sorption of V to the new mineral surfaces (Fig. 6.5). However, Ca removal is still seen in the synthetic leachate system which does not contain any Al or Fe. Therefore it is probable that a small amount of V is incorporated into neo-formed $CaCO_3$ at high pH. Currently no data is available concerning incorporation of VO_4^{3-} to $CaCO_3$ although studies by Goh et al. (2010) and Hua et al. (2007) have shown that similar tetrahedral anions (e.g. arsenate, chromate) may be sparingly incorporated into the trigonal carbonate site. V was not detected in $CaCO_3$ rinds during aerated weathering of slag blocks (Chapter 4), however, the low concentrations incorporated into carbonates would be below EDS detection limits (0.1 – 0.5 wt%, which are orders of magnitude greater than the likely concentrations in the calcite samples).
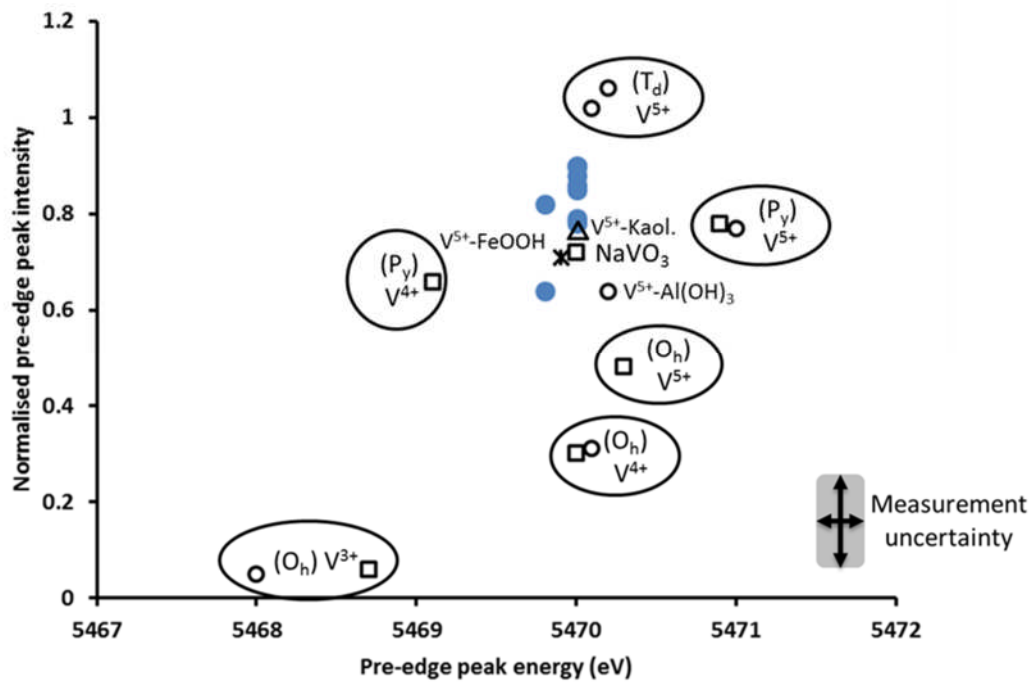
Figure 6.8 - Plot of pre-edge intensity vs. pre-edge peak energy derived from V K-edge XANES spectra. Symbols: (●) refers to the experimental samples; (✱,△) Vanadate adsorption standards; (O) standards from Burke et al. (2013); (□) standards taken from Bronkema and Bell (2007); Chaurand et al. (2007b). (T_d), (P_y) and (O_h) refers to tetrahedral, square pyramidal and octahedral co-ordination respectively.

All XANES spectra from leachate neutralisation experiment solids indicated the presence of V in the precipitates. Experimental samples display a prominent pre-edge peak at 5470 eV. Analysis of pre-edge peak intensity and absorption edge position ($E_{1/2}$; the energy halfway up the normalised absorption edge step) following the method of Chaurand et al. (2007b) shows that products from neutralisation reactions plot between the V^{4+} and V^{5+} standards. The data might therefore be interpreted as a mixture of several V-phases. However, when data from vanadate adsorbed to clay and hydroxide surfaces is also considered it is clear that lower pre-edge peak intensities are common for adsorbed vanadate (Fig 6.8; Bronkema and Bell (2007); Goh et al. (2010); Tanaka et al. (1988)). The pre-edge peak is formed during electron transitions from the 1s to hybridised 3d/4p

orbitals. The extent to which this hybridisation occurs is a function of speciation and coordination environment with the effect being most pronounced for V^{5+} in tetrahedral coordination.

EXAFS analysis of VO_4^{3-} has revealed that in sorption environments the VO_4^{3-} tetrahedra become distorted, reducing the effect of hybridisation and resulting in a correspondingly less intense pre-edge peak (Bronkema and Bell, 2007; Tanaka et al., 1988). A similar molecular distortion (and reduced pre-edge peak intensity) is noted for vanadate in some polyvanadate species such as sodium metavanadate ($NaVO_3$) (Bronkema and Bell, 2007). Therefore, detailed analysis shows the V K-edge XANES data for the leachate neutralisation samples are consistent with either vanadate incorporation to neoformed calcite precipitates or adsorption to added kaolinite or FeOOH surfaces during neutralisation.

6.4.3   *Additional effect of mineral presence on V removal.*

V removal in both unamended and kaolinite-amended systems follows a similar pattern of removal between pH 12 and 11 followed by a stabilisation in V concentrations. Final equilibrated pH values of between 7.5 and 8.5 were measured in all unamended and kaolininte-amended leachate systems which is well above the point of zero charge (PZC) of most clay minerals, including kaolinite (PZC = 3.6, Hu et al. (2003)). Therefore, at all leachate pH values, kaolinite is negatively charged and does not readily interact with anions in solution. As such, it is likely that in kaolinite-amended systems, the observed decrease in V concentrations is due to incorporation into neo-formed $CaCO_3$ as previously discussed, rather than sorption to (either AlOH or SiOH) kaolinite surfaces.

V concentrations in goethite-amended systems showed a similar rapid decrease between pH 12 and 11 followed by a continued removal throughout the remainder of the

experiments. The rate of removal subsequently increased slightly as the leachate approached equilibrium. The PZC of goethite is significantly higher than that of kaolinite (pH 7 – 9.5; Kosmulski (2016)) and so as leachate pH evolves towards these values, progressively stronger interactions with anions such as vanadate will take place. Therefore, whilst vanadate adsorption to iron oxides is expected across the range of leachate pH values observed in the experiments (12 – 7.5; Langmuir (1997)), it is expected to be significantly enhanced below pH 10.

XANES spectra obtained from all experimental samples indicate the presence of V^{5+} which is soluble at high pH as the vanadate ion (VO_4^{3-}, Wehrli and Stumm (1989)). EXAFS spectra from goethite amended synthetic leachate and α-FeOOH sorption standards both fitted to a very similar model consistent with vanadate sorption to goethite in an inner sphere bidentate corner sharing complex (in agreement with modelling and EXAFS data presented in Peacock and Sherman (2004)). These experimental results (and field data) indicate a system in which V^{5+} is released to leachate as VO_4^{3-}, followed by limited incorporation to neo-formed $CaCO_3$ at high pH following in-gassing of atmospheric CO_2. Whilst the concentration of V incorporated into carbonates is very low, the large volumes of $CaCO_3$ precipitated at legacy sites suggest that this is the most important mechanism of V removal during the initial stages of leachate neutralisation. Subsequently, increasing sorption of V to any Fe-(oxy)hydroxide (FeOOH) surfaces present also contributes to removal of VO_4^{3-} from the leachate, especially at pH values < 10.

6.4.4   *Implications for affected environments*

V concentrations in emerging leachate in Howden Burn regularly exceed chronic toxicity screening values (19 ppb; Buchman (2008)) and lab based leaching tests have

demonstrated the potential for V to accumulate in steel slag leachate at concentrations well in excess of acute toxicity screening values (280 ppb; Buchman (2008), see Chapters 4 and 5). Incorporation into neo-formed $CaCO_3$ phases and adsorption to iron oxides removes V from the leachate during aerobic neutralisation. These processes are expected to reduce the transport of V in affected rivers but instead lead to an accumulation of toxic V^{5+} in river sediments downstream. Indeed, environmentally significant V concentrations of > 42 ppm (Dutch Target Value; Buchman (2008)) were observed in sediments collected from the Howden Burn stream bed.

Overall, it appears that despite the reduction in V concentrations distal to the source, the combination of high metal loadings in both leachate and sediment, high pH leachate and carbonate smothering have had a deleterious effect the local ecosystem. Therefore, treatment of leachate to reduce alkalinity (and metal concentrations) within a short distance of the source is recommended. Previous studies have demonstrated the efficacy of wetland treatment (Mayes and Younger, 2006) or cascade systems (Gomes et al., 2017) in neutralisation of leachate and sequestering metals from solution.

6.5   Conclusions

Concentrations on V in steel slag leachate are frequently sufficiently high to be an environmental concern at the Howden Burn source, however, V is removed downstream by a mechanism contemporaneous with $CaCO_3$ precipitation. XANES analyses showed that V was present in the V^{5+} oxidation state (the most toxic form) in all solids recovered from neutralisation experiments indicating its mobilisation in leachate as the vanadate (VO_4^{3-}) oxyanion (which is the prevailing form at high pH). Leachate neutralisation experiments indicated that V is initially attenuated downstream due to incorporation into neo-formed $CaCO_3$. Whilst V incorporation is limited, mass balance suggests that this

mechanism is responsible for the majority of V removal at high pH due to the rapid rate of $CaCO_3$ precipitation and the large volumes produced. Subsequently, adsorption to Fe (oxy)hydroxides provides the most important sink for V. EXAFS analysis showed that V adsorbs to goethite by formation of strong inner-sphere complexes due to its higher pH_{pzc} (7 – 9.5) which increases interactions between vanadate oxyanions and the positively charged mineral surface as solution pH drops. Additional sites for adsorption may be provided by precipitation of Al or Fe^{3+} (oxy)hydroxides (e.g. ferrihydrite) as solution pH falls. Removal of V from solution may lead to a corresponding enrichment in sediments and future remediation schemes should look to balance efficient removal of V from leachates with safe management of any impacted sediments.

6.6   References

BOYLAN, A.A., STEWART, D.I., GRAHAM, J.T., TRIVEDI, D., BURKE, I.T., 2016. Mechanisms of inorganic carbon-14 attenuation in contaminated groundwater: Effect of solution pH on isotopic exchange and carbonate precipitation reactions. Applied Geochemistry, in press.

BRONKEMA, J.L., BELL, A.T., 2007. Mechanistic Studies of Methanol Oxidation to Formaldehyde on Isolated Vanadate Sites Supported on MCM-48. The Journal of Physical Chemistry C 111, 420-430.

BUCHMAN, M.F., 2008. NOAA Screening Quick Reference Tables.

BURKE, I.T., PEACOCK, C.L., LOCKWOOD, C.L., STEWART, D.I., MORTIMER, R.J.G., WARD, M.B., RENFORTH, P., GRUIZ, K., MAYES, W.M., 2013. Behavior of Aluminum, Arsenic, and Vanadium during the Neutralization of Red Mud Leachate by HCl, Gypsum, or Seawater. Environ. Sci. Technol. 47, 6527-6535.

CHAURAND, P., ROSE, J., BRIOIS, V., OLIVI, L., HAZEMANN, J.L., PROUX, O., DOMAS, J., BOTTERO, J.Y., 2007a. Environmental impacts of steel slag reused in road construction: A crystallographic and molecular (XANES) approach. J. Hazard. Mater. 139, 537-542.

CHAURAND, P., ROSE, J., BRIOIS, V., SALOME, M., PROUX, O., NASSIF, V., OLIVI, L., SUSINI, J., HAZEMANN, J.L., BOTTERO, J.Y., 2007b. New methodological approach for the vanadium K-edge X-ray absorption near-edge structure interpretation: Application to the speciation of vanadium in oxide phases from steel slag. J. Phys. Chem. B 111, 5101-5110.

CORNELIS, G., JOHNSON, C.A., GERVEN, T.V., VANDECASTEELE, C., 2008. Leaching mechanisms of oxyanionic metalloid and metal species in alkaline solid wastes: A review. Applied Geochemistry 23, 955-976.

COSTA, G., POLETTINI, A., POMI, R., STRAMAZZO, A., 2016. Leaching modelling of slurry-phase carbonated steel slag. J. Hazard. Mater. 302, 415-425.

DE WINDT, L., CHAURAND, P., ROSE, J., 2011. Kinetics of steel slag leaching: Batch tests and modeling. Waste Manage. 31, 225-235.

EFFLER, S.W., 1987. The impact of a chlor-alkali plant on Onondaga Lake and adjoining systems. Water, Air, and Soil Pollution 33, 85-115.

ENVIRONMENT AGENCY, 2014. EA Bespoke permit 2014 Permit for Scunthorpe Aggregate processing. Permit number EPR/LP3537VV/A001.

EUROSLAG, 2012. Statistics 2012, http://www.euroslag.com/products/statistics/2012/.

FJELLHEIM, A., RADDUM, G.G., 1995. Benthic animal response after liming of three south Norwegian rivers. Water, Air, and Soil Pollution 85, 931-936.

FORD, D.C., WILLIAMS, P.W., 1989. Karst geomorphology and hydrology. Unwin Hyman London.

GEISELER, J., 1996. Use of steelworks slag in Europe. Waste Manage. 16, 59-63.

GOH, K.H., LIM, T.T., DONG, Z.L., 2010. Removal of arsenate from aqueous solution by nanocrystalline Mg/Al layered double hydroxide: sorption characteristics, prospects, and challenges. Water Science and Technology 61, 1411-1417.

GOMES, H.I., ROGERSON, M., BURKE, I.T., STEWART, D.I., MAYES, W.M., 2017. Hydraulic and biotic impacts on neutralisation of high-pH waters. Science of The Total Environment 601–602, 1271-1279.

HOBSON, A.J., STEWART, D.I., BRAY, A.W., MORTIMER, R.J.G., MAYES, W.M., ROGERSON, M., BURKE, I.T., 2017. Mechanism of Vanadium Leaching during Surface Weathering of Basic Oxygen Furnace Steel Slag Blocks: A Microfocus X-ray Absorption Spectroscopy and Electron Microscopy Study. Environ. Sci. Technol.

HU, Y., LIU, X., XU, Z., 2003. Role of crystal structure in flotation separation of diaspore from kaolinite, pyrophyllite and illite. Minerals Engineering 16, 219-227.

HUA, B., DENG, B., THORNTON, E.C., YANG, J., AMONETTE, J.E., 2007. Incorporation of Chromate into Calcium Carbonate Structure During Coprecipitation. Water, Air, and Soil Pollution 179, 381-390.

HUIJGEN, W.J.J., COMANS, R.N.J., 2006. Carbonation of steel slag for CO2 sequestration: Leaching of products and reaction mechanisms. Environmental Science and Technology 40, 2790-2796.

HULL, S.L., OTY, U.V., MAYES, W.M., 2014. Rapid recovery of benthic invertebrates downstream of hyperalkaline steel slag discharges. Hydrobiologia 736, 83-97.

KORYAK, M., STAFFORD, L.J., REILLY, R.J., MAGNUSON, M.P., 2002. Impacts of Steel Mill Slag Leachate on the Water Quality of a Small Pennsylvania Stream. Journal of Freshwater Ecology 17, 461-465.

KOSMULSKI, M., 2016. Isoelectric points and points of zero charge of metal (hydr)oxides: 50years after Parks' review. Advances in Colloid and Interface Science 238, 1-61.

LANGMUIR, D., 1997. Aqueous Environmental Geochemistry. Prentice Hall.

MAYES, W.M., YOUNGER, P.L., 2006. Buffering of Alkaline Steel Slag Leachate across a Natural Wetland. Environ. Sci. Technol. 40, 1237-1243.

MAYES, W.M., YOUNGER, P.L., AUMONIER, J., 2008. Hydrogeochemistry of alkaline steel slag leachates in the UK. Water Air Soil Pollut. 195, 35-50.

OBER, J.A., 2017. Mineral commodity summaries 2017, Mineral Commodity Summaries, Reston, VA, p. 202.

PEACOCK, C.L., SHERMAN, D.M., 2004. Vanadium(V) adsorption onto goethite (alpha-FeOOH) at pH 1.5 to 12: A surface complexation model based on ab initio molecular geometries and EXAFS spectroscopy. Geochimica Et Cosmochimica Acta 68, 1723-1733.

PIATAK, N.M., PARSONS, M.B., SEAL, R.R., 2014. Characteristics and environmental aspects of slag: A review. Applied Geochemistry.

PROCTOR, D.M., FEHLING, K.A., SHAY, E.C., WITTENBORN, J.L., GREEN, J.J., AVENT, C., BIGHAM, R.D., CONNOLLY, M., LEE, B., SHEPKER, T.O., ZAK, M.A., 2000. Physical and chemical characteristics of blast furnace, basic oxygen furnace, and electric arc furnace steel industry slags. Environ. Sci. Technol. 34, 1576-1582.

RAVEL, B., NEWVILLE, M., 2005. ATHENA, ARTEMIS, HEPHAESTUS: data analysis for X-ray absorption spectroscopy using IFEFFIT. Journal of synchrotron radiation 12, 537-541.

RILEY, A.L., MAYES, W.M., 2015. Long-term evolution of highly alkaline steel slag drainage waters. Environ Monit Assess 187, 463.

ROADCAP, G.S., KELLY, W.R., BETHKE, C.M., 2005. Geochemistry of extremely alkaline (pH > 12) ground water in slag-fill aquifers. Ground Water 43, 806-816.

SHEN, D.H., WU, C.M., DU, J.C., 2009. Laboratory investigation of basic oxygen furnace slag for substitution of aggregate in porous asphalt mixture. Constr. Build. Mater. 23, 453-461.

TANAKA, T., YAMASHITA, H., TSUCHITANI, R., FUNABIKI, T., YOSHIDA, S., 1988. X-ray absorption (EXAFS/XANES) study of supported vanadium oxide catalysts. Structure of surface vanadium oxide species on silica and [gamma]-alumina at a low level of vanadium loading. Journal of the Chemical Society, Faraday Transactions 1: Physical Chemistry in Condensed Phases 84, 2987-2999.

TOSSAVAINEN, M., ENGSTROM, F., YANG, Q., MENAD, N., LIDSTROM LARSSON, M., BJORKMAN, B., 2007. Characteristics of steel slag under different cooling conditions. Waste Manage. 27, 1335-1344.

VAN OSS, H.G., 2016. 2014 Minerals Yearbook, Slag - Iron and Steel. USGS.

WANTY, R.B., GOLDHABER, M.B., 1992. Thermodynamics and kinetics of reactions involving vanadium in natural systems - accumulation of vanadium in sedimentary-rocks. Geochimica Et Cosmochimica Acta 56, 1471-1483.

WEHRLI, B., STUMM, W., 1989. Vanadyl in natural-waters - adsorption and hydrolysis promote oxygenation. Geochimica Et Cosmochimica Acta 53, 69-77.

WILKIE, M.P., WOOD, C.M., 1996. The adaptations of fish to extremely alkaline environments. Comparative Biochemistry and Physiology Part B: Biochemistry and Molecular Biology 113, 665-673.

YI, H., XU, G., CHENG, H., WANG, J., WAN, Y., CHEN, H., 2012. An Overview of Utilization of Steel Slag. Procedia Environmental Sciences 16, 791-801.

YILDIRIM, I.Z., PREZZI, M., 2011. Chemical, Mineralogical, and Morphological Properties of Steel Slag. Advances in Civil Engineering 2011, 1-13.

Chapter 7   Summary and future work

7.1   Summary

V is the principal contaminant of concern associated with steel slags due to its relatively high concentration in the waste (0.04 – 1.48 wt%; Proctor et al. (2000); Tossavainen et al. (2007)), its potential toxicity and its mobility at high pH waters as the vanadate oxyanion. V displays complex environmental behaviour with solubility which is strongly influenced by pH and redox conditions.

The aim of this study was to establish the mechanisms controlling the behaviour of V during leaching of steel slags, its subsequent mobility in the environment and the surface hydrochemistry of steel slag leachate. This thesis has presented a comprehensive study of the effects of different environmental conditions on the generation of steel slag leachate, precipitation of secondary phases and their effects on V release and fate in the environment. This concluding chapter summarises the major findings of the thesis and links to the original research objectives specified in Chapter 1. The wider implications of the work and potential avenues for future research are also discussed.

7.2 Major findings and implications
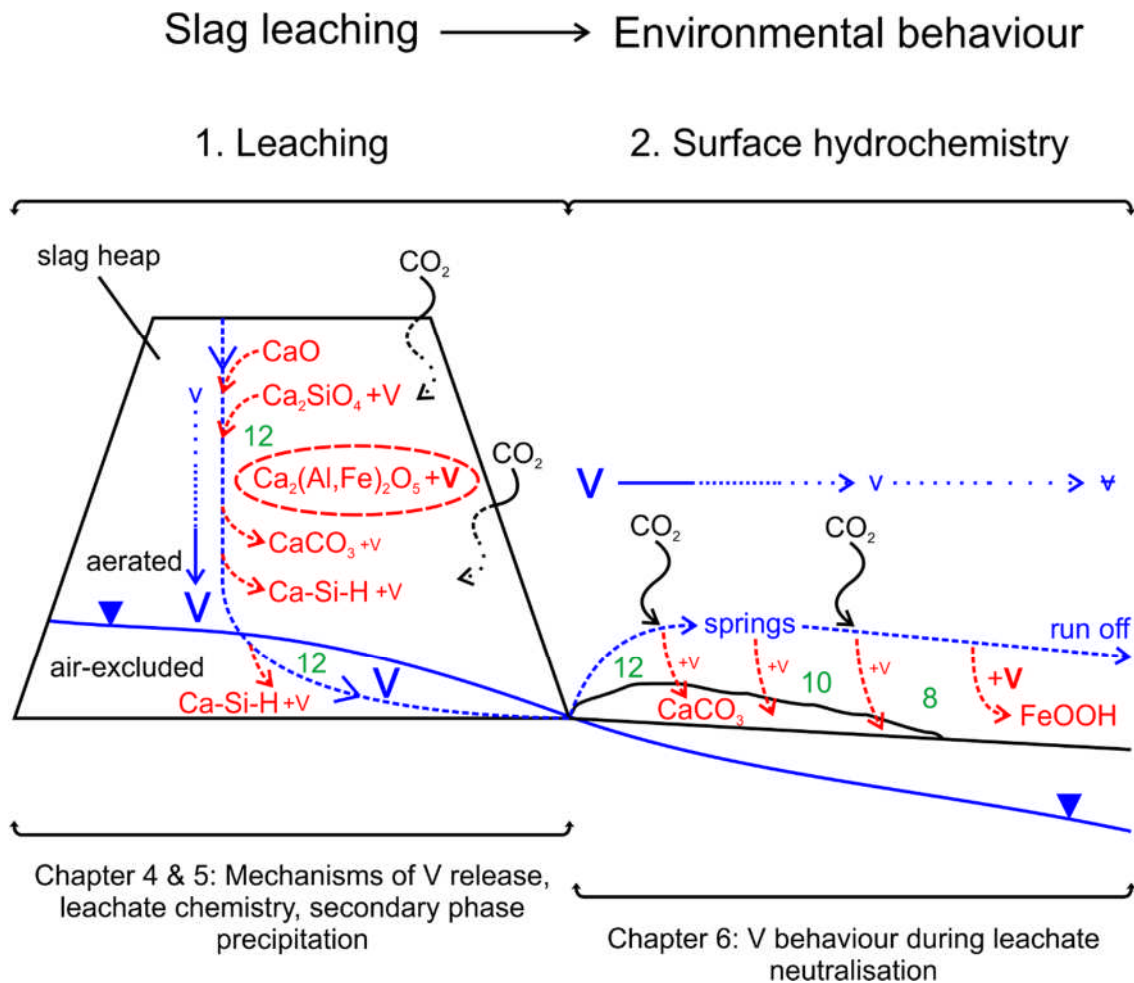
Figure 7.1 – Conceptual site model with V mobilisation/attenuation pathways indicated as determined by experimental work from this thesis. Blue dashed lines represent approximate flow pathways. Blue arrows represent relative V concentrations in leachate. Red dashed lines represent CO_2 in-gassing. Green numbers represent hypothetical pH values.

Despite the large volume of steel slag produced annually worldwide, in addition to abandoned legacy sites with a recognised environmental impact, previous studies of steel slag leaching behaviour have been limited in both number and scope, often focusing on air-excluded leaching or pH_{stat} leaching tests at circumneutral pH levels (despite steel slag leachate generally being > pH 9).

The research presented in this thesis provides the first comprehensive study of V mobility during heap leaching processes and the subsequent release of leachate to the wider environment (Fig. 7.1). It therefore demonstrates a significant advance in our understanding of the processes governing the mobility of V during weathering and leaching of steel slags. Development of leachate chemistry during leaching under aerated (unsaturated) and air-excluded (saturated) conditions is detailed with particular emphasis on V, including its mobilisation under both aerated and air-excluded conditions and its fate during neutralisation of leachate. The primary V-hosting phases within BOF slag have been clearly identified and their dissolution behaviour and thus contribution to V release during leaching has been determined. In addition, the role of secondary precipitates (including $CaCO_3$ and Ca-Si-H phases) in controlling leachate composition and V concentrations under differing conditions has been fully explored.

V was predominantly present in unweathered slag in dicalcium aluminoferrite as octahedrally coordinated V^{4+} and tetrahedrally coordinated V^{5+} in addition to a smaller proportion which was found as tetrahedrally coordinated V^{5+} in dicalcium silicate which had not previously been identified. V release was found to be significantly enhanced under aerated conditions (~860 ppb compared to ~490 ppb in block leaching experiments). Previous research had suggested that this may be due to oxidation of V^{3+} and V^{4+} to V^{5+} during weathering of dicalcium aluminoferrite (Chaurand et al., 2007; De Windt et al., 2011), however, µXAS data presented in Chapter 4 found no indication that this occurs and suggested that instead, V^{5+} is released during dissolution of dicalcium silicates. Dicalcium aluminoferrite dissolution does not contribute significantly to leachate composition. Subsequently equilibrium with neo-formed Ca-Si-H phases under air-excluded conditions resulted in high concentrations of Ca in leachate leading to saturation with respect to $Ca_3(VO_4)_2$ which precipitates, thus limiting V concentrations under these conditions. Under aerated conditions formation of $CaCO_3$ provide a sink for aqueous V.

Therefore V concentrations in aerated leachate steadily increase as Ca concentrations decrease during evolution of leachate from $Ca(OH)_2$ equilibrium through Ca-Si-H equilibrium to finally equilibrate with $CaCO_3$.

These results provide important insights for safe storage of steelmaking wastes where exposed to weathering processes. It is clear that the specific waste storage environment strongly influences both leachate chemistry and secondary phase formation. Therefore, storage of waste under saturated conditions designed to minimise in-gassing of atmospheric CO_2 would prevent significant accumulation of V in leachates by providing a Ca-rich environment leading to precipitation of $Ca_3(VO_4)_2$. In systems where aeration is high, the formation of a Ca-Si-H-rich altered zone on slag blocks may limit V concentrations, partly by incorporating aqueous V during precipitation but principally by providing a diffusion barrier kinetically slowing further dissolution of the dicalcium silicate phase. However, significant accumulations of V can still develop in leachates and careful treatment of the leachate would be required to prevent potential environmental harm. In scenarios where steel slags may be used for CO_2 sequestration the formation of weathering rinds may be problematic, as they limit the volume of the slag blocks available for conversion.

Results from this research and from observations at legacy sites indicate that V concentrations in emerging steel slag leachate can be environmentally significant. Data presented here shows that V is released in the toxic V^{5+} oxidation state as the vanadate oxyanion (VO_4^{3-} is the prevailing form at high pH; Wehrli and Stumm (1989)) which can persist in leachates at circumneutral pH (Takeno, 2005) making it potentially problematic. However, whilst declining V concentrations distal to the source during neutralisation of steel slag leachate have been noted at legacy sites, they have not investigated systematically. Leachate neutralisation experiments conducted under aerated conditions indicated that V could be incorporated sparingly into neo-formed $CaCO_3$ which is likely to represent an

important sink for V due to the large volumes precipitated at impacted sites. Addition of mineral surfaces showed that kaolinite clay had little to no effect on V removal due to leachate equilibrating at 7.5 – 8.5, which is well above the pH_{pzc} of most clay minerals. However, in the presence of goethite (α-FeOOH), V removal was significantly enhanced throughout the neutralisation experiments. The pH_{pzc} of goethite is between 7 – 9.5, therefore as the leachate pH evolves towards this value, interactions between the increasingly positively charged mineral surface and vanadate oxyanions increase. EXAFS analysis showed that vanadate adsorbs to goethite by the formation of strong inner-sphere complexes. TEM analysis of neutralisation products indicated the presence of nano-scale crystallites of 2-line ferrihydrite which may provide additional adsorption surfaces in leachates.

This study therefore provides a mechanism for V attenuation under both high pH and circumneutral regimes (either via incorporation into neo-formed $CaCO_3$ or via sorption to neo-formed, colloidal or streambed sediment Fe (oxy)hydroxides respectively). This data provides new insights into the spatial impact of steel slag leachate on the wider environment and also demonstrates that removal of V from leachate over long time periods may result in an enrichment in stream sediments. Therefore remediation schemes which may be implemented at legacy sites will need to balance effective removal of V from leachates with safe management of any impacted sediments.

7.3   Future considerations

The slag leaching system as described in this thesis presents both aerated (unsaturated) and air-excluded (saturated) conditions as discrete environments. In reality, as noted in Chapter 4, section 4.4.5, CO_2 concentrations within slag heaps are likely to be variable, with uptake due to carbonate precipitation and gas diffusion rates into the heap

leading to generally lower CO_2 concentrations compared to atmospheric values (~70 ppm, P. Renforth, personal communication, September 2017). CO_2 concentrations may influence both the rate and total extent of $CaCO_3$ precipitation within the heap. $CaCO_3$ appears to partially protect Ca-Si-H phases which would otherwise dissolve as leachate pH falls below 10, therefore the thickness of the $CaCO_3$ portion of the altered region is an important factor in controlling long-term V release. Future work investigating the rate of $CaCO_3$ deposition as a function of CO_2 concentration would begin to fully explore the processes taking place within slag heaps and their likely long term behaviour.

The results presented in this thesis are from a maximum of 6 months leaching. Long term leaching experiments were beyond the scope of this work. Previous studies have shown that leachates associated with legacy slag heaps show declining pH and Ca concentrations as Ca-rich phases are depleted over time (Riley and Mayes, 2015). Research has indicated that the many slag phases become increasingly soluble as solution pH decreases towards neutral values (Engström et al., 2013). The dicalcium aluminoferrite in BOF slag contains the highest concentrations of V by weight and thus represents a potentially significant source of V. Currently the potential for this phase to release V to leachates as pore water pH falls over time is unknown.

The role of organic matter in controlling V mobility in steel slag leachates was not investigated as part of this thesis. Complexation with humic acids can stabilise V^{5+} against reduction thus enhancing its mobility. Alternatively organic V^{5+} complexes can be essential intermediates during reduction. The vanadyl oxycation (VO^{2+}) is readily complexed by organic ligands which can enhance its mobility in groundwater. Since the dicalcium aluminoferrite phase contains V in both the V^{5+} and V^{4+} oxidation state, V released during its dissolution may persist in leachates as part of organic complexes (Huang et al., 2015). Similarly the microbial processes potentially affecting V mobility in leachates have yet to be determined.

CO_2 capture estimates using steel slags are generally based on crushed specimens or assume whole-mass conversion (Renforth et al., 2011). The formation of a Ca-Si-H-rich weathered region on the surface of slag blocks may reduce the volume of slag available for carbonation as well as the rate at which it occurs. Future research to quantify these effects are required to improve the prospects for slag reuse as a sink for atmospheric CO_2.

7.4   References

CHAURAND, P., ROSE, J., BRIOIS, V., OLIVI, L., HAZEMANN, J.L., PROUX, O., DOMAS, J., BOTTERO, J.Y., 2007. Environmental impacts of steel slag reused in road construction: A crystallographic and molecular (XANES) approach. J. Hazard. Mater. 139, 537-542.

DE WINDT, L., CHAURAND, P., ROSE, J., 2011. Kinetics of steel slag leaching: Batch tests and modeling. Waste Manage. 31, 225-235.

ENGSTRÖM, F., ADOLFSSON, D., SAMUELSSON, C., SANDSTRÖM, Å., BJÖRKMAN, B., 2013. A study of the solubility of pure slag minerals. Minerals Engineering 41, 46-52.

HUANG, J.-H., HUANG, F., EVANS, L., GLASAUER, S., 2015. Vanadium: Global (bio)geochemistry. Chemical Geology 417, 68-89.

PROCTOR, D.M., FEHLING, K.A., SHAY, E.C., WITTENBORN, J.L., GREEN, J.J., AVENT, C., BIGHAM, R.D., CONNOLLY, M., LEE, B., SHEPKER, T.O., ZAK, M.A., 2000. Physical and chemical characteristics of blast furnace, basic oxygen furnace, and electric arc furnace steel industry slags. Environ. Sci. Technol. 34, 1576-1582.

RENFORTH, P., WASHBOURNE, C.L., TAYLDER, J., MANNING, D.A.C., 2011. Silicate Production and Availability for Mineral Carbonation. Environ. Sci. Technol. 45, 2035-2041.

RILEY, A.L., MAYES, W.M., 2015. Long-term evolution of highly alkaline steel slag drainage waters. Environ Monit Assess 187, 463.

TAKENO, N., 2005. Atlas of Eh-pH diagrams. Geological survey of Japan open file report 419, 102.

TOSSAVAINEN, M., ENGSTROM, F., YANG, Q., MENAD, N., LIDSTROM LARSSON, M., BJORKMAN, B., 2007. Characteristics of steel slag under different cooling conditions. Waste Manage. 27, 1335-1344.

WEHRLI, B., STUMM, W., 1989. Vanadyl in natural-waters - adsorption and hydrolysis promote oxygenation. Geochimica Et Cosmochimica Acta 53, 69-77.

Appendix A   Detection limits of experimental methods

Table A 1 - Limit of detection (LOD) and uncertainty for aqueous analyses determined on Thermo iCAP 7400 radial ion-coupled plasma optical emission spectrometer (ICP-OES) and Thermo iCAP Qc ion-coupled plasma mass spectrometer (ICP-MS) reported in Chapter 4 – 5 and Chapter 6*.

	LOD	% Uncertainty @ 95% confidence interval
Major elements (ppm)		
Ca	0.01	1
Si	0.02	6.8
Mg	0.002	1
K	0.01	2.1
Na	0.002	1.3
Al	0.002	3.2
Minor elements (ppb)		
Cr	0.002	1
Fe	0.1	1.7
Li	0.1	3.2
Mn	0.04	3.1
V	0.001	1.5
Fe*	1.88*	2.34*
Li*	1.93*	4.4*

Table A 2 - LOD and standard deviation (mean from 3 x blank) for aqueous analyses determined on a Perkin Elmer Optima 5300DV ICP-OES reported in Chapter 5.

Determinand	mean SD blank (ppm)	LOD (ppb)
Ca 317.933	0.0008	2.4
Ca 315.887	0.0026	7.7
Si 251.611	0.0081	24.4
Si 212.412	0.0058	17.3
Mg 279.077	0.0116	34.9
Fe 238.204	0.0004	1.3
Fe 259.939	0.0005	1.5
V 290.880	0.0006	1.7
V 310.230	0.0003	1.0

Table A 3 - Lower limit of detection (LLD) for analysis undertaken on a PANalytical Axios Advanced X-ray Fluorescence (XRF) spectrometer reported in Chapter 5.

Determinand	LLD (wt %)
CaO	0.005
Fe_2O_3	0.004
SiO_2	0.062
MgO	0.010
Mn_3O_4	0.003
Al_2O_3	0.026
P_2O_5	0.002
V_2O_5	0.003
TiO_2	0.004
Cr_2O_3	0.004
SO_3	0.003
K_2O	0.003
Na_2O	0.012
SrO	0.002
ZrO_2	0.001
BaO	0.005
NiO	0.002
CuO	0.002
ZnO	0.001
PbO	0.002

Appendix B   Associated manuscript

Role of Calcium-Silicate-Hydrate in Controlling the Long-Term Leaching Behaviour of Basic Oxygen Furnace (BOF) Steel Slag: Effect of Particle Size on Leaching Properties.

Douglas I. Stewart[1*], Andrew W. Bray[2], Gideon Udoma[1], Andrew J. Hobson[2], William M. Mayes[3], Mike Rogerson[3] and Ian T. Burke[2]

[1]School of Civil Engineering, University of Leeds, LS2 9JT, UK

[2]School of Earth and Environment, University of Leeds, LS2 9JT, UK

[3]School of Environmental Sciences, University of Hull, Cottingham Road, Hull, HU6 7RX, UK

*Corresponding Author - E-mail: d.i.stewart@leeds.ac.uk; Phone: +44 113 3432287

Abstract

Alkalinity generation and toxic trace metal (such as vanadium) leaching from BOF steel slag particles must be properly understood and managed by pre-conditioning if beneficial reuse of slag is to be maximised. Water leaching under aerated conditions was investigated using fresh BOF slag at three different particle sizes (0.5-1.0 mm, 2-5 mm and 10 x 10 x 20 mm blocks) and a 6 month pre-weathered block. There were several distinct leaching stages observed over time associated with different phases controlling the solution chemistry: (1) free lime (CaO) dissolution (days 0 – 2); (2) dicalcium silicate (Ca_2SiO_4) dissolution (days 2 – 14); and (3) Ca-Si-H and $CaCO_3$ formation and subsequent dissolution (days 14 – 73). Experiments with the smallest size fraction resulted in the highest Ca, Si, and V concentrations, highlighting the role of surface area in controlling initial leaching. After ~2 weeks the solution Ca/Si ratio (0.7 – 0.9) evolved to equal those found within a Ca-Si-H phase that replaced dicalcium silicate and free lime phases in a 30 – 150 µm altered surface region. V release was a two stage process; initially V was released by dicalcium silicate dissolution, but V also isomorphically substituted for Si into the neo-formed Ca-Si-H in the alteration zone. Therefore, on longer timescales the release of V to solution was primarily controlled by considerably slower Ca-Si-H dissolution rates, which decreased the rate of V release by an order of magnitude. Overall the results indicate that the BOF slag leaching mechanism evolves from a situation initially dominated by rapid hydration and dissolution of primary dicalcium silicate / free lime phases, to a slow diffusion limited process controlled by the solubility of secondary Ca-Si-H and $CaCO_3$ phases that replace and cover more reactive primary slag phases at particle surfaces.

Keywords: Steel slag; Vanadium; Alkaline waste; Leaching; Particle size; Reuse.

Introduction

Steelworks slag is an important industrial by-product, with an annual global production of 170-250 million tonnes (van Oss 2016). It is produced when CaO (or limestone / dolomite) is added to the steel furnace as a flux that reacts with process impurities (primarily silica) and separates them from the molten steel (Bobicki et al. 2012, Eloneva et al. 2010). The slag produced is named after the steelmaking process in which it is generated: basic oxygen furnace (BOF), electric arc furnace (EAF) and ladle furnace (LF) (Bobicki et al. 2012, Bonenfant et al. 2008, De Windt et al. 2011, Navarro et al. 2010, Wang et al. 2010). At the start of the 21st century more than 60% of the world's steel is produced by the basic oxygen process, with the remaining production by EAF (Smil 2006).

BOF slag, which is sometimes called basic oxygen steelmaking or Linz-Donawitz slag, has a composition that varies slightly with the iron source and the processing details, but its bulk chemical composition is relatively consistent between locations worldwide. The major element chemistry is dominated by Ca, Fe and Si, with lesser amounts of Mg, Mn and Al (Hobson et al. 2017, Shen et al. 2009, Tossavainen et al. 2007, Yildirim &Prezzi 2011). The mineralogical composition can be complex but BOF slag typically contains Ca-rich silicates (e.g. Larnite, β-Ca_2SiO_4; Merwinite, $Ca_3Mg(SiO_4)_2$, Rankinite, $Ca_3Si_2O_7$, Akermanite, $Ca_2MgSi_2O_7$), Ca-Fe-Al-oxides (e.g. Brownmillerite, Ca_2FeAlO_5, Srebrodolskite, $Ca_2Fe_2O_5$), Periclase (MgO) and refractory Fe-Mg-Mn-Ca-oxides (e.g. Wustite, FeO) together with unused free lime (CaO) (Geiseler 1996, Hobson et al. 2017, Mayes et al. 2008, Piatak et al. 2015, Roadcap et al. 2005). EAF slag has a similar chemical composition to BOF slag, although its composition varies slightly with the type of scrap steel used, and it contains similar mineral phases (Tossavainen et al. 2007, Yildirim &Prezzi 2011).

The production of slag is an inevitable consequence of steel manufacturing, but this need not result in its disposal as waste, as steel slags have been used as secondary raw materials for more than 100 years (EuroSlag 2006). However steel slag reuse rates vary enormously around the world (published reuse rates rarely differentiate between chemically similar BOF and EAF slags). For example only 22% of steel slag is reused in China (Yi et al. 2012) and 30% is reused in India (Tiwari et al. 2016) whereas in Europe more than 75% of slag is reused (EuroSlag 2012), and in the USA 90% of steel slag is reused (van Oss 2016). These differences probably reflect differences in national policy and regulatory environments, which in the EU and USA promote the use of alternative raw materials, however even in these markets steel slag commands a low unit value (EuroSlag 2006, van Oss 2016).

The largest market for BOF slag is as aggregate for civil engineering applications, such as road construction (Ahmedzade &Sengoz 2009, Geiseler 1996, Huang et al. 2007, Qiang &Peiyu 2010, Yi et al. 2012). The most important properties of such aggregates are particle

shape, strength, bulk density, volume stability, water absorption characteristics, resistance to breakdown during freeze/thaw cycles, crushing resistance, and (for highway surface layers) resistance to abrasion and polishing (ASA 2002, Motz &Geiseler 2001). Many of these properties of slag-based aggregates are comparable with, or even better than those of natural aggregates (Motz &Geiseler 2001), but concerns about the volume stability of BOF slag can prevent its immediate use in significant quantities (Sasaki &Hamazaki 2015). Free (unhydrated) lime (CaO) and periclase (MgO) in BOF slag can result in volumetric expansion upon hydration (Ahmedzade &Sengoz 2009, Motz &Geiseler 2001, Wang et al. 2010). Therefore limits are sometimes placed on the free lime content of BOF slag, or a period of slag conditioning is required before reuse is permitted (ASA 2002, Dippenaar 2004, Huang et al. 2007, Wang et al. 2010). Typically it is stockpiled for a period of months, and rainfall (or other water) is allowed to infiltrate to promote the hydration process (Dippenaar 2004). In the UK a construction company is processing and conditioning BOF slag produced at a major steelworks in the North of England to produce an aggregate for road construction (UKEA 2014b, a). Here de-metallised BOF slag is crushed and screened to <20mm and left to weather in windrows for >6 months, to reduce the free lime content and make it suitable for road construction (UKEA 2014b, a).

When BOF slag comes into contact with water (e.g. when rainwater infiltrates a slag stockpile) it produces very highly alkaline leachate. Two processes generate alkalinity: rapid hydration and subsequent dissociation of free lime, and slower dissolution of Periclase (if present) and Ca-silicates minerals, such as Rankinite, Larnite, and Akermanite (Mayes et al. 2008, Roadcap et al. 2005). Steel slags can contain trace metals from the primary ore, such as Al, Cr, Mo and V, which become concentrated in the slag by processing (steel slag production is about 10% to 15% of steel output; van Oss 2016). The fate of these trace metals during slag leaching depends both on the chemical form of the trace metal, and the stability of the specific host phases present in the slag. For example vanadium can be hosted by dicalcium silicate phases as V(V) in tetrahedrally coordinated silicate sites, and by dicalcium aluminoferrite phases as both V(III) and V(IV) in octahedrally coordinated Fe(III) sites and as V(V) in tetrahedrally coordinated silicate sites (Chaurand et al. 2007a, Chaurand et al. 2007b, Hobson et al. 2017). Dissolution of dicalcium silicates can therefore release V(V) to solution to produce aqueous orthovanadate species at high pH (Wehrli &Stumm 1989), which may subsequently be precipitated in neo-formed phases (oxyanions CrO_4^{2-} and AsO_4^{3-} with a similar tetrahedral structure can substitute for silicate in calcium silicate hydrates; (Cornelis et al. 2008) or be released from the slag. Uncontrolled leaching of steel slag at abandoned sites has resulted in water containing up to 100 µg L^{-1} of vanadium entering local water courses (33 ±25 µg L^{-1}, n=12; (Mayes et al. 2008, Riley &Mayes 2015, Roadcap et al. 2005).

Currently there is significant uncertainty about the factors controlling the kinetics of slag leaching, particularly for aggregate-sized slag particles, where the formation of surface alteration layers on the slag significantly affects the leaching process (Costa et al. 2016, Hobson et al. 2017, Huijgen &Comans 2006, Huijgen et al. 2005, Nikolić et al. 2016). This makes it difficult to specify the optimum weathering/leaching regime for slag conditioning (for example the recommended weathering period for BOF slag varies widely between one month and 12 months; ASA 2002, Dippenaar 2004, Huang et al. 2007, UKEA 2014a, Wang et al. 2010). Also, the release of potentially toxic trace elements, such as Cr and V, from slag is not widely perceived as an issue, provided release occurs primarily during slag conditioning where the generated leachate can be managed. However, this implies that better understanding is needed of how trace metal release evolves over time with the geochemistry of the system to ensure that trace metals do not become an issue that adversely effects the beneficial reuse of slag.

This study will investigate leachate generation processes in BOF slag–water–air systems as a function of time (up to 3 months), and assess the effect of changing particle size on leachate generation. In addition, slag mineral alteration and the development of an alteration rind will be investigated using electron microscopy. The effect of pre-treatment (6 months total immersion in aerated water) will be determined with respect to the potential for further leachate generation after the initial treatment process.

Methods and Materials

2.1 Sample collection and preparation.

BOF steel slag was collected in May 2013, within one week of its deposition, from the Yarborough Landfill at the Tata Steel Europe steelworks in Scunthorpe, UK (LAT 53°35′22.24″ LONG 0°35′41.52″). The initial sample consisted of irregularly shaped 50 - 500 g blocks. Three 10 x 10 x 20 mm cuboids of BOF slag were cut from intact slag blocks using a diamond saw. Two were used directly in the leaching tests reported below (which will be referred to as the blocks), whereas one was soaked in deionised water (DIW; 18 MW; 2L; Hobson et al. 2017) that was continually aerated using an aquarium pump in a glass Duran bottle stoppered with an air-permeable foam bung for 6 months prior to use (the pre-weathered block). Water losses due to evaporation were regularly replaced by deionised water. The remainder of the BOF steel slag sample was crushed using a jaw crusher and sieved into separate size fractions. Two size fractions were retained for testing; 0.5 – 1 mm (sand particles), and 2 mm – 5 mm (fine gravel particles). This provided three sized fractions

representative of medium and fine gravels and sand used in standard aggregate mixtures for highway base and subbase layers (ASTM 2001).

2.2 Leaching Tests.

Triplicate crushed slag samples (~2 g) were placed in 250 ml Duran bottles (Duran Group) containing DIW (~200 mL) to produce a liquid to solid ratio of 10 g L^{-1}. The three 10 x 10 x 20 mm blocks (one pre-weathered, each ~8 g) were placed in 1 L Duran bottles containing DIW (~800 mL) to produce the same liquid to solid ratio. The Duran bottles were stoppered with air-permeable foam bungs to allow interaction with the atmosphere. The Duran bottles were kept on the lab bench at roughly 20 °C. Periodically (after 0, 1, 2, 5, 8, 14, 28, 57 and 73 days) the bottles were gently swirled, allowed to settle until the supernatant was visually clear, and then measured for pH and conductivity. Solution samples (1 mL) were taken of the clear supernatant from each replicate and acidified with 5% HNO$_3$ (9 mL; AnalaR NORMAPUR, VWR) before ICP-OES analysis. After sampling, the experiments were made-up to their initial volumes with DIW. After the final solution samples were collected, the entire solid fractions were recovered using a 90 mm Buckner funnel and micro-glass fibre filters (Fisherbrand MF200-90).

2.3 Scanning Electron Microscopy.

The recovered slag fractions were set in Araldite® epoxy resin (Huntsman Advanced Materials), and the surface of the resulting resin blocks were polished using 3, 1, and 1/4 µm diamond paste (Struers) to expose the slag pieces in cross-section. Back-scatter electron micrographs were collected on a Quanta FEG 650 scanning electron microscope (SEM), which was equipped with an Oxford Instruments INCA 350 energy-dispersive X-ray spectroscopy (EDS) system controlled by AZtec acquisition software (i.e. for semi quantitative elemental analysis and mapping applications; elemental composition data was calibrated using a Co metal target). The AZTec software only reports EDS peaks that are >3σ above baseline noise and uses theoretical element peak area relationships to deconvolute any overlapping EDS peaks (e.g. to avoid overestimation of the V Kα peak area in the presence of an overlapping Ti Kβ peak). Calibrated EDS data from each spot analysis was converted to mol%, and the total elemental abundance was normalised to 100% to allow determination of stoichiometric ratios (e.g. Ca/Si, V/Si etc.) within the phases analysed. Limits of detection are element specific, but normally were between 0.1 – 0.2 mol%. The average surface alteration depth for each sample was determined using perpendicular measurements at 50 µm intervals along the surface seen in 8-10 separate SEM images from each sample (n = 80 – 120; SI Fig. S1).

2.4 Geochemical Analysis.

Solution pH and conductivity were measured using a Hach HQ40d multi-parameter meter and regularly calibrated electrodes. Elemental concentrations in aqueous solutions were determined by inductively coupled plasma atomic emission spectroscopy using a Thermo Fisher iCAP 7400 Radial ICP-OES (limit of detection for each element is presented in SI Table S1). Major and minor element composition of solid samples was determined by x-ray fluorescence (XRF) spectroscopy using an Olympus X-5000 XRF analyser. Mineralogical analysis was performed using a Bruker D8 X-ray diffractometer (XRD) using Cu K-alpha radiation.

Results

3.1 Slag composition

The elemental composition of the slag was dominated by Ca, Fe and Si with Mn and Mg as minor constituents (Table 1). XRD analysis (SI Fig. S2) showed it contains phases structurally matched to larnite (dicalcium silicate; β-Ca_2SiO_4), brownmillerite (dicalcium aluminoferrite; $Ca_2(Al, Fe)_2O_5$), free lime (CaO) and a wüstite-like phase (FeO).

3.2 Leaching tests

The solution pH behaved similarly in the leaching tests of all the BOF slag size fractions (Fig. 1). After 20 minutes of reaction the pH of all tests was ≥ 9 (including the weathered block test), the maximum pH value was recorded after ~1 day and then the pH value gradually decreased with time. The sand-sized slag fraction reached the highest pH value after 24 hrs (pH 11.7), and the gravel-sized fraction and the blocks reached progressively lower maximum values (10.7, and 10.4 respectively). The pre-weathered block rapidly buffered the solution to pH 9.0, but only a very modest further increase over the first 24 hrs (to pH 9.1) before the pH decreased steadily until the end of the test.

The concentration of calcium ([Ca] mmol L^{-1}) in the leaching tests on fresh slag exhibited a similar pattern with time for all the size fractions (Fig. 1). Initially there was a rapid increase in [Ca] to a short-term peak, a decrease in [Ca] at intermediate times, followed by a subsequent increase in [Ca] in the long-term. Generally, the [Ca] was highest in the leaching test on the sand-sized fraction, and progressively lower with increasing slag particle size. The peak [Ca] in the leaching test on the sand-sized fraction occurred after 24 hrs (1.1 mmol L^{-1}), and unlike the tests on other size fractions, was larger than in the long-term [Ca] (0.58 mmol L^{-}

^{1}). With the gravel-sized fraction the short-term peak also occurred after 24 hrs (0.34 mmol L^{-1}), but was less pronounced and exceeded by the long-term [Ca] (0.60 mmol L^{-1}). With the block samples the short-term peak (0.30 mmol L^{-1}) occurred after 5 days, was quite modest in magnitude and was just exceeded by the long-term [Ca] (0.34 mmol L^{-1}). The leaching test on the pre-weathered block exhibited no short-term peak, just a gradual increase in the [Ca] with time, reaching a final [Ca] just slightly lower than other blocks (0.25 mmol L^{-1}).

The variation in silicon concentrations ([Si], mmol L^{-1}) with time exhibited a similar pattern in all the leaching tests (Fig. 1); a gradual increase in concentration with time to a near constant value after 73 days. Typically, at any time point, the [Si] was largest with the smallest size-fraction (sand-sized), decreased with increasing particle size, and was smallest with the pre-weathered block (the final concentrations were 1.1, 0.91, 0.47 and 0.08 mmol L^{-1} for sand-sized, fine gravel-sized, blocks and pre-weathered block, respectively). Aqueous [Ca]/[Si] ratios were consistently > 1 during the early part of the tests (< 5 days) for each size fraction (SI Fig. S3). However, at later time points (>14 days) the [Ca]/[Si] ratios are consistently between 0.7-0.9 (Table 2, SI Fig. S3) for all size fractions except the pre-weathered block ([Ca]/[Si] > 1 for the entire test).

The vanadium concentration ([V], mmol L^{-1}) during leaching tests (Fig. 1) exhibits very similar patterns to the [Si] concentrations, except [V] concentrations are approximately 4% of [Si] for each size fraction ([V]/[Si] ratios varied from 0.03-0.05 throughout each test; Table 1, SI Fig. S3). As with [Si], the [V] was highest in the sand-sized fraction tests. The concentrations of Na, Mg, K, Fe, Al, P, Cr, Mn, Ti, Zn, and As were also measured and largely below detection limit in all leaching tests (SI Table S2).

3.3 SEM analysis of slag recovered from the leaching tests.

SEM analysis showed that the centre of slag particles consist an interlocking crystalline matrix of typically 10-50 μm grains (Fig. 2; SI Fig. S1). The major phases identified by XRD analysis were also confirmed by EDS spot analysis (SI Fig. S4). The free lime phase was substituted with Fe, Mn, Mg and Sc; the wüstite-like phase contained Fe, Mn, Mg and Ca; the dicalcium silicate phase also contained a range of trace elements including P, Fe and V (SI Table S3); and the dicalcium aluminoferrite phase also contained Ti, Mn, Cr and V.

All size fractions exhibited an alteration zone around the edge of particles, visible on back-scatter electron micrographs (Fig. 2). The average alteration zone depth (as delineated by the unaltered dicalcium aluminoferrite and refractory oxide fragments) was highly variable within slag fractions, but generally increased with increasing particle size from ~30μm on the sand sized particles to ~150 μm on the blocks (Table 3). The alteration zone depth on the

surface of the pre-weathered block (~80μm) was thinner (but within error) of the blocks despite the additional period of leaching. EDS spot analysis indicated that dicalcium aluminoferrite and refractory oxide phases remained in the altered zone, but free lime and dicalcium silicate are largely absent, replaced by a low density Ca and Si containing phase, previously identified as a calcium-silicate-hydrate phase (Ca-Si-H; SI Table S3; Hobson et al. 2017). SEM images of the block samples (SI Fig. S5a) indicated that there were occasional voids within the specimens remote from the block surface, and that some of these voids contained Ca-Si-H after weathering. Furthermore, an additional Ca and O-containing layer (presumed to be $CaCO_3$) was occasionally seen on the surface of selected sand-sized slag particles, and the pre-weathered block (SI Fig. S5b).

Detailed analysis of the Ca-Si-H layer present in the altered surface region of the slag particles showed considerable variation between samples (Fig. 3a). Ca/Si ratios were generally lower in the Ca-Si-H than that recorded in the dicalcium silicate phase (2.3 ±0.2) and averaged 0.7, 1.1 and 1.4 respectively in the altered surface region found in the sand, gravel and blocks respectively (Table 2; SI Table S4). The Ca-Si-H phase was generally found to have an amorphous structure, except for parts of the alteration zone of the block samples, which had a blade like morphology similar to the Ca-Si-H(II) phase jennite (Allen et al. 2007, Richardson 1999). The surface (0-3 µm) of the Ca-Si-H phase was Ca depleted relative to the bulk phase, except in sand sized particles. V/Si ratios in the Ca-Si-H phases were generally within measurement error of the values found in the dicalcium silicates phase, although there was a slight trend to decreasing V/Si with decreasing Ca/Si ratio in the Ca-Si-H phase (Fig. 4a). This trend was also evident with some other trace elements within the Ca-Si-H (e.g. V, P, W, Al, Sc, Mg; see Fig. 4 for selected examples), which indicates preferential trace element uptake to Ca-Si-H with increasing Ca/Si ratio. However other trace constituents (e.g. Fe, Mn, Ti) do not exhibit a strong trend with changes in Ca/Si of the Ca-Si-H phase.

Discussion

4.1 Surface alteration during BOF slag weathering under aerated conditions.

Dicalcium silicate and free lime dissolution, constitute the initial sources of dissolved alkalinity, Ca, Si (and associated trace metals) during BOF slag weathering. The very high aqueous Ca/Si ratios observed in the first five days of the leaching tests (SI Fig. S3) most likely relate to a short period dominated by very rapid hydration and dissolution of free lime (Eqns 1 and 2; Shi et al. 2002).

$$CaO\ (s) + H_2O \rightarrow Ca(OH)_2\ (s) \tag{1}$$

$$Ca(OH)_2(s) \rightleftharpoons Ca^{2+}(aq) + 2OH^- \qquad\qquad (2)$$

This is followed by a longer period (5-14 days) when [Si] and [Ca] were increasing and slower dicalcium silicate dissolution dominates (Eqn. 3a; Taylor 1986);

$$Ca_2SiO_4(s) + 2H_2O \rightarrow 2Ca^{2+}(aq) + H_2SiO_4^{2-}(aq) + 2OH^- \qquad (3a; pH <9)$$

$$6Ca_2SiO_4(s) + 12H_2O \rightarrow Ca_5Si_6O_{16}(OH)_2 \cdot 4H_2O(s) + 7Ca^{2+}(aq) + 14OH^- \quad (3b; pH <11)$$

$$6Ca_2SiO_4(s) + 14H_2O \rightarrow Ca_9Si_6O_{18}(OH)_6 \cdot 8H_2O(s) + 3Ca(OH)_2(s) \qquad (3c; pH >12)$$
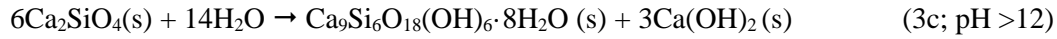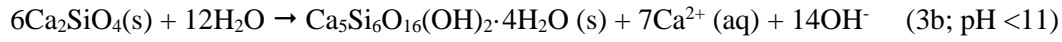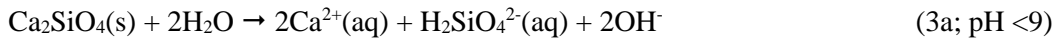
(reactions 3b and c are simplified equations for the formation of tobermorite (Ca-Si-H (I)) and jennite (Ca-Si-H (II)), respectively).

Weathering of BOF slag produced an altered zone at the surface on the slag particles where free lime and dicalcium silicate were largely absent. In this zone a new, low density, Ca-Si-H phase formed between the unaltered fragments of dicalcium aluminoferrite and wüstite. Ca-Si-H gel phases are the main products when dicalcium silicate reacts with water (Chen et al. 2004, Jennings 1986, Taylor 1986) and rapidly form from solution by heterogeneous nucleation (Garrault &Nonat 2001). In addition, the dicalcium silicate hydration mechanism is highly dependent on water availability, and therefore, there is propensity for oversaturation and retention of $Ca(OH)_2$ within the alteration products (Eqns. 3b, c). There was no evidence for extensive Ca-Si-H phases forming beyond the original surface of the slag particles. There were occasional observations of alteration in pore space within the slag (BOF slag has effective porosity of ~6% and accumulation of alteration products within voids is thought to contribute to the increased aggregate strength observed in post-weathered BOF slags; Wu et al. 2007).

An additional Ca-containing layer was occasionally observed on the surface of the slag particles that is consistent with calcium carbonate ($CaCO_3$) which readily forms where alkaline Ca^{2+}-rich solutions are in contact with atmospheric CO_2 (Eqn. 4).

$$Ca^{2+}(aq) + CO_2(aq) + 2OH^- \rightleftharpoons CaCO_3(s) + H_2O \qquad\qquad (4)$$
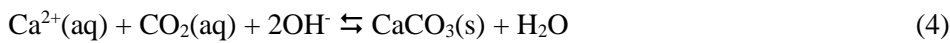
At high pH, $CaCO_3$ precipitation from $Ca(OH)_2$ solutions is rapid, and limited only by the rate of CO_2 in-gassing and diffusion (Hodkin et al. 2016, Inskeep &Bloom 1985, Noyes et al. 1996). Thus, CO_2 in-gassing and $CaCO_3$ formation was responsible for the rapid reduction in [Ca] immediately following the period of free lime dissolution and the general trend of reducing pH with time during these experiments.

4.2 Effect of particle size on dicalcium silicate reaction.

There was a clear difference in the Ca/Si ratio of the neo-formed Ca-Si-H phase in the slag leaching tests using sand, fine gravel, and the 10x10x20 mm blocks (0.7, 1.1 and 1.4 respectively). The Ca/Si ratio retained in Ca-Si-H phases gives a good indication of the solution

chemistry in contact with the Ca-Si-H during precipitation. Ca-Si-H phases with a Ca/Si ratio < 1.0 form at relatively low pH (< 11), low [Ca] (< 2 mmol L^{-1}) and high [Si] (> 1 mmol L^{-1}) (Walker et al. 2016, reviewed the experimental conditions in 777 separate Ca-Si-H crystallisation experiments which produced phases with Ca/Si ratios ranging from 0.0 to 3.0). Therefore the Ca-Si-H phase formed in the experiments using sand-sized particles is broadly consistent with the bulk solution chemistry measured after 5 (Eqn. 3b). The solution chemistry in the experiments using gravel particles and blocks also favour formation of Ca-Si-H with low Ca/Si ratios. However, the Ca/Si ratios in the altered zone of the fine gravel particles and medium gravel blocks were 1.1 and 1.4 respectively. Ca-Si-H phases with Ca/Si ratios >1 indicate formation from solutions with progressively higher [Ca], lower [Si] and high pH (up to 20 mmol L^{-1} Ca, pH 12.5, and <0.01 mmol L^{-1} Si; Walker et al. 2016). Therefore the local microenvironment within the gel phase during Ca-Si-H precipitation must have been at considerable disequilibria with respect to the bulk solution in these experiments. As there was no obvious difference in slag composition between the experiments, the variation in the Ca-Si-H Ca/Si ratios must relate to altered surface region thickness.

After the leaching tests, the depth of alteration zone increased with decreasing slag surface area to volume ratio, i.e. alteration zone depth was greatest in the largest particles. This was probably because systems with larger slag surface area initially caused more rapid changes in the solution chemistry (resulting in higher [Ca] and [Si] in solution). Thus, when averaged over the test, the degree of disequibria between the bulk solution and the alteration zone was lower in tests with larger surface area, resulting in slower progression of the alteration zone front into the smaller particles. For these particles, the shorter ion diffusion pathways led to formation of a Ca-Si-H phase in conditions close to equilibrium with the bulk solution. Conversely, for large particles, the thicker alteration zone indicates more rapid progression of the alteration front, which led to longer ion diffusion pathways and more difference between the chemistry of the alteration front and the bulk solution, and precipitation of Ca-Si-H with higher Ca/Si ratios (Eqn. 3c; explaining the occasional observed jennite-like structures and composition found in the block samples).

After two weeks in all experiments the rate of change in solution chemistry reduced and the aqueous Ca/Si ratio evolved from that expected from initial free lime and dicalcium silicate dissolution (> 2) to values much closer to those found in the Ca-Si-H layer (0.7 – 0.9). This suggests that the rate of slag leaching had slowed significantly over the period of testing, probably as a result of Ca-Si-H formation in the altered zone, and CaCO$_3$ on the slag surface. Thus leaching of fresh slag likely becomes a diffusion controlled process, limited by the rate at which water can diffuse through the neo-formed precipitates to the zone within the slag where free lime and dicalcium silicate are available to hydrate.

There is also evidence that the surface of the Ca-Si-H layer that was originally in contact with solution is depleted in Ca relative to the bulk of the Ca-Si-H layer. This may represent an incipient secondary alteration front forming within the Ca-Si-H layer. In Portland cement evolution, early formed Ca-Si-H(II) with an imperfect jennite structure containing $Ca(OH)_2$ and a Ca/Si of 1.5 – 2.2 (typically 2.0; Chen et al. 2004, Gard &Taylor 1976) commonly recrystallizes as pore fluid composition evolves to lower [Ca] and lower pH to form Ca-Si-H(I) with an imperfect tobermorite structure with a Ca/Si of 0.67 – 1.5 (typically ~0.8; Chen et al. 2004). In these experiments, however, it is more likely that this surface alteration simply represents the preferential loss of more soluble elements (i.e. Ca) from the Ca-Si-H phase prior to full dissolution. Trace element ratios (e.g. V/Si and P/Si) within the Ca-Si-H were also notable lower in areas with lower Ca/Si ratios (Fig. 4). Therefore, Ca-Si-H alteration potentially also offers a mechanism for trace element release to solution.

4.3 Controls on Vanadium release during slag weathering.

V release from BOF slag is of concern due to its generally high concentration in slag (Chaurand et al. 2006, De Windt et al. 2011, Proctor et al. 2000, Tossavainen et al. 2007), its high aquatic toxicity as dissolved V(V) (Barceloux 1999, Jensen-Fontaine et al. 2014, Mišík et al. 2014), and the increased mobility of the vanadate oxyanion at high pH (Peacock &Sherman 2004, Wehrli &Stumm 1989). During BOF slag leaching [V] is thought to be ultimately limited by $Ca_3(VO_4)_2$ solubility ($K_{sp} = 10^{-17.97}$; Allison et al. 1991, Cornelis et al. 2008, De Windt et al. 2011, Huijgen &Comans 2006, Schindler et al. 2000). Due to the inverse relationship of [Ca] and [V] implied by $Ca_3(VO_4)_2$ solubility, and high [Ca] due to $Ca(OH)_2$ equilibrium, [V] is normally limited to very low concentrations in slag leachates (Fig. 5). However, under aerated leaching conditions [Ca] and hydroxide are removed by $CaCO_3$ precipitation (Eqn. 4), leading the conditions where V can accumulate in solution at much higher concentrations. In all the slag leaching experiments, the solution composition evolves with time towards equilibrium with both $CaCO_3$ and $Ca_3(VO_4)_2$. Experiments using sand-sized particles reach this end point most rapidly due to higher surface area, and total Ca_2SiO_4 dissolved, but the experiments with the gravel and block samples show significant progression towards that end point. The initial release of V to solution is due to dicalcium silicate dissolution (Eqn. 3a) but as the reaction progresses V is probably isomorphically substituted for Si within the neo-formed Ca-Si-H phase (Eqn. 3b, c; as observed by Hobson et al. 2017). After 2 weeks, V release is reduced as slow Ca-Si-H dissolution becomes the dominant V leaching process in all experiments. This ultimate end-point is most clearly illustrated by the leaching experiment using the pre-weathered block, in which the initial rapid dicalcium silicate / free lime dominated leaching phase is not observed and solution chemistry is controlled by slower dissolution of secondary Ca-Si-H and $CaCO_3$ phases present at the slag surface (with notably lower rates of V release).

4.4 Implications of storage and reuse of BOF slag.

There are 3 distinct phases during the weathering on BOF slag particles under aerated conditions. Firstly, a relatively short period when leaching is dominated by hydration and dissolution of free lime; secondly the hydration and dissolution of dicalcium silicate present at the surface of the slag particles; and thirdly a longer period when leaching is primarily controlled by much slower dissolution of secondary phases that form on the surface of slag particles.

Although CO_2 is available from atmosphere the initial rate of leaching is such that high pH, high [Ca] leachates are rapidly produced, especially if fine high surface area particles are present with crushed slag gravels. Over time, CO_2 in-gassing removes Ca and hydroxide, moderating solution pH and [Ca]. However, This produces conditions highly conducive to the accumulation of the V released from dicalcium silicate in solution (i.e. low [Ca] permits much higher [V] before equilibrium with $Ca_3(VO_4)_2$ is reached). Therefore, it is important that during slag weathering (e.g. in windrows) the early formed leachates are carefully monitored and managed to avoid any potential for environmental harm. Potential environmental harm may be minimised by conducting initial BOF Slag pre-conditioning under water saturated conditions (limiting CO_2 in-gassing, and limiting V accumulation in leachates), followed by leachate treatment (e.g. aeration) designed to promote CO_2 in-gassing, Ca removal and pH reduction (Gomes et al. 2017).

After the initial weathering period, a Ca-Si-H surface layer was formed on the slag particles. The presence of this layer indicates a shift from rapid solubility controlled weathering of dicalcium silicate to a slower diffusion limited process. In addition, other slag phases embedded in the Ca-Si-H such as V-hosting brownmillerite (Chaurand et al. 2007a, Chaurand et al. 2007b, Hobson et al. 2017), which becomes unstable below pH 8 (Engström et al. 2013), will be protected by buffering of micro-habits within the surface region by Ca-Si-H to pH > 9, reducing the potential for metal leaching. Release of trace elements (including V) from the pre-conditioned blocks will largely depend on the dissolution / recrystallization rates of the Ca-Si-H host phases. However, the formation of thick alteration layers, and the fact that the Ca-Si-H is still present at the original slag surface after 9 months (in the pre-weathered block), indicates that Ca-Si-H weathering rates are slow. In addition, diffusion limited hydration of dicalcium silicate may cause the Ca-Si-H layer to thicken over time, increasing the water diffusion pathway until dicalcium silicate hydration also becomes limited by Ca-Si-H dissolution rates. Thus, unless the BOF slag particles are physically broken to expose fresh surfaces, future generation of highly alkaline metal-rich leachates during after use is not expected, leading to low potential for environmental harm during most after use situations.

Conclusions

Initial leaching of BOF slag under aerated conditions is dominated by rapid hydration and dissolution of the free lime and dicalcium silicate phases present at particle surfaces. Preconditioning of BOF slag under fully aerated water promotes accumulation of V in solution. Therefore, initial leaching under air-excluded conditions is advisable as V concentrations are orders of magnitude lower in $Ca(OH)_2$ saturated solutions (although this may necessitate separate leachate treatment to reduce alkalinity prior to leachate discharge). After a relatively short period (two weeks under water immersion) solution chemistry becomes dominated by dissolution of the secondary Ca-Si-H and $CaCO_3$ phases that replace and covered the primary slag phases at the surface of the particles. This isolates the more reactive primary slag phase in the interior of particles and slows the overall release of alkalinity and metals to solution, leading to much lower potential for environmental harm during after use in a range of engineering applications.

Associated Content

6.1 Supporting online Information.

XRD pattern from unreacted BOF slag, additional SEM images, EDS spectra and composition tables. Plots of aqueous elemental ratios in leaching tests.

Author information

Corresponding Author E-mail: d.i.stewart@leeds.ac.uk; Phone: +44 113 3432287

Notes: The authors declare no competing financial interests.

Acknowledgements

REFERENCES

Ahmedzade P, Sengoz B (2009): Evaluation of steel slag coarse aggregate in hot mix asphalt concrete. Journal of Hazardous Materials 165, 300-305

Allen AJ, Thomas JJ, Jennings HM (2007): Composition and density of nanoscale calcium-silicate-hydrate in cement. Nat Mater 6, 311-316

Allison JD, Brown DS, Novo-gradac KJ 1991: MINTEQA2 / PRODEFA2, A Geochemical Assessment Model for Environmental Systems: Version 3.11 Databases and Version 3.0 user's manual, Environmental Research Laboratory, Office of Research and Development, EPA, Athens, GA, USA

ASA 2002: A guide to the use of iron and steel slag in roads. Revision 2, Australian Slag Association Inc

ASTM (2001): Standard Specification for Materials for Soil-Aggregate Subbase, Base, and Surface Courses, ASTM D1241-00. American Society for Testing and Materials

Barceloux DG (1999): Vanadium. J. Toxicol. Clin. Toxicol. 37, 265-78

Bobicki ER, Liu Q, Xu Z, Zeng H (2012): Carbon capture and storage using alkaline industrial wastes. Progress in Energy and Combustion Science 38, 302-320

Bonenfant D, Kharoune L, Sauve´ S, Hausler R, Niquette P, Mimeault M, Kharoune M (2008): CO_2 Sequestration Potential of Steel Slags at Ambient Pressure and Temperature. Industrial & Engineering Chemistry Research 47, 7610-7616

Chaurand P, Rose J, Domas J, Bottero J-Y (2006): Speciation of Cr and V within BOF steel slag reused in road constructions. Journal of Geochemical Exploration 88, 10-14

Chaurand P, Rose J, Briois V, Olivi L, Hazemann J-L, Proux O, Domas J, Bottero J-Y (2007a): Environmental impacts of steel slag reused in road construction: A crystallographic and molecular (XANES) approach. Journal of Hazardous Materials 139, 537-542

Chaurand P, Rose J, Briois V, Salome M, Proux O, Nassif V, Olivi L, Susini J, Hazemann J-L, Bottero J-Y (2007b): New Methodological Approach for the Vanadium K-Edge X-ray Absorption Near-Edge Structure Interpretation: Application to the Speciation of Vanadium in Oxide Phases from Steel Slag. The Journal of Physical Chemistry B 111, 5101-5110

Chen JJ, Thomas JJ, Taylor HFW, Jennings HM (2004): Solubility and structure of calcium silicate hydrate. Cement and Concrete Research 34, 1499-1519

Cornelis G, Johnson CA, Gerven TV, Vandecasteele C (2008): Leaching mechanisms of oxyanionic metalloid and metal species in alkaline solid wastes: A review. Applied Geochemistry 23, 955-976

Costa G, Polettini A, Pomi R, Stramazzo A (2016): Leaching modelling of slurry-phase carbonated steel slag. Journal of Hazardous Materials 302, 415-425

De Windt L, Chaurand P, Rose J (2011): Kinetics of steel slag leaching: Batch tests and modeling. Waste Management 31, 225-235

Dippenaar R (2004): Industrial uses of slag-The use and re-use of iron and steelmaking slags, VII International Conference on Molten Slags Fluxes and Salts. The South African Institute of Mining and Metallurgy, Johannesburg, Republic of South Africa

Eloneva S, Puheloinen E-M, Kanerva J, Ekroos A, Zevenhoven R, Fogelholm C-J (2010): Co-utilisation of CO_2 and steelmaking slags for production of pure $CaCO_3$ – legislative issues. Journal of Cleaner Production 18, 1833-1839

Engström F, Adolfsson D, Samuelsson C, Sandström Å, Björkman B (2013): A study of the solubility of pure slag minerals. Minerals Engineering 41, 46-52

EuroSlag 2006: Legal status of slags position paper. Position Paper, European Slag Association

EuroSlag 2012: Status of ferrous slag. Position Paper, European Slag Association

Gard JA, Taylor HFW (1976): Calcium silicate hydrate (II) ("C-S-H(II)"). Cement and Concrete Research 6, 667-677

Garrault S, Nonat A (2001): Hydrated Layer Formation on Tricalcium and Dicalcium Silicate Surfaces: Experimental Study and Numerical Simulations. Langmuir 17, 8131-8138

Geiseler J (1996): Use of steelworks slag in Europe. Waste Management 16, 59-63

Gomes HI, Rogerson M, Burke IT, Stewart DI, Mayes WM (2017): Hydraulic and biotic impacts on neutralisation of high-pH waters. Science of The Total Environment 601–602, 1271-1279

Hobson AJ, Stewart DI, Bray AW, Mortimer RJG, Mayes WM, Rogerson M, Burke IT (2017): Mechanism of Vanadium Leaching during Surface Weathering of Basic Oxygen Furnace Steel Slag Blocks: A Microfocus X-ray Absorption Spectroscopy and Electron Microscopy Study Environmental Science and Technology Article ASAP

Hodkin DJ, Stewart DI, Graham JT, Burke IT (2016): Coprecipitation of 14C and Sr with carbonate precipitates: The importance of reaction kinetics and recrystallization pathways. Science of The Total Environment 562, 335-343

Huang Y, Bird RN, Heidrich O (2007): A review of the use of recycled solid waste materials in asphalt pavements. . Resources, Conservation and Recycling 52, 58-73

Huijgen WJJ, Witkamp G-J, Comans RNJ (2005): Mineral CO2 sequestration by steel slag carbonation Environ. Sci. Technol. 39, 9676-9682

Huijgen WJJ, Comans RNJ (2006): Carbonation of steel slag for CO_2 sequestration: Leaching of products and reaction mechanisms. Environmental Science and Technology 40, 2790-2796

Inskeep WP, Bloom PR (1985): An evaluation of rate equations for calcite precipitation kinetics at pCO2 less than 0.01 atm and pH greater than 8. Geochimica et Cosmochimica Acta 49, 2165-2180

Jennings HM (1986): Aqueous Solubility Relationships for Two Types of Calcium Silicate Hydrate. Journal of the American Ceramic Society 69, 614-618

Jensen-Fontaine M, Norwood WP, Brown M, Dixon DG, Le XC (2014): Uptake and Speciation of Vanadium in the Benthic Invertebrate Hyalella azteca. Environmental Science & Technology 48, 731-738

Mayes WM, Younger PL, Aumônier J (2008): Hydrogeochemistry of alkaline steel slag leachates in the UK. Water, Air, and Soil Pollution 195, 35-50

Mišík M, Burke IT, Reismüller M, Pichler C, Rainer B, Mišíková K, Mayes WM, Knasmueller S (2014): Red mud a byproduct of aluminum production contains soluble vanadium that causes genotoxic and cytotoxic effects in higher plants. Science of The Total Environment 493, 883-890

Motz H, Geiseler J (2001): Products of steel slags an opportunity to save natural resources. Waste Management 21, 285-293

Navarro C, Díaz M, Villa-García MA (2010): Physico-Chemical Characterization of Steel Slag. Study of its Behavior under Simulated Environmental Conditions. Environmental Science & Technology 44, 5383-5388

Nikolić I, Drinčić A, Djurović D, Karanović L, Radmilović VV, Radmilović VR (2016): Kinetics of electric arc furnace slag leaching in alkaline solutions. Construction and Building Materials 108, 1-9

Noyes RM, Rubin MB, Bowers PG (1996): Transport of Carbon Dioxide between the Gas Phase and Water under Well-Stirred Conditions: Rate Constants and Mass Accommodation Coefficients. The Journal of Physical Chemistry 100, 4167-4172

Peacock CL, Sherman DM (2004): Vanadium(V) adsorption onto goethite (alpha-FeOOH) at pH 1.5 to 12. Geochimica et Cosmochimica Acta 68, 1723-1733

Piatak NM, Parsons MB, Seal Ii RR (2015): Characteristics and environmental aspects of slag: A review. Applied Geochemistry 57, 236-266

Proctor DM, Fehling KA, Shay EC, Wittenborn JL, Green JJ, Avent C, Bigham RD, Connolly M, Lee B, Shepker TO, Zak MA (2000): Physical and Chemical Characteristics of Blast Furnace, Basic Oxygen Furnace, and Electric Arc Furnace Steel Industry Slags. Environmental Science & Technology 34, 1576-1582

Qiang W, Peiyu Y (2010): Hydration properties of basic oxygen furnace steel slag. Construction and Building Materials 24, 1134-1140

Richardson IG (1999): The nature of C-S-H in hardened cements. Cement and Concrete Research 29, 1131-1147

Riley AL, Mayes WM (2015): Long-term evolution of highly alkaline steel slag drainage waters. Environmental Monitoring and Assessment 187, 1-16

Roadcap GS, Kelly WR, Bethke CM (2005): Geochemistry of Extremely Alkaline (pH > 12) Ground Water in Slag-Fill Aquifers. Ground Water 43, 806-816

Sasaki T, Hamazaki T (2015): Development of steam-aging process for steel slag, Technical Report 109. Nippon Steel & Sumitomo Metal

Schindler M, Hawthorne FC, Baur WH (2000): A crystal-chemical approach to the composition and occurrence of vanadium minerals. The Canadian Mineralogist 38, 1443-1456

Shen DH, Wu CM, Du JC (2009): Laboratory investigation of basic oxygen furnace slag for substitution of aggregate in porous asphalt mixture. Construction and Building Materials 23, 453-461

Shi H, Zhao Y, Li W (2002): Effects of temperature on the hydration characteristics of free lime. Cement and Concrete Research 32, 789-793

Smil V (2006): Transforming the twentieth century: technical innovations and their consequences. Oxford University Press Online

Taylor HFW (1986): Proposed structure of calcium silicate hydrate gel. J. Am. Ceram. Soc. 69, 464-67

Tiwari MK, Barpai S, Dewangan UK (2016): Steel slag utilization – Overview in Indian perspective. International Journal of Advanced Research 4, 2232-2246

Tossavainen M, Engstrom F, Yang Q, Menad N, Lidstrom Larsson M, Bjorkman B (2007): Characteristics of steel slag under different cooling conditions. Waste Management 27, 1335-1344

UKEA 2014a: Scunthorpe Aggregate Processing Permit Number EPR/LP3537VV. EPR/LP3537VV, UK Environment Agency

UKEA 2014b: Scunthorpe Aggregate Processing Decision Document. EPR/LP3537VV/A001, UK Environment Agency

van Oss HG (2016): Slag - Iron and Steel, U.S. Geological Survey Minerals Yearbook U.S. Department of the Interior - 2014. U.S. Geological Survey

Walker CS, Sutou S, Oda C, Mihara M, Honda A (2016): Calcium silicate hydrate (C-S-H) gel solubility data and a discrete solid phase model at 25°C based on two binary non-ideal solid solutions. Cement and Concrete Research 79, 1-30

Wang G, Wang Y, Gao Z (2010): Use of steel slag as a granular material: Volume expansion prediction and usability criteria. Journal of Hazardous Materials 184, 555-560

Wehrli B, Stumm W (1989): Vanadyl in natural waters: Adsorption and hydrolysis promote oxygenation. Geochimica et Cosmochimica Acta 53, 69-77

Wu S, Xue Y, Ye Q, Chen Y (2007): Utilization of steel slag as aggregates for stone mastic asphalt (SMA) mixtures. Building and Environment 42, 2580-2585

Yi H, Xu G, Cheng H, Wang J, Wan Y, Chen H (2012): An Overview of Utilization of Steel Slag. Procedia Environmental Sciences 16, 791-801

Yildirim IZ, Prezzi M (2011): Chemical, Mineralogical, and Morphological Properties of Steel Slag. Advances in Civil Engineering 2011, 13

Tables and Figures

Table 1. Major element composition of Yarborough BOF steel slag (21 samples).

Oxide	% w/w
CaO	40 ±5.4
FeO	32 ±9.4
SiO_2	14 ±3.4
MgO	5.2 ±1.1
MnO	4.5 ±0.8
Al_2O_3	1.2 ±0.4
P_2O_5	1.3 ±0.4
V_2O_5	0.81 ±0.24
TiO_2	0.30 ±0.13
Cr_2O_3	0.24 ±0.13
SO_3	0.23 ±0.09
TOTAL	*98.7*

Table 2. SEM-EDS element ratios determined in the unreacted Ca_2SiO_4 phases and the Ca-Si-H phase found in slag particle surface layers after 73 days water leaching; and, corresponding aqueous solution ratios calculated for solutions in contact with the slag particles.

Fraction	Phase	Ca/Si[#]	V/Si[#]	n
Sand fraction 0.5-1 mm	Ca_2SiO_4	2.31 ± 0.02	0.011 ± 0.004	7
	Bulk Ca-Si-H	0.72 ± 0.29	0.008 ± 0.005	37
	Ca-Si-H Surface layer*	0.71 ± 0.15	0.006 ± 0.002	7
	Aqueous solution^	0.70 ± 0.23	0.033 ± 0.003	12
Gravel fraction 2-5 mm	Ca_2SiO_4	2.24 ± 0.02	0.010 ± 0.002	6
	Bulk Ca-Si-H	1.12 ± 0.54	0.009 ± 0.005	31
	Ca-Si-H surface layer*	0.73 ± 0.30	0.006 ± 0.003	4
	Aqueous solution^	0.67 ± 0.11	0.029± 0.002	12
Blocks 20x10x10 mm	Ca_2SiO_4	2.30 ± 0.16	0.029 ± 0.021	17
	Bulk Ca-Si-H	1.40 ± 0.32	0.051 ± 0.033	21
	Ca-Si-H surface layer*	1.15 ± 0.22	0.021 ± 0.012	4
	Aqueous solution^	0.89 ± 0.10	0.045 ± 0.006	8

[#]element ratio uncertainty is 1 SD.
*0-3 µm from particle surface
^average of data after 14 days reaction
n is the number of EDS measurements for each phase.

Table 3. Thickness of the weathered zone on different sized BOF slag particles after leaching for 73 days

Slag fraction	Size range	Specific Surface area (m²/kg)	Alteration depth (µm)[#]	n
Sand	0.5-1 mm	1.7-3.3*	31 ± 20	111
Gravel	2-5 mm	0.3-0.7*	57 ± 22	90
Block	10x10x20mm	0.15	147 ± 74	115
Pre-weathered block	10x10x20	0.15	80 ± 34	80

[#]Alteration depth uncertainty is 1 SD

*Assumes cuboid particles and a slag density of 3600 kg/m³

n is the number of alteration depth measurements.
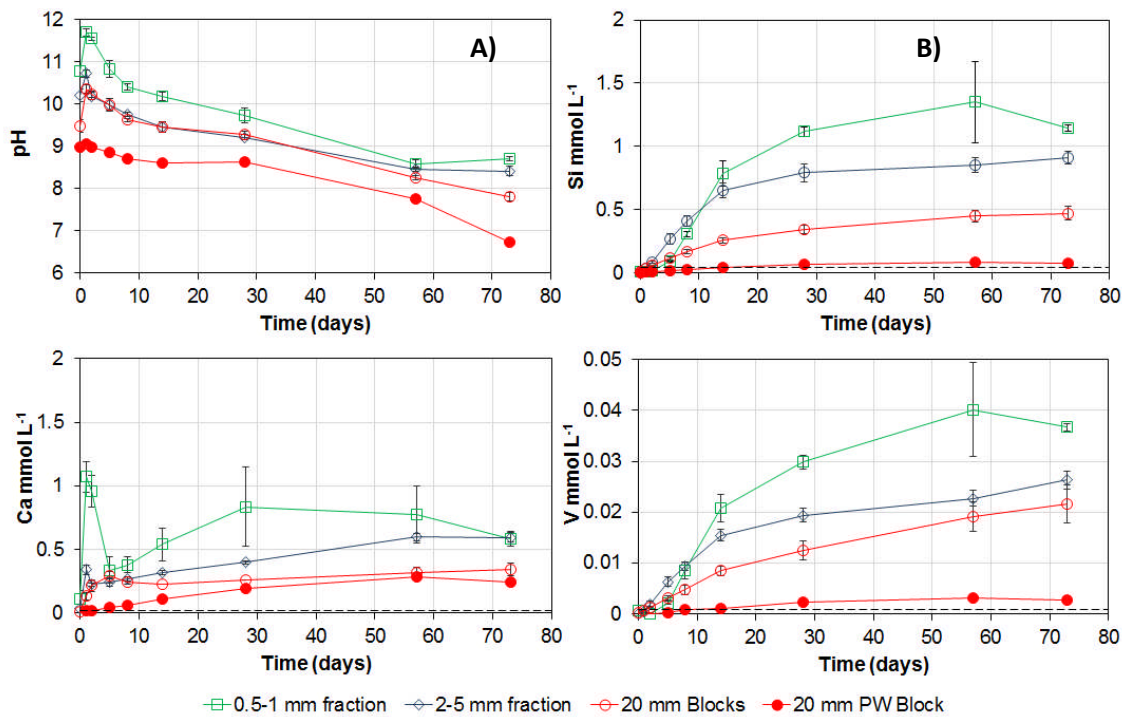
Figure 1. Evolution of solution pH, and aqueous Ca, Si and V concentrations (mmol L^{-1}) measured in leaching tests using 3 different sized BOF slag particles. Dashed lines show the limit of detections. Error bars show one standard deviation of triplicate measurements; where not shown, error bars are less than the size of the symbols used.
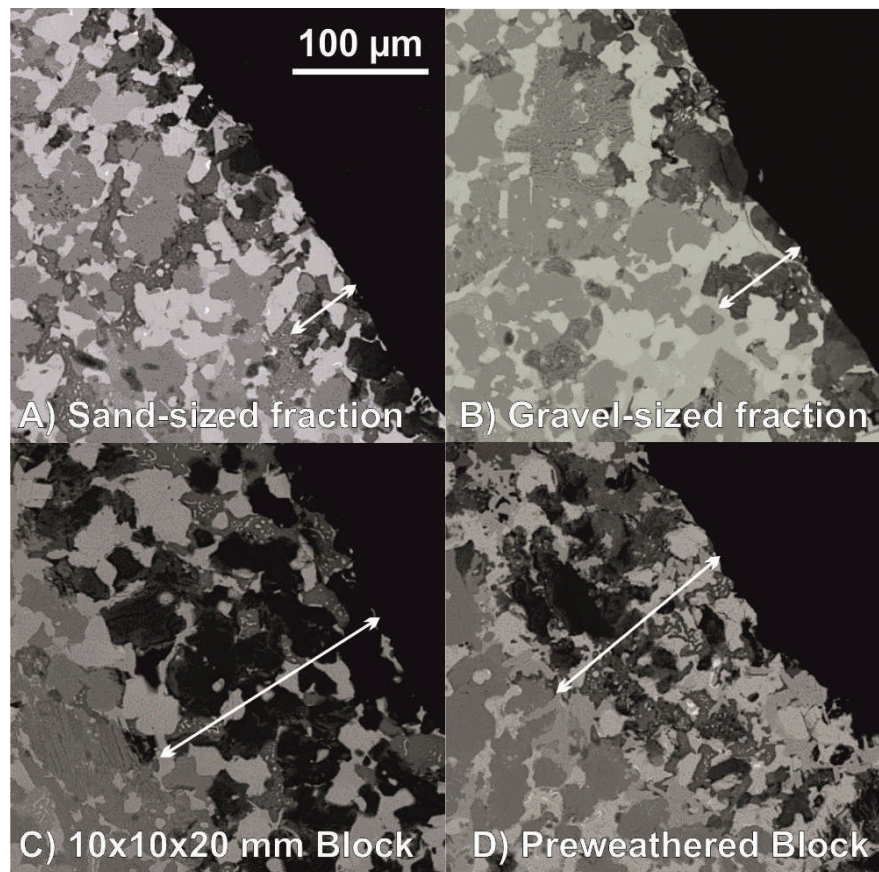
Figure 2. Example backscattered electron micrographs collected from the alteration zones present in different sized BOF slag particles after leaching for 73 days. All images shown at same scale, white arrows indicate measured alteration thickness.
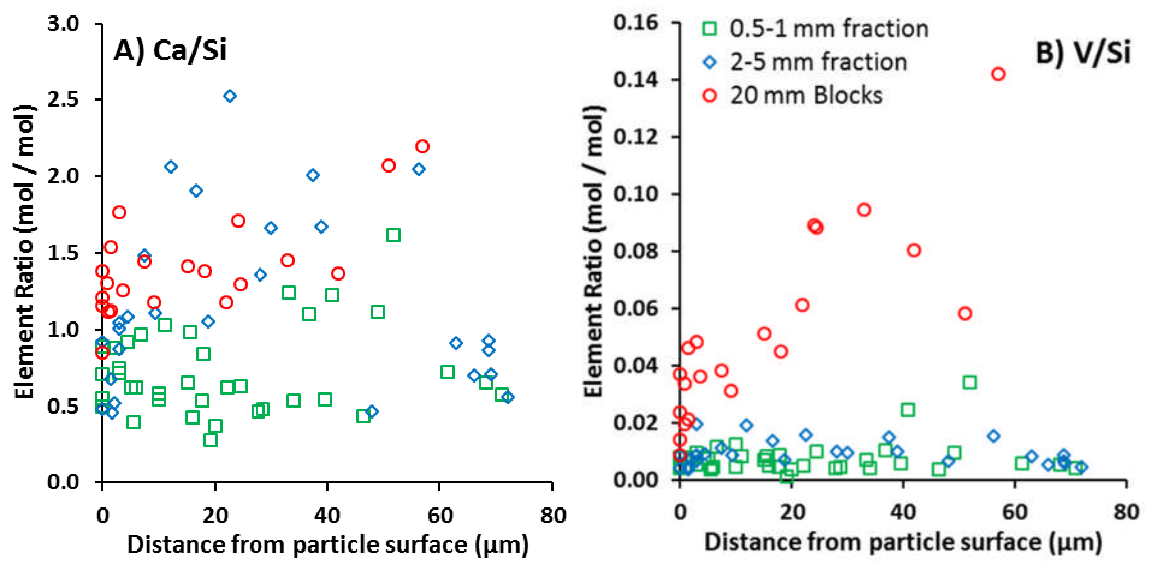
Figure 3. Distribution of SEM-EDS element ratios determined in the Ca-Si-H phase in the altered surface layer observed at the surface of slag particles after 73 days leaching.
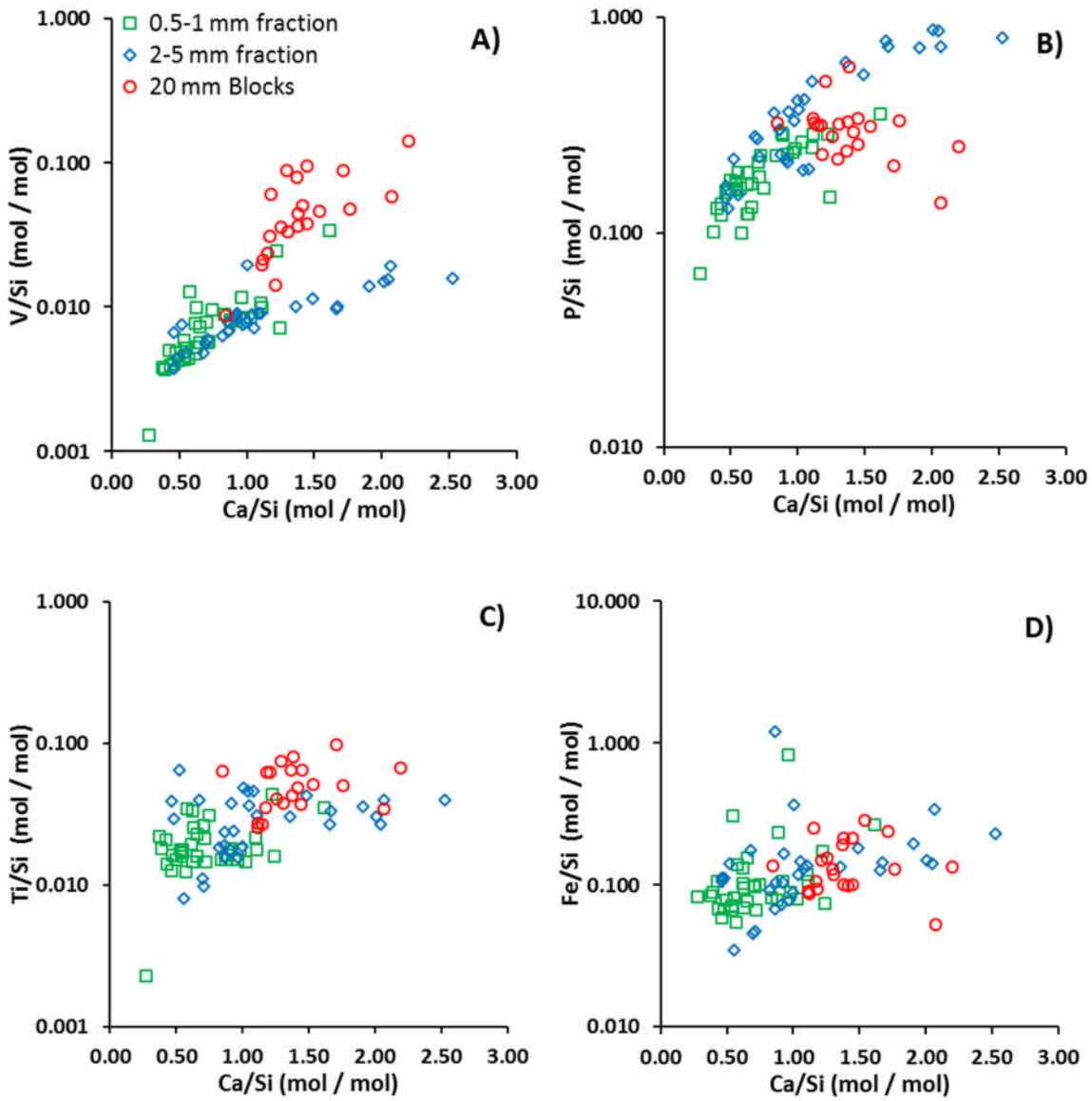
Figure 4. Variation in A) V/Si, B) P/Si, C) Ti/Si and D) Fe/Si as a function of Ca/SI ratio within the Ca-Si-H phases found in the surface alteration zone on slag particles.
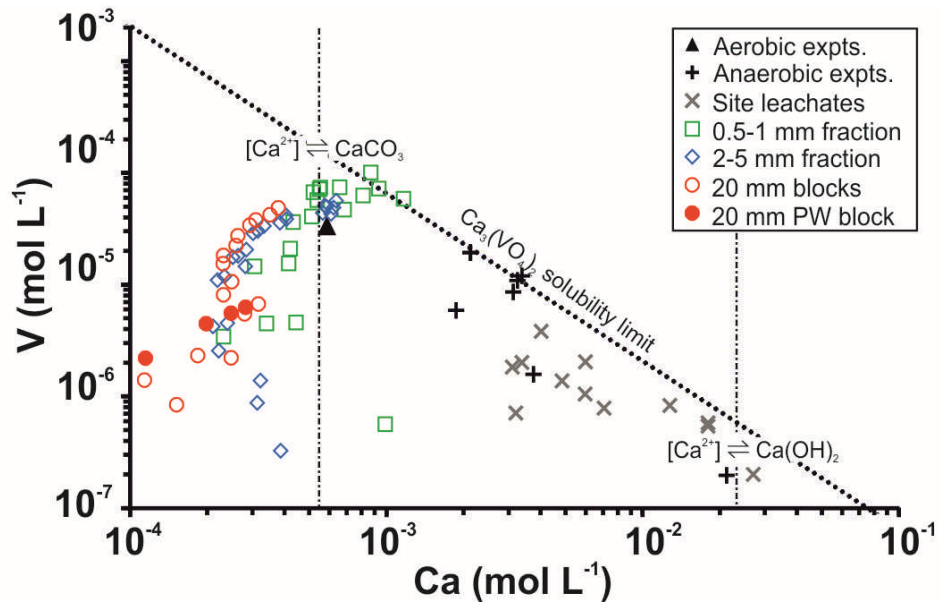
Figure 5. Plot of [V] versus [Ca] during the leaching tests on different BOF steel slag size fractions. Selected field data and end-point data from other aerated and air excluded leaching tests are shown for comparison (Experimental data from De Windt et al. 2011, Hobson et al. 2017, Huijgen &Comans 2006, site data from Mayes et al. 2008, Riley &Mayes 2015, Roadcap et al. 2005). Dotted line marks the solubility limit for $Ca_3(VO_4)_2$ at 20 °C (Log Ksp = -17.97; Allison et al. 1991). Vertical dashed lines indicate [Ca] in solutions in equilibrium with calcite in contact with atmospheric CO_2 or with $Ca(OH)_2$ respectively (both at 20 °C).

Supporting Information for:

Role of Calcium-Silicate-Hydrate in Controlling the Long-Term Leaching Behaviour of Basic Oxygen Furnace (BOF) Steel Slag: Effect of Particle Size on Leaching Properties.

Douglas I. Stewart[1*], Andrew W. Bray[2], Gideon Udoma[1], Andrew J. Hobson[2], William M. Mayes[3], Mike Rogerson[3] and Ian T. Burke[2]

[1]School of Civil Engineering, University of Leeds, LS2 9JT, UK

[2]School of Earth and Environment, University of Leeds, LS2 9JT, UK

[3]School of Environmental Sciences, University of Hull, Cottingham Road, Hull, HU6 7RX, UK

Corresponding Author - E-mail: d.i.stewart@leeds.ac.uk; Phone: +44 113 3432287

SI Table S1. Limits of detection for each element measured by ICP-OES.

Element	Limit of Detection (mmol L^{-1})
Na	0.2857
Mg	0.0178
K	0.0793
Fe	0.0075
Si	0.0416
Al	0.0312
P	0.0031
V	0.0008
Cr	0.0009
Mn	0.0011
Ti	0.0010
Ca	0.0204
Zn	0.0002
As	0.0004

SI Table S2. Experimental conditions and solution concentrations, as determined by ICP-OES. DL = below detection limit.

Size Fraction	Day	pH	Conductivity (µS)	Na	Mg	K	Fe	Si	Al	P	V	Cr	Mn	Ti	Ca	Zn	As
Sand (0.5-1.0 mm)	0	10.9	53	DL	DL	DL	0.020	DL	DL	DL	DL	DL	0.004	DL	0.155	DL	DL
		-	-	-	-	-	-	-	-	-	-	-	-	-	-	-	-
		10.7	32	DL	DL	DL	0.008	DL	DL	DL	DL	DL	0.002	DL	0.064	DL	DL
	1	11.8	790	DL	DL	DL	DL	DL	DL	DL	DL	DL	DL	DL	1.087	DL	DL
		11.6	664	DL	DL	DL	DL	DL	DL	DL	DL	DL	DL	DL	0.944	DL	DL
		11.7	725	DL	DL	DL	DL	DL	DL	DL	DL	DL	DL	DL	1.182	DL	DL
	2	11.6	731	DL	DL	DL	DL	DL	DL	DL	DL	DL	DL	DL	1.064	DL	DL
		11.5	575	DL	DL	DL	DL	DL	DL	DL	DL	DL	DL	DL	0.816	DL	DL
		11.5	679	DL	DL	DL	DL	DL	DL	DL	DL	DL	DL	DL	0.987	DL	DL
	5	11.0	186.1	DL	DL	DL	DL	0.091	DL	DL	0.002	DL	0.001	DL	0.443	0.001	DL
		10.6	105.7	DL	DL	DL	DL	0.081	DL	DL	0.002	DL	DL	DL	0.231	0.004	DL
		10.9	166.5	DL	DL	DL	DL	0.092	DL	DL	0.002	DL	DL	DL	0.340	0.001	DL
	8	10.5	137.5	DL	DL	DL	DL	0.333	DL	DL	0.011	DL	0.001	DL	0.420	DL	DL
		10.4	118.2	DL	DL	DL	DL	0.296	DL	DL	0.007	DL	DL	DL	0.306	DL	DL
		10.4	119.7	DL	DL	DL	DL	0.292	DL	DL	0.008	DL	DL	DL	0.415	DL	DL
	14	10.3	168.1	DL	DL	DL	DL	0.875	DL	DL	0.024	DL	0.003	DL	0.683	DL	DL
		10.2	146.9	DL	DL	DL	DL	0.793	DL	DL	0.020	DL	0.001	DL	0.511	DL	DL
		10.1	120.1	DL	DL	DL	DL	0.676	DL	DL	0.018	DL	0.002	DL	0.431	DL	DL
	28	9.5	133.2	DL	DL	DL	0.028	1.161	DL	DL	0.031	DL	0.008	DL	0.810	DL	DL
		9.8	127.5	DL	DL	DL	DL	1.100	DL	DL	0.029	DL	DL	DL	0.536	DL	DL
		9.9	133	DL	DL	DL	DL	1.092	DL	DL	0.029	DL	0.001	DL	1.163	DL	DL
	57	8.5	116.9	DL	0.019	DL	0.026	1.212	DL	DL	0.036	DL	0.006	DL	0.932	DL	DL
		8.6	118.6	DL	DL	DL	DL	1.119	DL	DL	0.034	DL	DL	DL	0.518	DL	DL
		8.7	122.9	DL	DL	DL	0.008	1.716	DL	0.004	0.051	DL	0.003	DL	0.867	DL	DL
	73	8.8	119.9	DL	DL	DL	DL	1.155	DL	DL	0.037	DL	DL	DL	0.551	DL	DL
		8.7	116.5	DL	DL	DL	DL	1.112	DL	DL	0.036	DL	0.001	DL	0.547	DL	DL
		8.7	114.2	DL	DL	DL	0.012	1.165	DL	DL	0.037	DL	0.004	DL	0.655	DL	DL

SI Table S2. Continued

Size Fraction	Day	pH	Conductivity (µS)	Na	Mg	K	Fe	Si	Al	P	V	Cr	Mn	Ti	Ca	Zn	As
										(mmol L^{-1})							
		10.3	24.9	DL	DL	DL	DL	DL	DL	DL	DL	DL	DL	DL	0.038	DL	DL
	0	10.2	20.59	DL	DL	DL	DL	DL	DL	DL	DL	DL	DL	DL	0.026	DL	DL
		10.0	19.22	DL	DL	DL	DL	DL	DL	DL	DL	DL	DL	DL	0.034	DL	DL
		10.8	156.9	DL	DL	DL	DL	DL	DL	DL	DL	DL	DL	DL	0.386	DL	DL
	1	10.7	132	DL	DL	DL	DL	DL	DL	DL	DL	DL	DL	DL	0.322	DL	DL
		10.7	134.4	DL	DL	DL	DL	DL	DL	DL	DL	DL	DL	DL	0.313	DL	DL
		10.3	89.7	DL	DL	DL	DL	0.070	DL	DL	0.001	DL	DL	DL	0.221	DL	DL
	2	10.2	94.1	DL	DL	DL	DL	0.083	DL	DL	0.002	DL	DL	DL	0.239	DL	DL
		10.1	86.2	DL	DL	DL	DL	0.091	DL	DL	0.002	DL	DL	DL	0.210	DL	DL
		10.0	85.9	DL	DL	DL	DL	0.255	DL	DL	0.006	DL	DL	DL	0.233	DL	DL
	5	9.8	80.2	DL	DL	DL	DL	0.229	DL	DL	0.006	DL	DL	DL	0.219	DL	DL
Gravel (2.0-5.0 mm)		10.1	96.4	DL	DL	DL	DL	0.315	DL	DL	0.007	DL	DL	DL	0.281	0.000	DL
		9.8	91.1	DL	DL	DL	DL	0.398	DL	DL	0.009	DL	DL	DL	0.263	DL	DL
	8	9.7	87	DL	DL	DL	DL	0.370	DL	DL	0.009	DL	DL	DL	0.251	DL	DL
		9.8	92.7	DL	DL	DL	DL	0.456	DL	DL	0.010	DL	DL	DL	0.283	DL	DL
		9.6	94.2	DL	DL	DL	DL	0.714	DL	DL	0.017	DL	DL	DL	0.332	DL	DL
	14	9.4	88.5	DL	DL	DL	DL	0.594	DL	DL	0.014	DL	DL	DL	0.301	DL	DL
		9.4	91.6	DL	DL	DL	DL	0.646	DL	DL	0.015	DL	DL	DL	0.314	DL	DL
		9.2	144.7	DL	DL	DL	DL	0.859	DL	DL	0.021	DL	DL	DL	0.405	DL	DL
	28	9.1	110.3	DL	DL	DL	DL	0.716	DL	DL	0.018	DL	DL	DL	0.384	DL	DL
		9.3	110.9	DL	DL	DL	DL	0.801	DL	DL	0.019	DL	DL	DL	0.407	DL	DL
		8.5	138	DL	DL	DL	DL	0.918	DL	DL	0.024	DL	DL	DL	0.620	DL	DL
	57	8.4	131.5	DL	DL	DL	DL	0.824	DL	DL	0.022	DL	DL	DL	0.562	DL	DL
		8.5	135.6	DL	DL	DL	DL	0.810	DL	0.003	0.022	DL	DL	DL	0.608	DL	DL
		8.5	133.3	DL	0.019	DL	DL	0.967	DL	DL	0.028	DL	DL	DL	0.636	DL	DL
	73	8.4	124.2	DL	DL	DL	DL	0.892	DL	DL	0.026	DL	DL	DL	0.572	DL	DL
		8.3	128.2	DL	DL	DL	DL	0.876	DL	DL	0.025	DL	DL	DL	0.581	DL	DL

SI Table S2. Continued

Size Fraction	Day	pH	Conductivity (µS)	Na	Mg	K	Fe	Si	Al	P	V	Cr	Mn	Ti	Ca	Zn	As
										(mmol L^{-1})							
Blocks (20 x 10 x 10 mm)	0	9.6	11.89	DL	DL	DL	DL	DL	DL	DL	DL	DL	DL	DL	DL	DL	DL
		9.4	11.57	DL	DL	DL	DL	DL	DL	DL	DL	DL	DL	DL	DL	DL	DL
	1	10.5	84.3	DL	DL	DL	DL	DL	DL	DL	DL	DL	DL	DL	0.152	DL	DL
		10.3	66.7	DL	DL	DL	DL	DL	DL	DL	DL	DL	DL	DL	0.114	DL	DL
	2	10.3	100.3	DL	DL	DL	DL	0.059	DL	DL	0.001	DL	DL	DL	0.248	DL	DL
		10.1	80.5	DL	DL	DL	DL	0.049	DL	DL	0.001	DL	DL	DL	0.183	DL	DL
	5	10.1	106.5	DL	DL	DL	DL	0.124	DL	DL	0.003	DL	DL	DL	0.316	DL	DL
		9.9	95.9	DL	DL	DL	DL	0.106	DL	DL	0.003	DL	DL	DL	0.279	0.001	DL
	8	9.7	85.2	DL	DL	DL	DL	0.178	DL	DL	0.005	DL	DL	DL	0.249	DL	DL
		9.6	81.5	DL	DL	DL	DL	0.153	DL	DL	0.004	DL	DL	DL	0.231	DL	DL
	14	9.5	73.3	DL	DL	DL	DL	0.271	DL	DL	0.009	DL	DL	DL	0.231	DL	DL
		9.4	72.8	DL	DL	DL	DL	0.240	DL	DL	0.008	DL	DL	DL	0.230	DL	DL
	28	9.3	77.9	DL	DL	DL	DL	0.366	DL	DL	0.014	DL	DL	DL	0.263	DL	DL
		9.2	79.2	DL	DL	DL	DL	0.321	DL	DL	0.011	DL	DL	DL	0.258	DL	DL
	57	8.3	101	DL	DL	DL	DL	0.479	DL	DL	0.021	DL	DL	DL	0.351	DL	DL
		8.2	94.2	DL	DL	DL	DL	0.415	DL	DL	0.017	DL	DL	DL	0.293	DL	DL
	73	8.0	95.6	DL	DL	DL	DL	0.508	DL	DL	0.024	DL	DL	DL	0.379	DL	DL
		7.6	87.3	DL	DL	DL	DL	0.434	DL	DL	0.019	DL	DL	DL	0.309	DL	DL
Pre-weathered Block (20 x 10 x 10 mm)	0	9.0	10.28	DL	DL	DL	DL	DL	DL	DL	DL	DL	DL	DL	DL	DL	DL
	1	9.1	18.45	DL	DL	DL	DL	DL	DL	DL	DL	DL	DL	DL	DL	DL	DL
	2	9.0	20.53	DL	DL	DL	DL	DL	DL	DL	DL	DL	DL	DL	DL	DL	DL
	5	8.9	28.5	DL	DL	DL	DL	DL	DL	DL	DL	DL	DL	DL	0.042	DL	DL
	8	8.7	33.6	DL	DL	DL	DL	DL	DL	DL	DL	DL	DL	DL	0.062	DL	DL
	14	8.6	43	DL	DL	DL	DL	DL	DL	DL	0.001	DL	DL	DL	0.115	DL	DL
	28	8.6	63.6	DL	DL	DL	DL	0.064	DL	DL	0.002	DL	DL	DL	0.198	DL	DL
	57	7.8	91	DL	DL	DL	DL	0.084	DL	DL	0.003	DL	DL	DL	0.282	DL	DL
	73	6.7	85.7	DL	DL	DL	DL	0.076	DL	DL	0.003	DL	DL	DL	0.248	DL	DL

SI Table S3. Average phase composition determined by SEM-EDS spot analysis performed on the unreacted Ca_2SiO_4 phase within BOF slag particles and the Ca-Si-H phase that replaces Ca_2SiO_4 in the surface alteration zone.

Element	A. Ca_2SiO_4 n = 17 Mol % ± 1σ	B. Ca-Si-H n = 89 Mol % ± 1σ	Enrichment factor (B/A)
O	56.4 ±2.7	55.6 ±9.2	1.0
Mg	0.13 ±0.09	0.41 ±0.77	3.2
Al	0.20 ±0.14	0.70 ±0.33	3.4
Si	11.8 ±0.65	17.7 ±5.9	1.5
P	1.41 ±0.08	4.45 ±1.46	3.2
S	n.d.*	0.16 ±0.14	-
Cl	n.d.*	0.12 ±0.07	-
Ca	27.4 ±1.4	16.1 ±5.1	0.6
Sc	0.19 ±0.04	0.12 ±0.08	0.6
Ti	0.14 ±0.10	0.50 ±0.28	3.6
V	0.22 ±0.22	0.28 ±0.35	1.3
Mn	0.05 ±0.02	0.25 ±0.44	5.5
Fe	0.50 ±0.11	2.43 ±2.43	5.0
W	0.06 ±0.01	0.13±0.04	2.2
Total	*98.5*	*99.0*	

*not detected.

SI Table S4. Chemical composition of phases in the surface alteration zone as a function of distance from the surface. Measured by SEM-EDS.

Size Fraction	Phase	Distance from surface (μm)	O	Mg	Al	Si	P	S	Cl	Ca mol %	Sc	Ti	V	Mn	Fe	Lu	W
Sand (0.5-1.0 mm)	Ca-Si-H	0	67.25	0.21	0.69	15.30	3.26	0.04	0.12	10.81	0.07	0.40	0.12	0.14	1.52	-0.02	0.09
	Ca-Si-H	3	49.11	0.24	0.78	24.01	3.88	0.06	0.12	17.92	0.12	0.74	0.23	0.15	2.43	0.04	0.18
	Ca-Si-H	5	38.82	0.24	0.83	31.47	3.84	ND	0.20	19.61	0.12	1.04	0.24	0.17	3.21	ND	0.23
	Ca-Si-H	10	49.61	0.33	0.72	26.09	2.62	0.18	0.17	15.13	ND	0.89	0.33	0.21	3.65	ND	0.07
	Ca-Si-H	15	43.79	0.29	0.86	27.52	3.63	0.07	0.20	18.03	0.13	0.63	0.20	0.26	4.26	-0.04	0.18
	Ca-Si-H	18	59.47	0.36	0.65	21.80	3.52	0.07	0.12	11.70	0.08	0.38	0.10	0.10	1.53	0.00	0.12
	Ca-Si-H	25	39.27	0.26	0.52	23.23	2.86	ND	0.17	14.63	0.10	0.59	0.23	0.14	2.20	ND	0.15
	Ca-Si-H	29	55.93	0.41	0.56	24.75	3.93	ND	0.11	11.79	0.11	0.40	0.12	0.08	1.67	ND	0.14
	Ca-Si-H	34	57.13	0.42	0.50	23.12	4.00	ND	0.11	12.35	ND	0.41	0.10	0.11	1.64	ND	0.13
	Ca-Si-H	40	55.98	0.39	0.46	23.83	3.98	ND	0.15	12.86	ND	0.38	0.14	0.08	1.58	ND	0.16
	Ca-Si-H	46	65.06	0.51	0.58	20.14	2.76	0.16	0.08	8.71	0.07	0.28	0.08	0.09	1.36	0.01	0.08
	Ca-Si-H/Ca$_2$SiO$_4$	52	62.32	0.19	0.19	11.32	1.39	0.06	ND	23.50	0.14	0.07	0.09	0.06	0.54	ND	0.05
	Ca$_2$SiO$_4$	60	57.38	ND	0.14	12.08	1.50	ND	ND	27.91	0.17	0.09	0.11	0.04	0.53	ND	0.05
	Ca$_2$SiO$_4$	63	52.07	0.23	ND	10.99	1.32	ND	ND	25.70	0.26	0.07	0.19	0.04	0.53	0.00	0.06
	Ca$_2$SiO$_4$	65	50.47	ND	0.16	10.66	1.30	ND	ND	24.82	0.24	0.07	0.16	0.06	0.54	ND	ND
	Ca-Si-H	0	55.84	0.30	0.65	23.12	4.41	ND	0.22	12.74	ND	0.39	0.12	0.17	1.87	0.00	0.11
	Ca-Si-H	3	44.99	0.35	0.55	26.44	4.82	ND	0.19	18.88	0.10	0.56	0.15	0.17	2.58	ND	0.23
	Ca-Si-H	6	36.24	0.50	0.67	31.73	5.29	ND	0.22	19.66	0.16	0.61	0.15	0.43	4.15	ND	0.19
	Ca-Si-H	10	37.81	1.26	0.62	28.67	4.53	0.19	0.21	15.63	0.10	0.51	0.13	1.26	8.79	ND	0.20
	Ca-Si-H	16	47.30	0.47	0.69	30.12	3.65	ND	0.19	12.88	0.08	0.62	0.15	0.34	3.22	ND	0.16
	Ca-Si-H	20	56.86	0.34	0.82	26.10	2.63	0.12	0.17	9.76	0.09	0.57	0.10	0.17	2.18	0.00	0.08

SI Table S4. Continued.

Size Fraction	Phase	Distance from surface (μm)	O	Mg	Al	Si	P	S	Cl	Ca mol %	Sc	Ti	V	Mn	Fe	Lu	W
	Ca-Si-H	0	65.06	0.51	0.47	18.69	3.27	0.11	0.12	9.29	0.07	0.28	0.08	0.40	1.45	ND	0.10
	Ca-Si-H	5	58.32	0.72	0.59	24.48	3.20	ND	0.15	9.61	ND	0.44	0.09	0.11	2.16	ND	0.13
	Ca-Si-H	19	53.42	0.80	0.69	31.03	1.99	ND	0.17	8.50	0.56	0.07	0.04	0.10	2.55	ND	0.15
	Ca-Si-H	37	42.48	0.40	0.38	22.43	5.57	ND	0.10	24.71	0.16	0.48	0.24	0.22	2.67	ND	0.16
	Ca-Si-H	41	58.02	0.29	0.92	14.62	4.19	0.05	0.05	17.86	0.15	0.63	0.36	0.20	2.51	ND	0.11
	Ca-Si-H	49	45.29	0.24	0.26	10.14	2.92	ND	0.06	11.26	0.08	0.18	0.10	0.06	1.07	ND	0.11
	Ca-Si-H	52	44.59	0.35	0.81	16.15	5.75	0.07	0.10	26.08	0.15	0.56	0.55	0.31	4.26	ND	0.13
	Ca-Si-H	61	52.57	0.49	0.40	22.62	5.18	ND	0.10	16.32	0.11	0.33	0.13	0.10	1.51	ND	0.13
	Ca-Si-H	68	47.27	0.54	0.51	26.61	4.50	0.06	0.13	17.39	0.10	0.42	0.15	0.08	2.03	ND	0.17
	Ca-Si-H	71	61.57	0.80	0.41	20.39	3.30	0.07	0.07	11.66	0.08	0.25	0.09	0.05	1.12	ND	0.11
	Ca-Si-H/Ca$_2$SiO$_4$	76	56.04	0.23	0.17	13.25	1.72	ND	ND	27.65	0.17	0.13	0.05	0.53	ND	ND	0.07
	Ca$_2$SiO$_4$	79	56.46	ND	0.13	12.34	1.51	ND	ND	28.62	0.19	ND	0.12	0.05	0.43	ND	0.07
Sand (0.5-1.0 mm)	Ca$_2$SiO$_4$	82	57.33	ND	0.15	12.10	1.51	ND	ND	27.89	0.18	0.10	0.14	0.05	0.47	ND	ND
	Ca-Si-H	0	61.93	0.44	0.53	14.90	4.24	ND	0.12	13.26	ND	0.24	0.12	0.57	3.49	0.02	0.10
	Ca-Si-H	2	62.35	0.21	0.53	16.08	4.69	ND	0.06	14.11	0.11	0.24	0.13	0.13	1.26	-0.02	0.12
	Ca-Si-H	4	37.73	0.58	0.39	21.29	4.94	ND	0.06	19.54	ND	0.38	0.17	0.10	2.26	12.38	0.19
	Ca-Si-H	7	26.63	0.55	0.39	22.48	5.34	ND	0.08	21.70	ND	0.34	0.26	3.23	18.66	ND	0.19
	Ca-Si-H	11	37.51	0.19	0.39	17.89	4.75	ND	0.08	18.40	0.12	0.26	0.15	0.14	1.43	-0.02	0.15
	Ca-Si-H	16	42.89	0.24	0.35	23.89	5.84	ND	0.10	23.45	0.12	0.42	0.20	0.16	2.12	ND	0.22
	Ca-Si-H	18	52.35	0.29	0.32	21.43	4.89	ND	0.06	17.99	0.08	0.32	0.19	0.17	1.74	ND	0.16
	Ca-Si-H	22	55.20	0.36	0.38	22.93	4.39	ND	0.09	14.32	0.07	0.33	0.12	0.10	1.57	ND	0.14
	Ca-Si-H	28	61.15	0.40	0.44	22.21	3.42	ND	0.12	10.32	0.08	0.28	0.09	0.08	1.31	ND	0.11
	Ca-Si-H	33	53.74	0.25	0.30	18.19	2.67	ND	0.06	22.59	0.15	0.29	0.13	0.10	1.34	ND	0.14
	Ca-Si-H/Ca$_2$SiO$_4$	36	58.90	0.23	0.23	15.47	2.22	ND	0.03	21.60	0.12	0.14	0.11	0.06	0.80	ND	0.10
	Ca$_2$SiO$_4$	38	58.29	0.06	0.10	12.00	1.44	ND	ND	27.24	0.15	0.07	0.08	0.05	0.46	ND	0.06
	Ca$_2$SiO$_4$	44	57.28	ND	0.11	12.23	1.48	ND	ND	28.12	0.19	ND	0.10	0.04	0.39	ND	0.07

SI Table S4. Continued.

Size Fraction	Phase	Distance from surface (μm)	O	Mg	Al	Si	P	S	Cl	Ca mol %	Sc	Ti	V	Mn	Fe	Lu	W
Gravel (2.0-5.0 mm)	Ca-Si-H	0	48.10	0.51	0.71	21.90	4.68	0.06	0.16	20.14	0.14	0.83	0.19	0.14	2.29	ND	0.16
	Ca-Si-H	3	52.03	0.45	0.54	19.30	3.76	ND	0.14	20.09	0.16	0.88	0.17	0.07	2.28	ND	0.15
	Ca-Si-H	5	41.22	0.55	0.48	23.08	4.60	0.09	0.20	25.00	0.17	1.06	0.21	0.10	3.05	ND	0.19
	Ca-Si-H	3	59.69	0.45	0.56	17.39	4.05	0.05	0.15	15.12	ND	0.41	0.12	0.08	1.81	ND	0.10
	Ca-Si-H	2	67.08	0.08	1.50	15.79	3.49	ND	0.15	8.21	0.06	1.01	0.12	0.13	2.24	ND	0.07
	Ca-Si-H	3	58.48	0.18	1.36	13.86	5.21	0.24	0.12	13.96	0.09	0.67	0.27	0.24	5.14	ND	0.09
	Ca-Si-H	2	51.91	0.37	0.92	10.38	2.90	0.04	0.08	7.02	0.05	0.41	0.05	0.17	1.82	ND	0.07
	Ca-Si-H	8	55.01	0.20	0.97	13.19	7.15	0.07	0.10	19.60	0.15	0.56	0.15	0.16	2.41	ND	0.15
	Ca-Si-H	12	61.21	0.14	0.67	8.82	6.46	0.08	0.07	18.21	0.11	0.35	0.17	0.29	3.04	ND	0.09
	Ca-Si-H	17	56.68	0.17	0.76	10.69	7.74	0.24	0.07	20.40	0.11	0.38	0.15	0.23	2.09	ND	0.13
	Ca-Si-H	23	63.36	0.20	0.48	7.60	6.16	0.31	0.06	19.20	0.11	0.30	0.12	0.19	1.75	ND	0.09
	Ca-Si-H	30	68.69	0.17	0.58	8.25	6.44	0.27	0.04	13.69	0.08	0.22	0.08	0.11	1.04	ND	0.09
	Ca-Si-H	39	58.98	0.14	0.62	10.96	8.03	0.16	0.09	18.32	0.14	0.36	0.11	0.17	1.57	ND	0.14
	Ca-Si-H	48	63.14	0.18	1.72	19.36	3.19	0.11	0.14	8.94	ND	0.75	0.13	0.16	2.06	ND	0.08
	Ca-Si-H	63	59.38	0.28	0.35	17.68	3.89	0.13	0.03	16.11	0.09	0.31	0.15	0.10	1.28	ND	0.12
	Ca-Si-H	66	69.45	0.36	0.38	14.47	3.95	0.11	0.02	10.07	0.07	0.16	0.08	0.05	0.66	ND	0.10
	Ca-Si-H	69	62.32	0.22	0.33	18.34	4.16	0.11	ND	13.01	0.08	0.18	0.11	0.07	0.86	ND	0.12
	Ca-Si-H	72	66.14	0.24	0.36	18.80	2.81	ND	ND	10.45	0.07	0.15	0.09	0.05	0.65	ND	0.10
	Ca-Si-H/Ca$_2$SiO$_4$	75	71.34	0.07	ND	10.63	1.31	ND	ND	15.88	0.12	0.07	0.03	0.34	ND	ND	0.04
	Ca$_2$SiO$_4$	78	60.35	ND	0.19	11.95	1.35	ND	ND	25.41	0.17	ND	0.10	0.03	0.39	ND	0.05
	Ca$_2$SiO$_4$	83	59.63	ND	0.17	12.00	1.34	ND	ND	26.01	0.18	ND	0.10	0.04	0.40	ND	0.06
	Ca$_2$SiO$_4$	90	57.99	0.09	0.20	12.06	1.47	ND	ND	26.64	0.31	ND	0.13	0.10	0.77	ND	0.05

SI Table S4. Continued.

Size Fraction	Phase	Distance from surface (μm)	O	Mg	Al	Si	P	S	Cl	Ca mol %	Sc	Ti	V	Mn	Fe	Lu	W
	Ca-Si-H	0	73.76	0.16	1.49	13.59	1.77	0.06	0.51	6.55	0.05	0.40	0.06	0.09	1.52	ND	ND
	Ca-Si-H	1.5	65.11	0.17	1.71	18.65	2.69	0.06	0.16	8.55	0.53	ND	0.07	0.11	2.11	ND	0.08
	Ca-Si-H	9	61.02	0.20	0.89	13.36	6.78	0.14	0.11	14.76	0.12	0.41	0.12	0.17	1.82	ND	0.12
	Ca-Si-H	19	57.59	0.15	0.85	15.37	6.37	0.08	0.07	16.15	0.12	0.56	0.11	0.15	2.27	ND	0.16
	Ca-Si-H	28	61.18	0.12	0.61	11.91	7.34	ND	0.13	16.18	0.10	0.36	0.12	0.13	1.60	ND	0.13
	Ca-Si-H	38	58.24	0.09	0.44	9.96	8.76	ND	0.11	20.02	0.15	0.30	0.15	0.18	1.50	ND	0.08
	Ca-Si-H	56	58.36	0.19	0.40	9.75	8.50	0.38	0.05	19.96	0.13	0.26	0.15	0.17	1.38	ND	0.13
Gravel (2.0-5.0 mm)	Ca-Si-H	69	64.58	0.36	0.75	13.30	4.83	0.32	0.08	12.37	ND	0.32	0.12	0.24	2.21	ND	0.10
	Ca-Si-H	69	48.90	7.30	0.71	11.70	3.53	0.22	0.08	10.11	ND	0.22	0.08	2.38	14.04	ND	0.08
	Ca-Si-H	88	61.38	0.28	0.50	15.86	5.72	0.54	0.12	13.06	0.10	0.29	0.10	0.14	1.45	ND	0.10
	Ca-Si-H	106	65.82	0.28	0.37	12.77	5.28	0.58	0.13	12.74	0.07	0.24	0.10	0.12	1.13	ND	0.11
	Ca-Si-H	125	56.46	0.34	0.42	17.26	5.76	0.45	0.07	16.75	0.12	0.27	0.13	0.12	1.35	ND	0.15
	Ca-Si-H	144	57.79	0.38	0.39	17.90	5.40	0.32	0.04	15.45	0.11	0.28	0.14	0.08	1.22	ND	0.15
	Ca-Si-H/Ca$_2$SiO$_4$	156	50.21	ND	0.11	10.05	1.34	ND	ND	22.77	0.13	0.08	0.09	0.05	0.43	ND	ND
	Ca$_2$SiO$_4$	163	57.31	ND	0.17	11.82	1.45	ND	ND	28.11	0.17	0.10	0.16	0.04	0.56	ND	0.06
	Ca$_2$SiO$_5$	181	57.22	ND	0.10	12.30	1.46	ND	ND	28.14	0.20	ND	0.10	0.04	0.40	ND	0.05
	Ca$_2$SiO$_6$	206	57.16	ND	0.11	12.35	1.41	ND	ND	28.25	0.18	ND	0.11	0.02	0.37	ND	0.05

SI Table S4. Continued.

Size Fraction	Phase	Distance from surface (μm)	O	Mg	Al	Si	P	S	Cl	Ca mol %	Sc	Ti	V	Mn	Fe	Lu	W
Blocks (20 x 10 x 10 mm)	Ca-Si-H	0	70.66	0.13	1.47	11.50	3.73	0.06	0.07	9.73	0.05	0.73	0.10	0.08	1.57	ND	0.06
	Ca-Si-H	0	71.39	0.13	1.11	8.10	4.80	0.13	0.20	11.18	ND	0.65	0.30	0.19	1.74	ND	0.09
	Ca-Si-H	0	53.78	0.30	1.55	14.90	7.53	ND	0.19	18.02	ND	0.92	0.21	0.21	2.22	ND	0.12
	Ca-Si-H	1	56.62	0.39	0.72	14.84	4.74	0.11	0.17	19.38	ND	0.56	0.50	0.08	1.75	ND	0.13
	Ca-Si-H	2	63.87	0.46	0.56	13.48	4.37	ND	0.13	15.09	0.10	0.34	0.29	0.05	1.18	ND	0.07
	Ca-Si-H	2	51.53	0.71	0.97	13.99	4.39	0.53	0.28	21.52	0.14	0.72	0.65	0.41	4.01	ND	0.11
	Ca-Si-H	3	51.84	0.30	0.59	14.07	4.69	0.06	0.12	24.77	0.15	0.70	0.68	0.04	1.81	ND	0.17
	Ca-Si-H	8	56.87	0.33	0.62	14.09	4.80	ND	0.10	20.36	0.15	0.52	0.54	0.07	1.43	ND	0.13
	Ca-Si-H	15	54.30	0.24	0.87	15.19	4.47	ND	0.08	21.50	0.14	0.74	0.78	0.08	1.49	ND	0.12
	Ca-Si-H	24	42.35	0.16	1.41	16.55	3.41	0.12	0.08	28.32	0.15	1.62	1.48	0.24	3.98	ND	0.14
	Ca-Si-H	33	55.85	0.18	1.07	13.61	3.53	0.33	0.05	19.71	0.14	0.88	1.29	0.35	2.92	ND	0.10
	Ca-Si-H	42	50.52	0.24	0.86	16.16	3.89	ND	0.05	22.11	ND	1.04	1.30	0.55	3.13	ND	0.15
	Ca-Si-H	51	59.57	ND	0.46	11.84	1.64	ND	ND	24.50	0.16	0.41	0.69	0.05	0.62	ND	0.06
	Ca-Si-H	57	49.35	ND	0.93	13.02	3.27	0.04	ND	28.62	0.16	0.87	1.85	0.08	1.74	ND	0.09
	Ca-Si-H/Ca$_2$SiO$_4$	60	56.90	ND	0.77	11.31	1.75	0.05	ND	26.85	0.15	0.39	0.86	0.05	0.86	ND	0.06
	Ca$_2$SiO$_4$	63	51.03	ND	0.57	10.17	1.31	ND	ND	26.39	0.14	0.26	0.77	0.04	0.46	ND	0.07
	Ca$_2$SiO$_5$	72	55.65	ND	0.54	11.10	1.40	ND	ND	29.20	0.16	0.37	0.76	0.05	0.72	ND	0.06
	Ca$_2$SiO$_6$	78	56.15	ND	0.19	12.12	1.37	ND	ND	29.00	0.17	0.15	0.31	0.04	0.46	ND	0.05

SI Table S4. Continued.

| Size Fraction	Phase	Distance from surface (µm)	O	Mg	Al	Si	P	S	Cl	Ca mol %	Sc	Ti	V	Mn	Fe	Lu	W
Blocks (20 x 10 x 10 mm)	Ca-Si-H	0	65.12	0.31	0.62	11.67	3.68	ND	0.29	13.43	ND	0.31	0.28	1.20	2.96	ND	0.11
	Ca-Si-H	1	72.27	0.34	0.50	10.21	3.49	ND	0.10	11.39	ND	0.28	0.20	0.12	0.93	ND	0.07
	Ca-Si-H	4	56.29	0.29	1.12	14.85	4.17	0.15	0.15	18.64	0.10	0.60	0.54	0.72	2.31	ND	0.09
	Ca-Si-H	9	63.47	0.25	0.63	13.16	4.16	ND	0.13	15.44	0.11	0.46	0.41	0.27	1.39	ND	0.11
	Ca-Si-H	18	60.92	0.18	0.59	13.08	4.30	ND	0.14	18.01	0.10	0.56	0.59	0.11	1.32	ND	0.10
	Ca-Si-H	22	56.35	0.19	0.94	16.01	3.70	ND	0.05	18.89	0.11	1.00	0.98	0.13	1.51	ND	0.13
	Ca-Si-H	25	51.85	0.21	1.05	16.49	3.64	0.05	0.05	21.36	0.14	1.22	1.46	0.20	2.13	ND	0.11
	Ca-Si-H/Ca$_2$SiO$_4$	28	58.13	ND	0.58	11.57	1.52	ND	0.03	25.99	ND	0.51	0.79	0.06	0.75	ND	0.05
	Ca$_2$SiO$_4$	32	56.37	ND	0.23	12.19	1.26	ND	ND	28.84	0.17	0.13	0.26	0.04	0.43	ND	0.05
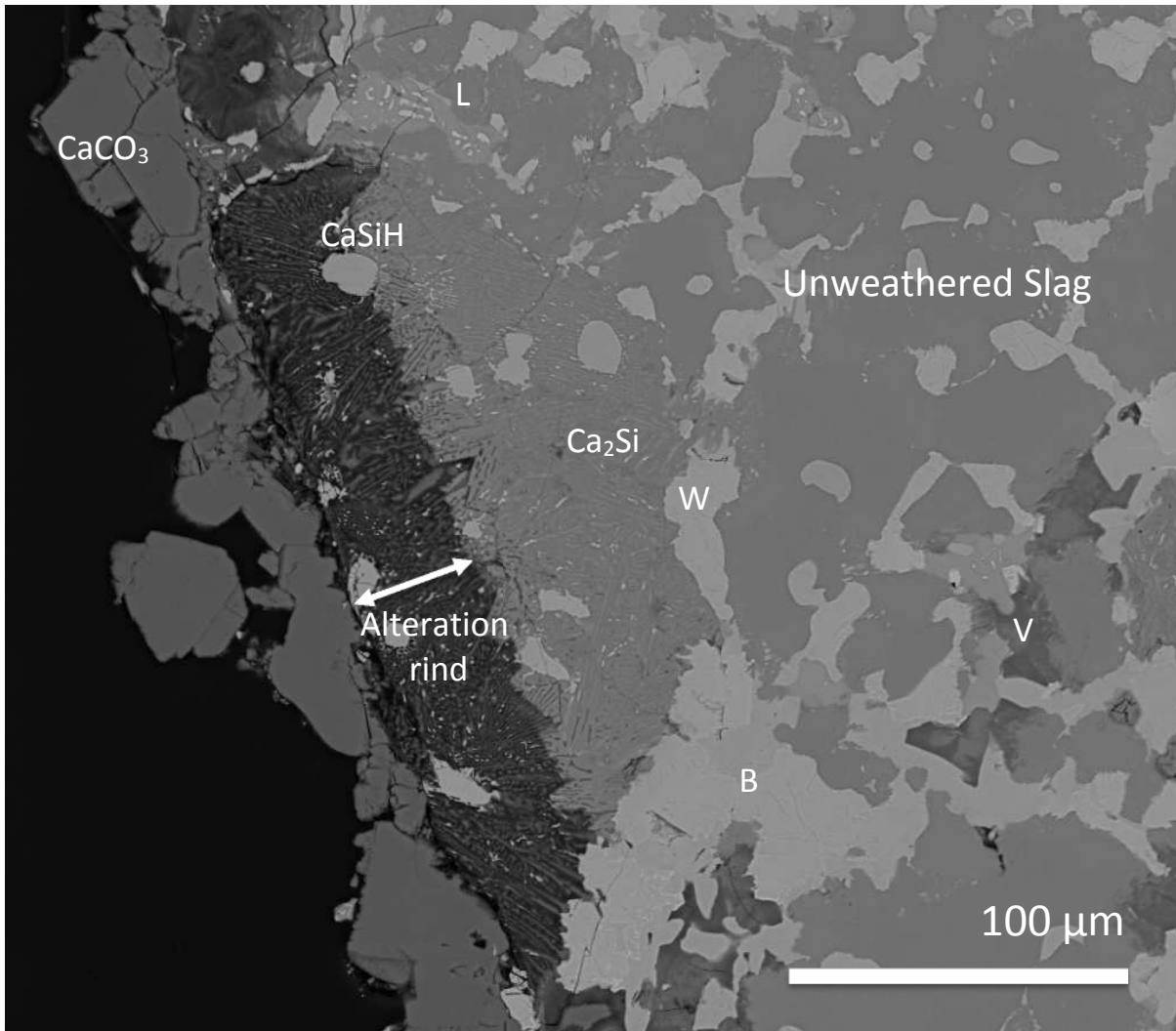
SI Figure S1. Example BSEI electron micrograph showing the primary (Ca_2S – larnite; B – Brownmillerite; L – Lime; W – Wusite; V – void space) and secondary Ca-Si-H and $CaCO_3$ phases present at the surface of the aerobically weathered 20 mm BOF slag blocks after 6 months total immersion. All phases where identified by EDS spot analysis of representative regions. Alteration depths were defined as the changed surface region within the original volume of the slag particle (presence of refractory phases allows good estimation of the original particle size); the thickness of any $CaCO_3$ layer was not included in the analysis.
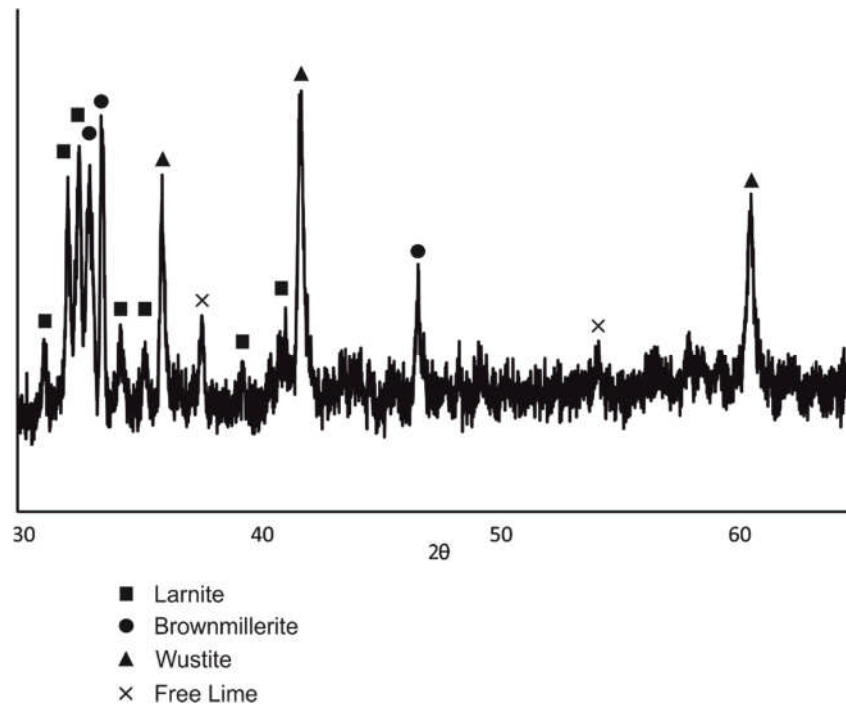
SI Figure S2. XRD pattern collected from the crushed steel slag sample annotated with major phase peaks detected.
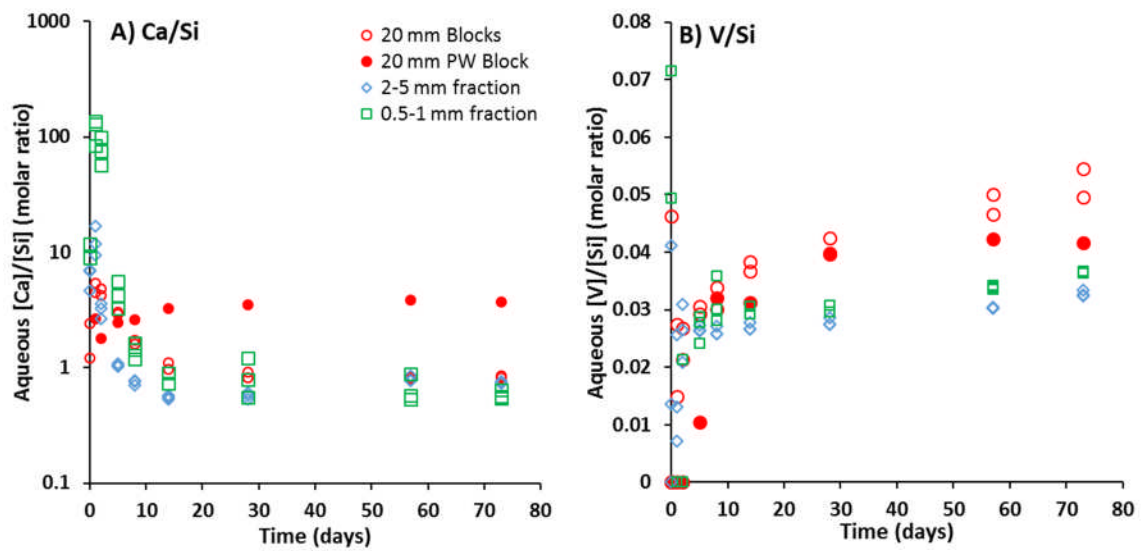
SI Figure S3. Elemental cross-plots showing; A) The relationships between aqueous [Ca] and [Si], and; B) Aqueous [Si] and [V] in individual replicates during the leaching tests.
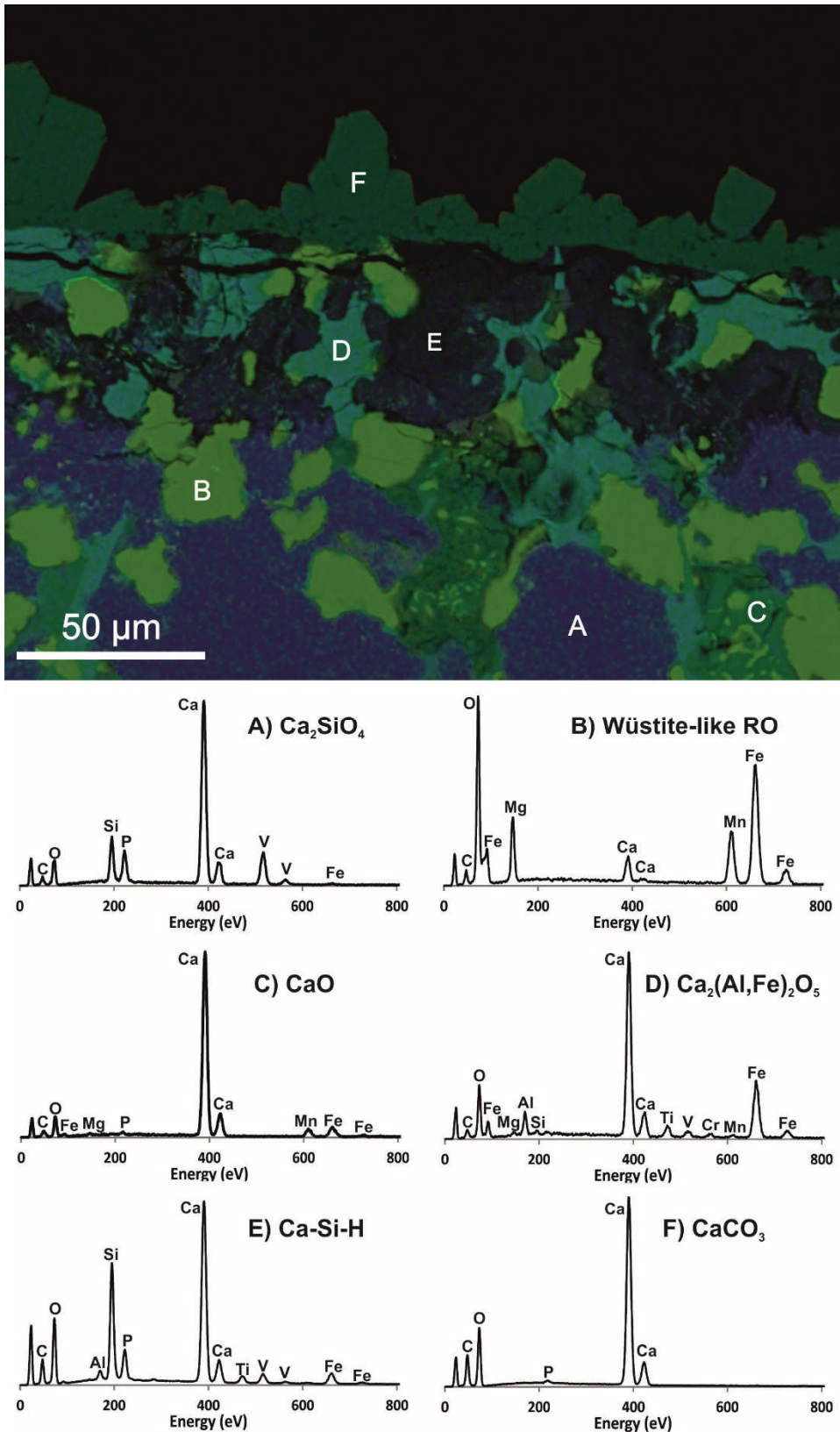
SI Figure S4. Composite false colour SEM-EDS elemental map showing phase discrimination within the 6 month pre-weathered BOF slag block. A-D) Example EDS spectra collected from each of the 6 major phases detected with the slag; and E-F) Example EDS spectra from neo-formed phases present in the altered surface layer.
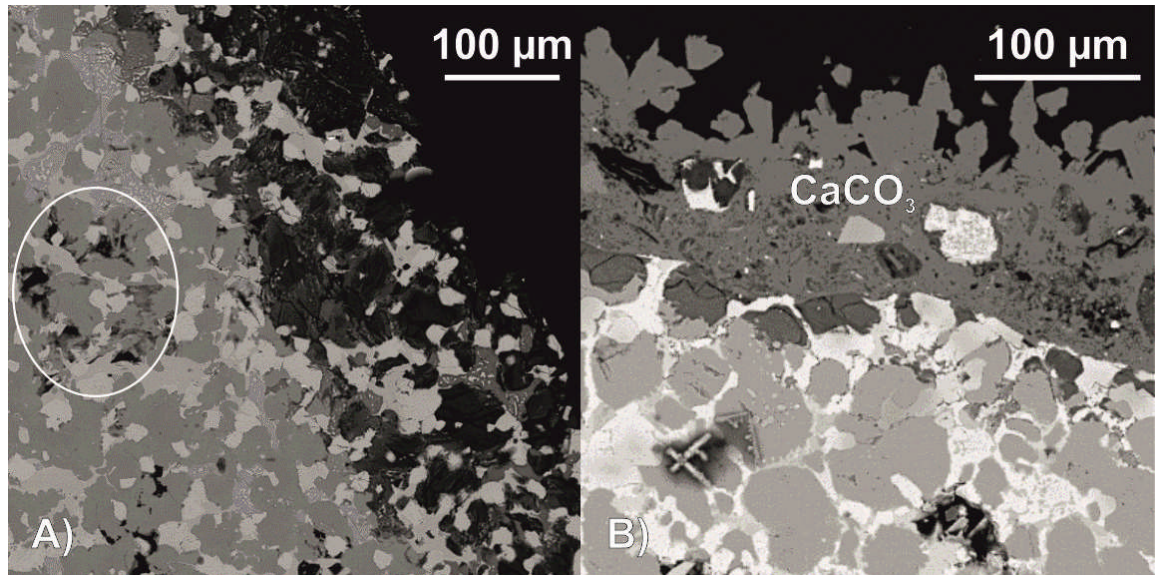
SI Figure S5. BSE images of different sized BOF slag particles after leaching for 73 days; (a) Block showing possible Ca-Si-H formation within occasional voids remote from the block surface, and (b) Sand-sized fraction showing $CaCO_3$ crystals on the weathered surface.

Appendix C   Conference presentations

This appendix provides a summary of all presentations given during the tenure of this PhD which have included contributions from the author.

Hobson, A. J., Stewart, D. I., Mortimer, R. J. G., Mayes, W. M., Rogerson, M., Burke, I. T., Leaching behaviour of a basic oxygen furnace steel slag: Implications for leachate chemistry and vanadium mobility, *Yorkshire Contaminated Land Forum, Sheffield, UK, 25 February 2015 (oral presentation, AJH)*

Hobson, A. J., Stewart, D. I., Mortimer, R. J. G., Mayes, W. M., Rogerson, M., Burke, I. T., Leaching behaviour of a basic oxygen furnace steel slag: Implications for leachate chemistry and vanadium mobility, *IPHEE Seminar Series, School of Civil Engineering, University of Leeds, Leeds, UK, 15 April 2015 (oral presentation, AJH)*

Hobson, A. J., Stewart, D. I., Bray, A. W., Mayes, W. M., Rogerson, M., Burke, I. T., Surface Leaching of Vanadium from BOF Steel Slag: a μXAS and SEM Study, *Geochemistry Group Research in Progress Meeting, School of Earth and Environment, University of Leeds, Leeds, UK, 30 – 31 March 2016 (oral presentation, AJH)*

Hobson A. J., Stewart D. I., Bray A. W., Mayes W. M., Rogerson M & Burke I. T., Surface Leaching of Vanadium from BOF Steel Slag: A μXAS and SEM Study, *Goldschmidt, Yokohama, Japan, 26 June – 1 July 2016 (oral presentation AJH)*

Hobson A. J., Stewart D. I., Bray A. W., Mayes W. M., Riley A & Burke I. T., Fate and Behaviour of Vanadium during the Aerobic Neutralisation of Alkaline Steel Slag Leachate, *Goldschmidt, Yokohama, Japan, 26 June – 1 July 2016 (oral presentation ITB)*